

UNIVERSITÄT BAYREUTH

WATER-CONTENT DEPENDENCE OF DISLOCATION MOBILITY OF
OLIVINE IN THE [100](010) SLIP SYSTEM

eingereicht bei der Bayreuther Graduiertenschule für Mathematik und Naturwissenschaften (BayNAT)
der Universität Bayreuth
zur Erlangung der Würde eines
Doktors der Naturwissenschaften
- Dr. rer. nat. -
Dissertation

vorgelegt von:

Stephan Blaha

supervised by
Prof. Dr. Tomo KATSURA



26.10.2016

Die vorliegende Arbeit wurde in der Zeit von 10/2011 bis 10/2016 in Bayreuth am Lehrstuhl Geowissenschaften unter Betreuung von Herrn Professor Dr. Tomo Katsura angefertigt.

Dissertation eingereicht am: 04.11.2016

Zulassung durch das Leitungsgremium: 07.11.2016

Wissenschaftliches Kolloquium: 09.02.2017

Amtierender Direktor: Prof. Dr. Stephan Kümmel

Prüfungsausschuss:

Prof. Dr. Tomo Katsura (Erstgutachter)

Prof. Dr. David Rubie (Zweitgutachter)

Prof. Dr. Hans Keppler (Vorsitz)

Dr. Hauke Marquart

Contents

1	Abstract	1
2	Introduction	4
2.1	Earth structure	4
2.2	Olivine	6
2.3	Plastic deformation in the Earth's upper mantle	7
2.3.1	Stress and strain	7
2.3.2	Creep models	9
2.3.3	Power-law creep	11
2.4	LPO in Earth's mantle	11
2.5	Dislocations	14
2.5.1	Properties of Dislocations	14
2.5.2	Dislocation motion	18
2.5.3	Dislocation immobilization and annihilation	20
2.5.4	Dislocation creep	21
2.6	Previous dislocation recovery experiments	22
2.6.1	Evaluation of dislocation mobility	24
2.7	Water in Olivine	25
2.7.1	Substitution mechanism	26
2.7.2	Previous hydration experiments of olivine	27
2.7.3	Already existing experimental olivine IR spectra	28
2.7.4	Influence of Hydrogen on the plastic deformation of olivine	30
2.8	Motivation	32
3	Experimental procedure	35
3.1	Starting Material	36
3.2	'Dry' and 'wet' experiments	37
3.2.1	Hydration	38
3.2.2	Deformation	39
3.2.3	Annealing	44
3.2.4	Annealing under hydrous conditions	45
3.2.5	Problems during hydrous experiments	45
4	Analytical Methods	48
4.1	Measurement of water content by FTIR-spectroscopy	48
4.2	Evaluation of water content	51

4.3	Scanning electron microscopy	54
4.3.1	EBSD-measurements	55
4.4	Oxidation decoration	57
4.5	Dislocation density	57
4.5.1	Calculating the dislocation density	59
5	Results	62
5.1	Deformation experiments	62
5.1.1	Observation plane	62
5.1.2	Dislocation structures of deformed samples	62
5.1.3	Spatial variation in dislocation density	70
5.1.4	Activation of other slip systems	78
5.2	Dislocation recovery experiments	83
5.2.1	Dislocation structures of annealed samples	83
5.2.2	Annealing time	83
5.2.3	Observation plane	83
5.2.4	Mobile dislocation density	94
5.2.5	Hydrostatic stress conditions	94
5.3	Dislocation densities	95
5.4	Dislocation microstructures	102
5.5	Water content	105
5.5.1	Hydration experiments	105
5.5.2	Deformation experiments	105
5.5.3	Annealing experiments	105
5.6	Water content vs. Dislocation annihilation rate	117
6	Discussion	120
6.1	Comparison with previous studies	120
6.1.1	Comparison to previous dislocation recovery experiments	120
6.1.2	Comparison of activation energies between recovery and deformation experiments	123
6.1.3	Comparison of the water effects with deformation experiments	125
6.2	Dislocation structures	129
6.3	Interpretation of hydrogen content	129
6.4	Geophysical applications	138
6.4.1	Strength models of the lithosphere	138
6.4.2	Influence of water on viscosity	139
6.4.3	Effect of water on strain rates in the upper mantle	140
6.4.4	Effect on hotspots	143
6.4.5	Extrapolation of single crystal data to aggregates	145
7	Conclusion	147
	Bibliography	148

8 Appendix	156
8.1 Matlab code	156

1 Abstract

The aim of this project is to study the water-content dependence of dislocation mobility in the [100](010) slip-system of olivine under upper-mantle conditions, namely at a pressure of 2.75 GPa and a temperature of 1500 K, using a multi-anvil apparatus. Since olivine is the most abundant mineral of the Earth's upper mantle, it is considered to control upper mantle rheology. Olivine is therefore targeted in this study. Plastic deformation of olivine is controlled by the motion of defects such as point defects, dislocations, and grain boundaries. In the upper mantle, dislocation creep is considered to be the dominant mechanism. Therefore, understanding of dislocation mobility in olivine is essential to investigate mantle dynamics.

Many deformation experiments demonstrated that creep rates dramatically increase by incorporation of water. However, deviatoric stresses and strain rates in deformation experiments are far higher than those in the upper mantle, and therefore those results should be examined by a technique independent from deformation experiments. Since the dislocation creep rate should be proportional to the dislocation mobility, water-content dependence independent of dislocation mobility of olivine is estimated by means of the dislocation-recovery technique in this study. In this technique, water-doped olivine crystals are deformed to form dislocations and then annealed under quasi-hydrostatic conditions. The dislocation annihilation rate is obtained by the following equation: $k = (1/\rho_f - 1/\rho_i)/t$, where ρ_i is the dislocation density before the annealing, ρ_f is the dislocation density after the annealing, k is the dislocation annihilation rate, and t is the duration of the annealing. The water-content dependence of the dislocation mobility is assumed identical to that of the dislocation annihilation rate. For these purposes the experimental setups were developed, which make it possible to dope water in an olivine single crystal, increase the dislocation density of a certain slip-system without the formation of sub-grains, and anneal the samples at quasi-hydrostatic conditions.

In the hydration experiments, up to 380 H_2O ppm by weight of water was successfully doped into olivine single crystals. The water doped olivine crystals were deformed in the [100] direction on the (010) slip plane to produce dislocations with densities from 4×10^{11} to $14 \times 10^{11} m^{-2}$. The deformed olivine crystals were annealed for 1 to 5 hours to decrease the dislocation density by 8 - 50 %. These data gave dislocation annihilation rates of $10^{-16.7}$ to $10^{-15.6} m^2/s$. The water-content exponent is found to be 0.17 ± 0.43 . Thus, the enhancement of the dislocation mobility by water incorporation is very small, or actually zero within the uncertainty. By examining the FT-IR spectra, it is found that the dislocation mobility is correlated with the intensity ratios of the peaks at 3612 and 3565 cm^{-1} and to those at 3170, 3320 and 3598 cm^{-1} rather than the total water content. Since the former and latter peaks are considered to be related to the hydration of Si and Mg sites, respectively, the dislocation mobility seems to be enhanced by the hydration of the Si sites, but suppressed by that of the Mg sites. The present results are in striking contrast with the results of deformation experiments, which gave a water-content exponent of 1.2. Although it has been

believed that presence of water should strongly enhance dynamic motion in the upper mantle, this paradigm is questioned by the present study together with the water-content dependence of the Si self-diffusion coefficients.

Ziel dieser Arbeit ist die Untersuchung des Einflusses von Wasser auf die Mobilität von Versetzungen des [100](010) Gleitsystems von Olivin unter Bedingungen des Erdmantels bei einem Druck von 2.75 GPa und einer Temperatur von 1500 K. Hierfür wird eine Viel-Stempel-Presse verwendet. Olivin ist das häufigste Mineral des oberen Erdmantels und daher wird angenommen, dass Olivine die rheologischen Eigenschaften in diesem Bereich des Mantels bestimmt. Aus diesem Grund wurde Olivine für diese Studie ausgewählt. Fehlstellen, Versetzungen und Korngrenzen haben einen großen Einfluss auf die plastische Deformation von Olivin. Unter den Bedingungen, die oberen Erdmantel herrschen, wird angenommen, dass Versetzungskriechen den größten Einfluss hat. Daher, um geologische Prozesse wie Konvektion besser verstehen zu können, ist es notwendig Versetzungskriechen von Olivin besser zu untersuchen.

In zahlreiche Deformationsexperimenten wurde festgestellt, dass durch die Anwesenheit von Wasser in Olivin-Aggregaten Versetzungskriechen stark zunimmt. Aufgrund dessen, dass Schubspannungen und Deformationsraten in Deformationsexperimenten um ein vielfaches höher sind als im Erdmantel, sollten Resultate von Deformationsexperimenten mit einer unabhängigen Methode untersucht werden. In dieser Studie wird die Methode des Temperns angewendet, um die Mobilität von Versetzungen und den Einfluss von Wasser auf diese in Olivin zu untersuchen. Hierbei werden mit Wasser angereicherte Olivinkristalle deformiert um Versetzungen zu erzeugen, welche in einem weiteren Experiment unter quasi hydrostatischen Bedingungen getempert werden. Die Rate der Versetzungsauflösung wurde auf folgende Weise berechnet: $k = (1/\rho_f - 1/\rho_i)/t$, wobei ρ_i die Versetzungsdichte vor und ρ_f die Versetzungsdichte nach dem Tempern ist. Die Zeit des Temperns ist t und k die Rate der Versetzungsauflösung. Es wird angenommen, dass die Abhängigkeit der Mobilität von Versetzungen vom Wassergehalt gleich der Rate von Versetzungsauflösung ist. Aus diesem Grund wurde ein experimenteller Aufbau entwickelt, der es ermöglicht den Wassergehalt in einem Olivin-Einkristall zu erhöhen, die Versetzungsdichte eines bestimmten Gleitsystems ohne das Ausbilden von Subkorngrenzen zu steigern und Proben unter quasi-hydrostatischen Bedingungen zu tempere. Hydratationsexperimente ermöglichen es den Wassergehalt in Olivin-Einkristallen bis zu 380 H_2O wt. ppm zu erhöhen. Diese Kristalle wurden in einem weiteren Schritt in [100]-Gleitrichtung und in der (010)-Gleitebene deformiert. Dabei wurden Versetzungsdichten von 4×10^{11} to $14 \times 10^{11} m^{-2}$ erreicht. Die deformierten Kristalle wurden zwischen 1 bis 5 h getempert, wobei sich die Versetzungsdichte um 8 bis 50 % erniedrigt. Diese Daten ergeben Raten für Versetzungsauflösung von $10^{-16.7}$ bis $10^{-15.6} m^2/s$. Der daraus resultierende Exponent des Wassergehaltes ist 0.17 ± 0.43 . Dies zeigt, dass die Zunahme der Mobilität von Versetzungen durch die Zugabe von Wasser nur sehr gering ausfällt, oder dass es sogar im Rahmen des Fehlers zu gar keiner Zunahme kommt. Untersuchungen durch FT-IR-Spektroskopie ergeben, dass die Mobilität der Versetzungen mit dem Verhältnissen der Intensitäten der Banden bei 3612 und 3565 cm^{-1} und denen bei 3170, 3320 und 3598 cm^{-1} und nicht mit dem totalen Wassergehalt in Verbindung steht. Es wird angenommen,

dass diese Gruppen von Banden mit der Hydratation von Si und Mg Fehlstellen korrelieren. Die Mobilität der Versetzungen scheint durch die Hydratation von Si-Fehlstellen zuzunehmen und durch die Hydratation von Mg-Fehlstellen gedämpft zu werden. Die Resultate dieser Studie stehen in einem großen Kontrast zu denjenigen von Deformationsexperimenten, welche einen Exponenten für die Abhängigkeit vom Wassergehalt von 1.2 ergeben. Obwohl generell angenommen wird, dass Wasser die dynamische Bewegung im Erdmantel stark fördert, muss diese Annahme aufgrund der Resultate dieser Studie in Verbindung mit Studien, die sich mit der Abhängigkeit der Diffusivität von Si in Olivin und dem Einfluss von Wasser auf diese beschäftigen, überdacht werden.

2 Introduction

2.1 Earth structure

The main seismological divisions of the Earth are the crust, the mantle and the core (Fig. 2.1). Usually the crust was described either as an outer layer of different composition or an outer layer of greater strength [Davies, 2000]. The border between the mantle and the crust is called the Mohorovicic Discontinuity (Moho), which is observed by seismology. The core-mantle boundary is at around 2900 km depth. The core itself can be divided in the liquid outer core and solid inner core which. It consists mostly of iron.

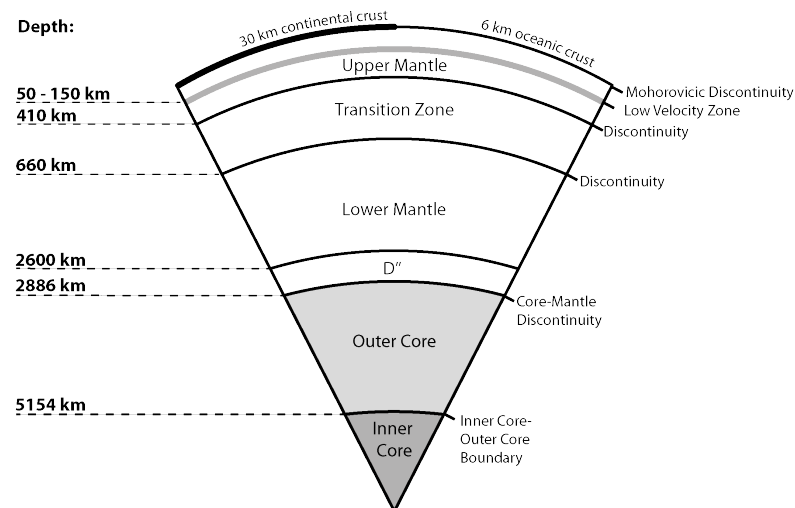


Figure 2.1: The main components of the Earth are the crust, the mantle, and the core. The continental crust is in average 30 km thick and has a silicic composition. The oceanic crust has a basaltic composition and an average thickness of about 6 km. The mantle features an ultrabasic composition. At depths of about 410 and 660 km, the mantle exhibits a major seismic discontinuity, the transition zone. The core-mantle discontinuity is located at a depth of 2886 km. The core consists of an outer liquid and an inner solid part.

The mantle can be seismologically divided into the following four layers, Fig. 2.2:

- Upper mantle: shallower than 410 km
- Transition zone: 410 ~ 660 km
- Lower Mantle: 660 ~ 2600 km
- D'' layer: 2600 ~ 2900 km

The upper mantle can be divided based on mechanical layering, which is the lithosphere-asthenosphere structure. The lithosphere is a strong and brittle layer with thickness of 50-200 km above the asthenosphere. The strength of the lithosphere is inferred from the high seismic wave velocity and low temperatures. It can be seen as the cool thermal boundary layer on the top of the mantle [Jackson, 2000]. The asthenosphere is considered to be a weak layer due to presence of the seismic low-velocity zone [Karato, 2008]. Direct samples of the upper 200 km of the earth mantle can be obtained as xenoliths in kimberlite and basalt, from which it is known that the composition of the upper mantle is mainly peridotitic. The major constituent of the mantle peridotite is olivine, and its volume fraction is 40-80%. The major constituting minerals other than olivine are Ca-poor and Ca-rich pyroxenes and smaller amounts of spinel and garnet [Jackson, 2000]. Within the mantle, there are two seismic jumps at 410 km and 660 km depth which are the borders of the transition zone [Davies, 2000]. The prevailing mineral assemblage is wadsleyite and ringwoodite. The lower mantle is dominated by bridgmanite and magnesiowustite and ranges over a depth of 660 to 2889 km. At the bottom 200 - 300 km of the lower mantle, seismic studies revealed changes in seismic velocity [Davies, 2000]. This region of the Earth is known as D'' layer.

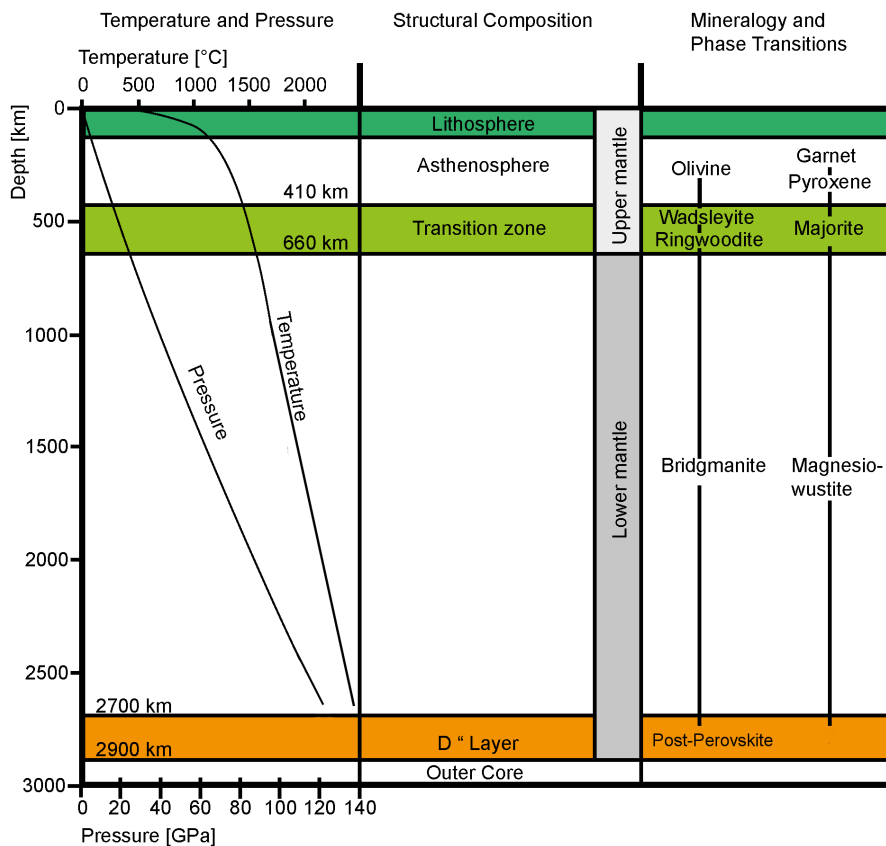


Figure 2.2: The main subsections of the Earth's mantle.

2.2 Olivine

Olivine is by far the most abundant mineral of the upper mantle. It is considered to be the weakest phase [Faul et al., 2011] and therefore, it is assumed that it controls the rheology of the upper mantle. For this reason, it has been clear for a long time that modelling the nature of convection above 400-km depth of the Earth's mantle requires reliable knowledge about the rheological properties of olivine [Couvy et al., 2004]. Furthermore, the lattice-preferred orientation (LPO) of this phase should control seismic anisotropy in the upper mantle. Flows of the mantle minerals develops LPO to cause anisotropic seismic wave propagation. In the case of olivine, the P-wave velocity travelling parallel to the a -axis is greater than perpendicular to the a -axis in olivine [Fowler, 2004]. Therefore, patterns of flow in the upper mantle can be identified by seismic studies if relations between flow and LPO of olivine is available from experimental studies. As we know from xenoliths, which are direct samples from the earth mantle, olivine is a solid-solution of the end-members forsterite Mg_2SiO_4 and fayalite Fe_2SiO_4 , and its approximate composition is $(Mg_{0.9}Fe_{0.1})_2SiO_4$. The olivine structure (Fig. 2.3) is orthorhombic, $Pbnm$, and exhibit two distinct octahedra, M1 and M2, and one silicate tetrahedron. The cell parameters of an ideal forsterite at ambient pressures and temperature are $a=0.475$ nm, $b=1.019$ nm and $c=0.597$ nm. The isolated silicon-oxygen tetrahedra are linked by (Mg, Fe) ions which are located at crystallographically different M-sites. M1 is in a centre of symmetry and M2 in a mirror plane. The Mg and Fe ions are surrounded by six nearest oxygen neighbours. The oxygen anions are arranged in a nearly hexagonal closed packing whose stacking planes are parallel to the (100) plane. There are three distinct oxygen sites, with O1 and O2 being located on the mirror, and O3 lying in a general position.

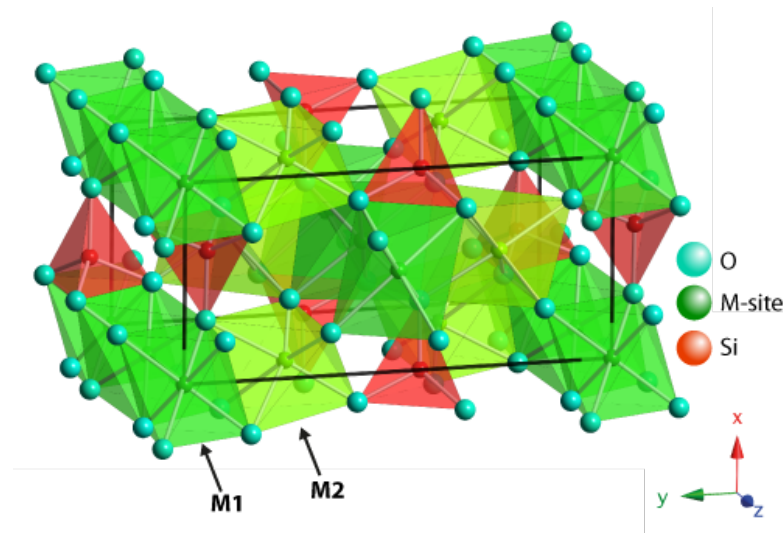


Figure 2.3: Olivine crystal structure with unit cell marked as black box. Silicon-oxygen tetrahedra shown in red and M-site octahedra in green. (Drawn with CrystalMaker)

2.3 Plastic deformation in the Earth's upper mantle

Plastic deformation is a transportation mechanism which is controlled by the motion of defects, such as point defects, dislocations and grain boundaries [Cordier, 2002].

2.3.1 Stress and strain

Deformation is the change of shape of a crystal caused by an external force. The change of shape is described by strain. Functions to produce a strain are called stresses that is caused by the external force.

Stress is the internal distribution and intensity of force acting on any point inside a geological media, such as a mineral [Gerya, 2010]. The reasons for the force can be various internal and external loads. Stresses can be expressed using a two-dimensional tensor, which is called stress tensor. The stress tensor composed of $3 \times 3 = 9$ stress components σ_{ij} 2.4:

$$\sigma_{ij} = \begin{pmatrix} \sigma_{11} & \sigma_{12} & \sigma_{13} \\ \sigma_{21} & \sigma_{22} & \sigma_{23} \\ \sigma_{31} & \sigma_{32} & \sigma_{33} \end{pmatrix} \quad (2.1)$$

where the first indices ($i = 1, 2, 3$) describe the axes in the directions of the stress component, and the second indices ($j = 1, 2, 3$) describe the axes in the directions of normal vectors on which the stress components work. Normal stresses forming the main diagonal of the matrix. The other components are the shear stress components.

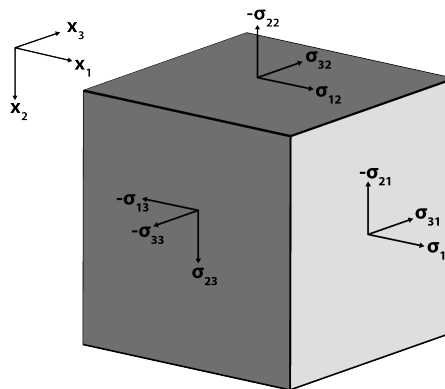


Figure 2.4: Components of the Stress tensor (black arrows) in three dimensions.

Strain γ quantifies the amount of deformation caused by stress acting on a geological media. It is defined by the change in length ΔL normalized to the initial length L of the deformed object [Gerya, 2010] and is applied for simple axial and shear deformation:

$$\gamma = \frac{\Delta L}{L} \quad (2.2)$$

When deformation is more complex, the strain tensor is defined as:

$$\epsilon_{i,j} = \frac{1}{2} \left(\frac{\delta u_i}{\delta x_j} + \frac{\delta u_j}{\delta x_i} \right) \quad (2.3)$$

where i and j are representing the coordinate indices (x, y) , and x_i and x_j are spatial coordinates. The displacement vector $u(x_i)$ characterises the movement of a point in the deformed material relative to its position before the deformation [Gerya, 2010]. If stresses are applied, a point of coordinates x_i moves by a displacement vector $u(x_i)$ [Poirier, 1985]. When the displacement of the points in a body is not uniform, it results in a gradient of displacement [Poirier, 1985]. This is shown in Fig: 2.5 where a cube deforms in a rhombus.

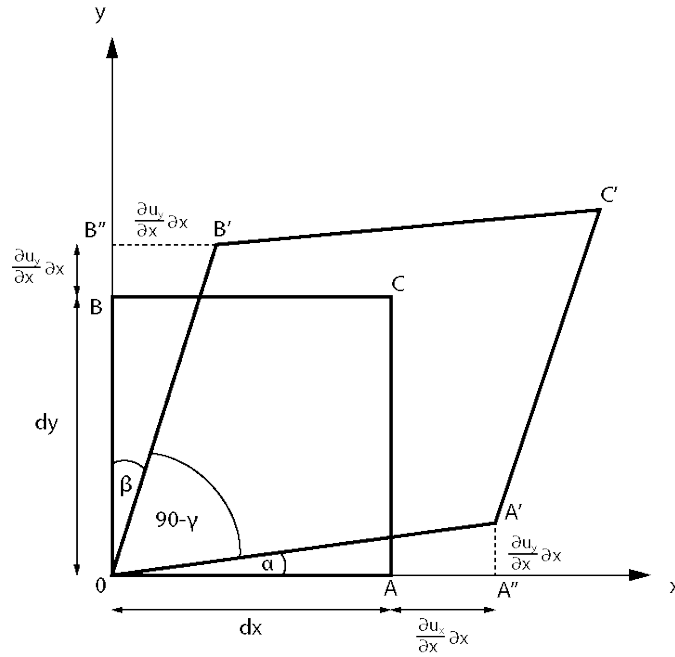


Figure 2.5: Display of strain involving shear in a two-dimensional space. An applied force causes the shape-change of the square $0ABC$ to the rhombus $0A'B'C'$.

The normal strain components for the 2D case are

$$\epsilon_{xx} = \frac{1}{2} \left(\frac{\delta u_x}{\delta x} + \frac{\delta u_x}{\delta x} \right) = \frac{\delta u_x}{\delta x} \quad (2.4)$$

$$\epsilon_{yy} = \frac{1}{2} \left(\frac{\delta u_y}{\delta y} + \frac{\delta u_y}{\delta y} \right) = \frac{\delta u_y}{\delta y} \quad (2.5)$$

and the shear strain components are defined as

$$\epsilon_{xy} = \epsilon_{yx} = \frac{1}{2} \left(\frac{\delta u_x}{\delta y} + \frac{\delta u_y}{\delta x} \right) \quad (2.6)$$

The deformation with time (t) is defined by strain-rate $\dot{\epsilon}$:

$$\dot{\epsilon}_{i,j} = \frac{d\epsilon_{i,j}}{dt} \quad (2.7)$$

The material constant viscosity η is the relationship between stress and strain rate in case of viscous flow (Eq. 2.8).

$$\sigma = \eta \dot{\epsilon} \quad (2.8)$$

For a linear viscous fluid, η is independent of stress (Newtonian viscosity). If the viscosity depends on the stress, the proportion between stress-strain is not linear (non-Newtonian viscosity.)

2.3.2 Creep models

In this project, the influence of water on dislocation creep is studied, and therefore this part mainly focuses on dislocation creep.

Diffusion creep model

Diffusion creep is dominant at relatively lower stresses and is the result of atoms moving along the boundaries (Coble creep) or through the interior (Nabarro-Herring creep) via vacancies due to stresses [Gerya, 2010]. As a result of diffusion, the grains deform and causing strain in rocks. Characteristic for diffusion creep is a linear (Newtonian) relationship between strain rate $\dot{\epsilon}$ and shear stress τ .

$$\dot{\epsilon} = A_{diff} \times \tau \quad (2.9)$$

A_{diff} is a proportional coefficient which depends on temperature, grain size, oxygen and water fugacity but not on stress [Gerya, 2010].

Dislocation creep model

Dislocation creep is typically active at higher stresses and is a result of dislocations moving through the crystal lattice. Because the dislocation density depends strongly on stress, dislocation creep shows a non-linear (non-Newtonian) relationship of strain rate on deviatoric stress:

$$\dot{\epsilon} = A_{disl} \times \tau^n \quad (2.10)$$

The proportional coefficient A_{disl} depends on pressure, temperature, oxygen and water fugacity in the case of olivine, and is independent from grain size and stress. The parameter n ($n > 1$) is called the stress exponent.

By using microscopic models, it is possible to give a physical basis to empirical constitutive relations. For dislocation creep, one of the most important properties is the average dislocation velocity in the Orowan's equation for stress- and temperature-dependent processes. Orowan [1934] described the mechanisms of plastic flow as a dynamical process and postulated a rate

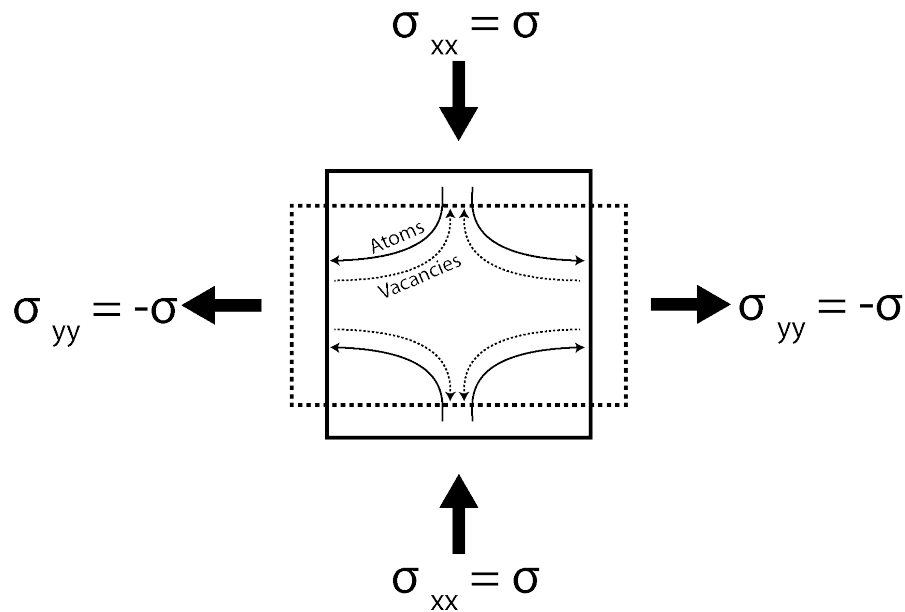


Figure 2.6: Principle of Nabarro-Herring creep. A vertical compressive stress and horizontal tensile stress cause diffusion of atoms from faces in tension to faces in compression and a flow of vacancies in the opposite sense. Because of diffusion, the original square transforms into a rectangular shape, marked by a dashed line.

equation: "The rate of glide flow will be determined by the number N of dislocations per unit volume and by their rate of propagation" [Gillis and Gilman, 1965]. The Orowan equation is:

$$\dot{\epsilon} = \rho b \bar{v} \quad (2.11)$$

where ρ is the density of mobile dislocations, b is the Burgers vector and \bar{v} is the average velocity of the dislocations. The Orowan equation connects the strain rate caused by glide or climb of mobile dislocations to the density, Burgers vector and velocity of the mobile dislocations [Poirier, 1985]. The average dislocation velocity \bar{v} can be further described as:

$$\bar{v} = \frac{\Delta L}{t_g + t_o} \quad (2.12)$$

where ΔL is the distance a dislocation glides after overcoming an obstacle in the time t_g and t_o is the time that is necessary to overcome the obstacle [Poirier, 1985].

Dislocation creep models can be further sub-divided into:

- Glide-controlled creep
- Climb-controlled creep

The concerning movements of dislocations are explained in section 2.5.2. In glide controlled creep, strain results from the glide of dislocations itself. The obstacles to dislocation

motion are in the scale of the dislocation core and are overcome by thermal activation assisted by stress [Poirier, 1985]. In this case, t_g and t_o are identical.

For recovery-controlled creep, the obstacles are formed by other dislocations. These obstacles are too large to be overcome by thermal agitation but they may disappear by diffusion controlled recovery [Poirier, 1985]. In this case, $t_g \ll t_o$ and t_o is controlled by the climb velocity of dislocations which is controlled by diffusion. Therefore, recovery-controlled creep is indirectly controlled by temperature.

2.3.3 Power-law creep

The Earth mantle behaves like a fluid in geological timescales and can therefore be described by a rate equation. The most important particular rate equation in the deformation of the material in the Earth's interior is the power-law creep [Jackson, 2000]. It describes the influence of temperature on dislocation creep.

$$\dot{\epsilon} = A\sigma^n d^{-m} \exp[-(E^* + PV)/RT] \quad (2.13)$$

where A is a constant, n is the stress exponent, d is the grain size, m is the grain-size exponent, E^* is the activation energy and V^* is the activation volume.

In the power-law creep model, strain rate is related to the n -th power of the stress ($n > 1$). Silicate polycrystals at high temperature ($T > 1/2 T_m$; T_m is the solidus temperature) and low stresses ($\sigma \simeq 10$ -100 MPa) show usually this non-Newtonian behaviour [Ranalli, 1995].

2.4 LPO in Earth's mantle

A lattice-preferred orientation (LPO) is a non-random distribution of crystallographic orientations of minerals in rocks. It is also called crystallographic-preferred orientation (CPO) or just fabric or texture. LPO is observed in naturally deformed rocks, also in samples directly from the mantle, such as peridotite xenolith. Two mechanisms can be responsible for the development of an LPO: deformation-induced lattice rotation and (re)crystallisation, Fig. 2.7 [Karato, 2008].

A deformation-induced LPO results from the deformation of crystals by slip and a lattice rotation due to constraints of neighbouring minerals. During dislocation slip, a crystal changes shape but does not rotate. But in polycrystalline material constraints, imposed by neighbours, are responsible for rotations which lead to the development of preferred orientations [Wenk and Christie, 1991]. The orientations of individual grains change by rotation relatively to an external reference frame, Fig. 2.8 [Karato, 2008].

Dynamic recrystallisation is controlled by formation of new grain boundaries and/or the migration of grain boundaries during deformation [Karato, 1987b]. Nucleation of new grains can either occur at pre-existing high-angle boundaries due to the accumulation of dislocations with the same Burger's vector which cause the formation of sub-grains. The misorientation increases with increasing strain. Or nucleation can be controlled by progressive misorientation of subgrains caused by the accumulation of dislocations at subboundaries. With increasing misfit angle, grain boundary energy increases and the grain boundaries become a favourable

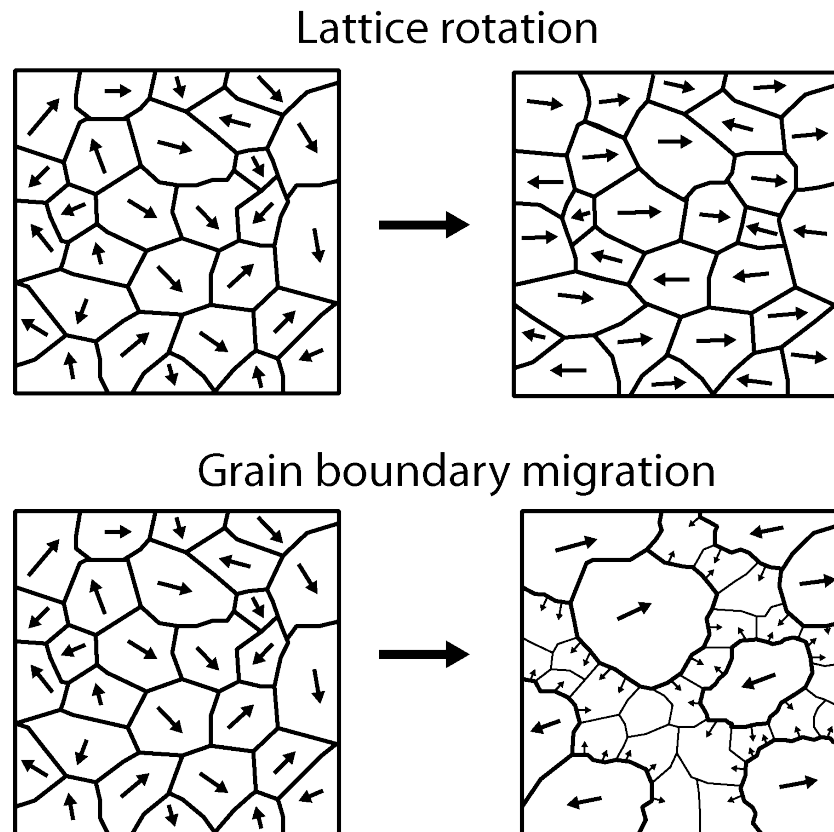


Figure 2.7: The mechanisms which cause a lattice preferred orientation are: Lattice rotation due to dislocation glide and grain boundary migration.

site for nucleation of new grains [Mitsuhiro Toriumi, 1985]. The development of a preferred orientation is caused by a selective-nucleation growth of new grains [Mitsuhiro Toriumi, 1985].

LPO can form by grain boundary migration when grains with a certain orientation grow at the expense of the others [Karato, 1987b]. Usually the boundaries migrate towards the grain with the higher dislocation density.

LPO in Olivine

Textural analysis of naturally deformed peridotites, including mantle xenoliths, shows the majority of olivine LPO has so-called A-type fabric [Katayama et al., 2004; Ismail and Mainprice, 1998]. Such LPO is supposed to be the major cause of seismic anisotropy in the upper mantle [Mainprice et al., 2000]. These anisotropies are indicated by azimuthal anisotropies shown by Pn travel time studies [Shearer, 2009] and SKS splitting studies [Ismail and Mainprice, 1998]. Seismic velocities in olivine are highly anisotropic in the different crystallographic axes (P-wave velocity for a -, b - and c -axis are 9.89, 7.73 and 8.43 km/s, respectively) [Kumazawa and Anderson, 1969]. Therefore, olivine crystals aligned along a

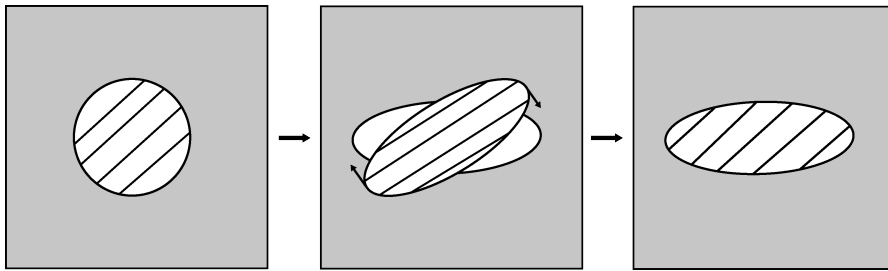


Figure 2.8: Illustration of constrained deformation of a single crystal with a single slip system (lines represent slip planes) in a polycrystalline material (indicated by grey box).

host-rock lineation and/or foliation, lead to a bulk anisotropy (Fig 2.9). By studying this anisotropy, it is possible to determine flow pattern in the mantle [Nataf et al., 1984].

Numerous experimental studies were conducted to investigate the development of LPO in olivine to understand the physical and chemical properties which control it [cf. [Jung and Karato, 2001; Faul et al., 2011; Katayama et al., 2004; Hansen et al., 2014]]. Dominant slip systems could be identified by determining crystallographic directions in deformed aggregates by electron backscatter diffraction (EBSD, chapter: 4.3.1). Main deformation fabrics proposed by the above studies are shown in the pole-figure plots in Fig. 5.1.

The five main fabrics in olivine aggregates are as follows [Karato et al., 2008]:

Name:	A-Type	B-Type	C-Type	D-Type	E-Type
slip system	[100](010)	[001](010)	[001](100)	[100](<i>Ok</i> l)	[100](001)

A-type fabric is the most frequent-appearing fabric in which the [100] axis of olivine is parallel to the shear direction and the (010) plane is parallel to the shear plane [Jung and Karato, 2001]. B-type fabric exhibits the [001] axis parallel to the shear direction and the (010) plane parallel to the shear plane. For C-type fabric, the [001] axis is subparallel to the shear direction and the (100) plane is subparallel to the shear plane. D-type fabric is not well defined and shows that the [100] axis is parallel to the shear direction, and the other two axes form a girdle normal to the shear directions. E-type fabric is characterised by the [100] axis subparallel to the shear direction and the (001) plane is subparallel to the shear plane.

These fabrics are observed by deformation under particular water content and stress conditions. A-type is typical for deformation under low-stress and low-water conditions and B-type is formed under water-rich and low stress conditions [Jung et al., 2006]. Ratteron (2007) notes that at pressures lower than 3 GPa and mantle temperatures higher than 1173 K, moderate differential stress ($\sigma \approx$ few hundred MPa or less), and in dry conditions, olivine 100 and [100](001) slip systems (a-slip) dominates the less active [001](010) and [001](100) systems (c-slip). The transition from a-slip to c-slip as assumed to occur at a pressure of 6 GPa [Ratteron et al., 2007]

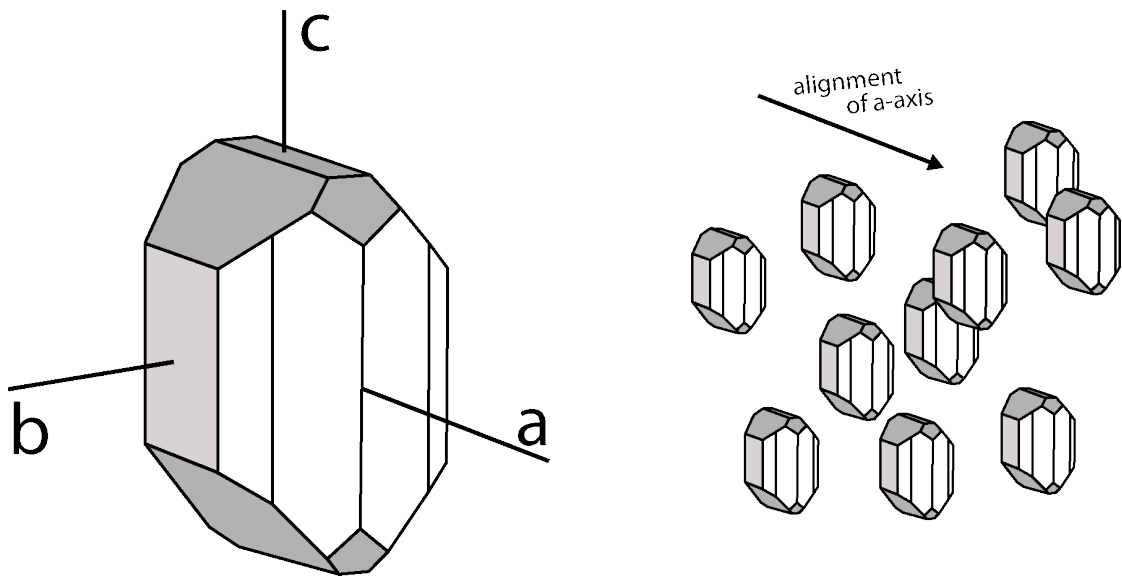


Figure 2.9: A single olivine crystal exhibit a strong anisotropy. If the crystals align with one or more of their axis in a rock, it causes a bulk anisotropy.

2.5 Dislocations

When creep of crystalline material is observed, it is necessary to understand the effects of lattice defects. The defects can be seen as breakages in crystal lattice. Defects are usually sub-divided into point defects, linear defects or planar defects. Dislocations are linear defects and occur as lattice imperfections along a line within the crystal. By describing the average motions of dislocations, it is possible to predict the macroscopic mechanical properties of materials. Because of the interaction of dislocations with all other types of defects, however, dislocation creep is a very complex process.

The idea of dislocations in crystals was introduced independently in 1934 by Orowan, Polany and Taylor to account for the plastic properties of matters. Two main observations lead to the idea of dislocations. First, it was observed that ductile deformation in crystals is inhomogeneous (i.e. it occurs in selected slip systems) and secondly, that the observed strength is much less than the theoretical strength [Ranalli, 1995]. This behaviour was explained by the assumption that slip appears by consecutive slip of rows of atoms along the slip plane, rather than by simultaneous slip of all atoms at the same time [Ranalli, 1995]. Therefore, dislocation motion through a crystal lattice cause shearing of the material by small steps, resulting in reasonable values for mechanical strength [Messerschmidt, 2010].

2.5.1 Properties of Dislocations

Dislocations are line defects in crystals and bounding areas where slip has already taken place. There are two special cases of dislocations, the edge and the screw dislocation, shown

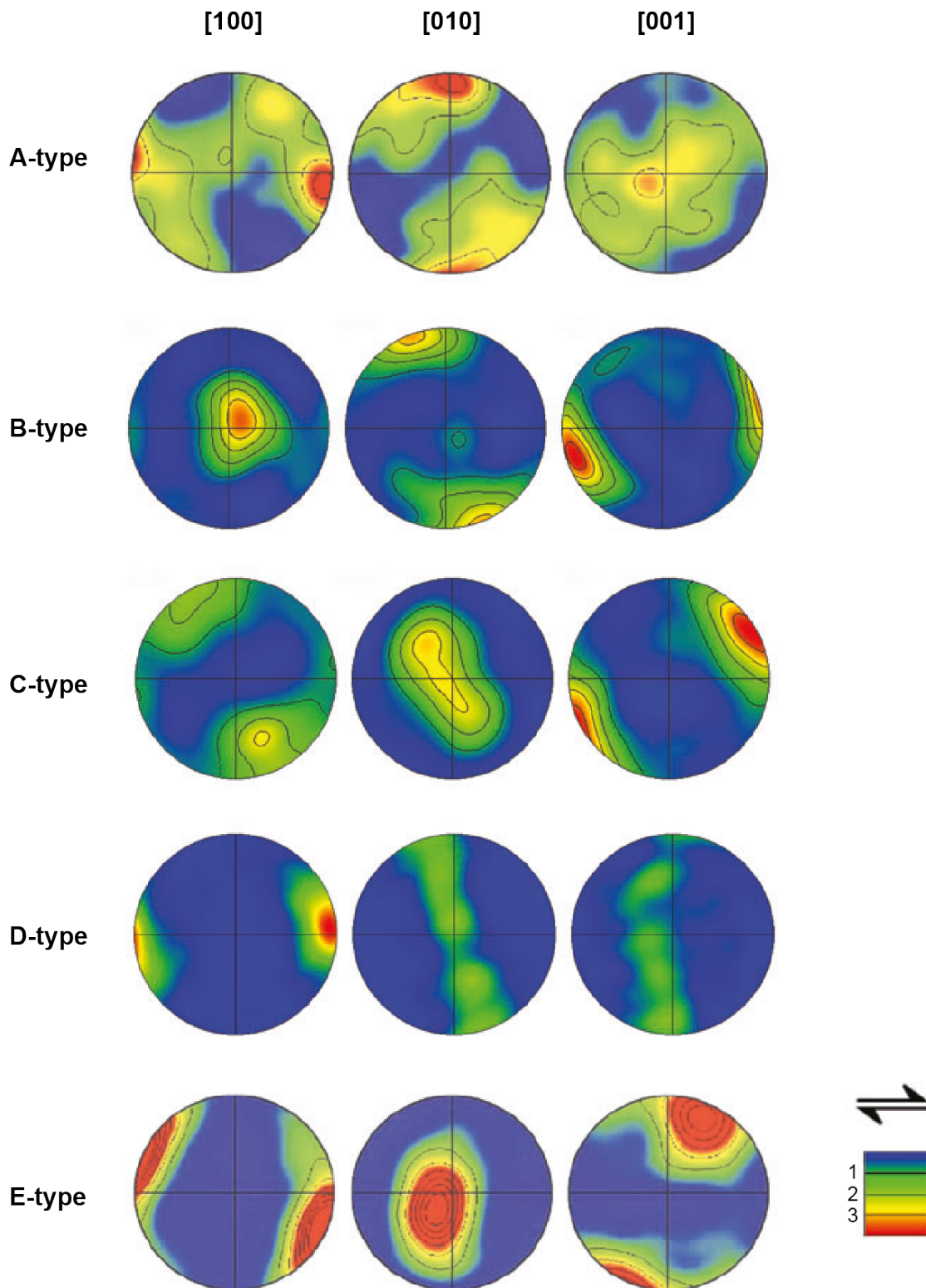


Figure 2.10: Pole-figure plots of the main five deformation textures in olivine [Karato et al., 2008]. Shear plane is horizontal and shear sense is dextral (indicated by the arrows on the right). The density of data is indicated by the color code (red, high; blue, low).

in Fig. 2.11 (the inserted extra half plain is shown by the full circles in case of the edge dislocation). The type of a dislocation is defined by the angle β between the Burgers vector b and the line vector ξ of the dislocation [Messerschmidt, 2010]. If b is normal to ξ ($\beta = 90^\circ$), it is called an edge dislocation. In case of a screw dislocation, the Burgers vector is parallel to ξ ($\beta = 0^\circ$). If the angle is between those two cases, the dislocation is called a mixed dislocation, Fig. 2.12.

A dislocation is characterized by a slip vector, the Burgers vector b . An exact definition of the Burgers vector is given by the Burgers circuit, shown in Fig. 2.13. The Burger circuit surrounds the dislocation and is divided in certain steps, Fig. 2.13 a. Start- and ending-point is A. If the same circuit is drawn in a perfect lattice for comparison, a vector b is necessary to close the circuit, Fig. 2.13b. This vector b is the Burger's vector.

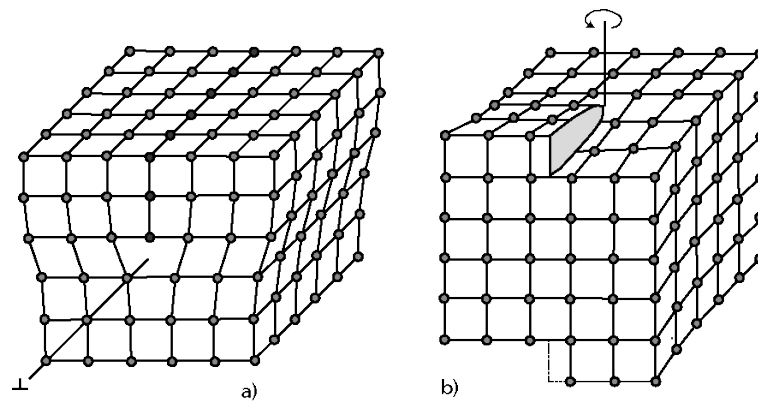


Figure 2.11: Graph of an edge a) and a screw b) dislocation in a cubic primitive lattice.

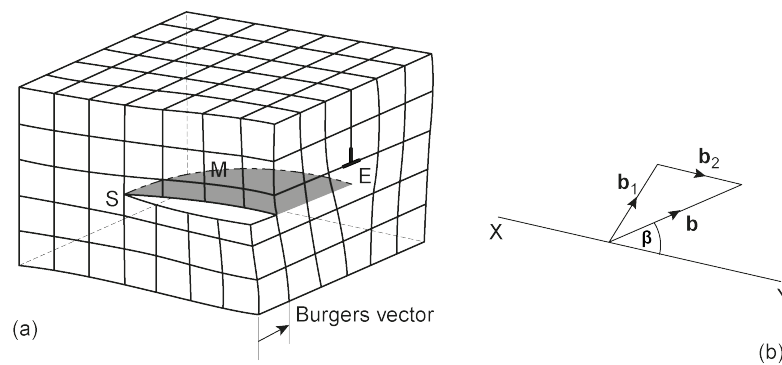


Figure 2.12: a) Plot shows a mixed dislocation, M. At point E it has a pure edge and at point S a pure screw character. b) mixed dislocation XY with a Burgers vector b which can be divided in an edge segment (b_1) and a screw segment (b_2).

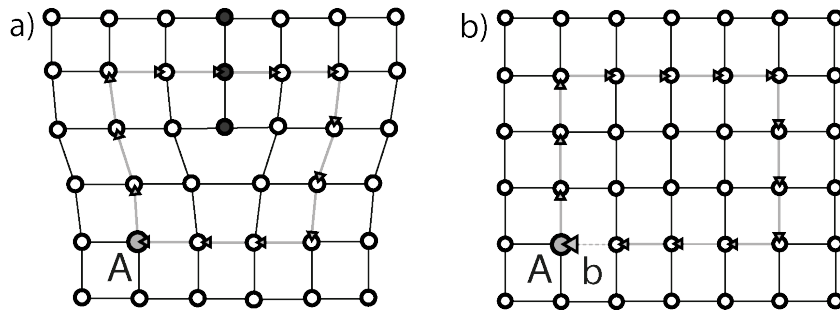


Figure 2.13: Definition of the Burgers vector by the Burgers circuit.

Slip planes in Olivine

The common Burger's vector in Olivine is in the $[100]$ ($b = 4.8 \times 10^{-10}$ m) direction, because this is the shortest lattice repeat. The most common slip systems at high pressure is slip in the $[100]$ direction in the (010) plane. However, the $[100]$ slip can be also active in $\{031\}$, $\{021\}$, $\{011\}$ and (001) [Cordier, 2002]. The (010) slip plane is shown in Fig. 2.14 and 2.15.

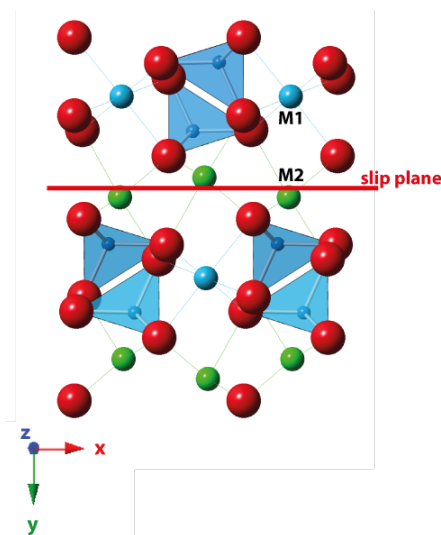


Figure 2.14: (010) slip plane in olivine shown in c-direction

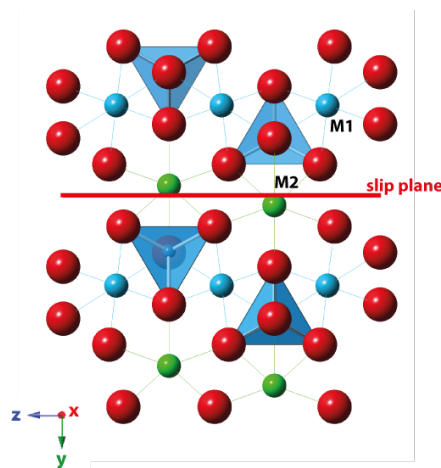


Figure 2.15: (010) slip plane in olivine shown in a-direction

2.5.2 Dislocation motion

Dislocation motion can happen by dislocation slip and dislocation climb. Generally, at lower temperatures plastic deformation is controlled by dislocation slip. At higher temperatures, point defects become mobile, start to interact with the dislocations and cause dislocation climb, which is the movement of a dislocation out of its slip plane [Cordier, 2002].

Another way to distinguish those two processes is by respect to the crystal volume. When the process is conservative in respect to the crystal volume ($dV = 0$), the motion occur by dislocation slip and when it is non conservative ($dV \neq 0$), the motion is climb controlled [Messerschmidt, 2010].

Dislocation slip

As mentioned above, if the dislocation moves in a plane which contains the Burgers vector and the line vector, the volume production is zero, Fig. 2.16. This plane is called the glide or slip plane. The slip plane is well defined for edge dislocation and mixed dislocations. For screw dislocations, any plane which contains the dislocation line can be the slip plane. Cross glide or cross slip is a process, which describes a motion of a screw dislocation from its glide plane into another glide plain, Fig. 2.17.

Dislocation climb

In case of an edge dislocation climb means movement of the dislocation in the plane normal to its slip plane. This process is usually slow and involves transport of matter by diffusion or from the extra half plane, Fig. 2.18 [Poirier, 1985]. Because screw dislocations have no extra half plane, they cannot climb.

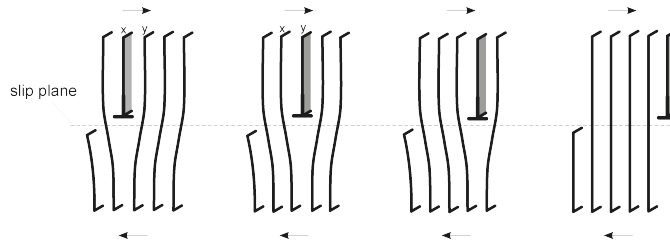


Figure 2.16: Glide of an edge dislocation through the crystal lattice.

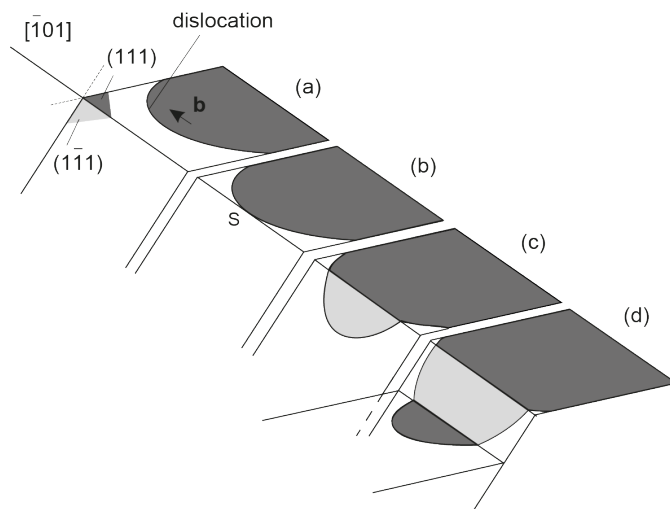


Figure 2.17: Cross slip of a dislocation in a face-centred metal. The development is given in four stages (a-d). At point b) the screw dislocation can change the slip plane which results in a non-planar slip surface.

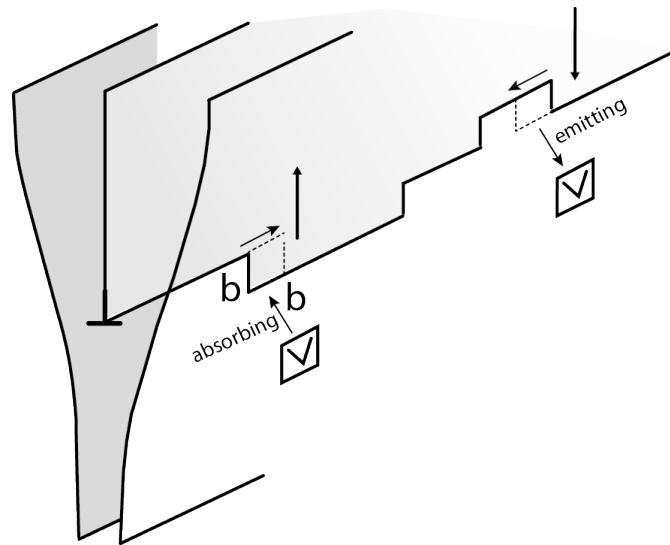


Figure 2.18: Climb of an edge dislocation. Climb occurs by the movement of jogs by absorbing or emitting vacancies.

2.5.3 Dislocation immobilization and annihilation

A dislocation can travel through a crystal in the case that the dislocation density is low and that no obstacles such as grain boundaries are in the way. It moves till reaching the surface and then disappears. In single crystals, dislocations can become immobile in regions of high internal stress caused by the presence of other dislocations [Messerschmidt, 2010]. Edge dislocations can reach equilibrium positions for equal and opposite signs of the Burgers vectors, Fig. 2.19. Dislocations with the same Burgers vector sign $b_2 = b_1$ form an array of dislocations, corresponding to the tilt boundary (Fig. 2.19a). For opposite signs of the Burgers vectors, the stable position is called edge dipole. Dipoles are created by dislocations with Burgers vector of opposite sign $b_2 = -b_1$ (Fig. 2.19b) [Messerschmidt, 2010]. The edge dislocation dipoles are stable in a position of 45° with respect to the direction of the Burgers vector. When dislocations form such equilibrium configurations, the stress field of one dislocation cancels out the stress field of another dislocation, which reduces the total strain energy [Messerschmidt, 2010]. These stress fields are caused by distortion of atomic planes in a crystal [Poirier, 1985]. The stress field becomes weaker with the distance r from the dislocation [Poirier, 1985]: $\sigma \propto \frac{\mu b}{r}$, where μ is the shear modulus.

Dislocation annihilation during high-temperature deformation is important also those due to internal stresses. Internal stresses enable the formation of low-energy dislocation structures and the annihilation of dislocations if this is not possible by glide or cross glide alone, thus contributing to recovery. Screw dislocations annihilate by cross-slip, if the attracting force is higher than the glide resistance on the cross-slip plane [Messerschmidt, 2010]. Non-screw dipole configurations can annihilate only by climb [Messerschmidt, 2010].

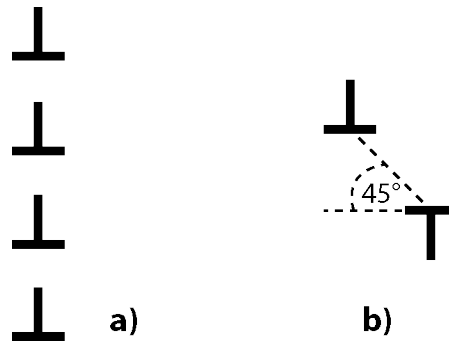


Figure 2.19: a) Subgrain boundary formed by edge dislocations with similar Burger's vector. b) Dislocation dipole formed by two dislocations with Burger's vector with opposite sign and an angle of 45° with respect to the direction of their Burgers vector.

Grain boundaries

Formation of subgrain boundaries or polygonization is one of the most common features during dislocation creep [Ranalli, 1995]. Subgrain boundaries are planar arrays of dislocations and separate areas in a crystal with misorientations less than 10° . Such grain boundaries are rows of edge type dislocations that have a Burgers vector of the same sign.

The misorientation-angle of the crystal lattice θ caused by such boundaries is inversely proportional to the dislocation spacing in the sub-boundary and is defined for tilt-walls as:

$$\frac{b}{D} = 2\text{Sin}\frac{\theta}{2} \quad (2.14)$$

where D is the spacing of the edge dislocations and b the Burgers vector [Poirier, 1985].

2.5.4 Dislocation creep

Dislocation creep refers to a steady state flow, which involves both a recovery process and the strain producing glide process. Over sixty years ago, it was already suggested that climb of dislocations is the rate-controlling step during high-temperature ($T > 2/3 T_m$, T_m = melting temperature) steady-state creep of crystalline materials [Weertman, 1955, 1957]. Glide alone would cause work hardening, from the tangling of dislocations gliding on intersecting planes or from obstacles in the glide plane [Tullis, 2002]. Therefore, steady state deformation is limited to high-temperature conditions where climb and dislocation annihilation is possible, because of diffusion [Messerschmidt, 2010].

One way of describing dislocation creep is by a power law, which describes the relation between strain rate $\dot{\epsilon}$ and differential stress $(\sigma_1 - \sigma_2)$ [Tullis, 2002].

$$\dot{\epsilon} = A(\sigma_1 - \sigma_2)^n \exp\left[-\frac{E}{RT}\right] \quad (2.15)$$

where A is a material parameter, n is called the stress exponent and has a value between 3 - 5. E is the activation energy, R the gas constant and T the absolute temperature.

2.6 Previous dislocation recovery experiments

In the last 40 years, several studies investigated dislocation annihilation rates of olivine in natural and synthetic, polycrystalline and single-crystal olivine, with various physical and chemical parameters by means of the dislocation recovery technique [cf. Toriumi and Karato, 1978; Kohlstedt et al. 1980; Karato and Ogawa, 1982; Karato and Sato, 1982; Karato et al., 1993; Farla et al., 2011].

In early studies, dislocation densities ρ were measured by optical microscopy [Toriumi and Karato, 1978; Karato and Ogawa, 1982] and TEM [Kohlstedt et al. 1980]. Later they were measured by SEM [Karato, 1987; Karato et al., 1993; Farla et al., 2010; Faul et al., 2011]. In the studies in which dislocations were observed using optical microscopy and SEM, dislocations were decorated by the oxidation decoration technique [Karato, 1987a]. The first SEM observation of dislocations with the oxidation decoration technique was reported by Karato [1987]. This study also described advantages of observation by SEM over optical microscopy and TEM. One of the advantages of SEM over optical microscopy is that this technique allows observing dislocations with density higher than 10^{12} m^{-2} . An advantage over TEM is that larger areal fractions of the sample can be observed, which makes it possible to calculate a robust average of dislocation density even when dislocations are heterogeneously distributed.

The work by Toriumi and Karato [1978] focused on naturally deformed samples, which were annealed at ambient pressure and temperatures between 1573 and 1773 K. The observed dislocation densities were between 10^{10} and 10^{11} m^{-2} . Few samples indicated densities above 10^{11} m^{-2} , especially from spinel-lherzolite. These dislocation densities were smaller than those in later studies. The use of optical microscopy in their study was suitable for determining such low dislocation densities, because observation of dislocations by optical microscopy is limited to a magnification of 1,000 times. When the dislocation density is higher, many dislocations could be missed.

Kohlstedt et al. [1980] studied the effect of pressure on dislocation annihilation. They pre-deformed their olivine crystals with compressional stresses in the $[101]^c$ direction, and therefore, dislocations with a $[100]$ or $[001]$ Burgers vector should have been activated in these crystals. The samples were annealed at temperatures of 1525 to 1675 K and pressures between 0.1 and 500 MPa. This study used a TEM to examine dislocation densities. It is mentioned that "dislocation density varied by less than 20 % from one micrograph to the next". This situation is similar to those by SEM observations. The determined dislocation densities in this study are in the order of 10^{10} m^{-2} . Kohlstedt et al. [1980] conducted the TEM observation at high magnification of 10,000 times and on small areas of $54 \mu\text{m}^2$. They obtained the activation energy and volume of $300 \pm 15 \text{ kJ/mol}$ and $11 \pm 1 \text{ cm}^3/\text{mol}$, respectively.

Karato and Ogawa [1982] observed dislocation density change of previously deformed olivine single crystals by optical microscopy with a 1,000-time magnification. As well as Kohlstedt et al. [1980] did, they applied a compressional stress on the olivine crystals in the $[101]^c$ direction. The initial dislocation density was $1 \sim 6 \times 10^{11} \text{ m}^{-2}$. They assumed the main slip system of $(010)[100]$. The goal of this study was to estimate the pressure effect

on dislocation annihilation. Therefore, the samples were annealed at high pressures up to 2 GPa using a piston cylinder apparatus. Temperatures were between 1673~1788 K. The dislocation densities were also below 10^{12} m^{-2} in this study. Therefore, the observation by optical microscopy was suitable for determining dislocation densities. Karato and Ogawa [1982] obtained the activation energy and volume of $390 \pm 60 \text{ kJ/mol}$ and $14 \pm 2 \text{ cm}^3/\text{mol}$, respectively.

Karato and Sato [1982] studied the effect of oxygen partial pressure on the dislocation annihilation rate of olivine. This study used the same deformed samples as Karato and Ogawa [1982], and the samples were observed by optical microscopy. The initial dislocation density was $1 \sim 2 \times 10^{11} \text{ m}^{-2}$. The goal of this project was to estimate effect of oxygen partial pressure on dislocation annihilation. Therefore, the samples were annealed at a different P_{O_2} . The temperature was 1627 K. The resulting log dislocation annihilation value k is between $1.4 \sim 6 \cdot 10^{-15} \text{ m}^2 \text{ s}^{-1}$ and it is decreasing with increasing P_{O_2} .

Karato et al. [1993] activated dislocations in the slip system (100)(010) in San Carlos olivine. They performed high-pressure annealing experiments in the pressure range between ambient pressure and 10 GPa and at temperatures of 1673 and 1773 K. Dislocation density was observed on the (001) plane. Furthermore, the silica activity was fixed at $a_{\text{opx}} = 1$ by co-existing with enstatite. The oxygen fugacity was controlled by the Ni-NiO buffer. The crystals were surrounded by NaCl during annealing to avoid their breakage during compression. The water contents were not controlled and not measured. It is assumed that their experiments were conducted in 'dry' environments. Total dislocation densities are in the orders of $10^{11} - 10^{12} \text{ m}^{-2}$. They obtained the activation volume of $6 \pm 1 \text{ cm}^3/\text{mol}$ by assuming the activation energy of 290 kJ/mol. Note that this activation energy was mainly obtained by comparing the data at ambient pressure and at pressures of 7 to 10 GPa.

Rubie et al. [1993] studied multianvil sample assemblies which provide sample environments in which the chemical environment is controlled and the stress is near-hydrostatic. Those assemblies were used in a 1200 tonne split-sphere multianvil apparatus to study the effect of pressure on the kinetics of dislocation recovery. They performed high-pressure annealing experiments of San-Carlos olivines up to a pressure of 10 GPa and at a temperature of 1673 K.

Farla et al. [2010] conducted dislocation recovery experiments of fine-grained San Carlos olivine at ambient pressure and temperatures between 1372 and 1772 K. Their annihilation rates were obtained from three-dimensional (3D) dislocation densities. The '3D data' means that dislocation density is estimated by measuring the cumulative lengths of dislocation lines and dividing them by the observation area and penetration depth of electron beams in the SEM observation [Farla et al., 2010]. They reported the activation energy of $360 \pm 80 \text{ kJ/mol}$.

Wang et al. [2016] compared annihilation rates of dislocations activated by [100](010) and [001](010) slip systems, which are called *a*- and *c*-dislocations, respectively, at ambient pressure and temperatures of 1450-1760 K. They reported that the annihilation rates of *c*-dislocations are by 0.3 orders of magnitude higher than those of *a*-dislocations. On the other hand, the activation energy of these two slip systems is identical, namely 400 kJ/mol.

The activation energy given by the above literatures are rather consistent, and in the

range of 350 to 400 kJ/mol. These values are significantly smaller than the activation energy obtained by deformation experiments, which is discussed later. Fig.6.1 b) shows pressure dependence of annihilation rates. Kohlstedt et al. [1980] and Karato and Ogawa [1982] provided significantly large activation volume, namely, 11 ± 1 and 14 ± 2 cm³/mol, respectively, whereas Karato et al. [1993] provided a relatively small one, namely 6 ± 1 cm³/mol. It is noted that the pressure ranges of Kohlstedt et al [1980] and Karato and Ogawa [1982] are relatively narrow, namely only up to 500 MPa and 2 GPa, whereas that of Karato et al. [1993] is up to 10 GPa. Therefore, it seems that a measurement over a narrow pressure range tends to exaggerate a pressure effect. It is possible that the real activation volume of dislocation annihilation rate constants of olivine would be even smaller than that given by Karato et al. [1993].

2.6.1 Evaluation of dislocation mobility

Following the work by Karato and Ogawa [1982], a second order kinetics is assumed for the evaluation of the kinetics of recovery of homogeneously distributed dislocations:

$$d\rho/dt = -k\rho^2 \quad (2.16)$$

where ρ is the dislocation density, t the annealing time and k is the dislocation annihilation rate. Dislocation recovery is controlled by annihilation of dislocation with opposite signs and is controlled by the mobility of the dislocation. Therefore, k is proportional to the dislocation mobility [Karato et al., 1993]. The annihilation rate was calculated by dividing the difference of the reciprocal dislocation density of the not annealed and annealed samples (ρ_i and ρ_f , respectively) by the annealing time:

$$k = (1/\rho_f - 1/\rho_i)/t \quad (2.17)$$

2.7 Water in Olivine

Water embedded as protons in the structure of nominally anhydrous minerals (NAM's) such as olivine, garnet and pyroxene, has substantial effects on many physical and chemical characteristics, even at very low concentration levels [Demouchy and Mackwell, 2006]. It may modify the mechanical strength of the host mineral, increase the internal rate of diffusion of ions, modifies the stoichiometry, influence the dielectric properties, change optical properties, and modify the response to radiation damage [Bell and Rossman, 1992].

The water contents of NAM's are usually measured by Fourier-Transformed infrared spectroscopy (FTIR spectroscopy), because it is one of the most sensitive techniques. Advantages of this method are that it provides site specific information and also that it is non-destructive [Bell et al., 2003]. This method is described in detail in chapter 4.1. Spectra can be collected in a unpolarized and polarized way. In case of polarized measurements a polarizer is used and spectra are taken to the three crystallographic axis of the sample. The directions of measurements are described by $E||a$, $E||b$ and $E||c$ which are the measurements parallel to the a-axis, the b-axis and the c-axis, respectively.

One of early experiments concerning the water solubility in olivine under mantle conditions was performed by Kohlstedt et al. in 1996. It was found that the water content increases with pressure (Fig. 2.20: open dots) and that the infrared bands were dominated by wave numbers of 3613, 3598, 3579 m^{-1} [Keppler and Bolfan-Casanova, 2006]. Water concentration in olivine can reach 0.6 - 0.8 wt% H_2O at conditions of 12 - 14 GPa and 1200 °C, demonstrated in studies of synthetic olivine (Fig. 2.20) [Jacobsen, 2006].

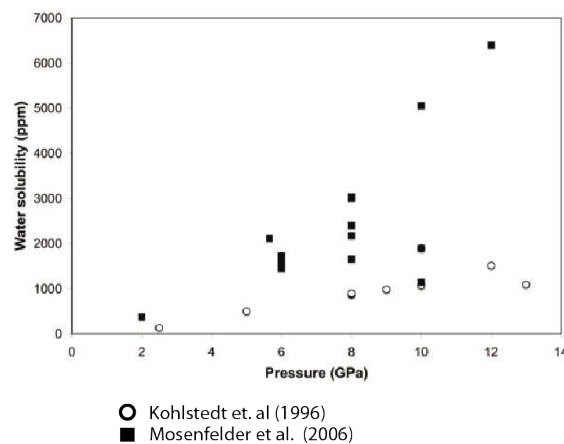


Figure 2.20: Water solubility in Olivine experimentally determined by Kohlstedt et al. (1996) and by Mosenfelder et al. (2006). Most of the experiments were carried out at 1100 °C and some between 1000 - 1300 °C by Mosenfelder. The difference between the two data-sets results from different infrared extinction coefficients; [Keppler and Bolfan-Casanova, 2006]

The incorporation of hydrogen in olivine is controlled by the chemical environment. Controlling parameters are silica activity and oxygen fugacity in addition to water fugacity.

Silica activity has a strong influence on the incorporation of hydroxyl groups in the olivine structure [Matveev et al., 2001], both on terms of defects substitution mechanism and absolute hydroxyl concentration. Olivine in equilibrium with magnesiowustite incorporates about a factor of 10 more hydroxyl than olivine coexisting with orthopyroxene.

Kröger-Vink-Notation

To describe vacancies, the so-called Kröger-Vink-Notation for defects is used. This notation makes it possible to clearly define a point defect and an effective charge compared to the perfect lattice.



- M ... atom species
- Y ... lattice site
- Z ... charge (• is + effective charge; " is effective 2- charge; X is neutral)

For example a vacancy at an M-site in Olivine would be written like V_M'' .

2.7.1 Substitution mechanism

There are four substitution mechanisms which are observed in natural mantle-derived olivine as well as in synthetic forsterite. Each of them can be identified by their characteristic bands in the infrared absorption mechanism and are related to Si vacancies ([Si]), Mg vacancies ([Mg]), octahedral Ti ([Ti]) and trivalent cations ([triv]) [Kovács et al., 2010].

The Kröger-Vink-Notation for protonated vacancies in olivine is:

- [Si] = $(4H)_{Si}^X$
- [Mg] = $(2H)_{Mg}^X$
- [Ti] = $\{(Ti^{4+})_{Si}'' (2H)_{Si}''\}$
- [triv] = $\{(Me^{3+})_{Mg}^\bullet (H)_{Mg}'\}$

By using FTIR-spectroscopy and the pleochroic behaviour of the OH absorption bands it is possible to set certain consideration about the orientation of OH dipoles. One example is the extremely strong pleochroism of three high energy "band doublets" in (010) caused by a preferred orientation in [100] [Libowitzky and Beran, 1995]. A possible vacancy for accommodation of proton is in the Si site. Oxygen at the O1 position is the donator oxygen and the OH bond is orientated along the O1-[Si] direction, as shown in Fig. 2.21 [Libowitzky and Beran, 1995]. Another possible donor oxygen of OH-dipoles lying near the O3-O1 tetrahedral edge and are more or less pointing towards a vacant M2 site [Beran and Libowitzky, 2006] This is suggested by a very strong absorbance features in the FTIR spectra that seems to correspond to protonation of octahedral edges, and polarisations are more consistent with protonation of M1 octahedral edges than of M2 edges. This protonation is

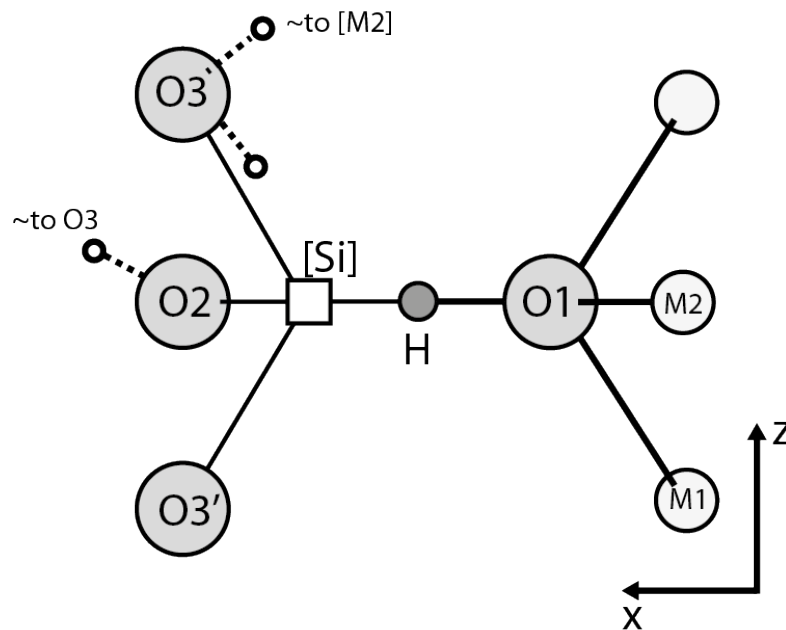


Figure 2.21: Diagram showing a Si vacancy in Olivine; possible OH-bonding orientations are shown.

supposed to be the dominant substitution mechanism for olivine hydration ($2H^+$ for Mg^{2+}) [Smyth et al., 2006]. O2 can also be an oxygen donor for an OH group which is oriented along the O2-O3 edge of a vacant M1 octahedron [Beran and Libowitzky, 2006]. So far there is still a debate which cation vacancy V_M or V_{Si} has a bigger influence on hydrogen solubility in olivine.

2.7.2 Previous hydration experiments of olivine

Many theories have been suggested to explain the incorporation of hydrogen in olivine. In several studies, the relations of the characteristics of FTIR-spectra of olivine with the chemical parameters were studied [cf. Miller et al, 1987; Zhao et al., 2004; Lemaire et al., 2004; Demouchy and Mackwell, 2006; Smyth et al., 2006; Mosenfelder et al. [2006]; Kovács et al., 2010]. Although the incorporation of hydrogen has been linked to certain point defects, the relations between the point defect species and chemical environment are still controversial [Mosenfelder et al., 2006], as reviewed below. The absorption peaks of olivine are usually classified in two groups. Group I is from 3640 to 3450 cm^{-1} and Group II from 3450 to 3170 cm^{-1} [Bai and Kohlstedt, 1993]. It is still not clear how those band groups are related to the cation vacancy (V_{M1} , V_{M2} and/or V_{Si}) and their relation to P , T , silica activity and oxygen fugacity [Beran and Libowitzky, 2006].

Zhao et al. [2004] studied the dependence of the solubility of water in olivine on

temperature and iron content. The main results are that hydrogen solubility increases with increasing iron content and also increases with increasing temperature [Zhao et al., 2004].

Lemaire et al. [2004] grew pure forsterite under hydrous conditions at 2 GPa at various Mg/Si (2.0 - 1.5) ratios and studied the influence of silicon activity on the incorporation mechanism of water in forsterite. It was shown that several bands indicate a significant change as a function of SiO_2 buffering conditions. They described that the bands at 3613, 3580, 3566, 3555, and 3480 cm^{-1} behave as a group, and are dominant in low-silica samples (LSA). The peaks at 3600, 3220 and 3160 cm^{-1} reveal large intensity changes relative to the above 5-peak group with the sample Mg/Si ratio. The peaks 3600 and 3220 cm^{-1} seem to behave as a pair, and are the most significant in high-silica samples (HSA). The broad band at 3160 cm^{-1} are not related to the 5-peak group and the paired peaks, and show a maximum intensity in medium-silica samples (MSA).

Demouchy and Mackwell [2006] studied the incorporation and diffusion of water in iron-bearing olivine. The silica activity of their experiments was buffered by San Carlos orthopyroxene powder. Experiments were performed at pressures of 0.2 and 1.5 GPa and temperatures of 1127 and 1227 K, respectively. The resulting spectra showed similarities to mantle peridotite xenoliths [Demouchy and Mackwell, 2006]. They observed infrared bands belonging to Group I and Group II. Group-I bands are dominant in measurement with $E \parallel a$. Group-II peaks have the largest intensities with $E \parallel c$ [Demouchy and Mackwell, 2006]. Kovács et al. [2010] analysed the substitution mechanisms and their associated vacancies of hydrogen in synthetic and natural olivine. They proposed four substitution mechanisms, which are associated with V_{Si} , V_{Mg} , V_{Ti} and V_{triv} . To generate different substitution mechanisms, they hydrated samples under periclase- and enstatite-buffered conditions. TiO_2 and Sc_2O_3 were added for [Ti] peaks and [triv] peaks, respectively [Kovács et al., 2010]. Each substitution mechanism produces characteristic peaks in the FTIR-spectra and can also be found in natural mantle-derived olivine and synthetic forsterite [Kovács et al., 2010]. The enstatite-buffered samples show Group II peaks at 3220 and 3170 cm^{-1} .

Smyth et al. [2006] investigated the effect of temperature and silica activity on the incorporation of water in olivine. The samples were synthesized at a pressure of 12 GPa, temperatures between 1327 and 1827 K and various silica activities. The maximum water content was attained at a temperature of 1427 K and the water contents are lower at higher temperatures [Smyth et al., 2006]. Further, Smyth et al. [2006] argued that the main substitution mechanism is $2H^+$ for Mg^{2+} for samples coexisting with and clinoenstatite and clinohumite. They therefore concluded that silica activity has little effect on the substitution mechanism under these conditions [Smyth et al., 2006].

Mosenfelder et al. [2006] studied the effect of pressure on incorporation of water in olivine. The main peaks were observed between 3500 and 3612 cm^{-1} , but Group II peaks are missing. This study stated no correlation between silica activity and Group II peaks.

2.7.3 Already existing experimental olivine IR spectra

Several studies investigated the hydroxyl-defect substitution in olivine. Table 2.1 shows a summary of results of Lemaire et al. [2004] and Berry et al. [2005].

$m (\pm 2 \text{ cm}^{-1})$	OH point defects	Maximum intensity	Pleochroism	Silica activity	Reference
3,613	VSi	High	$x \gg y$	LSA-MSA	Lemaire et al., 2004
3,600	VM2	High		HSA	Lemaire et al., 2004
3,580	VSi	High	$x > y$	LSA-MSA	Lemaire et al., 2004
3,566	VSi	High	$z \gg y$	LSA-MSA	Lemaire et al., 2004
3,555	VSi	High	$y \gg x$	LSA-MSA	Lemaire et al., 2004
3,572	Ti-clinohumite	point defect			Berry et al., 2005
3,542		Low	$y \gg z$	LSA-MSA	Lemaire et al., 2004
3,535		Low	y	LSA-MSA	Lemaire et al., 2004
3,527		Low	x	HSA	Lemaire et al., 2004
3,525	Ti-clinohumite	point defect			Berry et al., 2005
3,480		Low	$x \gg y \gg z$	LSA-MSA	Lemaire et al., 2004
3,402		Low	$z \gg x \quad yx = z$	LSA-HSA	Lemaire et al., 2004
3,355	Fe3+ defect				Berry et al., 2005
3,348		Low	$z > x > y$	LSA-HSA	Lemaire et al., 2004
3,325		Low	z	LSA-HSA	Lemaire et al., 2004
3,220	VM2	High	z	HSA	Lemaire et al., 2004
3,160	VM1	High	z	MSA	Lemaire et al., 2004
3,700		Low	z	HSA	Lemaire et al., 2004

Table 2.1: FTIR-spectra peak-positions and related vacancies in olivine. Cited study by Lemaire Lemaire et al. [2004] shows silican activity which is related to certain defects. Berry et al. studied the influence of Ti-clinohumite on incorporation of hydrogen in olivine Berry et al. [2005].

Several studies [*cf.* Smyth et al., 2006; Lemaire et al., 2004; Mosenfelder et al., 2006] identified the following main peaks: spectra show strong absorbance peak at 3612 and 3578 cm^{-1} . $E||b$ has a sharp feature 3578 and a much broader peak at 3552 cm^{-1} , and $E||c$ at 3566 cm^{-1} . Smith [Smyth et al., 2006] associate strong absorbance in the high frequency range of Group I with protonation of the octahedral edge.

Keppler and Bofan-Cassanova [Keppler and Bofan-Cassanova, 2006] presented a model for hydroxyl-defects with related vacancies:

- Silicon vacancies do not play an important role for dissolving hydrogen in olivine.
- The main dissolution mechanism of hydrogen in olivine is the substitution of Mg^{2+} by proton pairs. Especially at higher pressures (> 2 GPa) and under reasonably reducing conditions (Ni-NiO buffer, described by [Kohlstedt et al., 1996]). The main peak at 3600 cm^{-1} indicates this substitution mechanism
- The peaks in Group II are prominent in olivine sample equilibrium under high $aSiO_2$ and at relatively low pressures (< 2 GPa). Because the MgO activity is low, the density of Mg vacancies should be particularly high. The charge deficiency in the Mg sites is most likely balanced by oxidation of Fe^{2+} to Fe^{3+} and by simultaneous protonation. This can be seen by a peak around 3300 cm^{-1} .

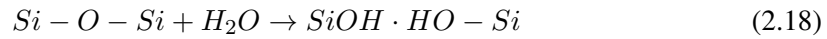
In order to investigate the effect of water on dislocation mobility, it is useful to understand the types of vacancies that dominate under particular physical and chemical conditions.

2.7.4 Influence of Hydrogen on the plastic deformation of olivine

Deformation experiments demonstrated that water enhances creep rate of olivine, *cf.* [Mackwell et al., 1985; Mei and Kohlstedt, 2000; Jung et al., 2006; Jung and Karato, 2001]. Two mechanisms have been proposed how hydrogen influences the strengths of NAM's. The first was *hydraulic weakening* for quartz by Griggs [Griggs, 1967] and has been confirmed also for other silicate minerals. It is based on the assumption that the Peierls stress is lowered by hydrolyzed Si-O-Si bridges [Kohlstedt, 2006]. For the second mechanism, the controlling interaction is between diffusion, point defects and dislocation climb [Kohlstedt, 2006]. Boioli et al. [2015] conducted dislocation dynamics simulation with coupling of dislocation glide and climb. Their simulation implies that, although the strain is mainly produced by dislocation glide, the creep rate is proportional to the ratio of the dimension of jammed dislocations to waiting time of dislocation climb [Boioli et al., 2015]. Since the jammed dimension is essentially constant, the dislocation creep rate is the function of dislocation climb rate [Wang et al., 2016]. Since dislocation climb is a diffusion-controlled process, and therefore, element diffusions should provide information about dislocation creep rates. In the silicate minerals, Si is usually the slowest diffusion species, and therefore, the Si self-diffusion should be vital for understanding dislocation creep.

In 1965, Griggs and Blair found that a small amount of water in quartz significantly reduce the high temperature strength of this mineral [Weertman and Weertman, 1975]. In

1967, Frank and Griggs proposed a dislocation double kink catalysis mechanism to explain this behaviour [Weertman and Weertman, 1975]. The proposed reaction is:



The idea is that the bonding between the two hydroxyls is weaker than the Si-O or Si-OH bonds and further a dislocation kink can form which moves where the Si - O - Si bridges have been hydrolysed [Weertman and Weertman, 1975]. Because kink migration is a controlling factor of dislocation glide, hydraulic weakening may be important at low temperatures.

At higher temperatures ($T > 2/3 T_m$, T_m = melting temperature), dislocation climb is the controlling mechanism for creep and it is strongly related to point defect migration. Point defect migration itself is enhanced by the presence of hydrogen [Mei and Kohlstedt, 2000]. Hence, dislocation climb rates will increase with increasing water content. The main argument in favour of dislocation climb in olivine being controlled by diffusion of the slowest ionic species (Si) are the nearly identical activation energies for creep under anhydrous and hydrous conditions, $E_c^{dry} = 530 \pm 40$ kJ/mol and $E_c^{wet} = 520 \pm 40$ kJ/mol, and those for self-diffusion of Si, $E_{Si}^{dry} = 530 \pm 40$ kJ/mol and $E_{Si}^{wet} = 450 \pm 50$ kJ/mol [Kohlstedt, 2006]. Furthermore, dislocation recovery rates, which require dislocation climb, in olivine increase by 4 and 15 times compared to samples annealed under dry conditions at pressured of 0.3 and 0.5 GPa [Mei and Kohlstedt, 2000].

Costa and Chakraborty [2008] and Fei et al. [2013] measured Si lattice diffusion coefficients in natural olivine and synthetic forsterite as a function of water content. Fei et al. [2013] suggested that the water-content exponent of Si lattice diffusion coefficient in forsterite is 0.32 ± 0.07 . This value is within the range of those of the dislocation annihilation rates (0.17 ± 0.43) obtained in this study. Although Costa and Chakraborty [2008] suggested a large water-content dependence for the Si lattice diffusion in natural olivine by comparing their measured values with ca 50 wt. ppm of water with those of dry olivine measured at ambient pressure by Dohmen et al. [2002], comparison of the diffusion coefficients of samples with 50 60 and 370 wt.ppm of water gives the water-content exponent of 0.23 ± 0.15 . This range is also in the present range of the water-content exponent of the dislocation annihilation rate. As discussed in Wang et al. [2016], the activation energy of dislocation annihilation rate is identical to that of the Si lattice diffusion (400 kJ/mol). These facts are consistent with the idea that the dislocation motion is controlled by Si lattice diffusion.

2.8 Motivation

The Earth's most outer part is called the crust. The interior is mainly divided into two parts, the inner part is called the core and the outer part is called the mantle. Information about the Earth's structure is obtained by seismological investigations. The composition is investigated by petrological and geochemical studies in combination with high-pressure and high-temperature experiments [Schubert et al., 2011]. Dynamic processes in the mantle are of great interest, because their strong connection to geological processes on the Earth's surface, such as volcanism, earthquakes and continental drift [Tackley, 2000]. Although the structure and composition are rather static, these features should change with time in the Earth's history as the results of dynamic processes in the mantle. Hence, understanding the dynamic processes in the mantle is one of the most important tasks for solid Earth geophysics.

Dynamic processes in the mantle are driven by viscous flow of solid rocks, because the mantle rocks behave as a viscous fluid on geological time scales. Theoretical studies showed that the geodynamic processes in the Earth's interior are controlled by rheological flow laws of constituent materials [Karato and Wu, 1993]. To utilise these flow laws in continuum-mechanical models of the Earth's mantle, it is essential to have knowledge of the rheological properties of Earth's materials, such as olivine. Olivine is the most abundant mineral and also considered to be the rheologically weakest phase in the upper mantle. Therefore, it should control the rheology of the upper mantle.

Rheological properties of olivine were studied in numerous deformation experiments, cf. [Chopra and Paterson, 1981; Bai et al., 1991; Raterron et al., 2007; Kohlstedt et al., 1980; Demouchy et al., 2009]. Many studies paid attention especially to the effect of water on various physical and chemical parameters of olivine. Their results indicated that even a small amount of hydrogen (> 0.005 wt.%) has a large effect on viscosity of olivine [Mackwell et al., 1985; Mei and Kohlstedt, 2000]. Similar phenomena were also observed in electrical conductivity studies [Wang et al., 2006]. Mackwell et al. [1985] reported a strength reduction of hydrothermally treated olivine single crystal by a factor of 1.5 - 2.5. Mei and Kohlstedt [2000] demonstrated that creep of olivine increase at a water fugacity (i.e. water concentration) of 300 MPa by 5-6 times higher than those with no water. Within the observed water fugacity, it leads to a proportion of water fugacity to strain $\dot{\epsilon} \propto f_{H_2O}^r$, where r is 0.69 - 1.25 [Hirth and Kohlstedt, 2003].

Geophysical observations indicate that the upper mantle exhibits seismic anisotropy. This can be observed from a azimuthal anisotropy of Pn velocities in the oceanic mantle [Ismail and Mainprice, 1998] and from polarisation anisotropy in long-period surface waves [Aki and Kaminuma, 1963; Nataf et al., 1984; Ismail and Mainprice, 1998]. The studies of long-period surface waves demonstrated that azimuthal and SH/SV polarisation anisotropy were observed globally, especially in the upper 200 km of the sub-continental mantle [Nataf et al., 1984]. Strong seismic anisotropy may be an indication of flow dynamics controlled by dislocation creep [Jackson, 2000]. It is assumed that this anisotropy is due to the statistical alignment of the crystal axis of the dominant phases, which are olivine and orthopyroxen [Ismail and Mainprice, 1998]. Such an alignment is also called lattice-preferred orientation (LPO). Understanding which physical and chemical conditions forming such an alignment makes it

possible to interpret processes in the mantle better. Natural samples indicate a correlation between water and olivine lattice preferred orientation [Skemer et al., 2013]. Furthermore, deformation experiments demonstrated that water incorporation into olivine changes the LPO patterns in olivine [Jung et al., 2006; Jung and Karato, 2001]. Different LPO pattern can be produced by different water content dependence of dislocation creep rate in different slip systems. Actually, Mackwell et al. [1985] showed that the water content dependence of creep rate is different in different shear geometries.

However, deformation experiments have certain drawbacks, because, in order to estimate the viscosity of rocks in Earth processes, the results of experiments in the laboratory undertaken on small samples (< 1 cm) and convenient time scales (1 day) are extrapolated over many orders of magnitudes to scales corresponding to geological processes (10 - 10^3 km, 10^5 - 10^6 years). Therefore the results obtained by deformation experiments must be examined in an independent way. Dislocation recovery experiment is one method to examine the results of deformation experiments. In this method, decrease in dislocation density by annealing under hydrostatic conditions is observed. The rate of dislocation density change should be proportional to the dislocation mobility, which should control the dislocation creep rate.

One advantage of this method compared to deformation experiments is that information of strain rate and deviatoric stress, which are difficult to measure, are unnecessary. Another advantage is that dislocation annealing is conducted under quasi-hydrostatic/low-differential stress conditions. Such conditions are more relevant to simulate the Earth's interior than the high-stress conditions in deformation apparatus. A third reason is dislocation recovery experiments can be conducted under well-controlled thermodynamic conditions. This advantage is particularly useful to examine the water content dependence.

Si-self diffusion is another way to examine results of deformation experiments. Since the rate-limiting process of dislocation creep is dislocation climb, and dislocation climb is a diffusion-controlled process. This method has similar advantages to deformation experiments as the dislocation recovery experiment. Fei et al. [2013] investigated the water content dependence of Si self-diffusion rate in synthetic forsterite, and showed that the Si-diffusion coefficient is proportional to only $1/3$ power of the water content. Based on this observation that the exponent is significant lower than expected from deformation experiments, Fei et al. [2013] raised a possibility that the deformation experiment may have overestimated the water content dependence of strain rate. However, the relations between creep rate and Si self-diffusion coefficient are rather indirect, and therefore it is also questionable whether the results of Si self-diffusion coefficients are essential. Particularly, although the formation and motion of dislocation are specific to slip systems, the Si self-diffusion coefficients are isotropic, and does not provide any information about each slip system. On the other hand, the dislocation recovery experiment measures dislocation mobility, which is more direct information to investigate the effects of water on creep rate than the Si self-diffusion coefficient measurement. In particular, the dislocation recovery experiment allows us to investigate dislocation dynamics in each slip system.

The goal of dislocation recovery experiments is to understand the dislocation microstructures and the effect of different physical and chemical parameters on them. The present study focuses on water content dependence of mobility of dislocations in the $[100](010)$ slip system

using single crystals. Use of single crystal samples is beneficial because grain boundaries may affect dislocation recovery rates, which is suggested by comparison of previous dislocation recovery experiments using single-crystal and polycrystalline samples. The [100](010)-slip system was chosen as a target slip system because, it is known from observations of xenoliths, which are direct samples of the uppermost mantle, that it is the most dominant slip system in olivine at this part of the Earth's mantle. We will compare the water content dependence obtained by dislocation recovery experiment with that obtained by deformation experiment and Si-self diffusion experiment. Based on this comparison, we will investigate how creep rate depends on the water content in the upper mantle. Creep rates are known to be strongly related to dislocation creep, which is assumed to be the main non-elastic transport mechanism in the upper 400 km of the Earth. To understand creep rates render possible to understand numerous geophysical phenomena, such as convection, seismic attenuation, and the response of Earth's surface to transition loads such as glaciation and earthquakes. Finally we investigate the dynamics of the mantle under the western U.S. as a test locality [Freed and Bürgmann, 2004; Dixon et al., 2004].

3 Experimental procedure

To observe the changes in dislocation density, several experimental and analytical steps are necessary. Those steps are show in Fig. 3.1, and are explained in the following sections.

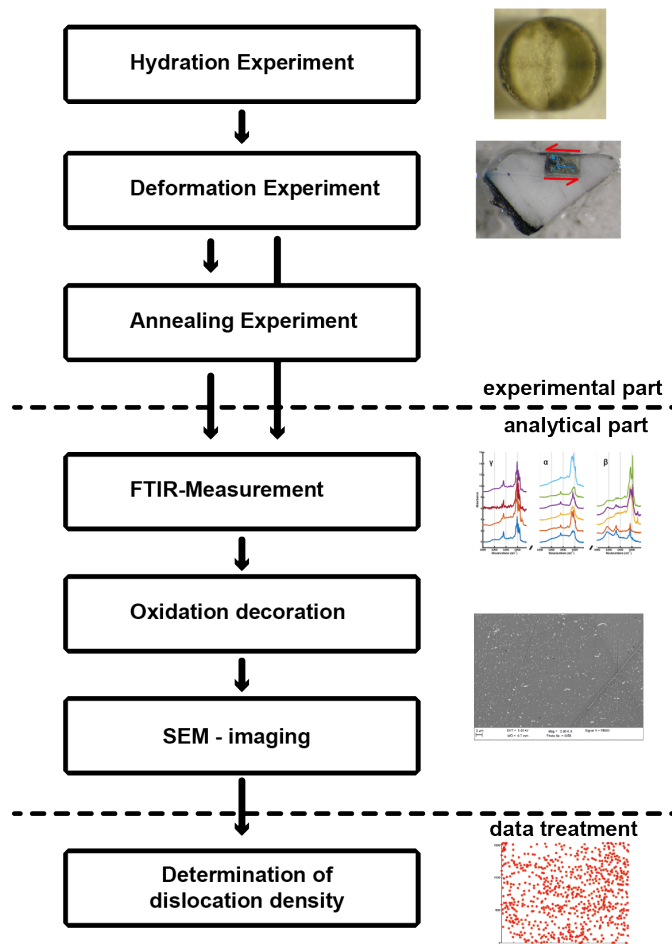


Figure 3.1: Sequence of the experimental and analytical steps, which are necessary to reach the calculation of dislocation density and the related hydrogen content.

3.1 Starting Material

The starting material was natural olivine single crystals from Pakistan with sizes between 1 and 3 cm (Fig. 3.2 a), whose compositions were measured by an electron microprobe. The results (Table 3.1) reveal that the compositions of these olivine crystals are similar to that of San Carlos olivine. To orient the crystals, cleavage planes, usually consistent with the (100) plane, were polished and the orientations of all three crystallographic axis were examined by using the EBSD technique. Furthermore, it is possible to control by orientation-contrast imaging that the crystals are perfect single crystals by checking for existing subgrains.

For deformation experiments, cubic and cylindrical olivine samples were prepared. Results of the experiments were identical for both shapes. The cylinders had diameters of 1.5 to 2 mm and were drilled out from previously oriented single crystals by a coring machine. The cylinders were cut into pieces of 1.5 mm - 2.0 mm in length. The surfaces of the top and bottom of each cylindrical sample were polished. For polishing, the sample was mounted by *g-aenial* composite to a glass-slide. Polishing was carried out by abrasive paper with different grit-sizes and fine polishing was conducted with a $1/4 \mu\text{m}$ diamond paste. The oriented cubic olivine crystals were prepared with an edge length of 1.5 - 2.0 mm (Fig. 3.2 c). The faces parallel to the (010) plane were usually polished in the same way as the cylindrical samples. The orientations of the resulting crystals were examined again by the EBSD technique, and the misorientations were found to be less than 3° . The crystals were examined by an optical microscope, and samples free of cracks and inclusions were selected for further experiments.

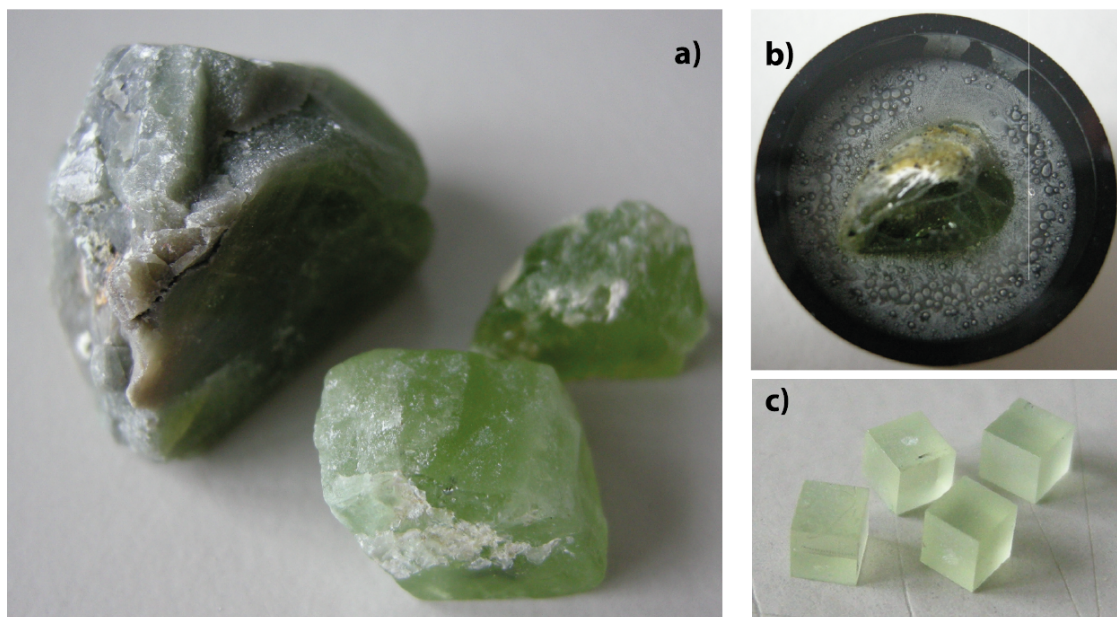


Figure 3.2: a) Natural olivine crystals; b) Natural olivine mounted in epoxy for EBSD-measurement; c) Oriented olivine cubes with an edge length of 1.5 mm.

	SiO ₂	MgO	FeO	MnO	Total
Olivine 1					
Average 1	41.4 ± 0.3	49.4 ± 0.2	8.3 ± 0.2	0.14 ± 0.03	99.3 ± 0.5
Average 2	41.5 ± 0.2	49.4 ± 0.2	8.3 ± 0.2	0.13 ± 0.04	99.4 ± 0.3
Olivine 2					
Average 1	41.3 ± 0.3	49 ± 0.7	7.9 ± 0.7	0.14 ± 0.03	98.4 ± 0.7
Average 2	41.1 ± 0.2	48.5 ± 0.5	8.3 ± 0.3	0.13 ± 0.03	98.1 ± 0.7
Olivine 3					
Average 1	41.4 ± 0.5	48.4 ± 0.9	8.2 ± 0.3	0.13 ± 0.03	98.2 ± 1.6
Average 2	41.6 ± 0.2	48.6 ± 0.3	8.4 ± 0.1	0.14 ± 0.04	98.8 ± 0.5

Table 3.1: Compositions of three olivine single crystals in wt. % determined by an electron microprobe. The shown values are obtained by averaging measured values of 99 points per crystal.

3.2 'Dry' and 'wet' experiments

The main goal of this study is observation of changes in dislocation density caused by annealing. For this purpose, the pressure assemblies usually used in the multi-anvil laboratory of the Bayerisches Geoinstitut were modified for the present purpose. These setups are described in the following sections in detail.

The deformation experiments were conducted by using the large-volume presses of the BGI. Annealing and deformation experiments were without exception conducted using the 5000-ton large-volume multi-anvil apparatus of the BGI with inner tungsten carbide anvils with 17 mm truncation and an edge length of 55 mm (the same set was used for all experiments at the 5000-ton press). Hydration experiments were conducted using the 5000-ton multi-anvil apparatus, 1200-ton multi-anvil apparatus, and the 500-ton multi-anvil press with the Walker-type module also with inner anvils with 17 mm truncation.. Although glass-epoxy sheets are placed between inner and outer anvils in usual set up, mica-sheets were placed in the annealing and deformation experiments. The confining pressures were calibrated at room temperature using the transitions of bismuth. Temperatures were monitored for hydration/annealing experiments using $W_{97}Re_3$ / $W_{75}Re_{25}$ thermocouple consisting of 0.25-mm diameter wires. Usually an MgO thermocouple tube containing four holes was used. The thermocouple junction was made mechanically by crossing the wires. The wires were separated from the Pt-capsule by an MgO spacer on top of the capsule. For deformation experiments, a special set-up was used and is explained in the concerning chapter. No pressure correction was made to the thermocouple readings.

To study the effect of hydrogen, 'wet' experiments contained a hydrogen source which causes hydration of the olivine-single crystals. Usually, a mixture of talc+brucite powder with a weight ratio of 4:1 was used. For experiments under water saturated conditions, also distilled water was added to the capsule. The oxide activity, was controlled by using orthopyroxene which was added as powder and also using the hydrogen source of talc+brucite with the ratio of 4:1 which produces pyroxene during dehydration.

The order of experiments is:

- Hydration
- Deformation
- Annealing

To identify the effect of hydrogen on dislocation mobility, it was necessary to perform experiments without water sources, which are called 'dry' experiments in this thesis..

The order of 'dry' experiments is:

- Deformation
- Annealing

3.2.1 Hydration

Prior to deformation experiments, it is necessary to increase the water contents and achieve point defect density equilibrium in the preexisting single crystal, and recovering it for further deformation experiments under hydrous conditions. For these purposes, a single crystal was kept at controlled pressure, temperature and if possible oxygen fugacity. The major problems are fracturing during the decompression and recrystallisation. To solve these problems, miscellaneous experimental setups were tested. Several pressure-conditions between 1.5 - 5.0 GPa were tested. The goal was to find a matrix which is soft enough and unreactive with the olivine crystal. Different capsule-styles were tried with different materials surrounding the olivine single crystal, such as platinum or/and gold powder. It was found that the metals are too hard at high pressures to prevent the fracturing of the crystals. Graphite was finally chosen as the most suitable material. A double capsule design where the outer and inner capsule, respectively, were made of platinum and graphite, gave the best results for the cylindrical crystals. To synthesize olivine with high water content, the space between graphite capsule and platinum capsule was filled with talc+brucite. A Ni-foil and a Ni-NiO-foil was placed at the bottom of the Pt-capsule to control oxygen fugacity. The later one gets heated in the furnace for several hours to create an oxidation layer. If the hydrogen content should be low, the space between the inner graphite and outer platinum capsules was filled by a graphite matrix. For cubic shaped crystals, graphite matrix was placed around the crystal and the water source was separated by Ni-discs from the graphite. To reach water-saturated conditions (around 400 ppm wt% water), 10-20 mg of talc+brucite have to be inside the capsule. For low-hydrogen contents (100 ppm) around 3 mg was enough. The sealing of the capsule was made by welding of the lids with the tube. By using the Lampert PUK 04 welding machine it is possible to seal the capsules without water loss. Using these two setups, it is possible to recover undamaged single crystals of olivine in most cases (Fig. 3.5).

The most favourable experimental conditions are a sample size of 1.5 mm, a temperature of 1227 °C, a pressure of 2.75 GPa and run duration longer than 20 hours. Costa and Chakraborty [2008] mention similar run-times for samples with a comparable sample size and P-T conditions. It is possible to run experiments with a high success-rate at water saturated

conditions (400 ppm wt% ppm). By piercing recovered capsules, it is clearly verifiable that samples were at saturated conditions by water escaping from the recovered platinum capsules.

The samples were usually quenched over one minute to retain the hydrogen contents in olivine close to the annealing conditions. Also, it allows excess H to escape from the olivine crystals without the formation of inclusions [Costa and Chakraborty, 2008].

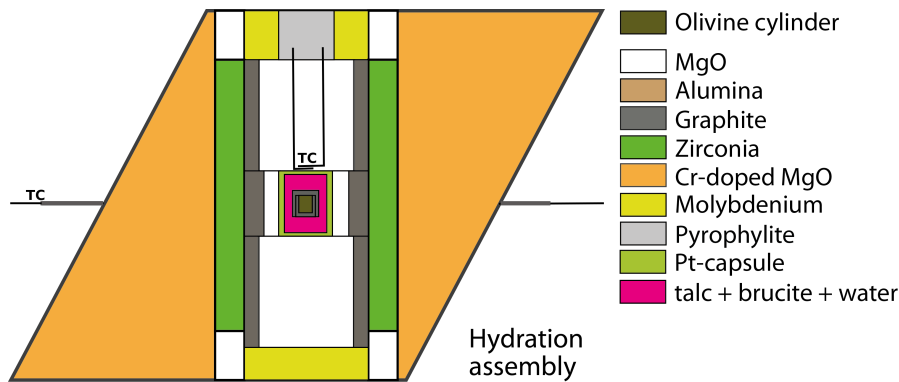


Figure 3.3: The hydration assembly is a standard 25M assembly; TC = thermocouple

3.2.2 Deformation

Deformation under dry conditions

Olivine single crystals are deformed in a simple-shear geometry, using a split-cylinder shear configuration (Fig. 3.7). For this purpose, a modified pressure assembly had to be developed which permits the uniaxial compression into a simple-shear deformation.

A pressure media with an edge length of 25 mm was used. A resistance heater was made of graphite in a stepped-heater geometry, in which the inner part of the heater had a larger outer diameter than the top and bottom parts. Because of the 7.0-7.5 mm long capsule, the inner part had the same length as the outer part, which was longer compared to a standard 25M assembly of BGI. Nevertheless, the necessary power to reach the same temperature was comparable.

The piston for deforming a sample is mostly made of crushable alumina. Due to the fact that it is initially soft, but becomes hard relative to olivine after heating, it is possible to deform olivine crystal mildly to create dislocations with avoiding breakage during cold compression and dynamic recrystallisation of crystals.

The central part of the assembly sits inside a platinum capsule with inner and outer diameters of 4 or 4.5 mm and 5.0 or 5.5 mm, respectively. Mostly the capsule with 4.0 mm inner diameter was used for samples with a height shorter than 1.2 mm. Two crushable alumina pistons were placed in the capsule to deform the sample in a simple-shear geometry. They were made by cutting a crushable alumina column at an angle of 45°. After cutting, the pistons were cleaned in an ultrasonic bath with acetone and heated to 1000°C to remove contamination. The olivine crystal is loaded between the pistons. It is surrounded by an MgO

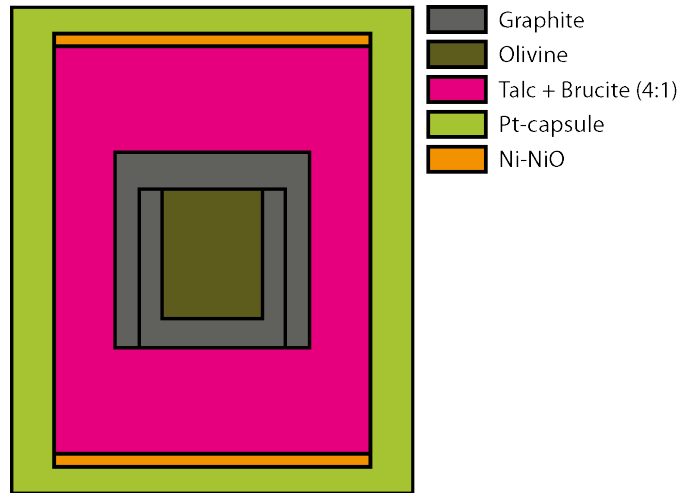


Figure 3.4: Details of hydration experiments shows the capsule-setup before the experiment.

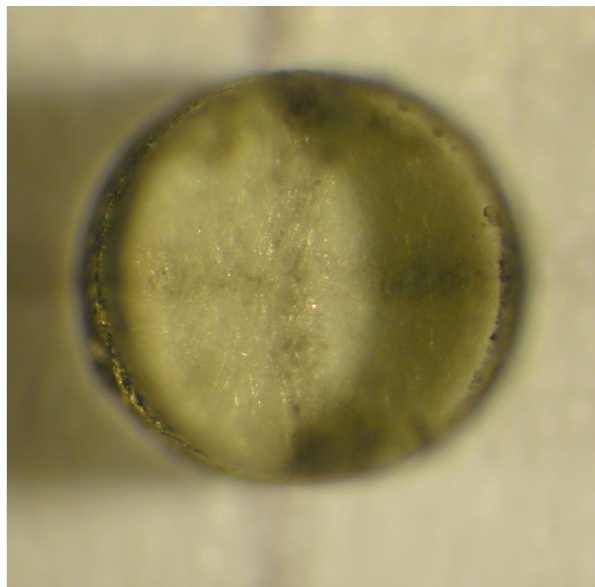


Figure 3.5: Cylindrical olivine crystal recovered from a hydration experiment Z1123. The cross which can be seen through the crystal is from paper below the crystal. The crystal is completely free of inclusions and cracks, and contains 200 ppm (wt%) of water.

spacer, which keeps the olivine crystal in place. The orientation of olivine after placing it inside the MgO spacer was corrected with observing using a cross-polarized optical microscope. Temperatures were monitored using $W_{97}Re_3 / W_{75}Re_{25}$ thermocouple consisting of 0.25 mm diameter wires. The wires were flattened at the ends and bend by 90° . To separate the wires, a cylinder made of crushable alumina with grooves on the side was placed between them. At the bottom of this cylinder and on top of the Pt-capsule, those flattened ends of the wires are supposed to touch each other.

The standard procedure for deformation experiments consists of increasing the press load till a target load is reached. During compression, the sample temperature was kept at 600 K to avoid fractures. After reaching the target press load, temperature was increased to 1500-1600 K and kept constant during the deformation process. During heating, the press load was increased slightly to avoid stress relaxation and to produce a more or less homogeneously distributed dislocation density. Following the deformation, the experiment was quenched in several seconds by turning off power by sending the command *immediate quench* from the controlling computer to the temperature-control box.



Figure 3.6: Parts of deformation experiments. Not shown in this image is the thermocouple.

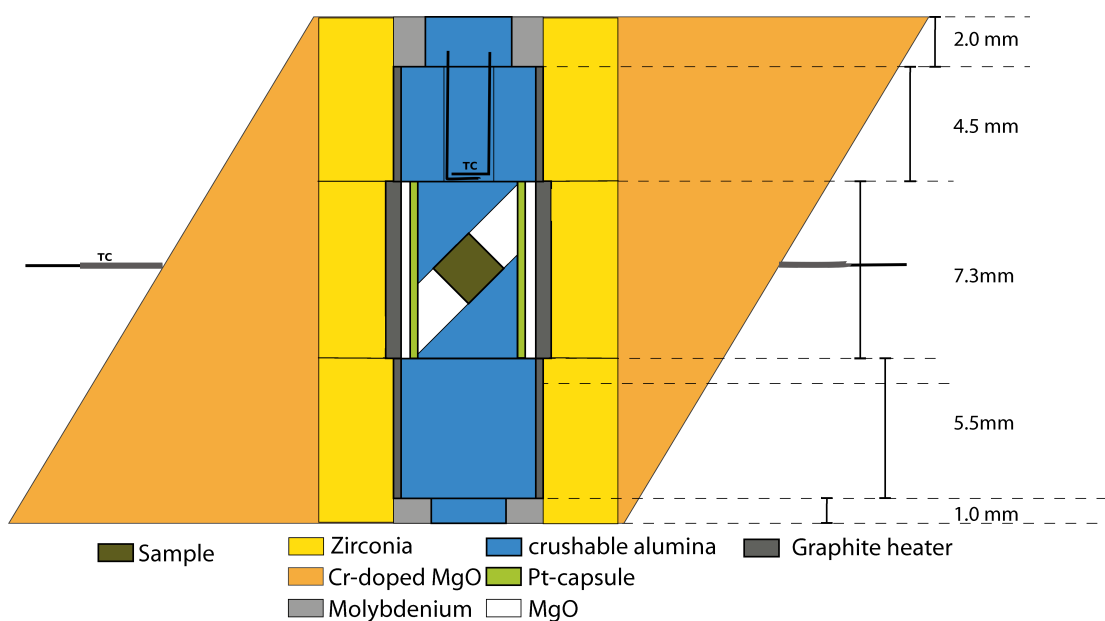


Figure 3.7: Deformation assembly; TC = thermocouple

Deformation under hydrous conditions

Deformation experiments under hydrous conditions were similar to the 'dry' experiments. However, the samples were contained with the crushable alumina pistons and talc+brucite powder for water source in a sealed Pt-capsule (Fig. 3.8) in order to keep the water in the doped crystals. The talc+brucite powder was placed on the bottom of the crushable alumina pistons. The sealing of the capsule was made, similar to the annealing experiments, by welding of the lids with the tube.

The recovered olivine cylinders from the hydration experiments were polished on the upper and lower faces. Because of geometrical reasons (talc, brucite and Ni-NiO discs taking a certain space), it is necessary to use cylinders with a height of 0.8 - 1.0 mm. The talc+brucite powder was separated by two discs from the crushable alumina. One is made of Ni and the other one is Ni-NiO. The later one gets heated in the furnace for several hours to create an oxidation layer. It was also verified after the experiments, using optical microscopy, that neither component of the buffer (Ni and NiO) had been totally consumed. On one hand, both foils prevented the powder from migrating between two of the olivine crystal, the MgO spacer and the alumina pistons, in the case that there was a gap between the alumina and the platinum capsule. Another important role of these discs was controlling the oxygen-fugacity. Enstatite-powder with a Fe-content of 10 % is placed between the olivine crystal and the MgO spacer to prevent diffusion of iron from the olivine to the MgO and also to control the a_{SiO_2} . The experiments were relatively short (45 min). Note that iron was lost from the olivine to the surrounding MgO spacer without the enstatite. No reaction was observed between the alumina-piston and the olivine, probably because of the short run-time of the experiments.

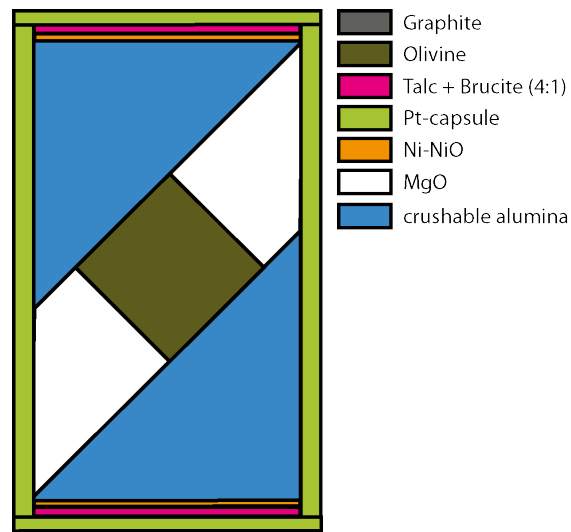


Figure 3.8: Details of deformation experiments under hydrous conditions: shows the capsule-setup before the experiment

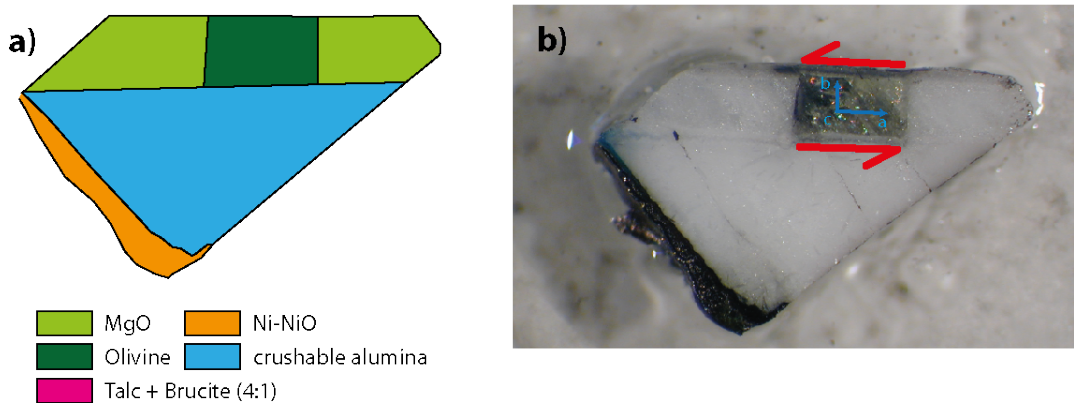


Figure 3.9: The sample environment in the hydrous deformation experiment. a) a schematic drawing of the sample environment design. The sample, MgO holder, crushable alumina piston and talc+brucite powder are sealed in a welded Pt capsule. b) photograph of the recovered sample after cutting it in half parallel to slip direction; the observed plane of the olivine is equal to the c-plane; one piston and talc+brucite is missing.

3.2.3 Annealing

After recovering the single crystals from the deformation experiments, they were annealed under quasi-hydrostatic conditions using the 5000-ton multi-anvil press at a pressure of 2.75 GPa and a temperature of 1500 K. The assembly is the standard 25M of BGI.

During annealing, the dislocation density decreases due to coalescence of two dislocations. For this purpose, the deformed crystals were cut into 4 or 8 pieces, and one piece was placed inside a Pt-capsule with surrounding graphite matrix (Fig. 3.10), which is much softer than the olivine crystals, and therefore no deformation but annealing of the olivine occurs.

The samples assembly was compressed to a desired press load, temperature was then increased to 1500-1600 K and kept constant during the annealing process. The experiment was usually quenched in several seconds by turning of power by sending the command *immediate quench* from the controlling computer to the temperature-control box.

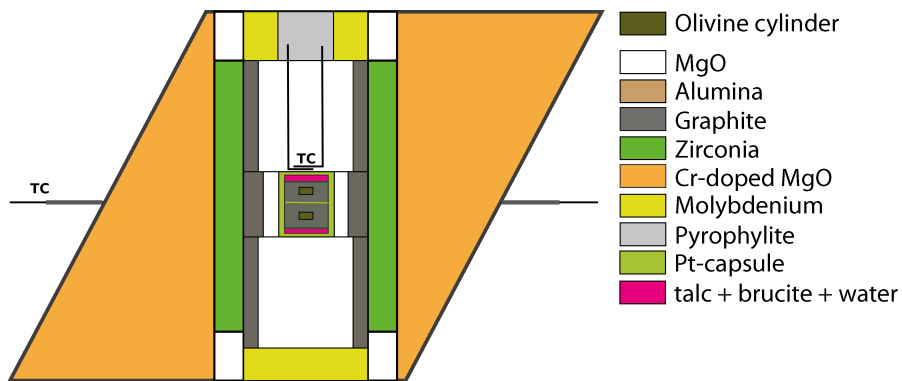


Figure 3.10: Annealing assembly; TC = thermocouple

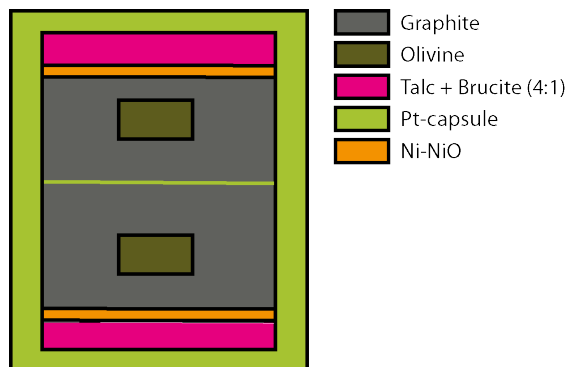


Figure 3.11: Details of annealing under hydrous conditions shows the capsule-setup before the experiment

3.2.4 Annealing under hydrous conditions

Annealing under 'dry' and 'wet' conditions is similar except for the water source. Details of the capsule are shown in Fig. 3.11. Olivine crystals were embedded in a graphite matrix, and talc+brucite powder were loaded at bottom and the top of the capsule. The talc+brucite powder was separated from the graphite powder by Ni-NiO foils. Furthermore a small amount of Fe-powder/foil was added with the talc+brucite powder to prevent iron leaching from the olivine crystal. This problem is explained in the following section.

3.2.5 Problems during hydrous experiments

Several problems occurred during experiments under hydrous conditions at high pressures and temperatures. It was challenging to ensure mechanical as well as the chemical stability of the olivine single crystals.

One of the main problems was iron loss during the deformation and annealing experiments. As explained later, the dislocation densities were measured by oxidising the dislocation. If the samples lose too much iron, the dislocations cannot be oxidised, and therefore the dislocation density cannot be measured. A patchy distribution of BSE image contrast was visible after oxidation of the sample (Fig. 3.12). Also in an EDS map (Fig. 3.13), these effects can be seen. The EDS maps demonstrate that the distribution of Fe and Mg are anti-correlated, which suggest an Fe/Mg-exchange occurred between the olivine crystal and surrounding MgO.

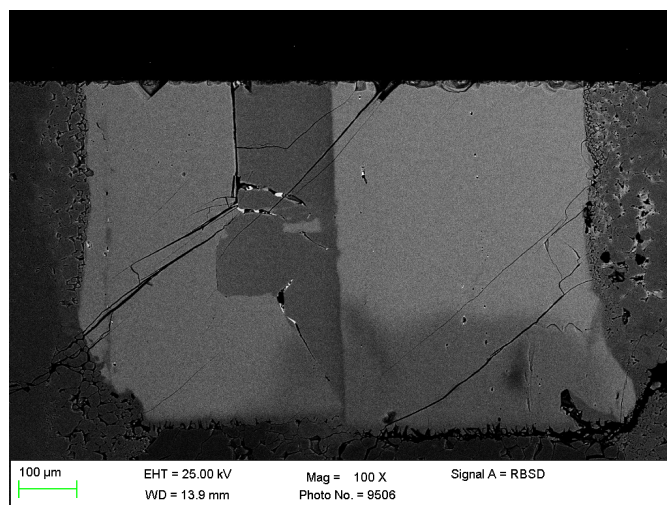


Figure 3.12: BSE-image of sample Z1161 after oxidation. The different grey colours of the sample show the difference in chemical composition. The dark grey areas are regions with an high-Mg and low-Fe content. Left and right of the crystal the alumina pistons are visible and at the bottom edge, the crystal is in contact with the MgO spacer.

Fig. 3.14 demonstrates the effect of iron loss on the result of the oxidation process. The darker areas in a BSE-image cannot be oxidised because of the low iron content. However, this effect can be minimised by adding Fe-foil next to the talc-brucite powder and by surrounding

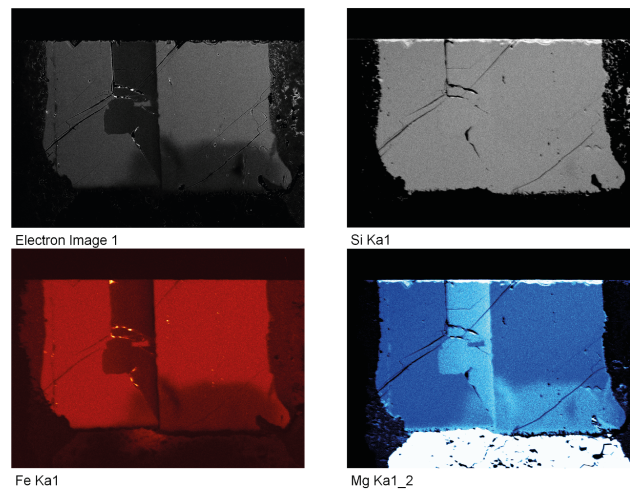


Figure 3.13: EDS-mapping of sample Z1161 (same as Fig. 3.12). The right upper image shows the Si-content, the left lower image the Fe-content and the right lower one the Mg-content. It is clearly visible that Fe diffused along certain cracks out of the crystal towards the MgO and the Mg-content increased at that regions. also the Fe-content of MgO increase.

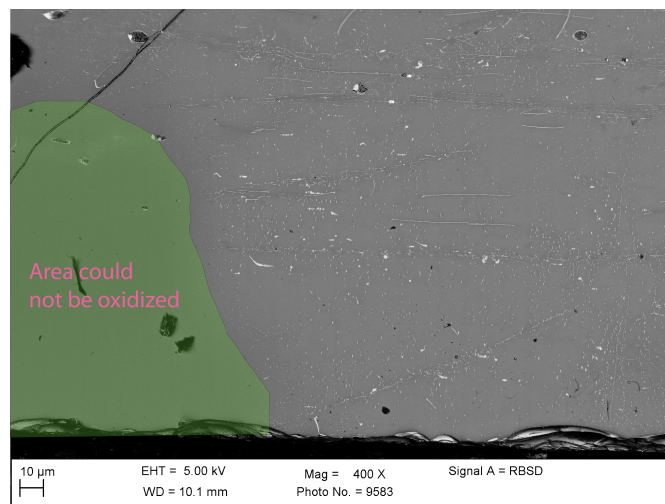


Figure 3.14: Image shows the influence of iron distribution on the possibility to observe dislocations after the oxidation process. The area which is highlighted by the green overlay has a low Fe-content and therefore it is not possible to decorate dislocations in this area.

the olivine cylinder with enstatite with a 10 % of FeSiO_3 component. Samples which are deformed in such a setup show a homogeneous distribution of iron after the deformation experiments.

Costa and Chakraborty [2008] adopted a similar setup in piston cylinder experiments to that of the present study. The pressure-and temperature-conditions under which olivine can be hydrated in the presence of graphite are limited by the formation of orthopyroxene + magnesite.

At pressures of 2.5 - 3.0 GPa olivine can be present only at temperature between 1227°C and 1400 °C. However, the water loss through the Pt-capsule increases with increasing temperature. Therefore the target temperature for the hydration experiments was chosen to be 1227 °C.

4 Analytical Methods

For analysing dislocation density and hydrogen content several analytical methods were adopted, Fig. 3.1. The necessary analytical methods are:

- FTIR-spectroscopy
- Oxidation decoration
- SEM: BS-imaging, EDS- and EBSD-measurements
- Dislocation counting

4.1 Measurement of water content by FTIR-spectroscopy

Infrared (IR) spectroscopy is a vibrational spectroscopy technique which is an ideal method to estimate water content down to few ppm in optical transparent materials, because infrared lights in a wavenumber range between 3000 and 4000 cm^{-1} are absorbed by stretching the OH bonding [Libowitzky and Beran, 2006].

This wavenumber range is very characteristic because of the low mass of H, and therefore does not overlap with other peaks from the lattice [Libowitzky and Beran, 2006]. In the modern interferometer-based spectrometers, the collected interferogram is mathematically Fourier-transformed to an IR spectrum [Libowitzky and Beran, 2006]. This Fourier-transform infrared (FTIR) spectroscopy is based on the concept of the interference of radiation between two beams to yield an interferogram [Stuart, 2004]. Those two beams produce a signal as a function of difference of their path-lengths. The signals in the distance domain are converted to those in the frequency domain by the Fourier-transformation [Stuart, 2004].

The basic components of an FTIR spectrometer are illustrated in (Fig. 4.1a). The light source emits the beam, and the beam passes through the interferometer. Then passing through the sample and reaches the detector. After converting the signal from an analog to digital form, it is transferred to the computer for Fourier-transformation.

Fig. 4.1b shows the principle of the most common FTIR spectrometer, the Michelson interferometer. The main part of the interferometer is the beamsplitter. The beam splitter reflects, ideally 50 % of the incoming beam to the stationary mirror, which is called the reflected beam. The other 50 % of the incoming beam passes through the beam splitter to the moving mirror, which is called the transmitted beam. These two beams are reflected by these two mirrors to return to the beamsplitter, and they are recombined, and interfere each other [Stuart, 2004]. The moving mirror continuously changes the length of the optical path of the transmitted beam to produce a continuous difference of the optical paths of the transmitted and reflected beams.

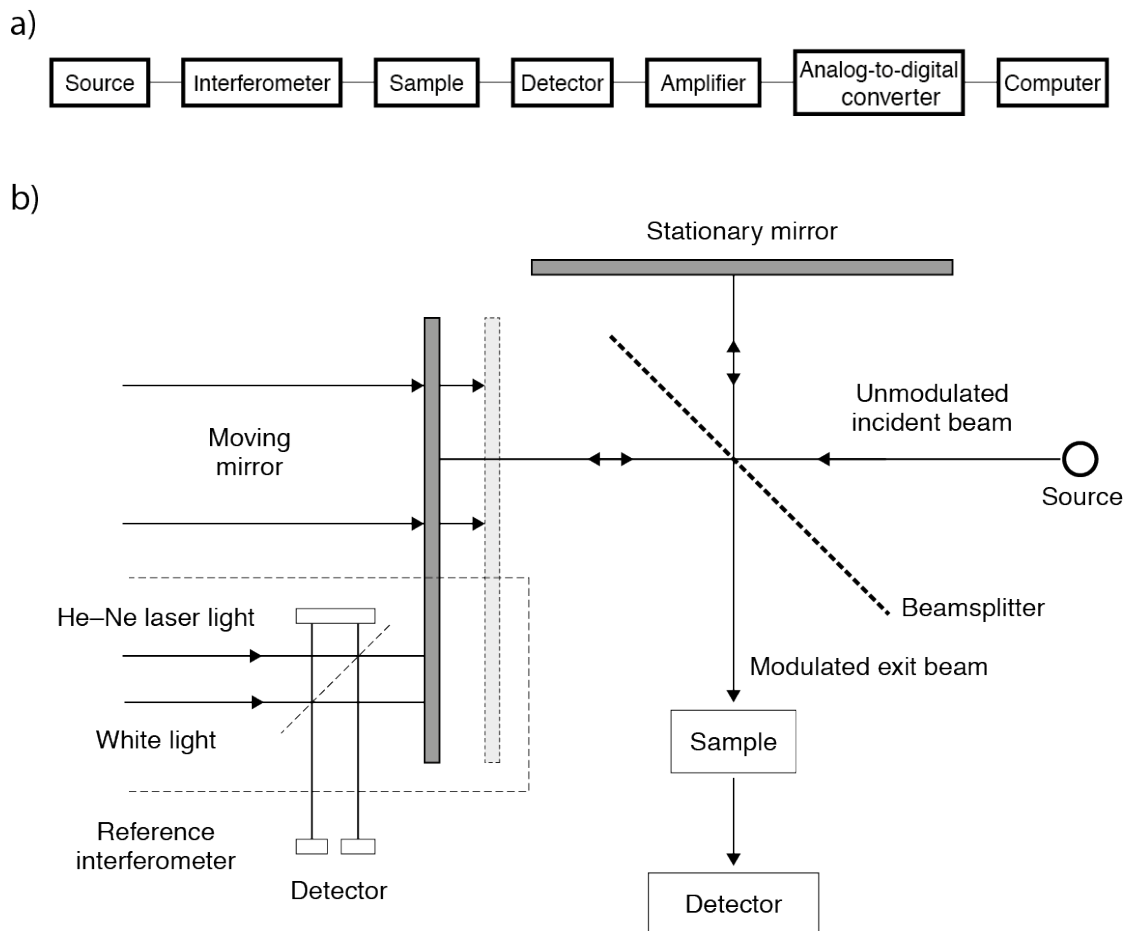


Figure 4.1: Components of a FTIR spectrometer.

The fundamental concept of IR-spectroscopy is that an electromagnetic wave, the beam created at the interferometer, interacts with the sample. The wave moves with the velocity of light c_{light} ($2,9978925 \times 10^8$) and is characterised by a wavelength, λ , and frequency, ν of the infrared light.

$$c_{light} = \lambda\nu \quad (4.1)$$

Usually, to plot infrared spectra, the unit wavenumber k in cm^{-1} is used. It specifies the number of waves in a length of one centimetre and has the advantage that it is linear with energy [Stuart, 2004]:

$$k = \frac{1}{\lambda} = \frac{\nu}{c_{light}} \quad (4.2)$$

$$k = \frac{\epsilon}{hc_{light}} \quad (4.3)$$

where ϵ is the photon energy and h is the Planck constant.

The experimental setup for absorbance measurements is based on a light source, the sample with a defined thickness (t) and a detector. The transmittance (T) is defined by the ratio of the intensity of the transmitted light (I) and the intensity of the incident light (I_0):

$$T = \frac{I}{I_0} \quad (4.4)$$

However, usually Absorbance (A) is used which is the negative logarithm of T . Absorbance can be calculated from the infrared spectra based on the Beer-Lambert law for quantitative analyses:

$$Absorbance = \epsilon \times c \times t \quad (4.5)$$

Where ϵ is the molar attenuation coefficient (not the photon energy defined above), and c is the amount concentration. Using this relation, the OH content in an unknown sample can be estimated based on an FT-IR spectrum of the sample with its thickness.

Measurement of OH in Olivine

To determine the OH concentration of olivine from IR spectra it is more beneficial to use a modified version of the Beer-Lambert law that applies the integrated area under the OH absorption bands. Also, because olivine is featured by pleochroic absorption bands, it is necessary to determine the absorption spectrum of polarised light preferably on two orthogonal sections to be able to measure parallel to all three principal vibration directions of the optical indicatrix of olivine [Libowitzky and Rossman, 1996]. Therefore, for orientated samples the absorbance spectra of crystallographic orientations a , b and c are normalised to a unit thickness and summed up to obtain a "total" integral absorbance, Ab_{stot} [Bell et al., 2003].

$$Abs_{tot} = \frac{1}{t_a} \int_{v_1}^{v_2} Abs_a dv + \frac{1}{t_b} \int_{v_1}^{v_2} Abs_b dv + \frac{1}{t_c} \int_{v_1}^{v_2} Abs_c dv \quad (4.6)$$

The thicknesses of the three different slices are specified by t_a , t_b and t_c . The integrated absorbance is given by Abs_a in the $\mathbf{E} \parallel \mathbf{a}$ direction, Abs_b for $\mathbf{E} \parallel \mathbf{b}$ and Abs_c for $\mathbf{E} \parallel \mathbf{c}$.

To calculate the OH contents of minerals it is important to have the calibration formula. In case of forsterite this work was done by Bell et al. (2003):

$$H_2O (ppm wt) = 0.188 \times Abs_{tot} (integrated per cm) \quad (4.7)$$

The advantages of polarised measurements if single crystals is that it is possible to avoid over-/underestimation like in unpolarised measurements, if just one crystallographic plane is observed. Furthermore it makes it possible to compare the measurement to other polarised measurements in the literature, which is not possible for unpolarised measurements [Withers et al., 2012].

One of the biggest problems with the IR-spectroscopy is, as mentioned by Bell et al. (2003), the baseline correction of the acquired spectra, which is a source for subjectivity and inaccuracy especially for low-OH samples. The challenge is the commonly curved background because of the broadtail overtones of Si-O vibrations. Also Fe^{2+} can cause such overtones. Furthermore scattering due to imperfect surface polishing and imperfections of the crystal may result in sloped backgrounds with absorption proportional to ν^4 [Bell et al., 2003].

4.2 Evaluation of water content

To evaluate the water content of olivine after each experiment, the hydroxyl distribution of the recovered olivine samples was measured by a Bruker IFS 120/125 HR FTIR spectrometer in combination with a Bruker IR microscope. Spectra were collected in near-infrared band (NIR) using a tungsten light-source, a Si/CaF₂ beam splitter and a MCT (Mercury cadmium telluride) detector. For each measurement two hundred scans were performed at a resolution of 1 cm^{-1} . Spectra were collected in the range of 1000 to 10000 cm^{-1} . Depending on the quality of the crystal such as inclusions and cracks the size of the circular aperture was chosen. The size of the apertures was normally 1.20 - 90 μm in diameter or the aperture was open for high-quality single-crystal cylinders. The collected spectra were treated by the OPUS software (Bruker Inc.). For the background correction the concave rubber band correction which is implemented in the OPUS software was used at the IFS 125 HR FTIR spectrometer. For measurements with the IFS 120 spectrometer, which is of the older generation than IFS 125 spectrometer, the background correction was performed manually.

To calculate the water content after normalising the spectra to a thickness of 1 cm, a Matlab script was used to estimate the integrated intensities of the main absorption bands with polarisation directs parallel to the crystallographic direction \mathbf{a} , \mathbf{b} and \mathbf{c} (equivalent to γ , α and β of the principal directions of the optical matrix) of olivine. According to the Bell calibration [Bell et al., 2003] the "total" integral absorbance, Abs_{tot} , was calculated, using

Equ. 4.6. For the measurements, doubly polished thin section were made by the sample preparation lab of the BGI. The samples had usually a thickness between 600 - 400 μm .

Optical photos of the thin sections were taken for documentation of the areas of measurement by an optical microscope. Positions of the measurement were marked in these pictures (See 4.2 for measurements of Z1272). Polarised FTIR-spectra of the sample Z1272 are shown also in Fig. 4.2 as an example.

Sample Z1272 is a deformed sample with an activated slip system $[100](010)$. The sample height after the deformation experiment is 755 μm . The water content is around 130 ppm calculated from the average of the FTIR spectra of the three principal directions of the optical matrix.

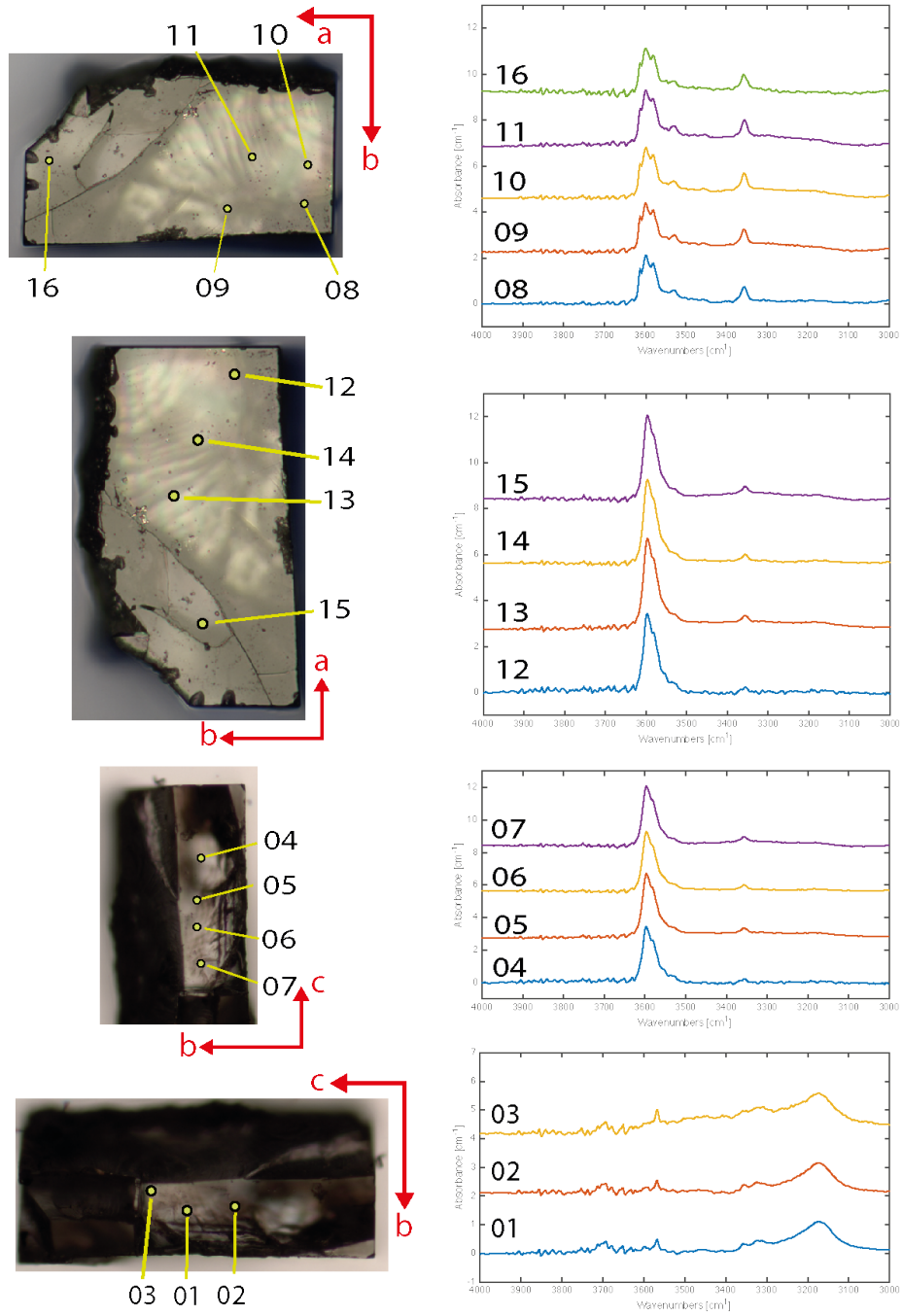


Figure 4.2: Polarised FTIR-spectra of the deformed sample Z1272 on the right and the corresponding locations where the FTIR spectra were taken on the left. The measurements show from the top measurements $E \parallel a$ (in the c-plane), $E \parallel a$ (in the c-plane), $E \parallel b$ (in the a-plane) and $E \parallel c$ (in the a-plane).

4.3 Scanning electron microscopy

In a scanning electron microscope (SEM), electrons are extracted from a source by an electric field. The electrons which are generated in such a way are called the primary electrons. The primary electron beam is focused to interact with the specimen. This interaction causes various charged particles and photons which can be used for imaging, diffraction pattern and chemical compositions [Stokes, 2008]. The main two signals which are used for SEM imaging are secondary electrons (SE) and backscattered electrons (BSE) 4.3. When a primary electron interacts with the sample, random elastic and inelastic collisions occur.

In the case of BSE, the electron accumulates enough deviation from the incident beam by elastic scattering to reach the surface of the sample again. When inelastic scattering occurs, a secondary electron is emitted. These electrons are loosely bound outer shell electrons of the atoms of the specimen which receive enough kinetic energy to be separated from the atom and be able to leave the specimen [Goldstein et al., 2002]. There are two types of secondary electrons, as shown in Fig. 4.3. SE1 in Fig. 4.3 is generated by the primary electron beam and SE2 is related to backscattered electrons [Stokes, 2008].

The interaction volume of the electron beam with the sample is given in Fig. 4.4. The distribution and the shape of the interaction volume depends on both the nature of the sample and the energy of the primary beam [Stokes, 2008]. Secondary electrons are emitted just from a small volume of the total interaction volume, because of their low energy [Stokes, 2008].

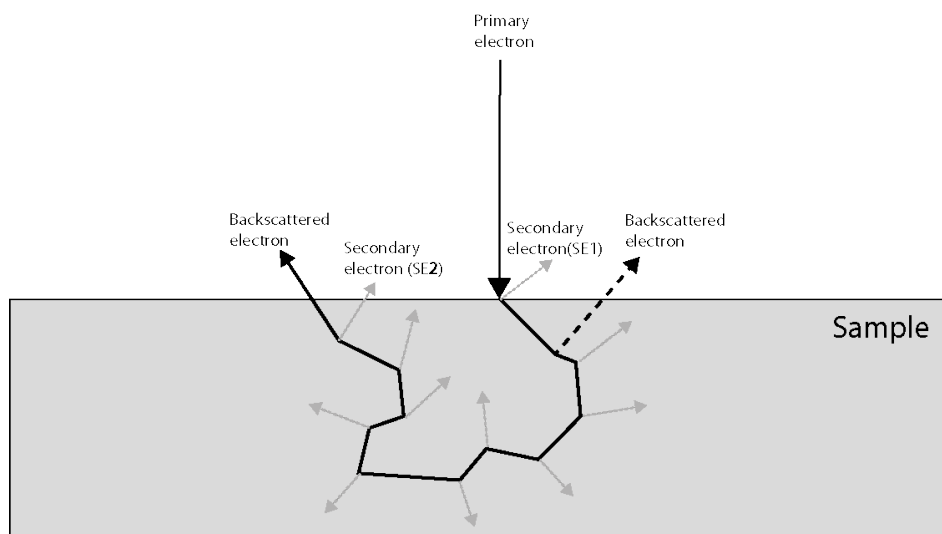


Figure 4.3: Simplified diagram of interaction of the primary electron with the sample and the resulting backscattered and secondary electrons.

A SEM consists of [Stokes, 2008]:

- Electron source
- Apertures and lenses

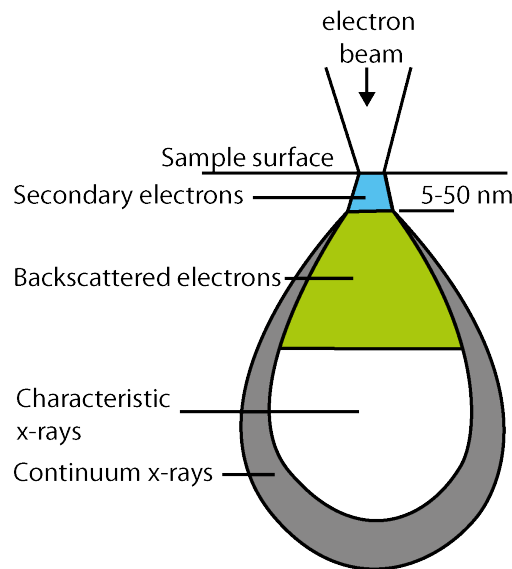


Figure 4.4: Diagramm shows the interaction volume of the primary electron beam. Modified from Goldstein et al. 2002

- Coils for rastering (scanning) the beam
- Control electronics and high-voltage supplies
- Computer to control the SEM and display the information
- Deflector/acquisition system for processing and collecting the information of the signal
- Vacuum system

There are certain modes of the SEM which are selected depending on the task. Two modes are mentioned here because they were used in this study.

High-current mode: Usually the high-current mode was used for imaging. A large beam current is necessary for best image visibility and quality because it is necessary that the contrast between an image feature and background is distinguishable above a random signal fluctuation (noise) [Goldstein et al., 2002].

Low-voltage mode: If an SEM is used in low-voltage mode (≤ 5 kV) the beam interaction with the specimen is limited to regions very close to the surface [Goldstein et al., 2002]. The resulting image is rich in surface details compared to those obtained at higher acceleration voltages (15 - 30 kV), where the beam penetrates beneath the surface and the appearing signal electrons mostly carry information of the interior of the sample [Goldstein et al., 2002].

4.3.1 EBSD-measurements

Electron backscatter diffraction (EBSD) is usually carried out in a scanning electron microscope. The electron beam is inclined to the sample surface. After penetrating the

sample, the electron beam gets backscattered according to Bragg's law, by lattice planes inclined with respect to the surface of the specimen. These backscattered and diffracted electrons can produce a diffraction pattern on a phosphor screen and observed by a CCD device or a video camera [Wenk, 2002]. On the phosphor screen the electrons are converted to light, which can be recorded by a camera. The resulting diffraction pattern (Fig. 4.5), which is similar to Kikuchi patterns in a transmission electron microscope, shows bands corresponding to diffracting lattice planes. Diffraction patterns are interpreted automatically and make it possible to determine the crystallographic orientation of the sample in a reference frame [Mittemeijer, 2010]. The results are illustrated in a so-called pole figure, which is a two-dimensional distribution of crystal directions [Wenk, 2002].

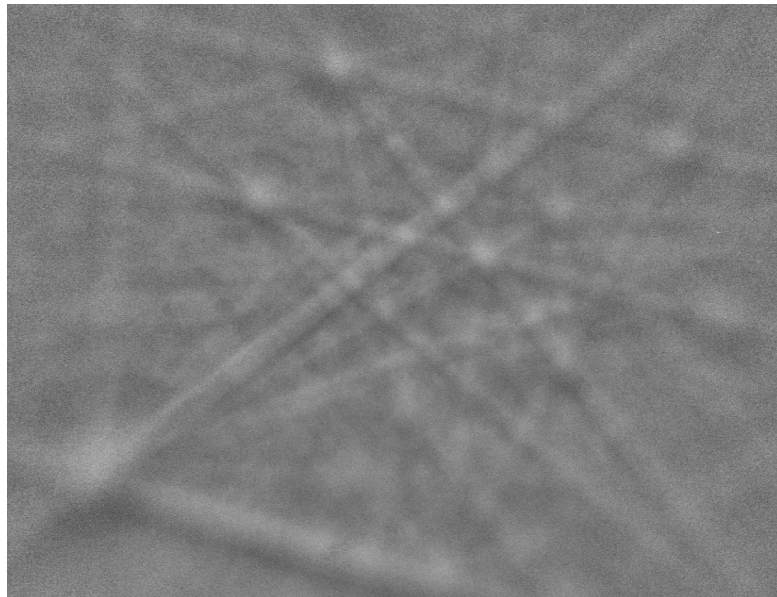


Figure 4.5: EBSD patterns of a deformed olivine single crystal.

4.4 Oxidation decoration

Decorating dislocations by oxidation in air is a popular way to observe dislocations by using an SEM. Several studies [Kohlstedt et al., 1976; Toriumi and Karato, 1978; Karato and Ogawa, 1982; Karato and Sato, 1982; Karato, 1987a; Karato et al., 1993; Farla et al., 2010], adopted this technique. The first study used an optical microscope for dislocation observation [Kohlstedt et al., 1976]. Karato [1987a] started to use a scanning electron microscopy to observe decorated samples. If an optical microscope is used, the resolution is limited to ca. 1 μm , and it is not possible to use this method for reliable measurement of dislocation densities when the dislocation density is higher than 10^{12} m^{-2} , the typical values for olivines from kimberlite nodules and alpine type peridotites and also of experimental deformation.

The observation of dislocations by the oxidation decoration technique was conducted in the following way. For polishing, the sample was mounted by *g-aenial* composite to a glass-slide. Fine polishing was carried out with a 1/4 μm polishing spray. Then, the sample was heated at 900° C in air for oxidation. The heating durations were 45 minutes and up to 3 h, respectively, for samples with a water content lower and higher than 200 ppm. By this heating, the oxidation layers were formed not only at dislocations but also the other part of surface, which prevents observation of oxidized dislocations. Hence, the oxidation layers were removed by polishing. After polishing, the oxidized dislocations become visible even by optical microscope (Fig. 4.6 a). Then, the samples were coated by carbon to observe the sample surface by an SEM with the backscatter-imaging mode. Dislocations appeared as dots or lines, which depend on the orientation of the observed surface (Fig. 4.6 b).

4.5 Dislocation density

The dislocation density was calculated following the work by Karato and Ogawa [1982] as mentioned in Chapter 2. To evaluate dislocation density, the surface areas of the oxidized samples were observed by the implemented *stage scan mode* of the Zeiss SEM-software. The areas consisted of at least 9 images taken in a 3x3 grid pattern with a 5000 times magnification, resulting in an area wider than $4 \times 10^{-10} \text{ m}^2$. Because most of the dislocations appeared as dots, the numbers of dislocations could be counted easily. To detect the dislocations in the images a Matlab-code was used (see Appendix 8.1). Image processing was done by using similar parameters for all the images which made the results more comparable. Such parameters are *threshold, minimum and maximum size of objects, how objects are separated*. Fig. 4.7 illustrate an area of a sample Z1227 which is used to calculate the initial dislocation density before annealing, ρ_i . The white rectangle marks the area which was chosen for *stage scan mode*. The lower two pictures were taken with a higher magnification and the orange arrows show their positions in the lower magnification image. The images at higher magnification (5000 \times) show the difference in total dislocation density (615 and 711 dislocations), but the density of mobile dislocations was interpreted as being essentially identical (5.9×10^{11} and $5.8 \times 10^{11} \text{ m}^{-2}$). If it is assumed that the strain rate is distributed equally for an area observed as shown in Fig. 4.7, then the density of mobile dislocations should be similar. Furthermore, it can be assumed that, when dislocation density is high,

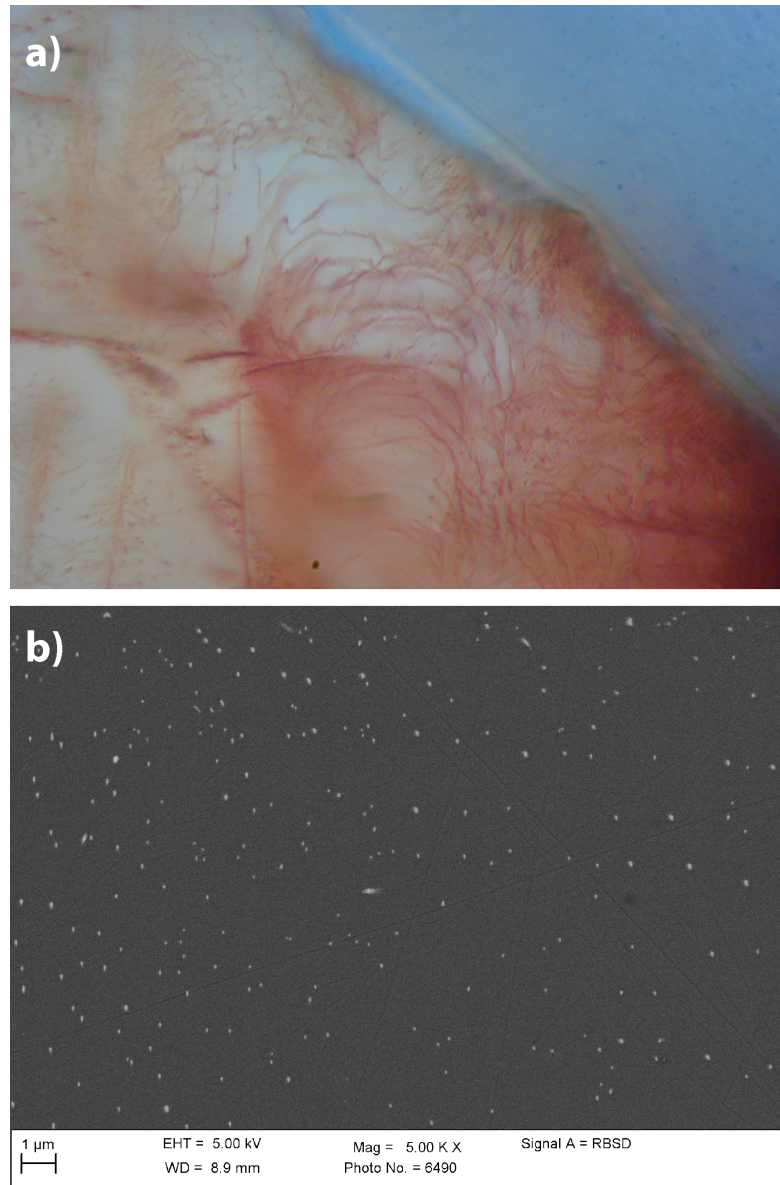


Figure 4.6: a) Image of an oxidized sample taken by an optical microscope with 50x magnification. b) Backscatter image of an oxidized sample taken by a secondary electron microscope with 5000x magnification. The cut is normal to edge dislocations, therefore they are visible as dots. The sample images were taken by BSE at 5 kV accelerating voltage.

also the number of interacting dislocations (dislocations with a distance smaller than 25px between each other) is high. This heterogeneity, which was seen in those two pictures, was typical for all deformed and annealed samples and is the reason why it is necessary to calculate the average mobile dislocation density of larger areas.

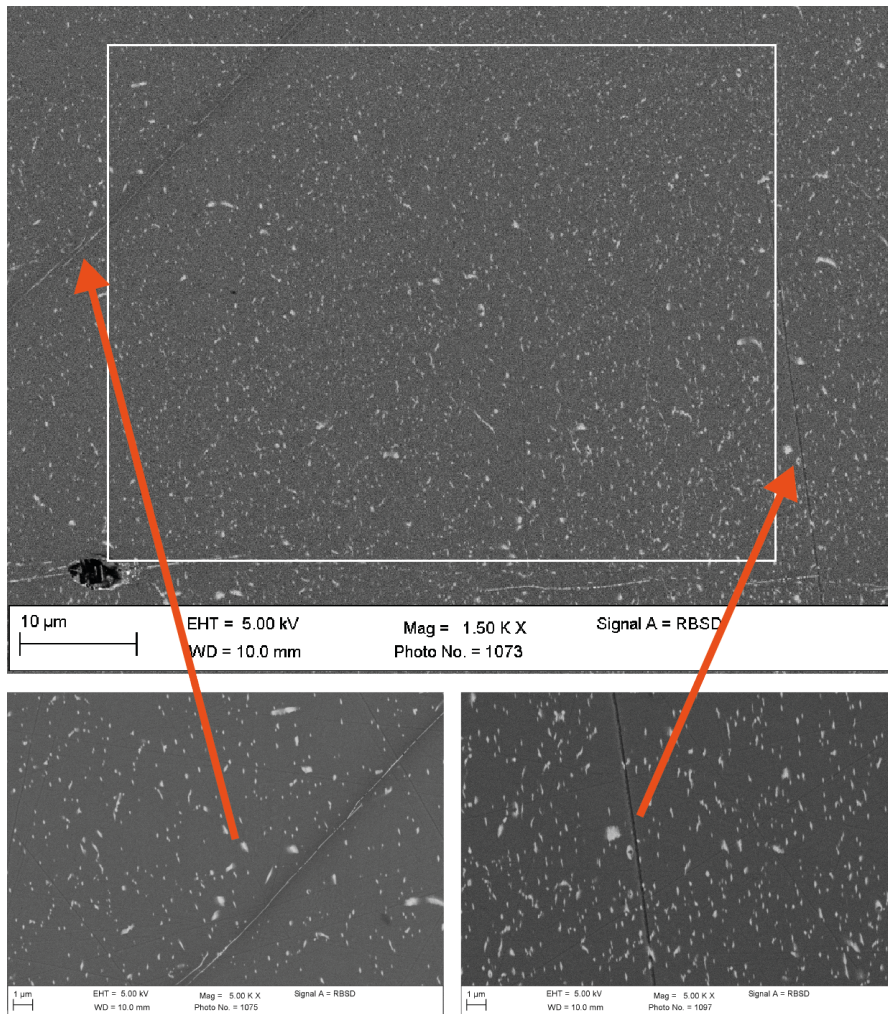


Figure 4.7: Representative image for counting dislocations. The top picture shows an area with a 1500 times magnification. The white square indicates the analysed area. The lower two images are taken with a 5000 times magnification and are used for dislocation counting. The arrows indicating the position of the lower images in the higher image.

4.5.1 Calculating the dislocation density

To calculate the dislocation density of the deformed and annealed samples, the already mentioned Matlab code (8.1) was used to detect dislocations in the SEM-images collected by using a BSE-detector. All images have a resolution of 2048×1536 pixels. In the MATLAB

workspace, images are represented as two-dimensional arrays (matrices), in which each element of the matrix corresponds to a single pixel in the displayed image. The images collected by BSE-imaging were composed of 2048 rows and 1536 columns of different coloured dots stored as a 2048-by-1536 matrix. Since the images were stored with RGB (Red, Green, and Blue) colours, they were transferred to greyscale images. This procedure results in that every pixel in the images contain a value between 0-255. To remove noise from the images, 2-D adaptive noise-removal filtering was made. The *wiener2* lowpass filter, an implemented command in *Matlab*, was used for this purpose, which is a pixel wise adaptive *Wiener filtering*. It uses neighbourhoods of size m-by-n (for this study a 3×3 matrix) to estimate the local image mean and standard deviation. After filtering, the image was transferred into a black-white image. After removing small objects (< 8 pixels) from the binary image, the Matlab command *bwboundaries* was used to trace the exterior boundaries of objects in the binary images. After that step, dislocations were identified and properties like size, location, distance between objects were calculated. This was done by using the command *regionprops*. From the resulting file, the value *Area* was extracted. *Area* includes the number of pixels of every detected object. Having this information, it was possible to select objects of certain size. Usually objects with a pixel size of 780 pixels were treated as objects that were too large. They were interpreted as artefacts of the oxidation process, because it is very unlikely that dislocation cores are $1 \mu\text{m}$ in diameter. As shown in Fig. 4.8, the typical values for objects interpreted as dislocations were >8 and <780 .

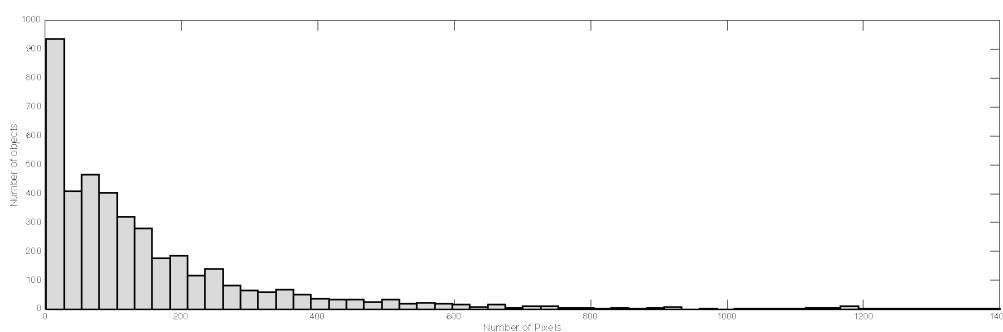


Figure 4.8: Distribution of number of pixels per object. Shown here is the sum of ten pictures of sample Z1272

Furthermore, objects which had a certain distance to each other were subtracted from the total number of dislocations. The distance was calculated from centre to centre of the dislocations. Those objects are interpreted as dislocation dipoles or, when they occur in a linear array, as tilt-walls. Usually a distance of 25 (corresponding to ca. 250 nm) pixels was used to trace such objects. Dislocation dipoles represent immobile dislocation which are not taking part at the deformation process. The chosen distance to define dislocation dipoles is $0.25 \mu\text{m}$. This distance was chosen empirically by observing dislocation clusters, usually dipoles or tripoles, in the samples. By using this distance it was possible to locate automatically dipoles/tripoles by using the Matlab-code. This distance is not sufficient enough to locate tilt walls automatically.

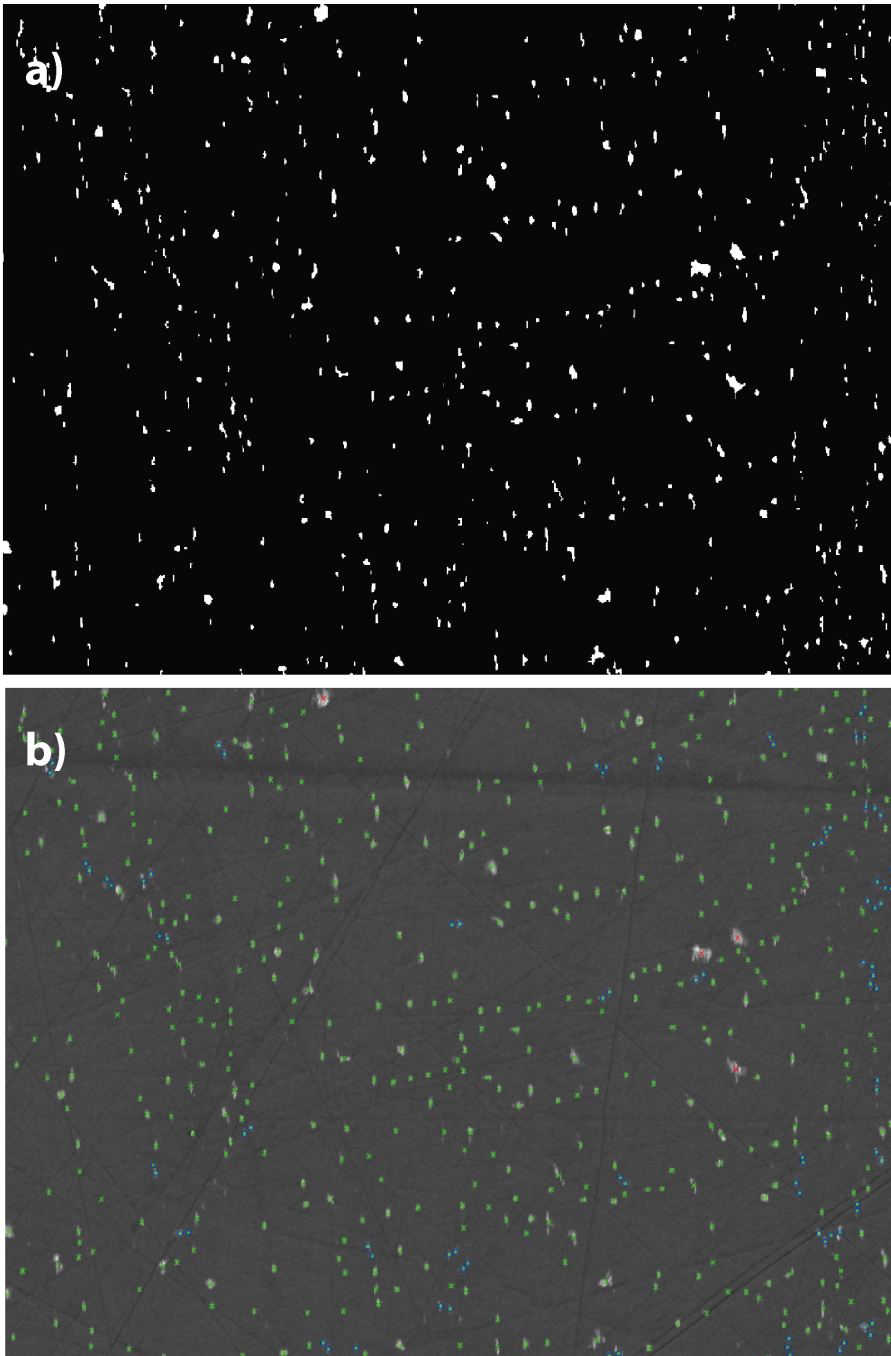


Figure 4.9: a) Original image transferred to a black-white image. This image can be used to track closed objects in the image which are in this case the dislocations. b) Original image with dislocations marked by green dots; objects marked by red crosses are not counted because these objects are too big (probably represent artefacts of the decoration process); objects marked by blue dots are too close to each other and therefore not counted as mobile dislocations.

5 Results

This chapter summarises the observation of dislocation density changes of deformed and annealed samples under 'dry' and 'wet' conditions. Several deformation and annealing experiments were conducted under different water-content conditions to evaluate the effect of hydrogen on dislocation mobility under upper-mantle conditions. Dislocation structures of deformed and annealed samples are described in the subsequent chapters. Furthermore, the results of the FTIR-spectroscopy analysis of water contents of each sample are shown. Finally, the dependence of dislocation annihilation on water content is described.

5.1 Deformation experiments

The majority of the samples were deformed in [100] direction in the (010) plane before annealing to produce high dislocation density. Table 5.1 is a summary of performed deformation experiments in the [100](010) direction. In total, two samples were deformed under 'dry' conditions, and three were under 'wet' conditions.

5.1.1 Observation plane

The dislocation density in the samples was measured in the plane parallel to slip direction and perpendicular to the slip plane, the 001 plane, by the oxidation decoration technique. The orientation of the observation-planes were examined by means of EBSD. The misorientations of (001) plane from the ideal observation orientation were usually less than 15° (Fig. 5.1) and are described in Table 5.1. The misorientation up to 15° should result in deviations of the observation plane area by up to 4% and be therefore negligible for counting dislocations.

Examination by EBSD suggest that the intragranular misorientation of the samples is usually very small (1-2 degrees) over large areas and no subgrain-formation occurred by the shear deformation (Fig. 5.2 a). The directions of the crystalline axes of the deformed samples determined by EBSD analysis are accumulated in concentric circles, which are indicators for the absence of subgrains (Fig. 5.2 b). The existence of subgrains should cause a rotation of the crystal lattice. In case of samples deformed in the [100] direction, a rotation of the crystal lattice around the *c*-axis should be noticeable. This effect is described in section 5.1.3.

5.1.2 Dislocation structures of deformed samples

Examples of typical dislocation structure of the deformed samples are shown in Fig. 5.3 for 'dry' and in 5.4 for 'wet' samples.

Name	H_2O [ppm by weight]	Deviation observation plane	Deviation shear plane	dislocation density [m^{-2}] $\times 10^{11}$	Density loops [m^{-2}] $\times 10^8$	Pile-ups [m^{-2}] $\times 10^7$	Tilt walls [m^{-2}] $\times 10^7$
Z923	[20]	12°	4°	4.2	0	60	0
Z931	17 ± 3	12°	10°	6.1	22	32	3
Z1227	308 ± 60	12°	5°	13.6	22	7	35
Z1272	140 ± 15	3°	2°	6.7	53	0	49
Z1276	240 ± 35	0°	0°	7.2	2.2	52	140

Table 5.1: List of deformation experiments which were successfully performed in this study. Water content of Z923 was not measured and is assumed to be similar to that of Z931.

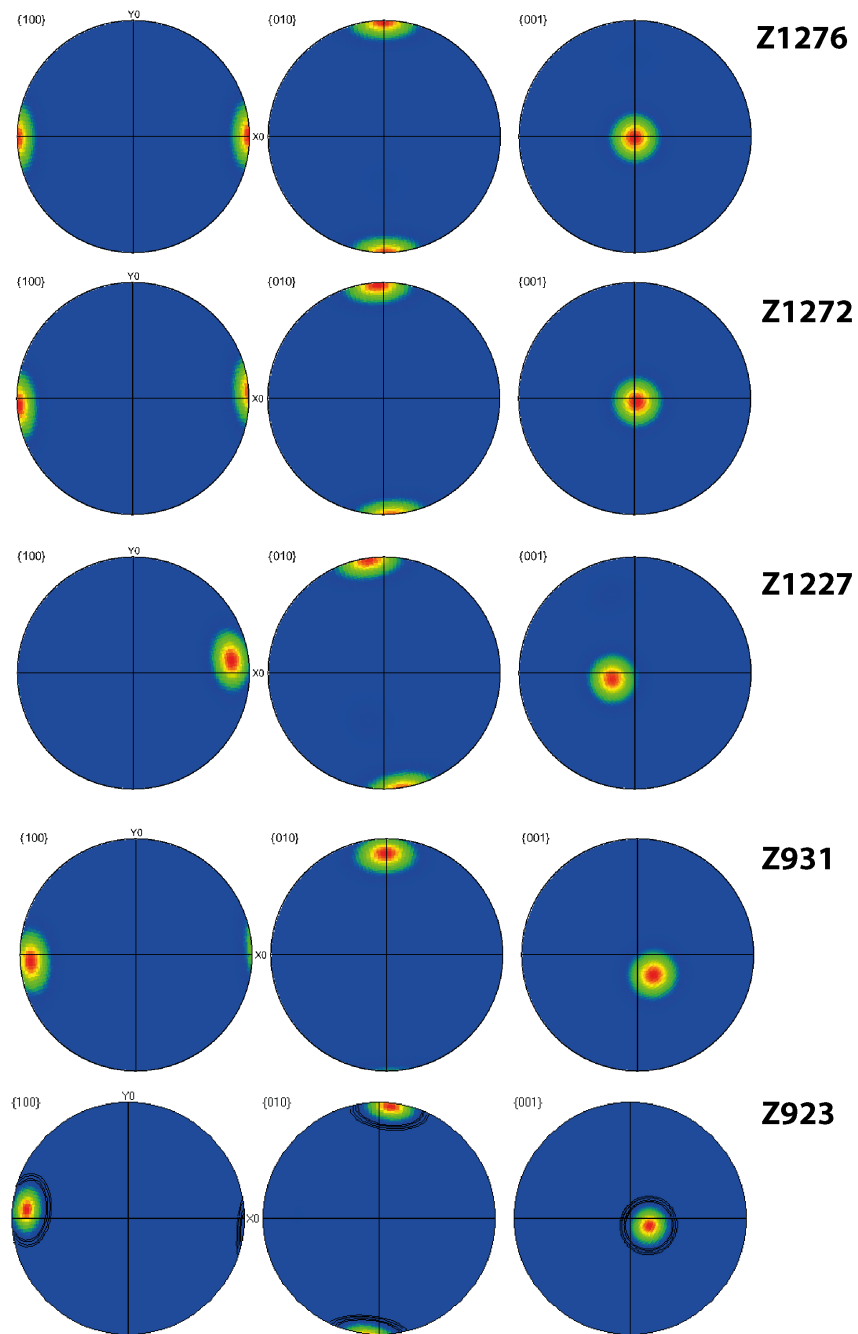


Figure 5.1: Pole figure plots of the deformed samples: Z923, Z931, Z1227, Z1272 and Z1276. The shear planes are horizontal.

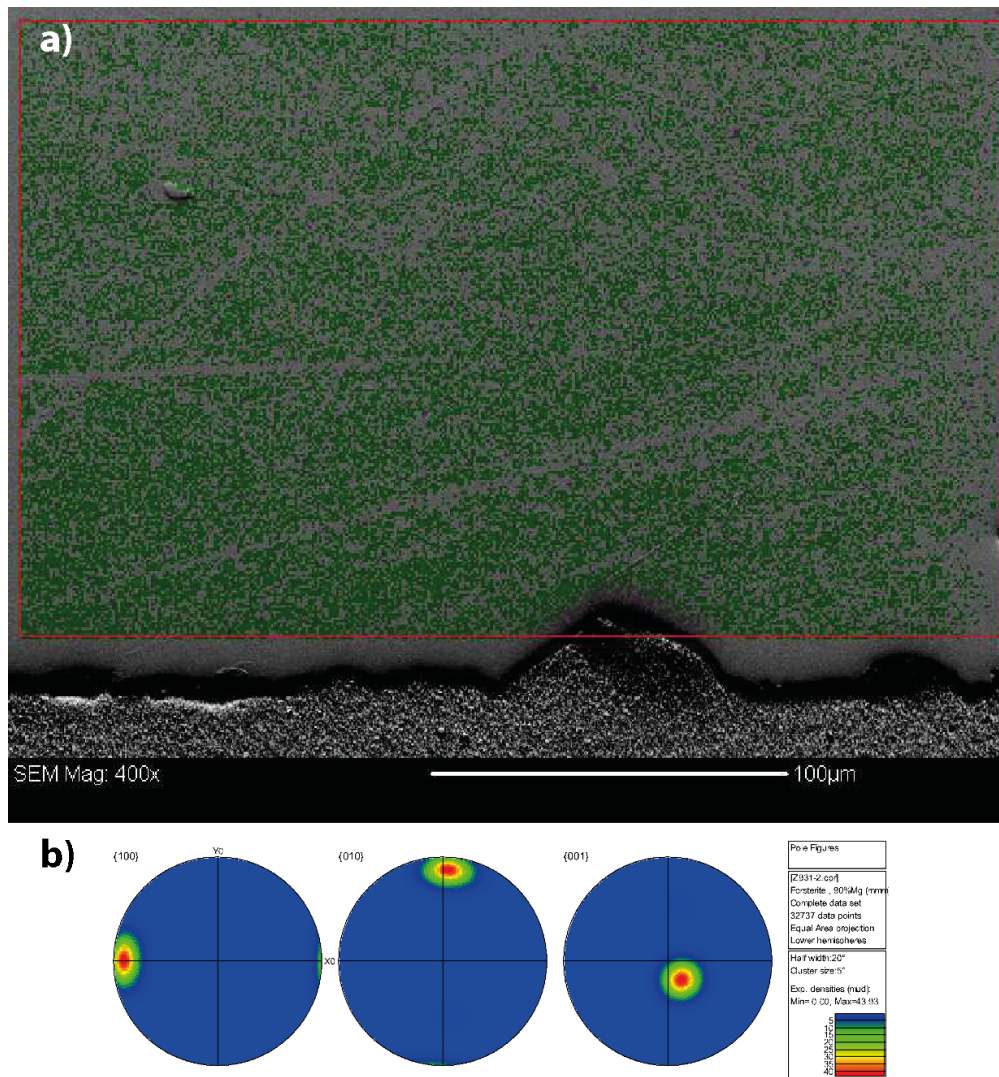
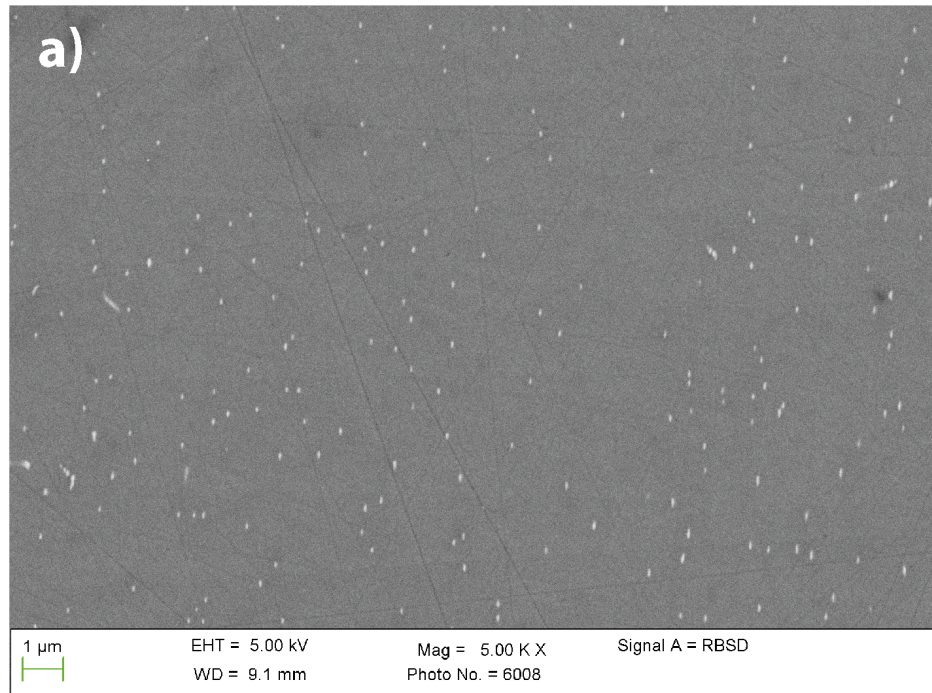


Figure 5.2: a) EBSD-map of sample Z931: each measurement-point has the same orientation indicated by the same colour (green). b) Pole figure plot of the measurements in a).

Dry samples are characterised by a homogeneous distribution of dislocations. The distribution of the dislocation density of sample Z923 is shown in Fig. 5.5 and of sample Z931 in Fig. 5.6. Fig. 5.5 and 5.6 show total, mobile and immobile dislocation densities, where the y-axis represents the number of images with a certain dislocation density and the x-axis represents the density of dislocations. Dislocations which have a distance more than $0.25 \mu\text{m}$ between each other are considered to be mobile, others are considered to be immobile. The maximum for the total dislocation density of sample Z923 is at $\sim 4 \times 10^{11} [\text{m}^{-2}]$, Fig. 5.5 a), and for the mobile dislocations at $4 \times 10^{11} [\text{m}^{-2}]$, Fig. 5.5 b). The number of immobile dislocation show a minor variation and indicate a maximum at $0.5 \times 10^{11} [\text{m}^{-2}]$, Fig. 5.5 c).

Z923



Z931

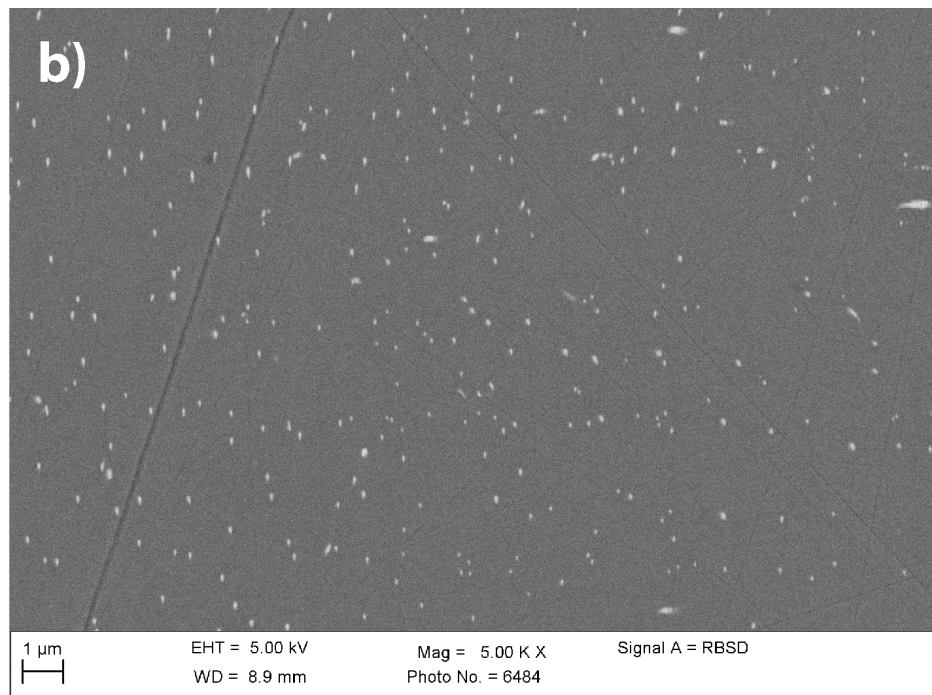


Figure 5.3: Dislocation structures of the samples a) Z923 and b) Z931, which are deformed under 'dry' conditions.

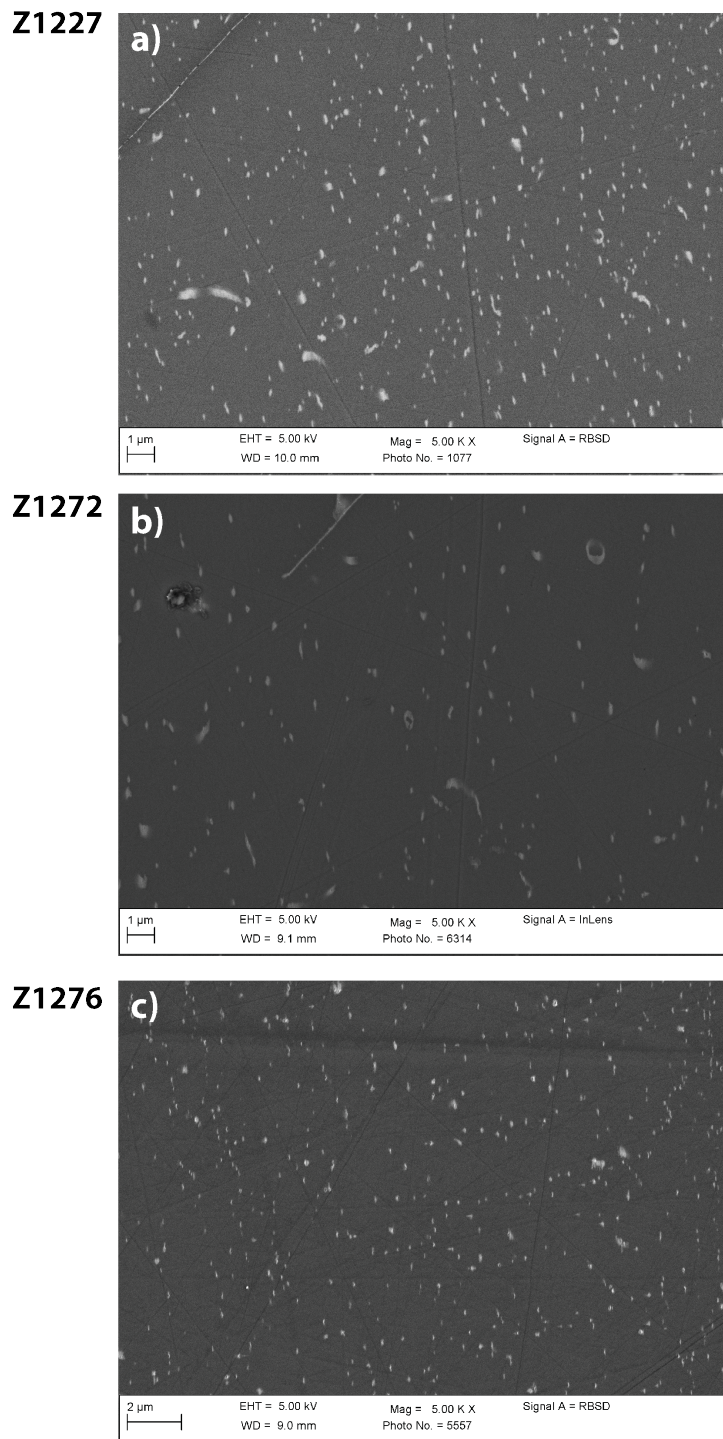


Figure 5.4: Dislocation structures of the samples a) Z1227 b) Z1272 and c) Z1276, which are deformed under 'wet' conditions.

The maximum for the total dislocation density of sample Z931 is at $\sim 6 \times 10^{11} [m^{-2}]$, Fig. 5.5 a), and for the mobile dislocations at $5 \times 10^{11} [m^{-2}]$, Fig. 5.5 b). The number of immobile dislocation indicate a maximum at $1.5 \times 10^{11} [m^{-2}]$, Fig. 5.5 c).

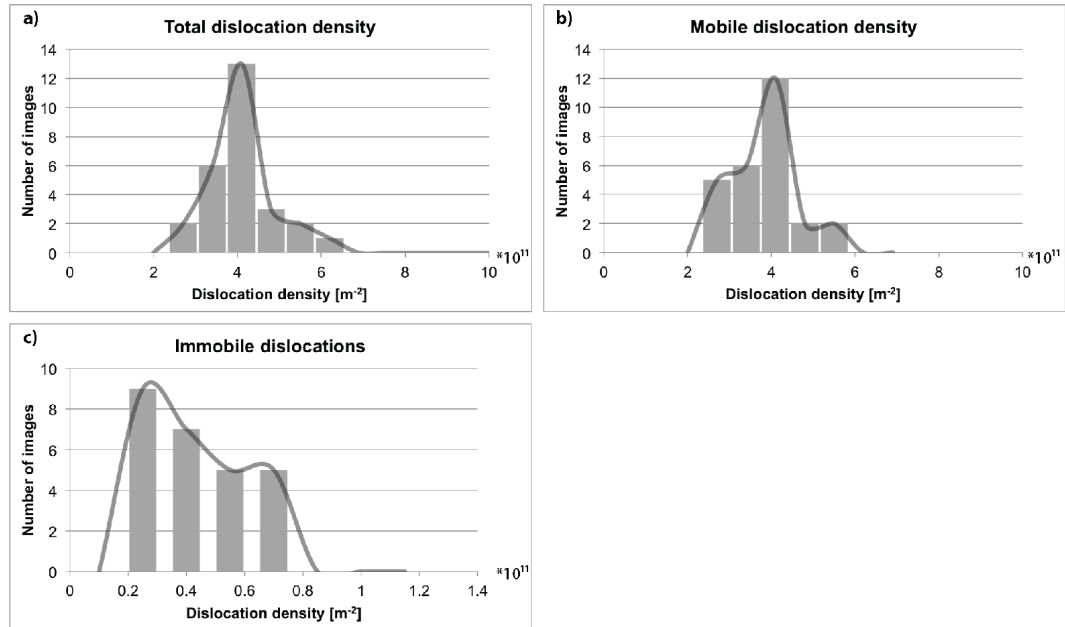


Figure 5.5: Variation in dislocation densities of dry sample Z923. Shown are plots for a) total, b) mobile and c) immobile dislocation densities.

Wet samples are characterised by more heterogeneous distribution of dislocations in comparison with the dry samples. Figure 5.7 shows the dislocation density variation per image. The maximum for the total dislocation density is at $\sim 6 \times 10^{11} [m^{-2}]$, Fig. 5.7 a), and for the mobile dislocations at $4 \times 10^{11} [m^{-2}]$, Fig. 5.7 b). Fig 5.7 c) exhibit the variation of the immobile dislocations with several maxima. The main maximum of immobile dislocations can be found at 2×10^{11} .

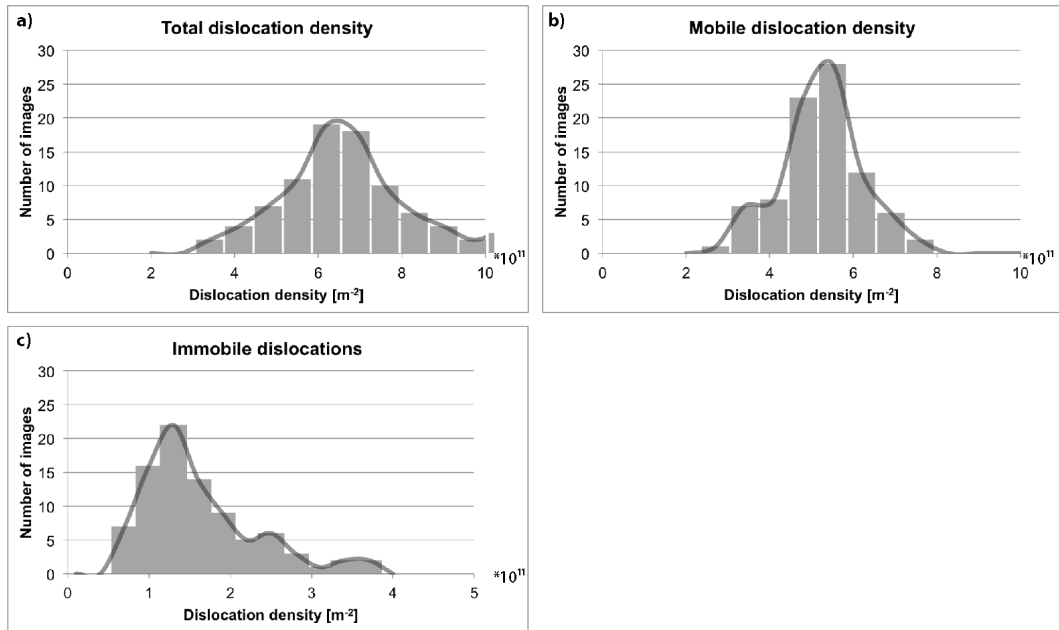


Figure 5.6: Variation in dislocation densities of dry sample Z931. Shown are plots for a) total, b) mobile and c) immobile dislocation densities.

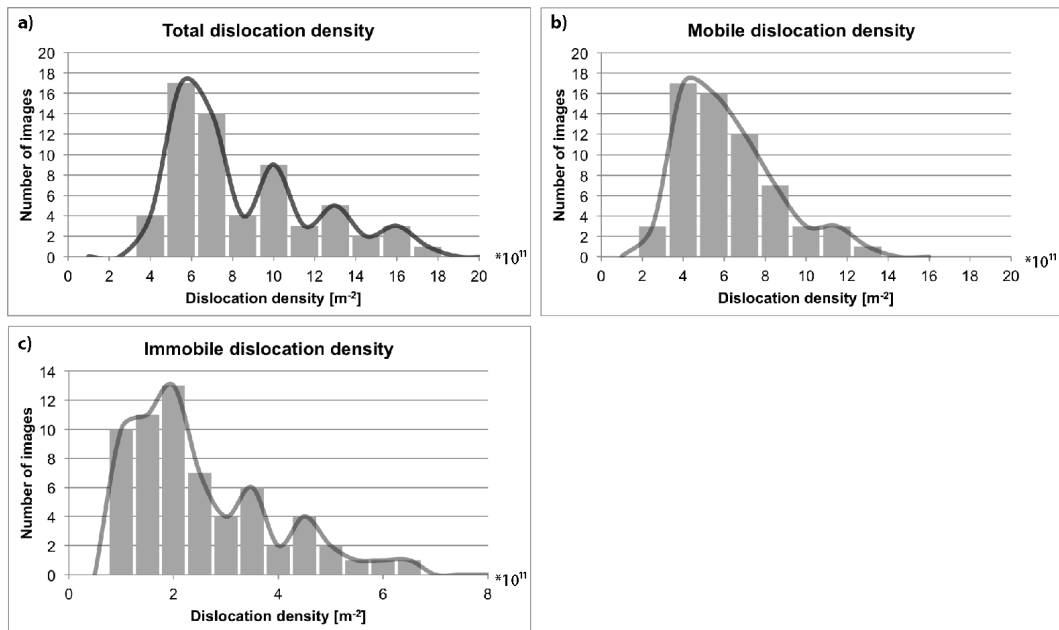


Figure 5.7: Variation in dislocation densities of sample Z1276. Shown are plots for a) total, b) mobile and c) immobile dislocation densities.

5.1.3 Spatial variation in dislocation density

Deformed samples exhibit a variation in dislocation density, especially within 120 μm from the interface with alumina-piston-sample towards the centre of the sample. Dislocation density of deformed samples is higher near to the pistons, probably because of higher stresses at the interface between sample and the pistons. Fig. 5.9 a) reveals the decrease in dislocation density by $\sim 50\%$ from the sample-piston interface towards the centre in the first seven images in the 'dry' sample Z923. The total dislocation density decrease from $4.0 \times 10^{12} [\text{m}^{-2}]$ at the piston to $2.2 \times 10^{12} [\text{m}^{-2}]$ at the centre. Dislocation densities were evaluated in the centre of the crystal. Fig. 5.9 exhibits spatial variation in dislocation density of sample Z1227, which was deformed under 'wet' conditions. Image a) was taken close to the piston and b) at the centre. The total dislocation density changes from $\sim 2 \times 10^{12} [\text{m}^{-2}]$ close to the piston to $1.2 \times 10^{12} [\text{m}^{-2}]$ at the centre. Fig. 5.10 shows the variations of the mobile and total dislocation densities from the interface with the piston to the center. As you can see, the variations, especially of the mobile dislocation density changes gradually.

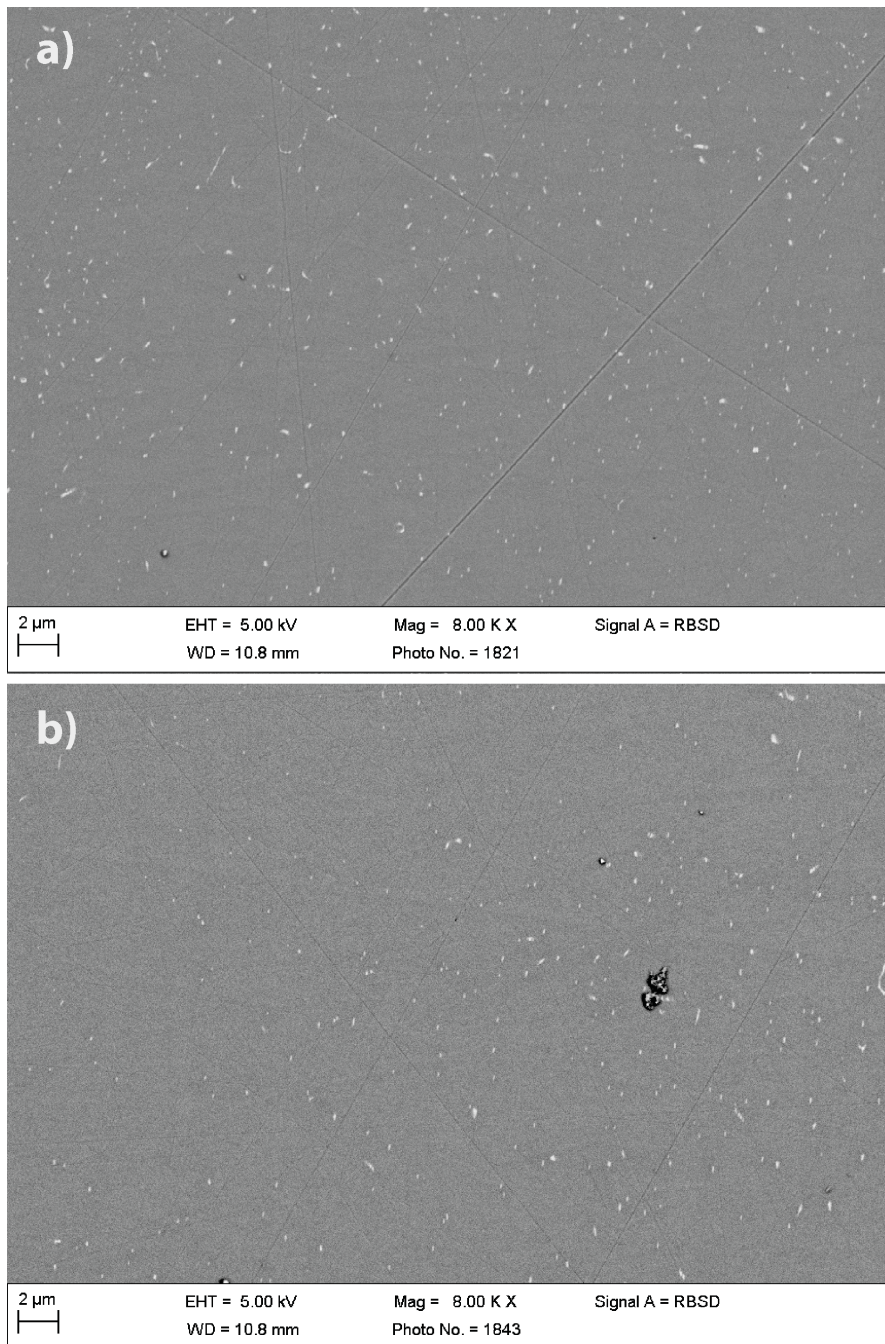


Figure 5.8: Dislocation structure of 'dry' sample Z923 observed by SEM. a) Dislocation close to the deformation piston. Total dislocation density is $4 \times 10^{12} [m^{-2}]$ in this image. b) The centre of the sample. The total dislocation density is $2.2 \times 10^{12} [m^{-2}]$.

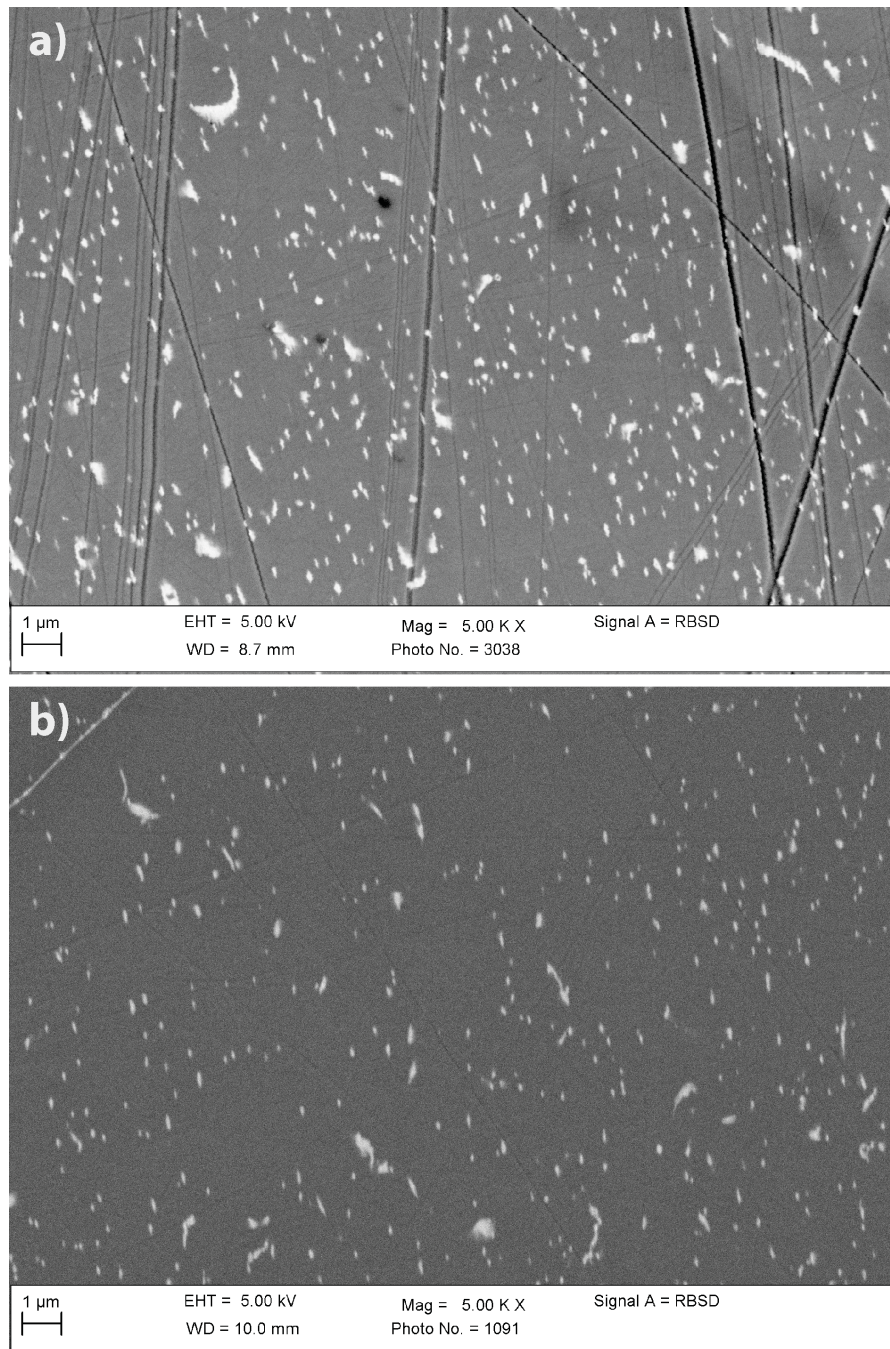


Figure 5.9: Dislocation structure of 'wet' sample Z1227 observed by SEM. a) Dislocation close to the deformation piston. Total dislocation density is $2 \times 10^{12} \text{ [m}^{-2}\text{]}$ in this image. b) The dislocation microstructure at the centre of the sample. The total dislocation density in this image is $1.2 \times 10^{12} \text{ [m}^{-2}\text{]}$.

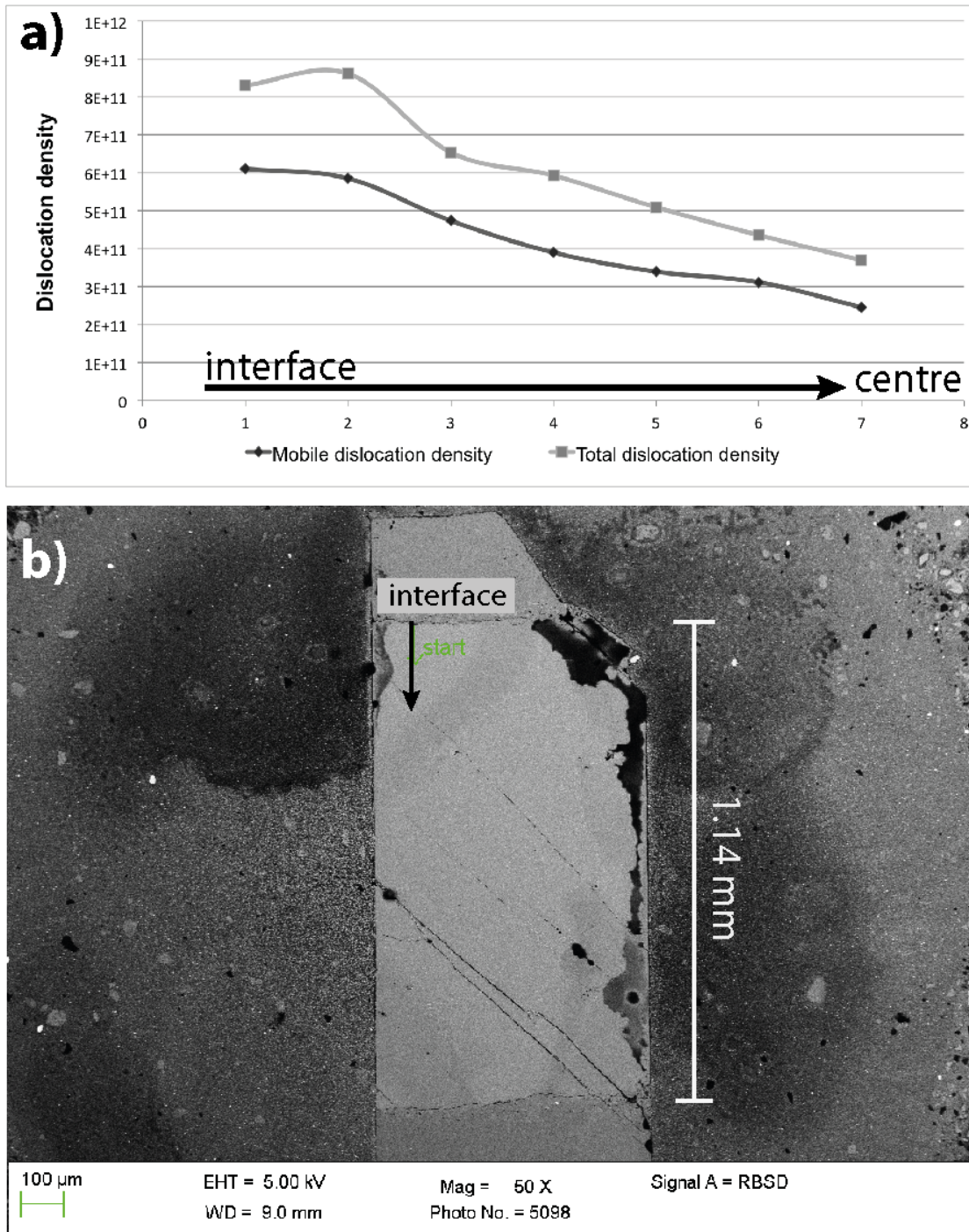


Figure 5.10: a) Total and mobile dislocation densities of the first seven images from the interface between olivine and alumina piston towards the centre of the sample Z1276. b) The black arrow indicates the position of the first seven images in the sample.

Tilt-walls, pile-ups and large objects

Linear arrays of dislocations, such as tilt walls and pile-ups, are sometimes found. Tilt walls are linear alignments of dislocations, usually oriented normal to the shear direction. Dislocation pile-ups are linear arrays which are arranged parallel to the shear direction. Furthermore, the samples exhibit dislocation loops and large objects. Objects larger than $1.7 \times 10^{-5} [m^2]$ (=780 pixels) are defined as large objects and can be found in all samples.

Dry samples Z923 and Z931 reveal only small numbers of dislocation pile-ups and loops. Fig 5.11 shows examples of dislocation loops, which are more common in sample Z931 than in Z923, even though they were deformed under the same dry conditions. Z931 has a dislocation loop density of $2.2 \times 10^9 [m^{-2}]$, whereas images of Z923 show no loops. The pile-up density of Z923 is $6 \times 10^8 [m^{-2}]$ and $3.2 \times 10^8 [m^{-2}]$ for Z931. The tilt wall density of Z931 is $3 \times 10^7 [m^{-2}]$. Z923 indicates no tilt wall.

Wet samples have by more than one order of magnitude higher densities of tilt walls than dry samples. Among hydrous samples, however, the water content and tilt wall densities have no correlation. The wet sample with the highest water content, Z1227 (360 ppm), and that with the second highest water content, Z1276 (240 ppm), are characterised by a number of tilt walls of $3.5 \times 10^8 [m^{-2}]$ and $1.4 \times 10^8 [m^{-2}]$, respectively. Fig. 5.12 a) shows a dislocation loop in samples Z1227 and Fig. 5.12 b) shows dislocation tilt walls and loops in sample Z1276. Z1227 has a loop density of $2.2 \times 10^9 [m^{-2}]$ and Z1276 has a loop density of $2.2 \times 10^8 [m^{-2}]$. The tilt wall density of Z1227 is $3.5 \times 10^8 [m^{-2}]$ and $1.4 \times 10^9 [m^{-2}]$ in sample Z1276. Sample Z1272, Fig. 5.13, has the lowest water content (140 ppm) among the samples deformed under 'wet' conditions and is characterised a very high number of loops, $5 \times 10^9 [m^{-2}]$. Each image has in average two dislocation loops. This sample exhibits a tilt wall density of $4.9 \times 10^8 [m^{-2}]$ and no pile-ups.

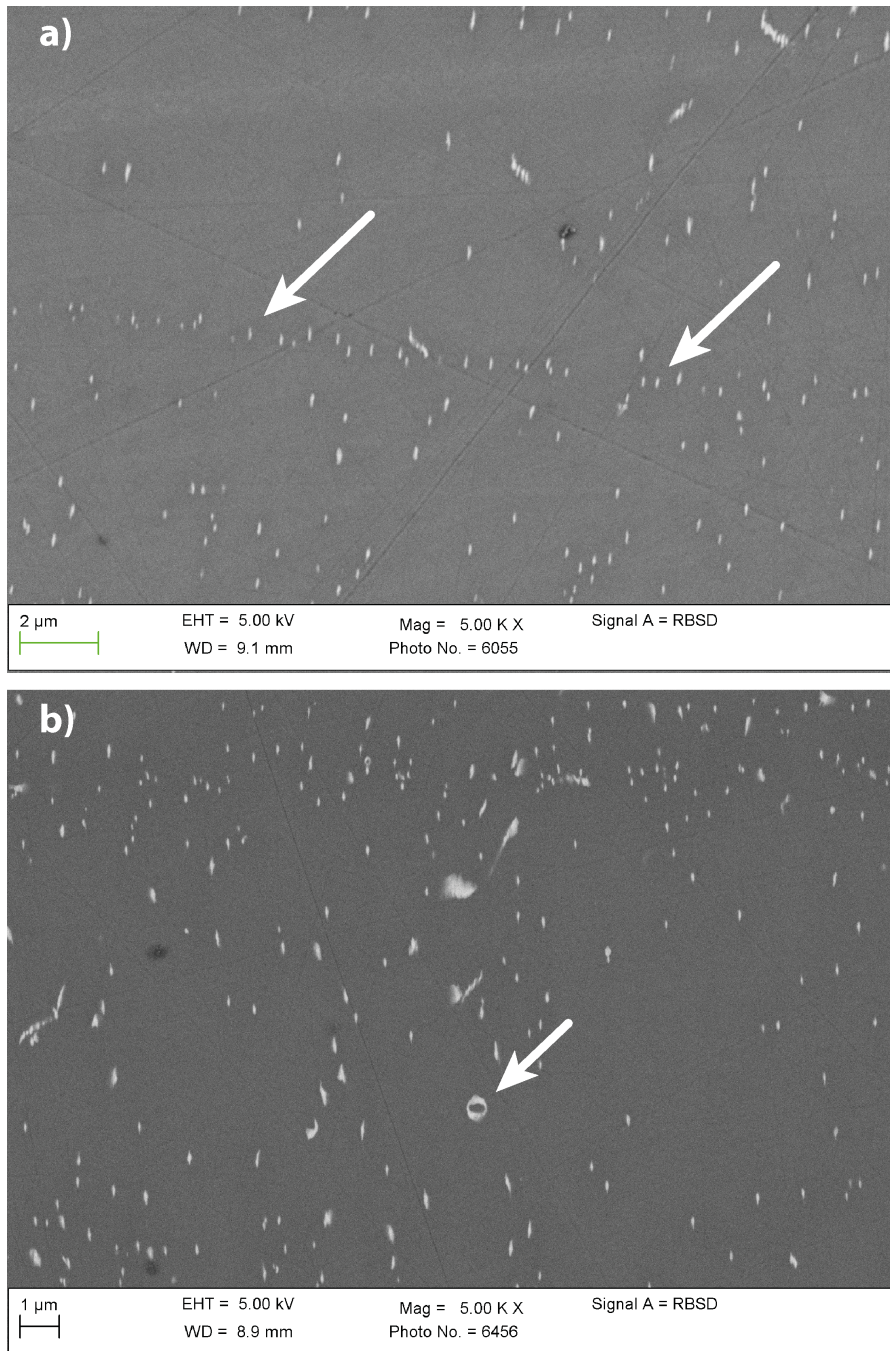


Figure 5.11: Dislocation pile-up and large object in dry samples. a) Dislocation pile-up in sample Z923. Dislocations are aligned parallel to the shear direction. b) Dislocation loop in sample Z931

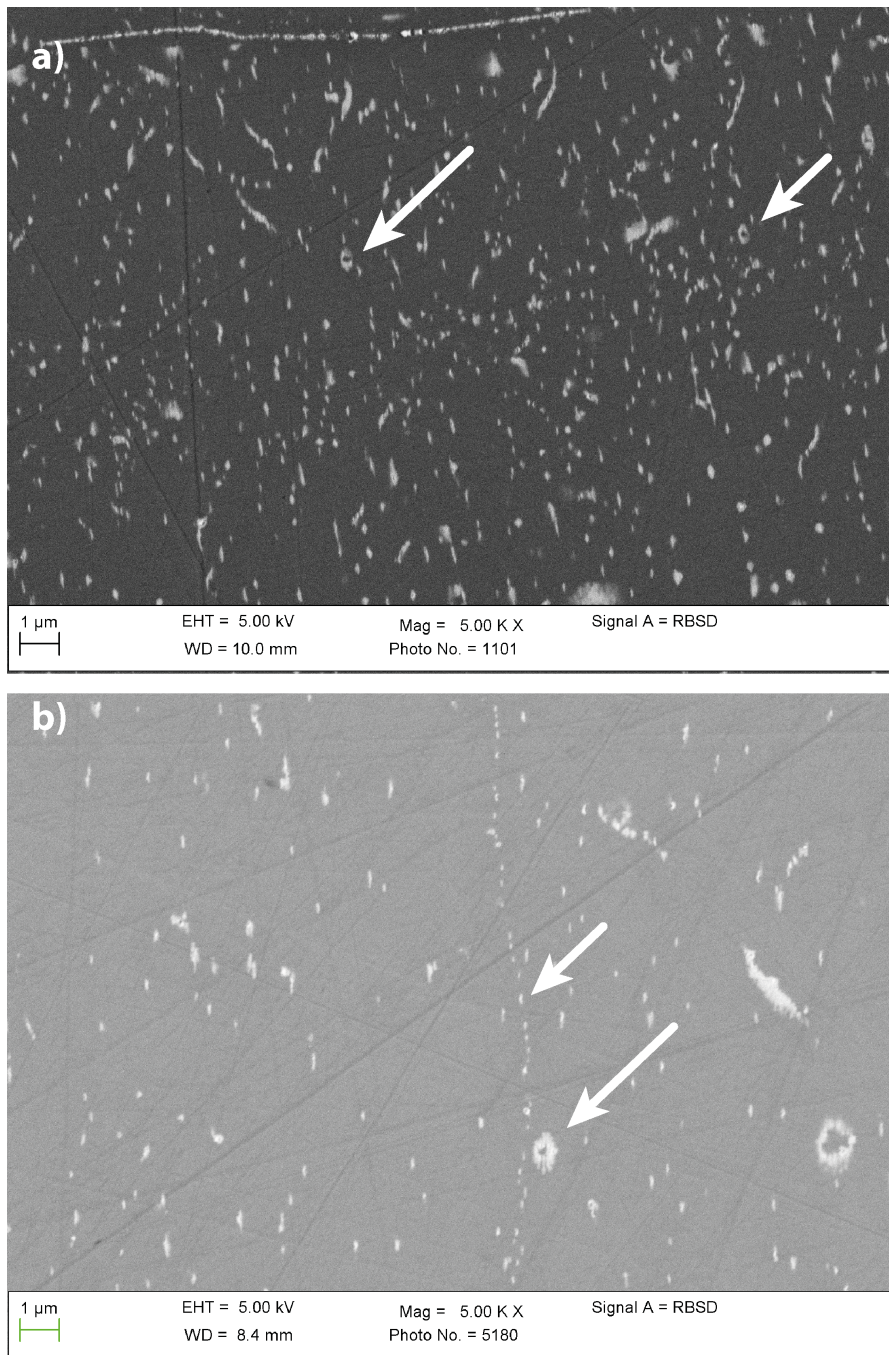


Figure 5.12: Dislocation loops and tilt walls in wet samples. a) Dislocation loops in sample Z1276. b) Tilt wall and loop in sample Z1227.

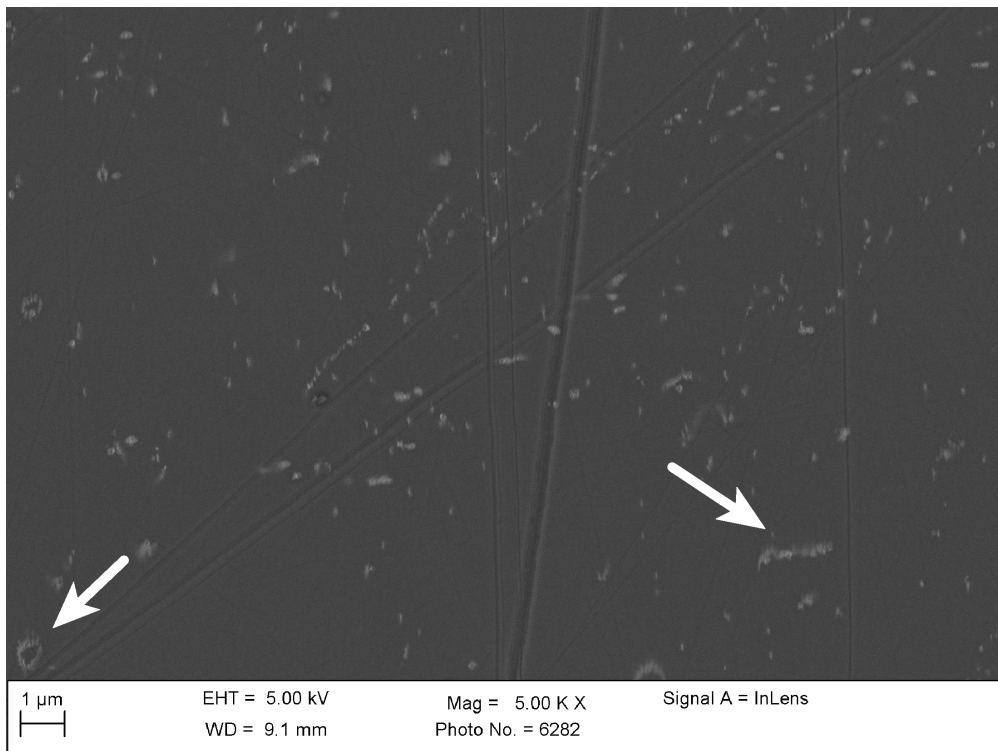


Figure 5.13: Dislocation loop in the lower left corner in sample Z1272. This sample is also characterised by large objects. These large objects are assumed not to be dislocations.

Tilt-wall formation

Sample Z1276 shows a structure in which tilt walls are aligned around a small inclusion grain at the interface (Fig.5.14). This structure should be exceptional, but it is described here because it provides some hints about the formation of tilt walls. This structure was found in the region of the olivine crystal near the interface of the olivine crystal and MgO spacer, and hence should have had no influence on the dislocation density at the centre of the bulk crystal, which was used to obtain the dislocation annihilation rate.

The inclusion grain seems to have already existed inside the host crystal before the deformation. As shown in Fig. 5.14, the inclusion grain is free of dislocations, and therefore no slip should have been activated in this inclusion by the shear deformation. The tilt walls in the host crystal have a constant distance between each other and the tilt-walls seem to start at the interface with the inclusion grain.

Diffraction-patterns collected by EBSD indicate the small difference in crystallographic orientations of the areas across the tilt-walls, which is a rotation around the c-axis (Fig. 5.14). The accumulation of small crystallographic orientations results in a large misorientation of 14° . This gradual change in crystallographic orientations can be observed by the blue to the red color from the right to the left in Fig. 5.15. The sharp change in crystallographic orientation, visible by the sudden colour-change from red to blue at the centre of the image, indicates the existence of a grain boundary. It is also evident that the distance between the walls is very narrow, about $1 \mu\text{m}$. Such a dense distribution of tilt-walls was usually not observed in other samples. Hence, the studied olivine crystals can be assumed to be single crystals.

5.1.4 Activation of other slip systems

In this study, olivine single crystals were deformed in other crystallographic directions than $[100](010)$, but were not used in annealing experiments to obtain the annihilation rates. As shown in Tab. 5.2, deformation experiments to activate $[001](010)$, $[001](100)$ and $[100](001)$ slip systems were performed successfully. Of great interest are the different microstructures of the different slip systems.

Fig 5.16 a) exhibits sample Z1178, which was deformed to activate $[100](001)$ slip system. Dislocation microstructure of a samples with an activated $[100](001)$ slip systems are comparable to samples with an activated $[100](010)$ slip system. Mainly dislocations oriented normal to the observation plane can be observed. Therefore, mainly edge dislocations are activated.

When the $[100](001)$ slip system is activated, as shown for sample Z1228, a particular dislocation microstructure develops: the dislocations form rectangular arrays and the number of mobile dislocation is low. Patterns shown in 5.16 b) are typical for this sample. Therefore, this slip system can be distinguished from other slip systems by observing the dislocation microstructure. Furthermore, this pattern was still visible after annealing. The number of mobile dislocations just decreased.

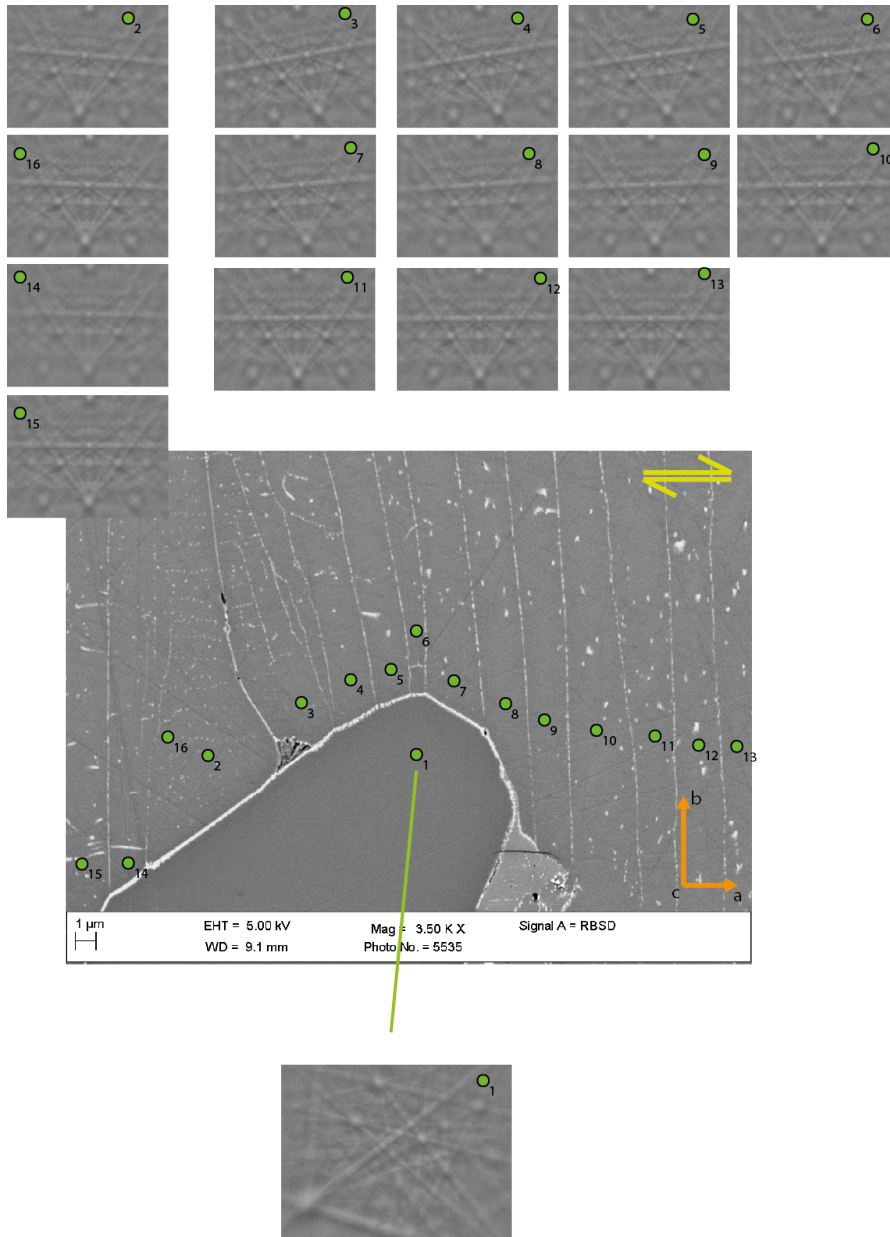


Figure 5.14: Dislocation pileup caused by a smaller grain inside an single crystal of olivine. The rotation of the crystal-lattice caused by the tilt-walls is shown by EBSD-diffraction patterns. The numbers of the pattern correspond to the areas which are indicated by the corresponding numbers.

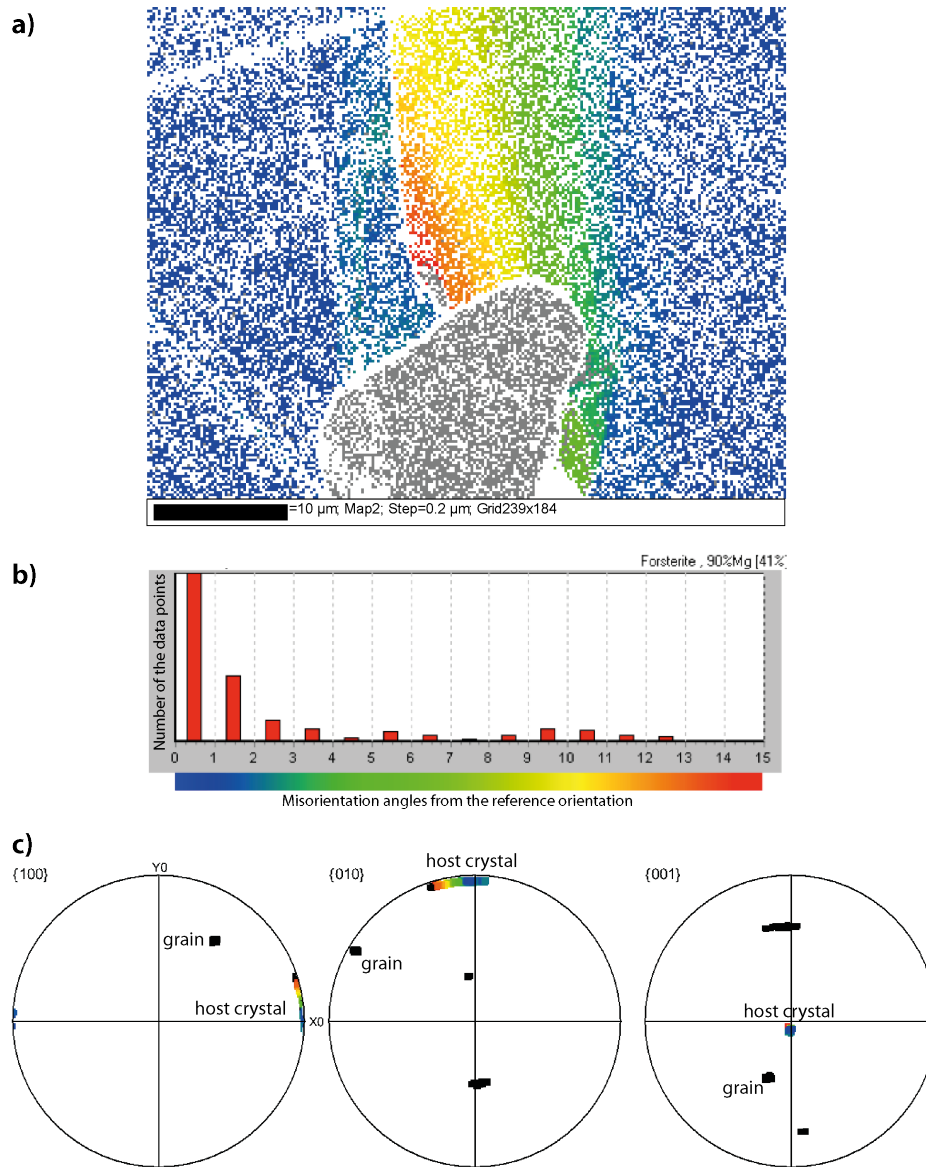


Figure 5.15: a) EBSD-map of the area shown in Fig. 5.14. Step-size of the measurements is $0.2\mu\text{m}$. The difference in orientation is shown by the colour-coding. b) The reference orientation is the average of the blue points in a). The other colours representing the misorientation angles from the reference orientation, which is also shown in the pole-figure plot in c). The points representing the small inclusion grain are not shown in b), because their misorientation from the reference orientation is above 15° .

Name	activated slip plane	dislocation density [m^2] x 10^{11}	Water content (wt. ppm)
Z1178	[001](010)	1.47	250
Z1202	[001](100)		
Z1205	[001](100)		
Z1226	[001](100)		180
Z1228	[100](001)	1.24	
Z1273	[001](010)		

Table 5.2: List of deformation experiments to activate [001](010), [001](100) and [100](001) slip systems, which were successfully performed during this study.

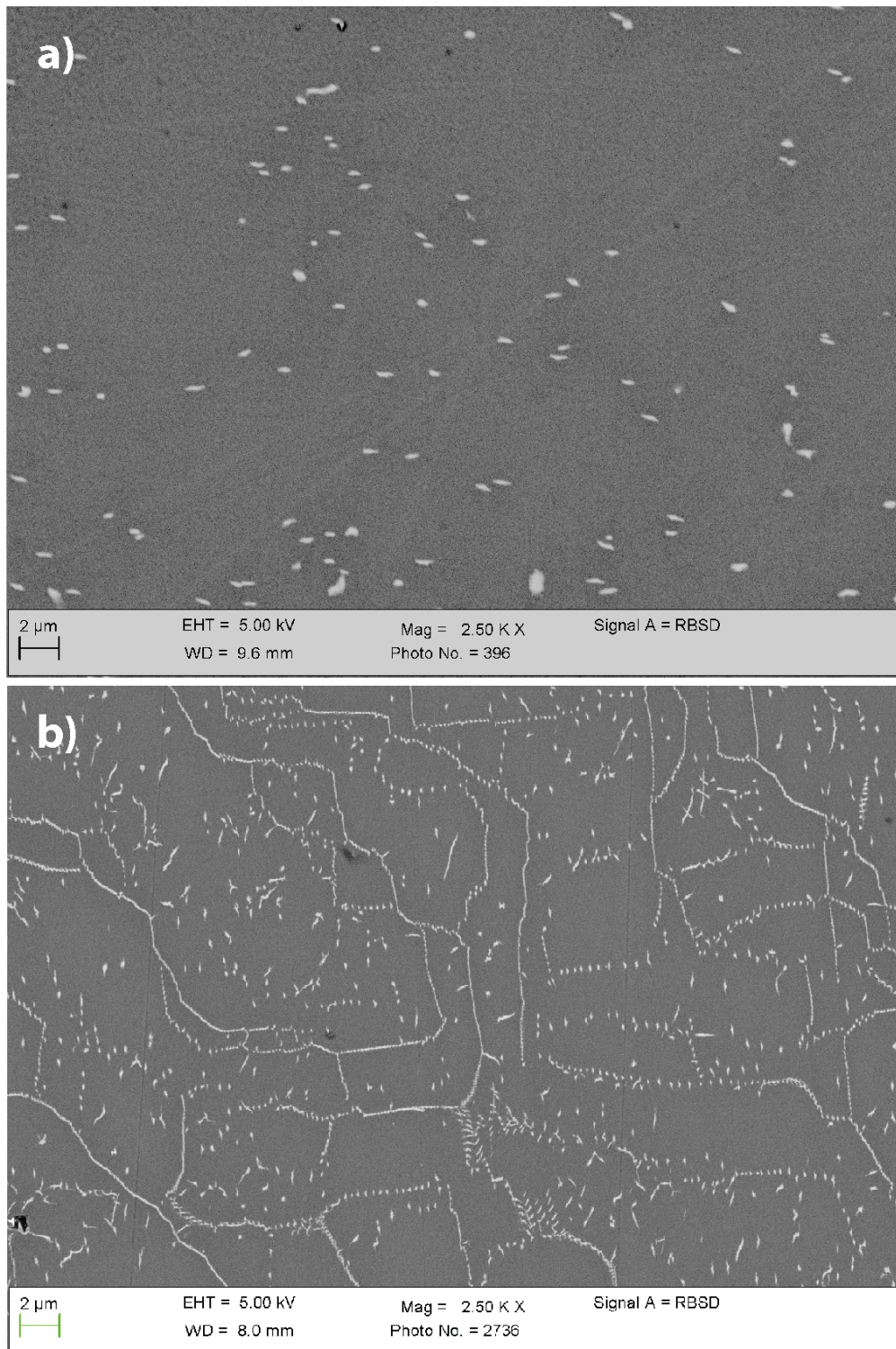


Figure 5.16: a) Dislocation microstructure of sample Z1178 with activated [001](010) slip system.
b) Dislocation microstructure of sample Z1228 with activated [100](001) slip system

5.2 Dislocation recovery experiments

5.2.1 Dislocation structures of annealed samples

Dislocation densities after annealing, ρ_f , are obtained by examining an annealed piece from the deformed crystals. The dislocation densities of in total 13 samples were observed. Typical structures of dislocations are shown in Fig. 5.20, 5.21, 5.22, 5.23 and 5.24. Clustering is more pronounced after annealing at high temperature.

5.2.2 Annealing time

A key factor of annealing experiments is the annealing time. Experiments under 'dry' condition were very stable. The samples were free of chemical reactions or physical damage after recovering the samples from the experiments. Therefore, it was possible to anneal samples in test-experiments up to 50 h. Samples which were used to determine dislocation annihilation rates under 'dry' conditions were annealed between 3 h and 5 h. Annealing for 3 h caused a change in dislocation density of 8 % and up to 22 %. Annealing for 5 h caused a change in dislocation density of 30 %.

Experiments under 'wet' condition were less stable than the 'dry' experiments. The most serious problems is iron loss, which is explained in section 3.2.5 and recrystallisation, which was usually a problem after more than 10 h of annealing. For 'wet' samples, an annealing time of 1.5 to 3 h is enough to see a significant change in density of mobile dislocations by 15 to 20 %.

5.2.3 Observation plane

The dislocation density in the samples was measured as for the deformation experiments in the plane parallel to slip direction and perpendicular to the slip plane, namely the (001) plane. The orientation of the observation-plane was examined by means of EBSD and the misorientation of the observation plane from the (010) plane was less than 15° from ideal observation orientation, and similar to the unannealed samples. Pole figure plots of the observed samples are shown in Fig. 5.17, 5.18 and 5.19.

Variation in dislocation density

The annealed samples exhibit greater spatial variation in dislocation density than the unannealed ones. Fig. 5.25 demonstrate variation in dislocation densities in four adjacent pictures. The average density is $2.2 \times 10^{11} \text{ m}^{-2}$. The pictures with denser dislocations ($3.1 \times 10^{11} \text{ m}^{-2}$, Fig. 5.25 b), show smaller special variation in dislocation density and reveals the largest density of clusters and tilt-walls, whereas those with lower densities have more homogeneously distributed dislocations and almost no clusters and tilt walls.

The dislocation density variation per image for annealed sample Z1287 is shown in Fig. 5.26. The maximum of the total dislocation density is $9 \times 10^{11} \text{ m}^{-2}$ (Fig. 5.26 a), and those of the mobile dislocation density are 3×10^{11} and $4.5 \times 10^{11} \text{ m}^{-2}$ (Fig. 5.26 b). Fig 5.26

Sample	Deformation experiment	Mobile dislocation density before annealing $[\text{m}^{-2}] \times 10^{11}$	Mobile dislocation density after annealing $[\text{m}^{-2}] \times 10^{11}$	Annealing time [h]	Water content before annealing (wt. ppm)	Water content after annealing (wt. ppm)	Density loops $[\text{m}^{-2}] \times 10^8$	Pile-ups $[\text{m}^{-2}] \times 10^8$	Tilt walls $[\text{m}^{-2}] \times 10^8$
Z1237	Z1227	14 ± 2.6	6.5 ± 1.0	1	308 ± 60	285 ± 45	22	2	76
Z1244	Z1227	14 ± 2.6	7.0 ± 1.9	3	308 ± 60	380 ± 20	16	6	5
Z1248	Z923	4.2 ± 0.9	3.7 ± 1.9	3	[20]	[60]	0	0	0
	Z931	6.1 ± 0.9	4.7 ± 0.9	3	17 ± 3	60 ± 6	1	10	0
Z1285	Z1272	6.4 ± 1.7	4.8 ± 1.0	3	140 ± 15	320 ± 25	25	0	22
	Z1276	6.1 ± 2.2	4.9 ± 1.2	3	240 ± 35	240 ± 25	134	76	7
Z1286	Z923	4.2 ± 0.9	2.8 ± 0.8	5	\pm	50 ± 3	0	4	3
Z1287	Z1272	6.8 ± 1.7	5.8 ± 1.0	1.5	140 ± 15	285 ± 25	90	0	0
	Z1276	7.5 ± 2.7	3.9 ± 0.9	1.5	240 ± 35	255 ± 30	9	4	0
Z1288	Z1272	6.9 ± 1.7	5.3 ± 2.2	3	140 ± 15	380 ± 25	27	0	0
Z1290	Z1276	7.6 ± 2.7	2.7 ± 1.2	3	240 ± 35	160 ± 15	23	0	4
Z1291	Z1276	7.5 ± 2.7	3.6 ± 0.9	1.5	240 ± 35	165 ± 20	0	23	0
Z1292	Z1276	7.4 ± 2.7	4.5 ± 1.9	3	240 ± 35	140 ± 10	5	7	43

Table 5.3: Successfully performed annealing experiments with different water contents.

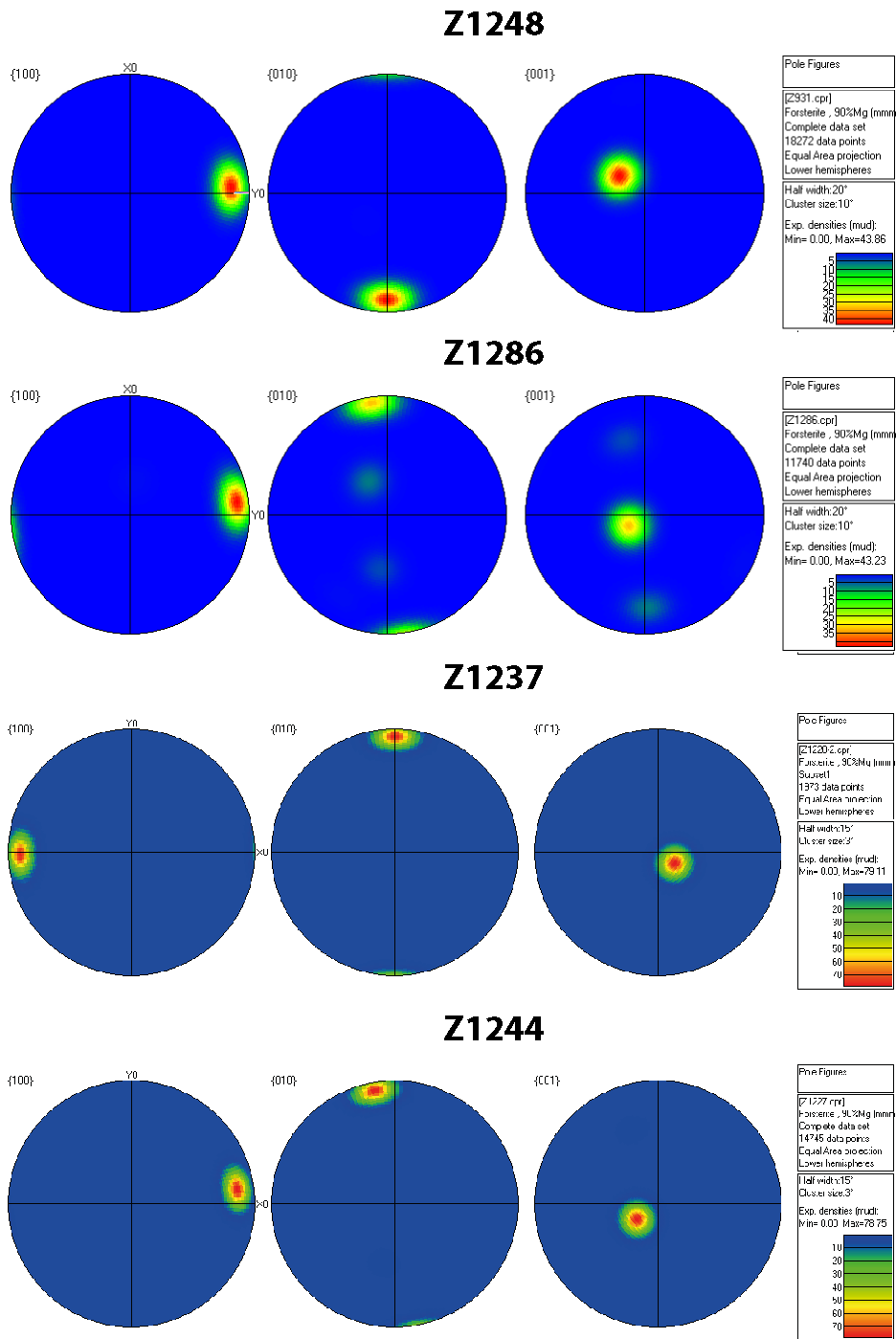


Figure 5.17: Pole figure plots of the annealed samples of Z931: Z1285, Z923: Z1286 and Z1227: Z1237 and Z1244. Shear plane is horizontal.

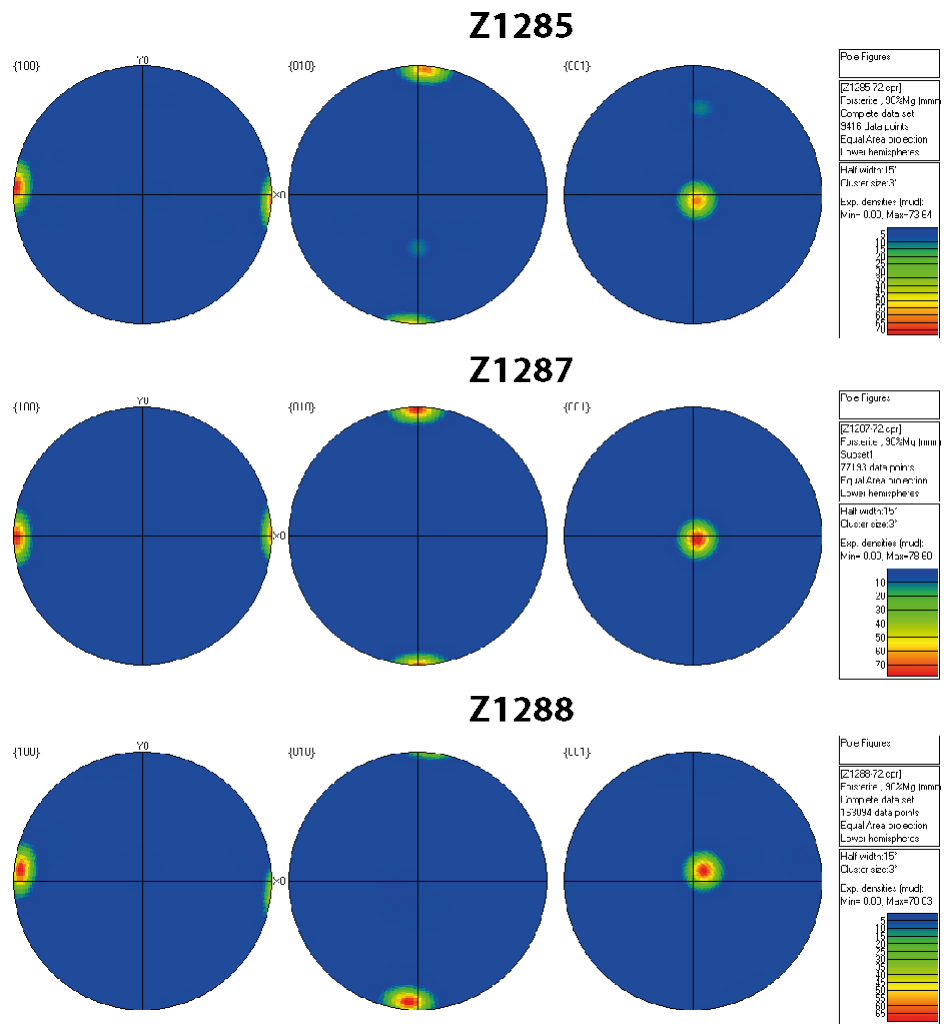


Figure 5.18: Pole figure plots of the annealed samples of Z1272: Z1285, Z1287 and Z1288. Shear plane is horizontal.

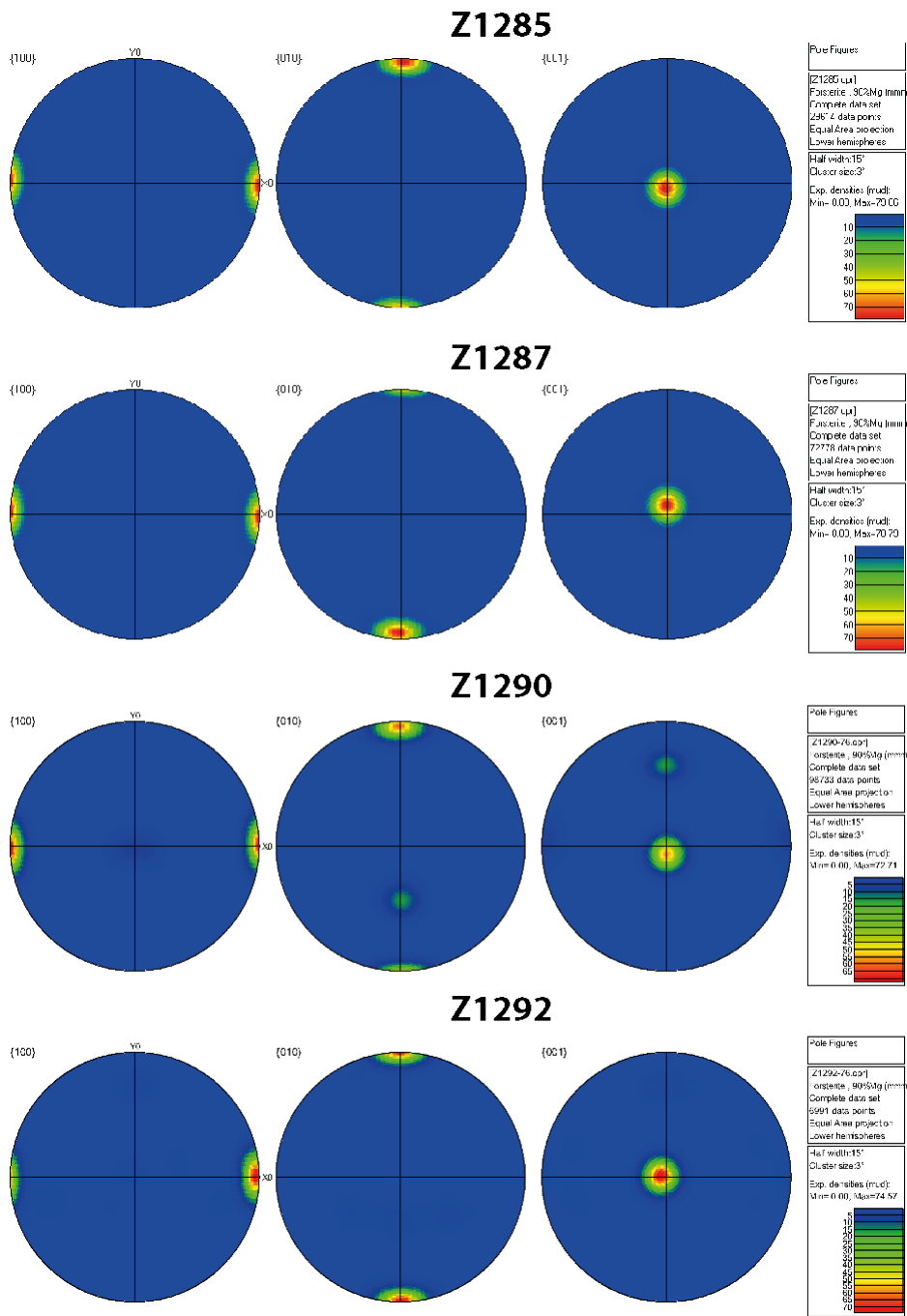


Figure 5.19: Pole figure plots of the annealed samples of Z1276: Z1285, Z1287, Z1290 and Z1292. Shear plane is horizontal.

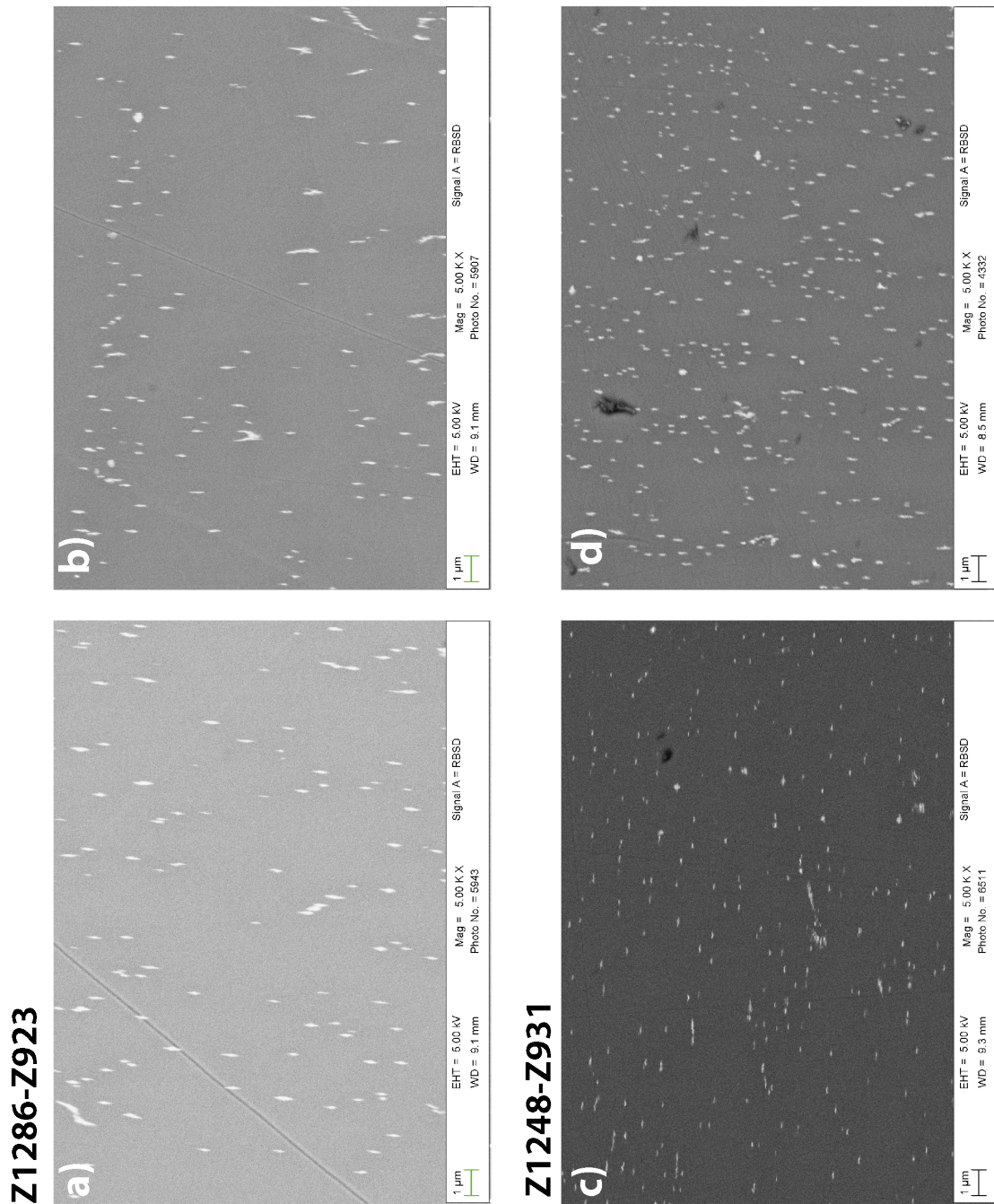


Figure 5.20: Dislocation structures of samples Z1286 a) and b) and Z1248 c) and d) annealed under dry conditions. Sample Z1286 was deformed in experiment Z923. Annealing time was 5 h and the sample contains 50 ppm of water. Sample Z1248 was deformed in experiment Z913 and annealed for 3h. The water content is 60 ppm.

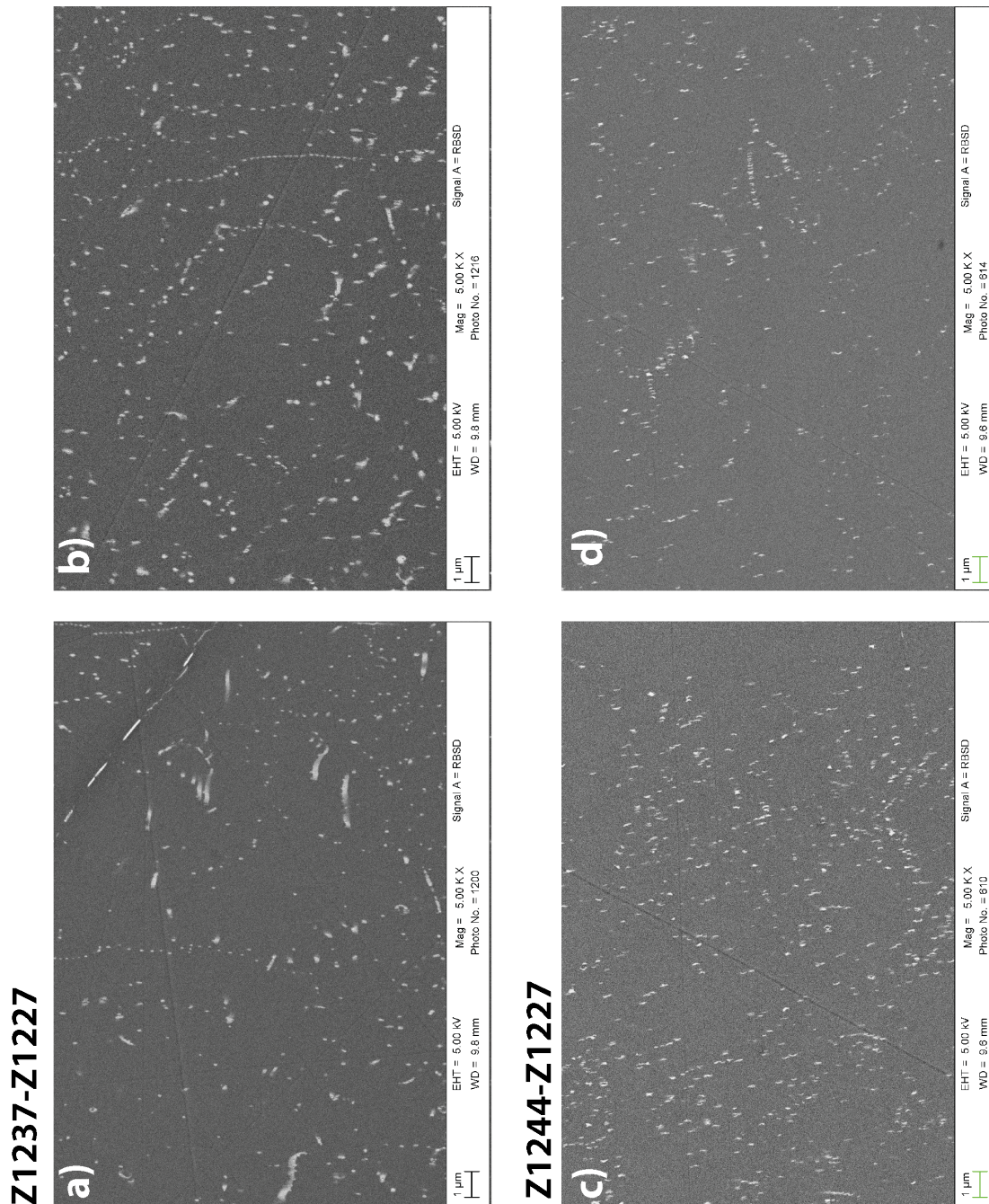
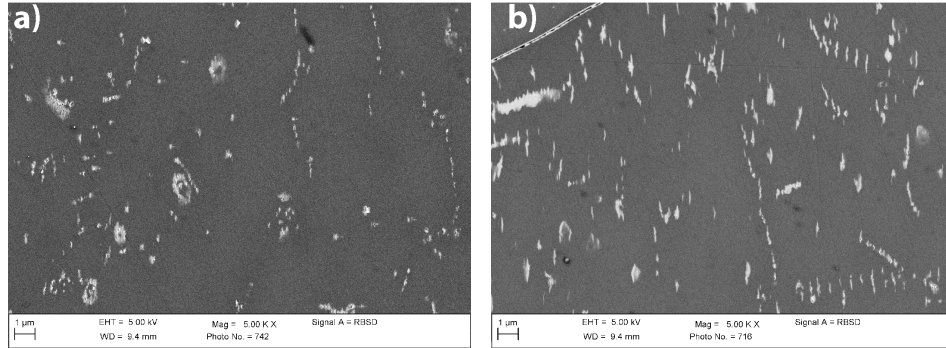
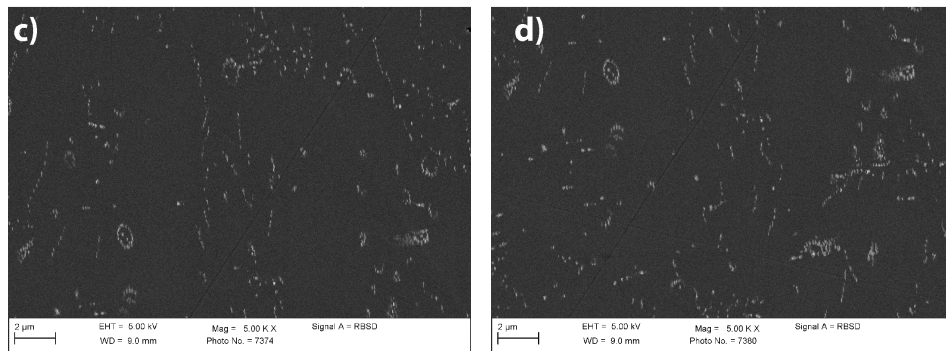


Figure 5.21: Dislocation structures of annealed sample Z1237 a) and b) and Z1244 c) and d) under wet conditions. Both samples were deformed in experiment Z1227. Annealing time was 1 h for Z1237 and the sample contains 285 ppm of water. Sample Z1244 was annealed for 3h. The water content is 380 ppm.

Z1285 - Z1272



Z1287 - Z1272



Z1288 - Z1272

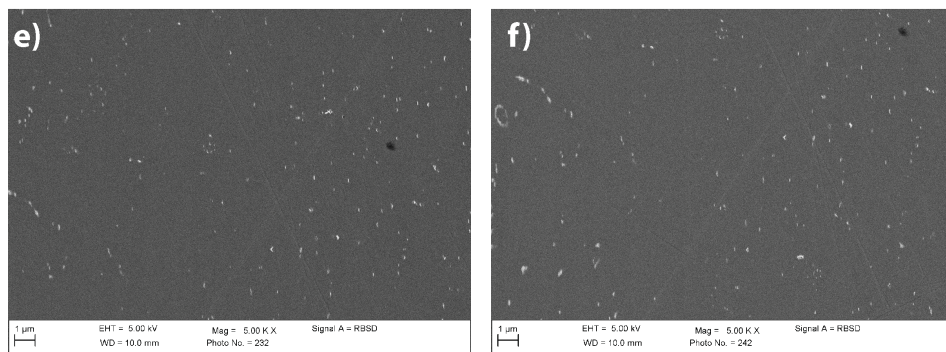
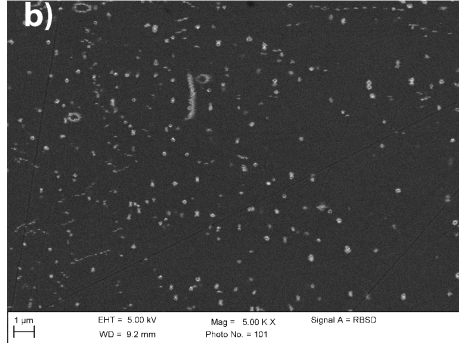
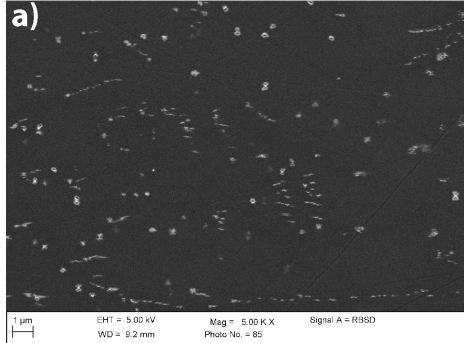
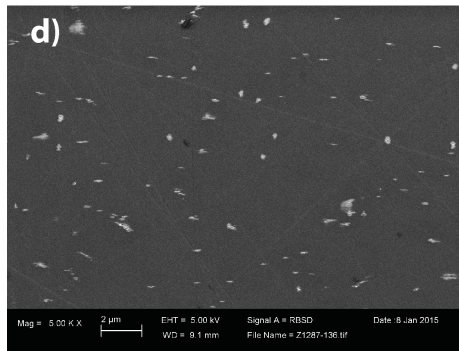
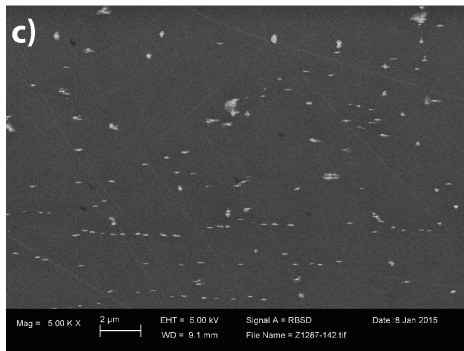


Figure 5.22: Dislocation structures of annealed sample Z1285 a) and b), Z1287 c) and d) and Z1288 e) and f) under wet conditions. These samples were deformed in experiment Z1272. Sample Z1285 contains 320 ppm of water, Z1287 290 ppm and Z1288 380 ppm. Annealing time was 1 h for Z1237 and the sample contains 285 ppm of water. Annealing times are 3h, 1.5h and 3h, respectively.

Z1285 - Z1276



Z1287 - Z1276



Z1290 - Z1276

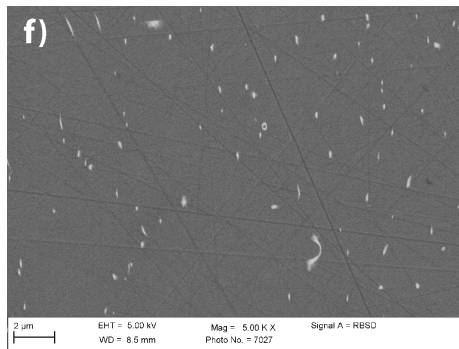
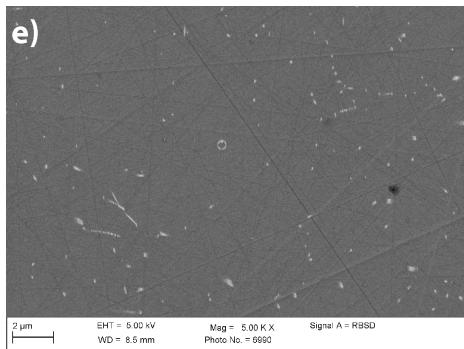


Figure 5.23: Dislocation structures of annealed sample Z1285 a) and b), Z1287 c) and d) and Z1290 e) and f) under wet conditions. The starting materials for these annealing experiments were deformed in experiment Z1276. The water contents of the samples are 240 ppm for Z1285, 260 ppm for Z1285 and 160 ppm for Z1290 and annealing times are 3h, 1.5h and 3h, respectively.

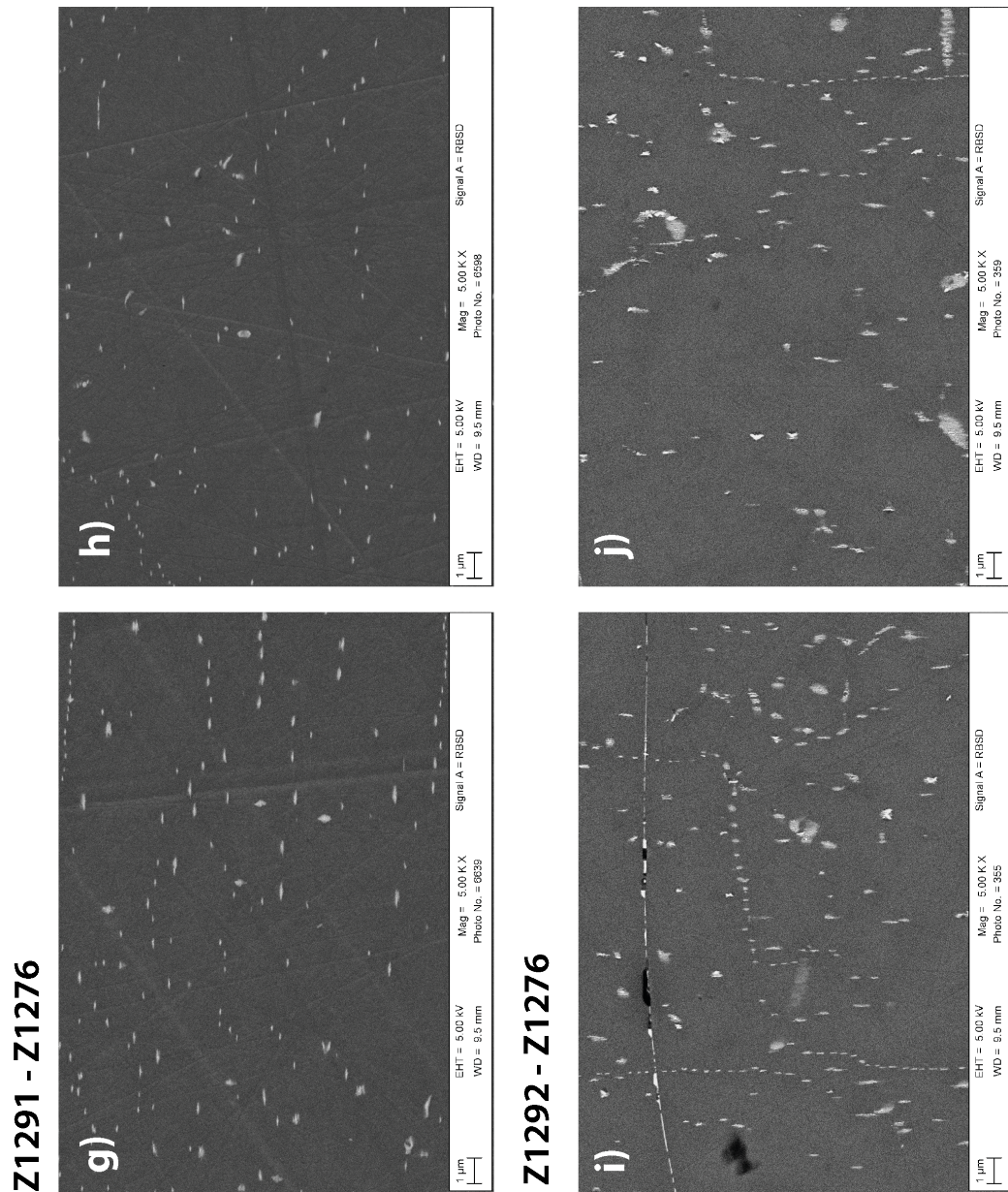


Figure 5.24: Continuation of Fig. 5.23: Dislocation structures of annealed sample Z1291 g) and h) and Z1292 i) and j) under wet conditions. Z1291 contains 165 ppm of water and was annealed for 1.5 h and Z1292 contains 140 ppm of water and was annealed for 3h.

Sample	Deformation experiment	Deviation observation plane	Slip direction
Z1237	Z1227	10°	9°
Z1244	Z1227	12°	7°
Z1248	Z931	11°	4°
Z1285	Z1272	3°	4°
	Z1276	3°	2°
Z1286	Z923	10°	5°
Z1287	Z1272	0°	0°
	Z1276	3°	0°
Z1288	Z1272	4°	6°
Z1290	Z1276	0°	0°
Z1292	Z1276	0°	0°

Table 5.4: Deviation of the observation plane and the main slip direction from the perfect observation directions.

c) exhibits the variation of the immobile dislocations. The maximum is located at $5 \times 10^{11} m^{-2}$.

Dislocation clusters

By annealing, part of dislocations is annihilated and part of the remaining dislocations moves into more energetically stable sub-structures. The remaining dislocations form clusters and are less homogeneously distributed compared to the unannealed samples. Examples of clusters are shown in Fig. 5.27 and Fig. 5.28

Tilt walls, Pile-ups

Formation of tilt-walls sometimes occurs in changes in dislocation structure during annealing. Some images show tilt-walls but they are not a main feature. It can be observed that tilt-walls are more common in samples with a lower water content. Dislocation-dislocation annihilation seems to be the dominant recovery process. It is sometimes observed the dislocation densities near tilt boundaries are asymmetric. The dislocation density on one side is much smaller than the other side, suggesting that these tilt boundaries moved in the crystals. Especially in 'dry' samples, dislocations blocked by a tilt wall are observed (Fig. 5.29), although such phenomena are not observed in samples with a higher water content. We note that, however, areas in which the asymmetry in dislocation density is observed are limited even in dry samples, and the change in dislocation density is observed away from tilt-walls. We note that, however, areas in which such asymmetry in dislocation density is witnessed is limited even in dry samples.

Dislocation pile-ups are also be found in the annealed samples. The highest density of pile-ups, $76 \times 10^8 \text{ m}^{-2}$, is found in sample Z1285-1276.

5.2.4 Mobile dislocation density

The chosen distance to define dislocation dipoles is 0.25μ . As mentioned earlier, this distance was chosen empirically by observing dislocation clusters, usually dipoles or tripoles, in the samples. By using this distance it was possible to locate automatically tripoles by using the Matlab-code. This distance is not sufficient enough to locate tilt walls automatically. The distance between dislocations in a tilt wall is typically 0.45μ . Because the process observed in this study is a recovery process, the formation of dislocation dipoles and dislocation annihilation occur. The number of dislocation dipoles is larger in annealed samples rather in the deformed samples. Therefore, removing dipoles from the total number of dislocations, has a small influence on the dislocation annihilation exponent. Dislocation dipoles represent immobile dislocation which are not taking part at the deformation process. By using 0.45μ for the distance of dipoles the dislocation annihilation exponent increased to 0.8 which is still lower than the value expected from deformation experiments. However, the distance of 0.45μ is overestimating the numbers of mobile dislocations.

5.2.5 Hydrostatic stress conditions

Annealing experiments should be performed under conditions of perfectly hydrostatic stress. The compressional stage of the experiment is considered to be the most critical stage during the experiment. By using graphite surrounding the olivine crystals during the annealing process, hydrostatic stress is assumed to be achieved closely. This was tested by using an olivine cube with edge length of $1.5 \times 1.5 \times 1.5 \text{ mm}$. An experiment was terminated after reaching target pressure and before increasing power for heating. The cube was nearly free of dislocations before and also after recovering it from the press. Therefore, it can be assumed that the stress during the annealing process at high temperatures is near-hydrostatic.

5.3 Dislocation densities

As explained previously, dislocations were observed by means of the BEI technique in combination with the oxidation decoration technique. Since the dislocations were observed only on the (001) plane, three-dimensional information of the third dimension is largely lost, which would be needed for understanding spatial network configuration. However, this information is not necessary in this project. The majority of dislocations appear as bright dots, because the dislocations are elongated in the [001] direction. Since the samples were sheared in the [100] direction on the (010) plane, it is considered that the majority of the dislocations are edge or mixed dislocations with the Burgers vector of $h\ 0\ 0$. The annealing process decreases density of homogeneously distributed dislocations and sometimes it also forms tilt-walls by accumulation of dislocations. The case that dislocation densities near tilt boundaries are asymmetric, i. e. the dislocation density on one side is much smaller than the other side [Karato et al., 1993] was observed in some cases. Resulting densities of mobile dislocations of the experiments are summarised in table 5.5. The rate constant k , based on dislocation density change calculation is also shown in table 5.5.

The density of mobile dislocations measured in this study ranges from $2\sim 4 \times 10^{11} - 4 \times 10^{11} m^{-2}$. These are comparable values to previous dislocation recovery studies of single crystal olivine, cf. [Kohlstedt et al., 1980]; [Karato and Sato, 1982]; [Karato et al., 1993]. The rate constants k , based on the dislocation density change and annealing duration are also shown in this Tab. 5.5. The k ranges from $10^{-16.6}$ to $10^{-15.6} m^2 s^{-1}$. The errors are calculated from the standard deviation of the dislocation densities among different images, which are caused by the heterogeneity in dislocation density.

Deformation experiment	Annealing experiment	t [h]	$\rho_i [\frac{10^{11}}{m^2}]$	$\rho_f [\frac{10^{11}}{m^2}]$	$\log(k) [\frac{m^2}{s}]$	H_2O [ppm by weight]
Z923	Z1248	3	4.2 ± 0.9	3.7 ± 1.9	-16.57 ± 1.1	60 ± 6
	Z1286	5	4.2 ± 0.9	2.8 ± 0.8	-16.22 ± 0.4	51 ± 3
Z931	Z1248	3	6.1 ± 0.9	4.7 ± 0.9	-16.4 ± 0.3	60 ± 6
Z1227	Z1237	1	14 ± 2.6	6.5 ± 1.0	-15.6 ± 0.1	285 ± 44
	Z1244	3	14 ± 2.6	7.0 ± 1.9	-16.2 ± 0.3	378 ± 21
Z1272	Z1285	3	6.4 ± 1.7	4.8 ± 1.0	-16.2 ± 0.2	320 ± 47
	Z1287	1.5	6.8 ± 1.7	5.8 ± 1.0	-16.3 ± 0.4	286 ± 25
	Z1288	3	6.9 ± 1.7	5.3 ± 2.2	-16.4 ± 0.6	380 ± 24
Z1276	Z1285	3	6.1 ± 2.2	4.9 ± 1.2	-16.4 ± 0.4	237 ± 23
	Z1287	1.5	7.5 ± 2.7	3.9 ± 0.9	-15.6 ± 0.2	256 ± 31
	Z1290	3	7.6 ± 2.7	2.7 ± 1.2	-15.7 ± 0.4	157 ± 15
	Z1291	1.5	7.5 ± 2.7	3.6 ± 0.9	-15.6 ± 0.2	165 ± 20
	Z1292	3	7.4 ± 2.7	4.5 ± 1.9	-16.1 ± 0.4	143 ± 11

Table 5.5: Results of recovery experiments. ρ_i is the initial dislocation density after the deformation experiment and ρ_f the final dislocation density after the annealing experiment. Rate constant, k is obtained based on the dislocation density and the annealing duration. The annealing time, h is the time at maximum temperature in hours. Water content is measured by FTIR-spectroscopy.

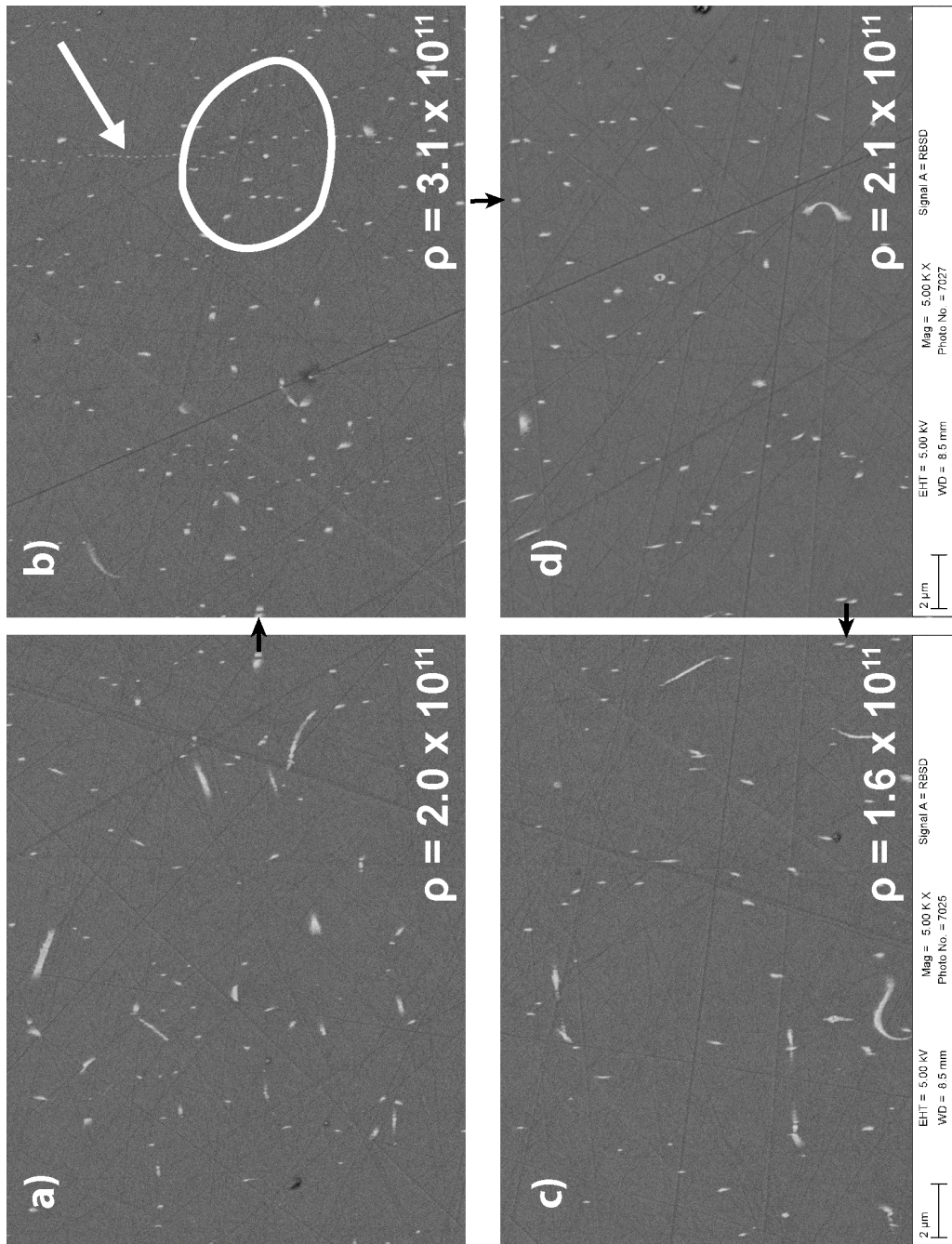


Figure 5.25: Four neighbouring images of the annealed sample Z1290. In each image the calculated density of mobile dislocation is shown. The black arrows indicate the corresponding points in the adjacent images. The individual densities of mobile dislocations in these four images are a) 2.0×10^{11} b) 3.1×10^{11} , c) 1.6×10^{11} and d) $2.1 \times 10^{11} m^{-2}$, and the average density is $2.2 \times 10^{11} m^{-2}$. The highest density is show in image b) as well a tilt wall (white arrow) and a cluster (white outline).

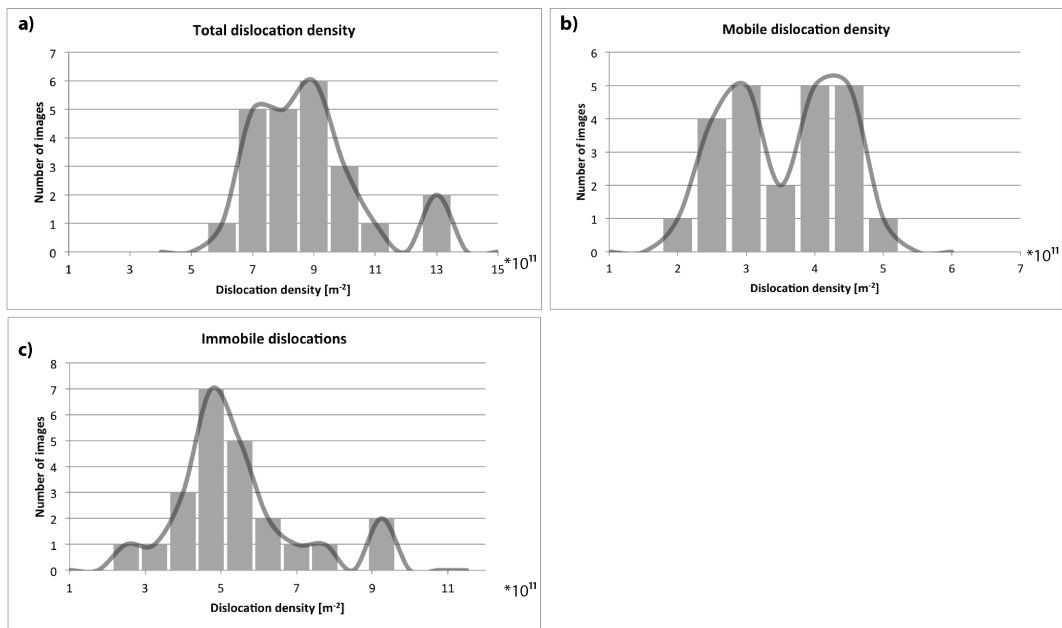


Figure 5.26: Variation in dislocation densities of the annealed sample Z1287 of the deformed sample Z1272. Shown are for the numbers of analysed images against a) total, b) mobile and c) immobile dislocation densities.

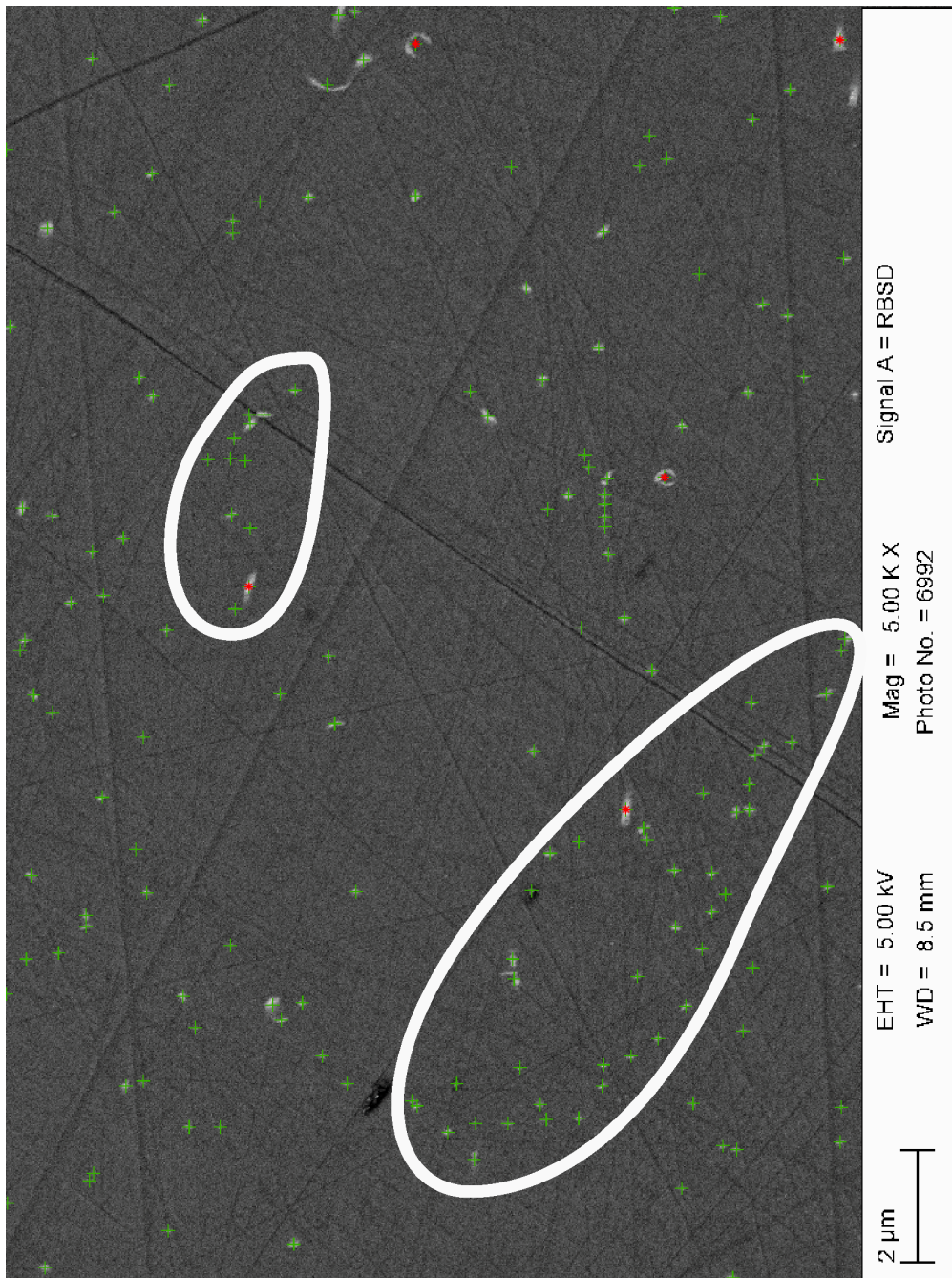


Figure 5.27: Dislocation clustering of sample Z1290. White outlines surround the clusters.

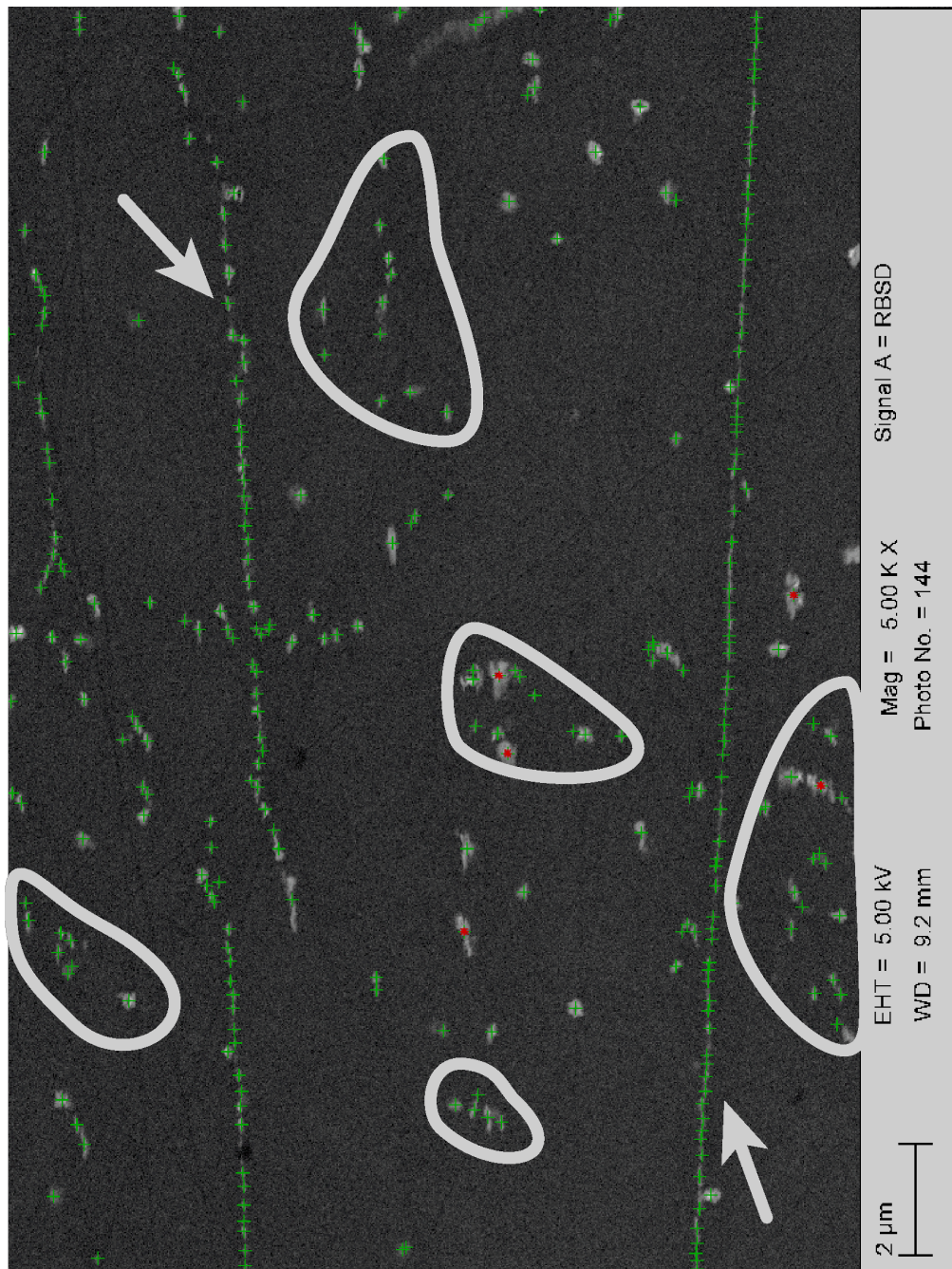


Figure 5.28: Dislocation clustering of sample Z1285. Clusters are marked by a white outline and dislocation pile-ups by white arrows.

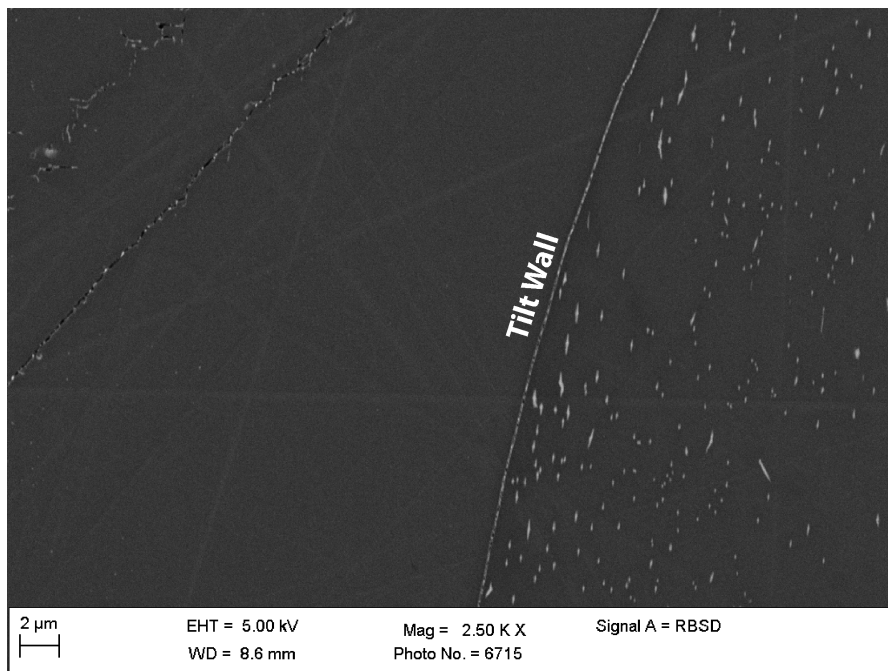


Figure 5.29: Tilt wall moving through an annealed sample. The dislocations are asymmetrically distributed.

5.4 Dislocation microstructures

Comparison of dislocation microstructures of different slip-systems

During this study a method to activate certain slip systems under 'dry' and 'wet' conditions in olivine was developed. As shown in Table 5.1, experiments for four different slip systems were performed successfully. Interesting are the different microstructures of different slip systems. Samples deformed in $[001](010)$ have a lower dislocation density even though they were deformed at the same condition as $[100](010)$ -samples, which is probably related to the difference of the burgers vector. When the $[100](001)$ slip system is activated as shown for sample Z1228, a particular dislocation microstructure was developed. The dislocations formed rectangular arrays and the number of mobile dislocations are low. Patterns, as shown in Fig. 5.30, are typical for this sample. Therefore, just by observing the dislocation microstructure, this slip system can be distinguished from other slip systems. Further, after annealing, this pattern was still visible, just the number of mobile dislocations decreased.

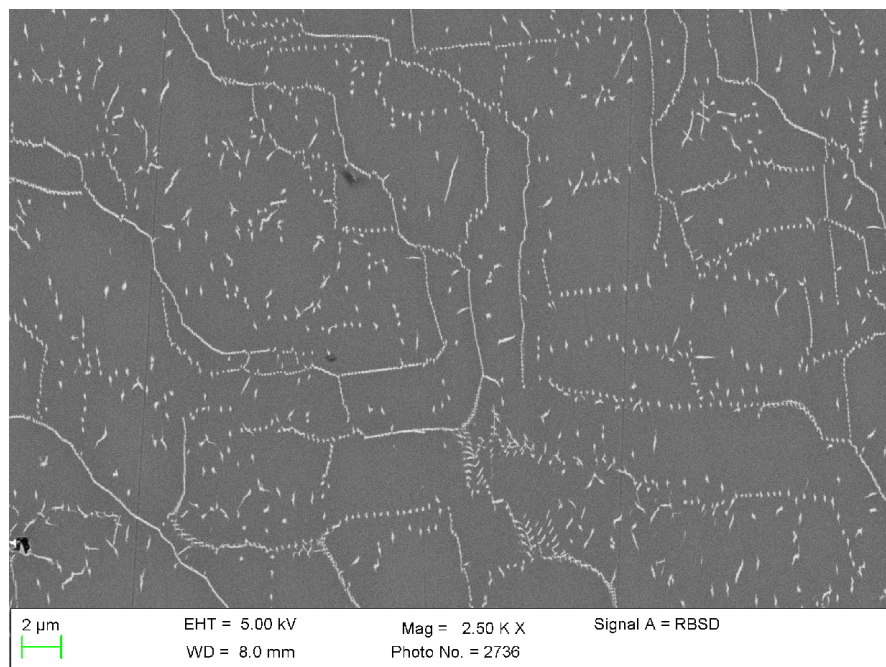


Figure 5.30: Dislocation microstructure of sample Z1228 with activated $[100](001)$ slip system. A number of tilt walls are observed.

Dislocation microstructures of natural samples

A natural sample was oxidised to examine whether the experimental samples have similar dislocation textures as the natural one. Fig. 5.31 and 5.32 display a oxidised sample from an alpine type peridotite which was cut parallel to the lineation and normal to the foliation. The majority of dislocations appear as dots in this sample. The dislocation microstructures,

such as tilt-walls (white arrows in Fig.: 5.32), are comparable to the experimental deformed samples of this study. Hence, the dislocation creep processes observed in this study are assumed to be similar to those in the Earth's upper mantle.

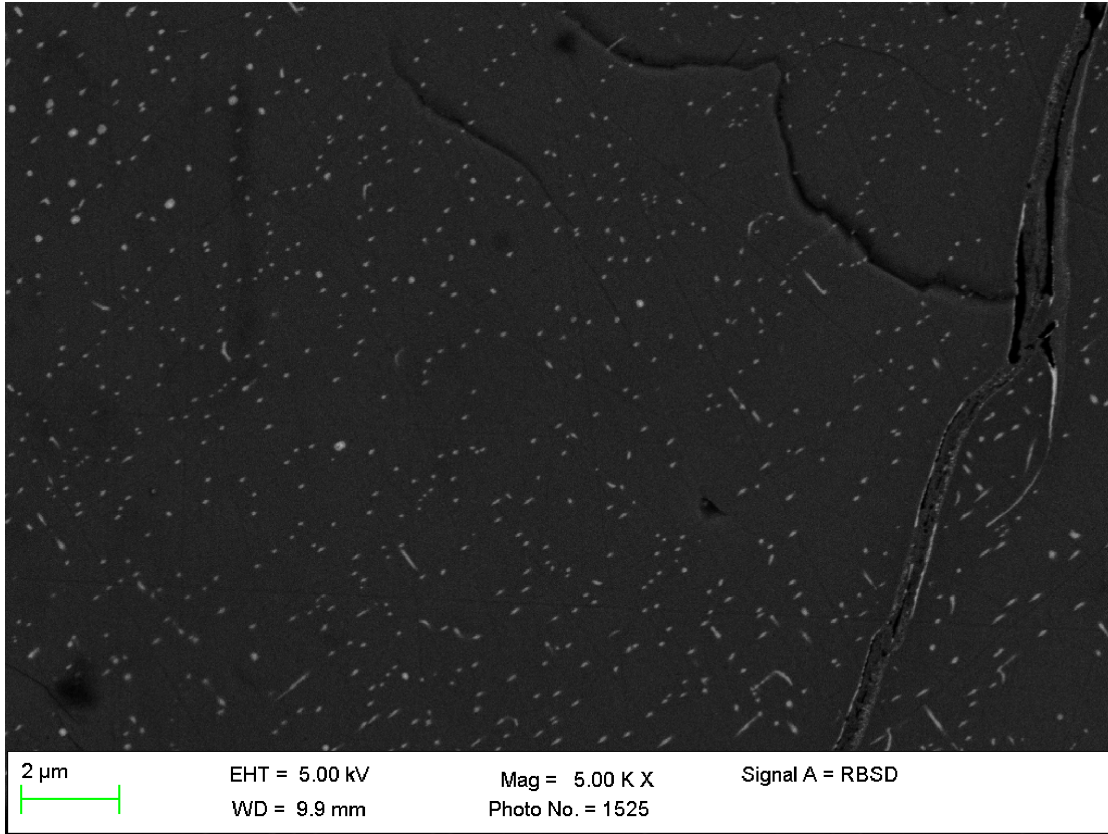


Figure 5.31: Dislocation microstructure of a natural sample that was cut parallel to the lineation and normal to the foliation.

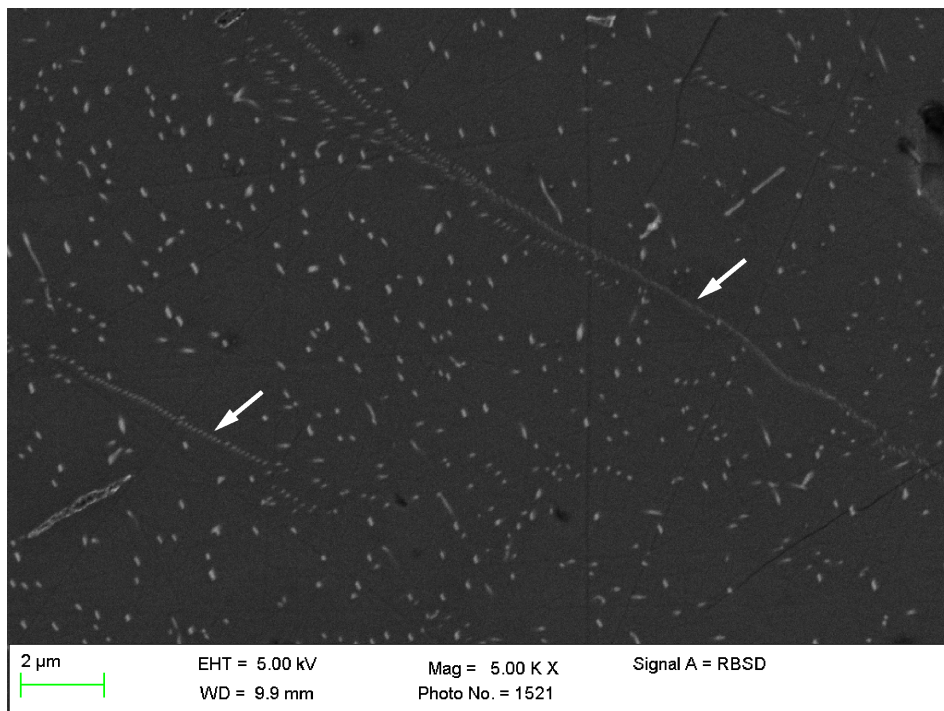


Figure 5.32: Dislocation microstructure of a natural sample observed by SEM. Sub-grain boundaries are indicated by white arrows.

5.5 Water content

The amount of hydrogen which protonates point defects in olivine was evaluated by FTIR-spectroscopy. The method is described in the previous chapter (Chapter 4.1). To calculate the hydrogen content, the calibration by Bell [Bell et al., 2003] was used. Water content of deformed and annealed samples are given in Tab. 5.6. Further the amounts of water subdivided in group I (3640 to 3450 cm^{-1}) and II (3450 to 3170 cm^{-1}) are shown.

5.5.1 Hydration experiments

Several experiments were conducted to hydrate cylinders of natural olivine single crystals with an height of 1.0-1.5mm and a diameter of 1.5 mm. The goal of these experiments was to increase the water content before the deformation experiment. Sample H4089, H4045 and V897 were used in deformation experiments Z1272, Z1227 and Z1276, respectively. FTIR-spectra of the recovered samples are shown in Fig. 5.33. Because the crystals were used in further experiments, spectra could only be collected $E \parallel a$ and $E \parallel c$, respectively. The minimum water contents are 192 ± 3 wt. ppm for H4089, 355 ± 66 wt. ppm for H4045 and 270 ± 17 wt. ppm for V897. Measurements $E \parallel b$ are missing, therefore the water content must be assumed to be higher. During deformation experiments water was lost from olivine. The sample with the highest water content before the deformation process H4045 with 355 ± 66 wt. ppm of water revealed after the deformation experiment the highest water content of 308 ± 62 wt. ppm in sample Z1272. Sample H4089 with the lowest water content of 192 ± 3 wt. ppm was used in experiment Z1272 with the lowest water content after deformation of 132 ± 14 wt. ppm. The intermediate sample V897 with 270 ± 17 wt. ppm revealed 209 ± 26 wt. ppm after the deformation experiment.

5.5.2 Deformation experiments

The water contents of deformed samples are between 17 ± 2 and 308 ± 62 wt. ppm. The difference in water contents result from different amounts of talc+brucite, which was added to the experiments. Samples Z923 and Z931 represent 'dry' deformation experiments, because no water source was added to the experiments. Z931 contains around 50 ppm of water. The water content of Z923 was not measured, but is assumed to be equivalent to Z931. The water content were measured at least 9 up to 30 positions in the samples. The example of resulting FTIR-spectra from 16 positions of a deformed sample Z1272 was shown in Fig. 4.2. From the division of the IR-spectra in two groups, it is evident that sample Z1272 is slightly different compared to sample Z1227 and Z1276, because its intensity ratio of Group I/Group II is higher (2:1 for Z1272, 3:1 for Z1227 and 4:1 for Z1276) than those of these two.

5.5.3 Annealing experiments

For annealed samples, the hydrogen content is between 51 ± 3 , Z1248, up to 378 ± 21 wt. ppm, Z1288. The lowest water content was found in a sample that was not hydrated. It can be assumed, that the increase in hydrogen from the deformed to the annealed samples results

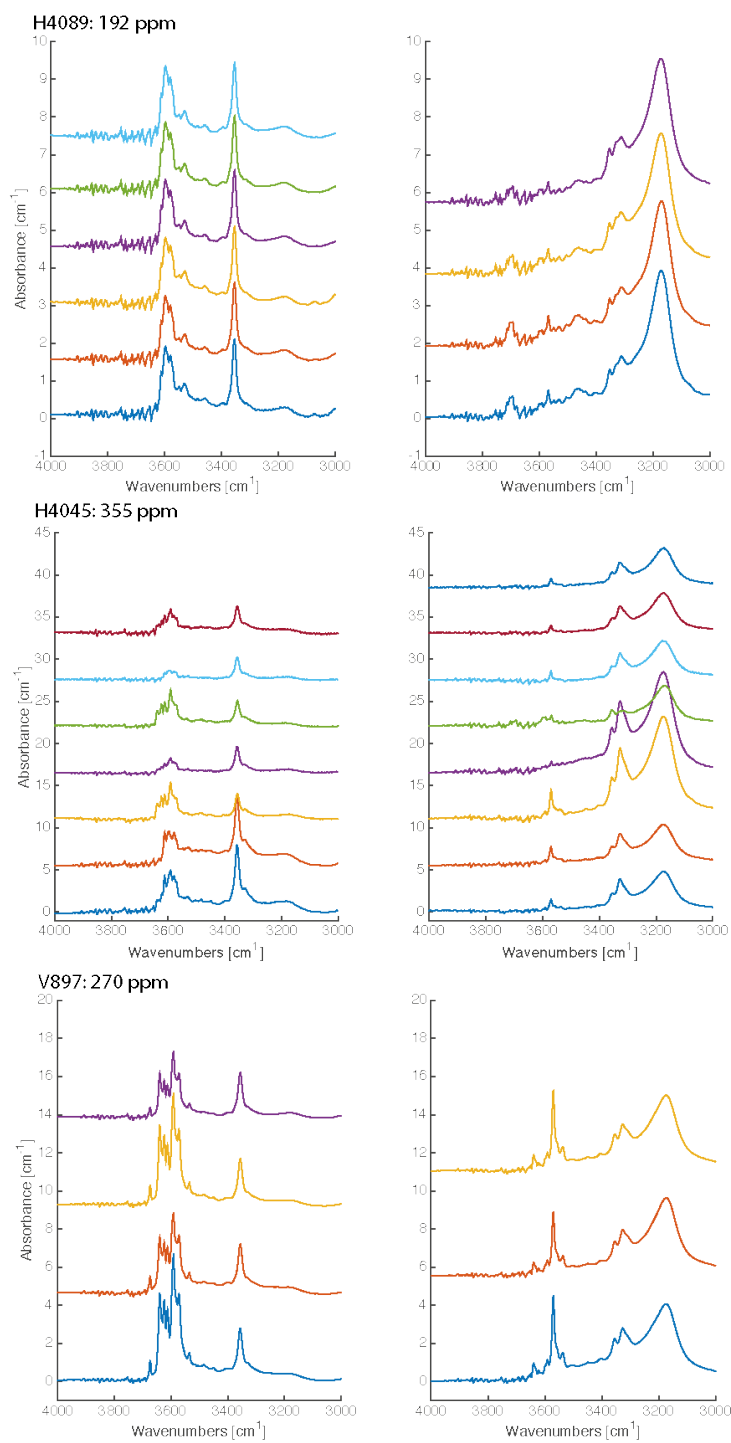


Figure 5.33: Polarised FTIR-spectra of hydrated samples H4089, H4045 and V897. The left and right diagram of each sample are $E \parallel a$ and $E \parallel c$, respectively.

from water of the assembly parts, even they were kept dry for 24 h and heated to 1000°C before assembling. Samples with the highest water content were hydrated using distilled water and talc+brucite powder together as hydrogen source at 2.75 GPa and 1500 K. IR-spectra of annealed samples are homogeneous. Water content annealed samples are given in Tab. 5.6.

Sample	Deformed samples				Amount of talc+brucite [mg]
	H_2O [ppm by weight]	Group I 3620-3300 [cm^{-1}]	Group II 3300-3000 [cm^{-1}]		
Z923	'dry'	-	'dry'		
Z931	17 ± 2	0	17 ± 2	'dry'	
Z1227	308 ± 62	235 ± 53	73 ± 15	8.5	
Z1272	132 ± 14	91 ± 9	41 ± 6	5	
Z1276	209 ± 26	168 ± 25	41 ± 2	4	
Annealed samples					
Z923					
Z1286	51 ± 3	45 ± 2	6 ± 1	'dry'	
Z931					
Z1248	60 ± 6	52 ± 6	8 ± 3	'dry'	
Z1227					
Z1237	285 ± 43	195 ± 37	90 ± 8	6	
Z1244	378 ± 21	260 ± 16	116 ± 10	11	
Z1272					
Z1285	320 ± 47	200 ± 35	120 ± 14	4.1	
Z1287	286 ± 25	177 ± 16	108 ± 10	4	
Z1288	378 ± 24	241 ± 19	136 ± 6	7	
Z1276					
Z1285	237 ± 23	200 ± 19	37 ± 8	4.1	
Z1287	256 ± 31	208 ± 23	48 ± 10	4	
Z1290	157 ± 15	140 ± 14	17 ± 2	1.6	
Z1291	164 ± 20	131 ± 16	33 ± 6	2.2	
Z1292	143 ± 11	122 ± 11	21 ± 3	1.1	

Table 5.6: Water content of deformed samples Z932, Z931, Z1227, Z1272 and Z1276 and its annealed samples. For all samples, the water content was discriminated in Group I and II. The amount of talc and brucite added to the experiment is given in mg

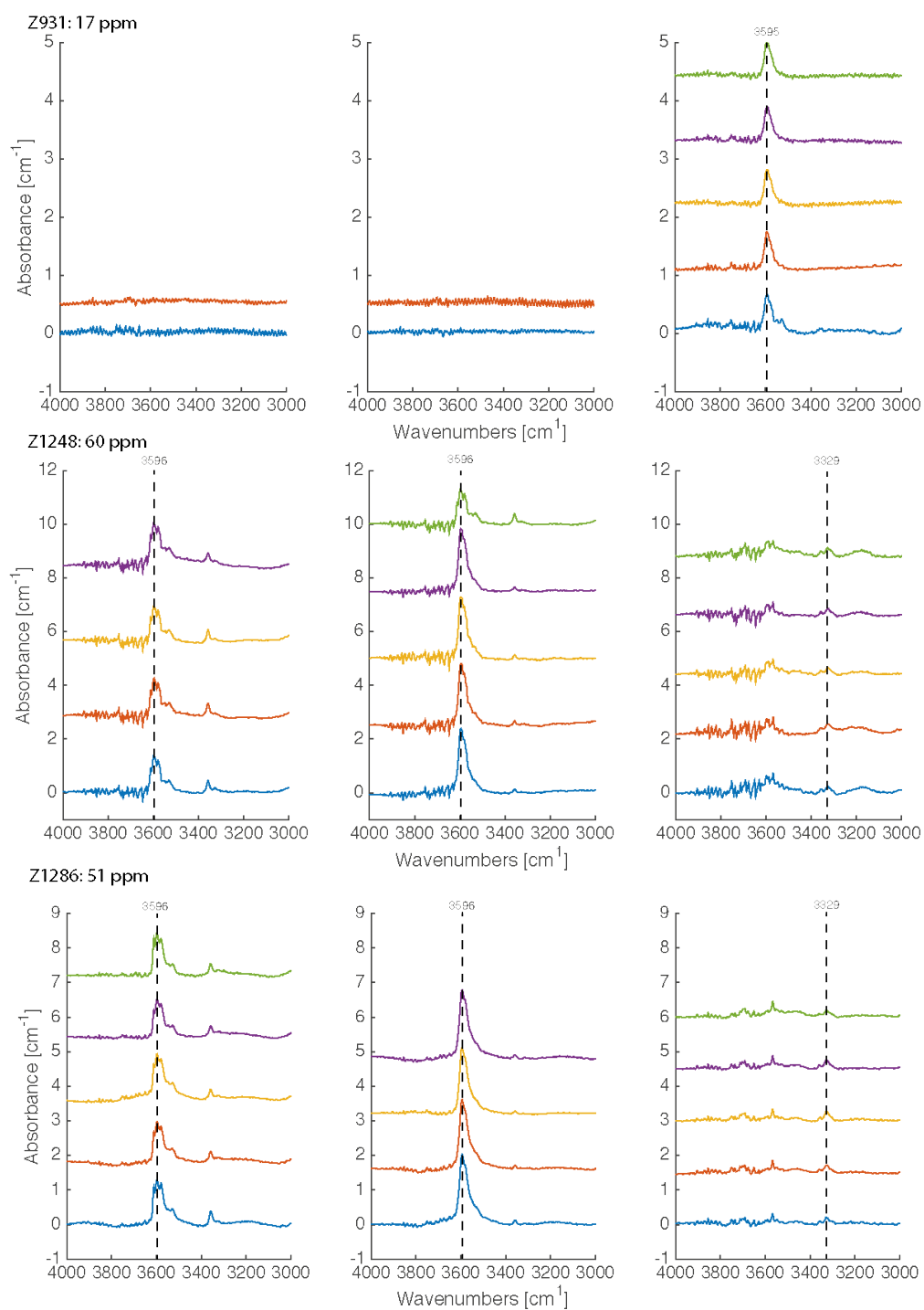


Figure 5.34: Polarised FTIR-spectra of deformed Z931 and its annealed samples Z1248. Z1286 is the annealed sample of Z923. The left, centre, right diagram of each sample are $E \parallel a$, $E \parallel b$ and $E \parallel c$, respectively.

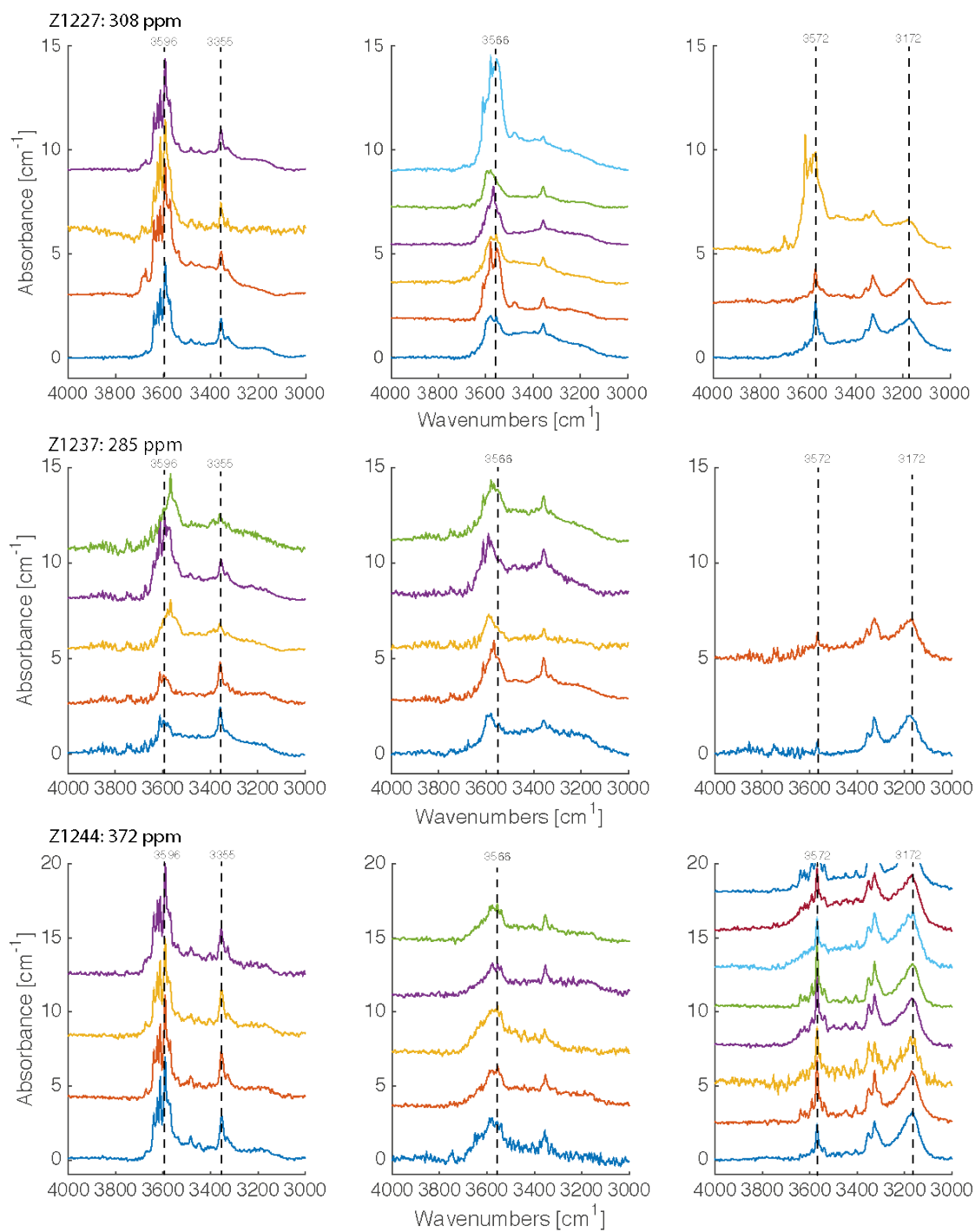


Figure 5.35: Polarised FTIR-spectra of deformed Z1227 and its annealed samples. The left, centre, right diagram of each sample are $E \parallel a$, $E \parallel b$ and $E \parallel c$, respectively.

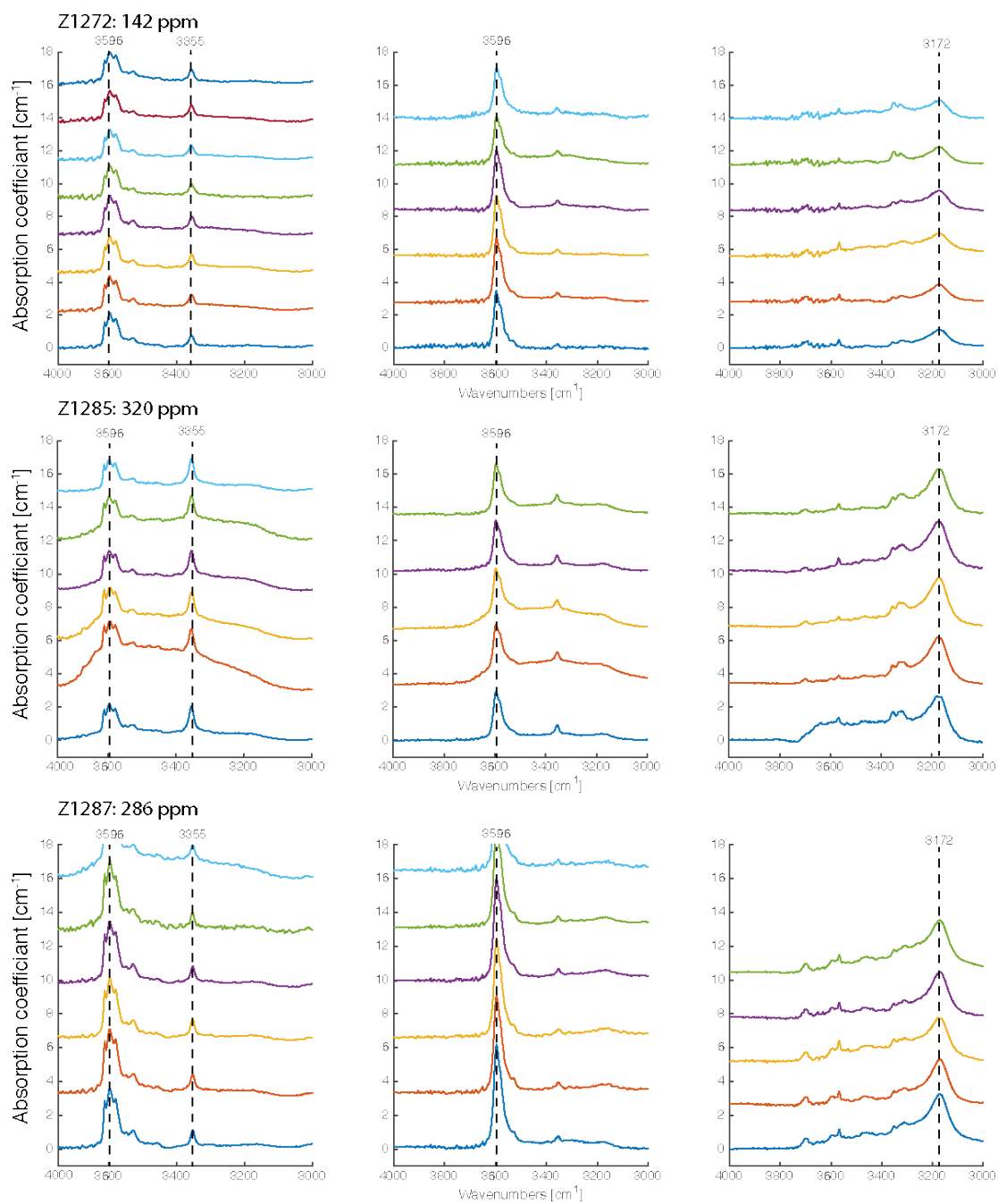


Figure 5.36: Polarised FTIR-spectra of deformed Z1272 and its annealed samples. The left, centre, right diagram of each sample are $E \parallel a$, $E \parallel b$ and $E \parallel c$, respectively.

Main peaks

5 Results

Sample	thickness [cm]	n.o.m	main absorbance bands [cm^{-1}]
Z1227			
E a	0.0405	4	3355, 3571, 3590, 3612, 3623
E b	0.0405	6	3357, 3556, 3579, 3590, 3612
E c	0.0495	5	3172 - 3180 , 3326, 3569, 3612
Z1237 - Z1227			
E a	0.0440	5	3357, 3567
E b	0.0440	5	3357, 3567, 3579, 3588
E c	0.0406	2	3166, 3326
Z1244 - Z1227			
E a	0.0359	4	3353, 3569, 3590, 3612
E b	0.0359	5	3356, 3579, 3596
E c	0.0361	8	3170, 3326, 3351, 3569
Z1248 - Z931			
E a	0.0492	4	3357, 3579, 3596, 3612
E b	0.0492	5	3357, 3581, 3596
E c	0.0481	5	3172, 3569, 3598
Z1286 - Z923			
E a	0.0648	4	3353, 3594
E b	0.0648	5	3357, 3529, 3579, 3596, 3612
E c	0.0534	5	3328, 3567
Z1272			
E a	0.0633	6	3355, 3529, 3579, 3596, 3612
E b	0.0633	8	3357, 3581, 3596
E c	0.0473	6	3172, 3567
Z1285 - Z1272			
E a	0.0372	6	3355, 3529, 3579, 3598, 3612
E b	0.0372	5	3355, 3596
E c	0.0690	5	3176, 3317, 3355, 3567
Z1287 - Z1272			
E a	0.0314	7	3353, 3529, 3548, 3581, 3596, 3612
E b	0.0314	6	3353, 3531, 3596
E c	0.0610	5	3170, 3257, 3288, 3307, 3567
Z1288 - Z1272			
E a	0.0314	7	3351, 3529, 3579, 3596, 3612
E b	0.0314	6	3351, 3531, 3596
E c	0.0610	5	3170, 3315, 3324, 3351, 3567
Z1276			
E a	0.0480	13	3357, 3579, 3590, 3596, 3612
E b	0.0480	9	3357, 3579, 3590, 3623
E c	0.0625	5	3180, 3220, 3326, 3357, 3536, 3569, 3590
Z1285 - Z1276			
E a	0.0372	6	3357, 3502, 3534, 3539, 3571, 3590, 3612, 3623 , 3639, 3702
E b	0.0372	7	3357, 3515, 3556, 3563, 3577, 3596, 3623
E c	0.0690	8	3176, 3218, 3326, 3355, 3536, 3571, 3590, 3639
Z1287 - Z1276			
E a	0.0314	7	3357, 3502, 3534, 3571, 3590, 3612, 3623, 3639, 3671
E b	0.0314	6	3357, 3517, 3342, 3502, 3556, 3563, 3574, 3596, 3623
E c	0.0610	5	3176, 3218, 3326, 3536, 3353, 3536, 3571, 3590, 3639
Z1290 - Z1276			
E a	0.0496	15	3357, 3534, 3571, 3591, 3612, 3623, 3639, 3673
E b	0.0496	12	3359, 3540, 3556, 3579, 3596, 3623
E c	0.0670	5	3536, 3571, 3590, 3639
Z1291 - Z1276			
E a	0.0303	15	3357, 3581, 3591, 3612
E b	0.0303	16	3357, 3515, 3540, 3565, 3596, 3623
E c	0.0646	4	3220, 3326, 3536, 3571, 3590
Z1292 - Z1276			
E a	0.0303	11	3357, 3534, 3571, 3590, 3612, 3623, 3639
E b	0.0303	9	3359, 3556, 3561, 3573, 3596, 3623

E c	0.0674	5	3218, 3221, 3326, 3355, 3536, 3571, 3590,3639
--------	--------	---	---

Table 5.7: Main absorption peaks of the polarised FTIR-spectras of unannealed and annealed samples. The main features are given for all three crystallographic directions. (n.o.m = number of measurements)

Table: 5.5.3 summarises the main peaks of deformed and annealed samples, which were used for evaluating the water-dependence of dislocation mobility. The dominant peaks for $E \parallel c$ and $E \parallel a$ of the deformed samples Z1227, Z1272 and Z1276 are similar, which means the main peaks are at the same position in the IR-spectra. By comparing the spectra taken $E \parallel b$, it emerge that sample Z1272 is missing the main peak at 3572 cm^{-1} .

Annealed samples with a low hydrogen content, Z1248 and Z1286, reveal spectra which are characterised by peaks at $E \parallel b$ at 3596 cm^{-1} and at $E \parallel a$ at 3579 , 3596 and 3612 cm^{-1} . Absorption with $E \parallel c$ the main peaks are at 3172 , 3569 and 3598 cm^{-1} .

Annealed samples of Z1227 show in their spectra characteristic peaks at $E \parallel b$ at 3357 and 3556 cm^{-1} . In $E \parallel a$ the spectra show main peaks at 3353 , 3590 and 3612 cm^{-1} and minor peaks at 3579 cm^{-1} . When $E \parallel c$, the main peaks are at 3166 , 3326 and 3569 cm^{-1} .

Annealed samples of Z1272 are dominated in their spectra by peaks for $E \parallel b$ by 3353 and 3565 cm^{-1} at and for $E \parallel a$ by 3355 , 3598 and 3612 cm^{-1} . For absorption with $E \parallel c$ the main peak is at 3170 cm^{-1} and is usually a wide peak. Minor peaks are at 3326 and 3567 cm^{-1} . This wide peak is the main difference to the two other sets of Z1227 and Z1276.

Annealed samples of Z1276 are dominated in their spectra by peaks for $E \parallel b$ by 3565 cm^{-1} at and for $E \parallel a$ by 3591 and 3612 cm^{-1} . When $E \parallel c$, the main peak is at 3571 cm^{-1} and is usually a distinct peak. Minor peaks are visible at 3218 and 3326 cm^{-1} .

The deformed samples Z1227 and Z1276 seem to have the same main peaks compared to sample Z1272. It has the lowest hydrogen content of these deformed samples. Furthermore, the number of characteristic peaks is lower. The measurements with $E \parallel \beta$ indicate the main differences between the three deformed samples. The spectra of Z1272 are dominated by a peak at 3172 cm^{-1} . Such peaks are not observed in the spectra of Z1227 and Z1276 but they are dominated by peaks at 3569 and 3220 cm^{-1} . This difference is also evident by comparing the proportion of group I and II hydrogen contents in Table: 5.6. A common observation is that spectra have a more complex characteristics when the hydrogen content is high. The number of dominant peaks is lower at lower hydrogen contents, which can be observed in sample Z1272. Another very important observation is that the characteristics of the spectra does not change during the annealing process. The dominant peaks are more or less the same for annealed and the associated deformed samples.

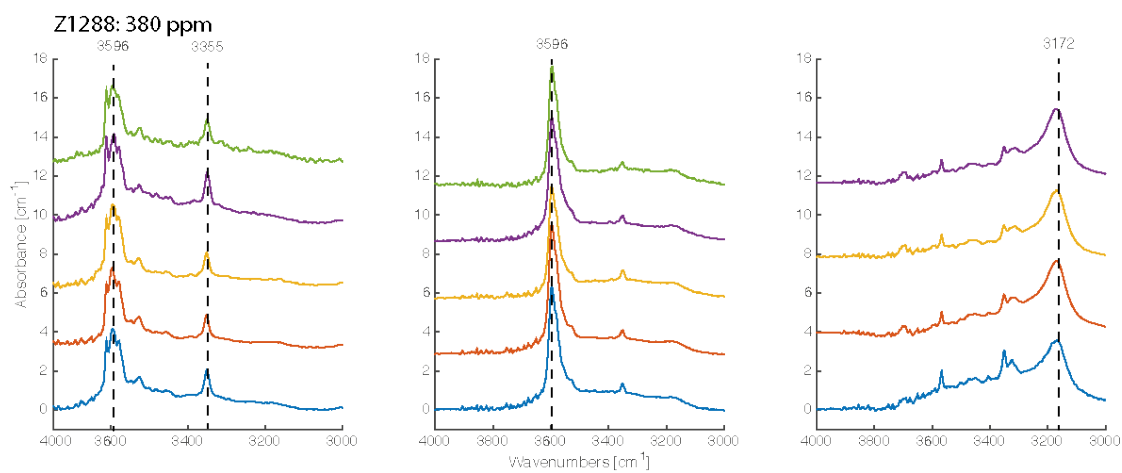


Figure 5.37: Prosecution of 5.36

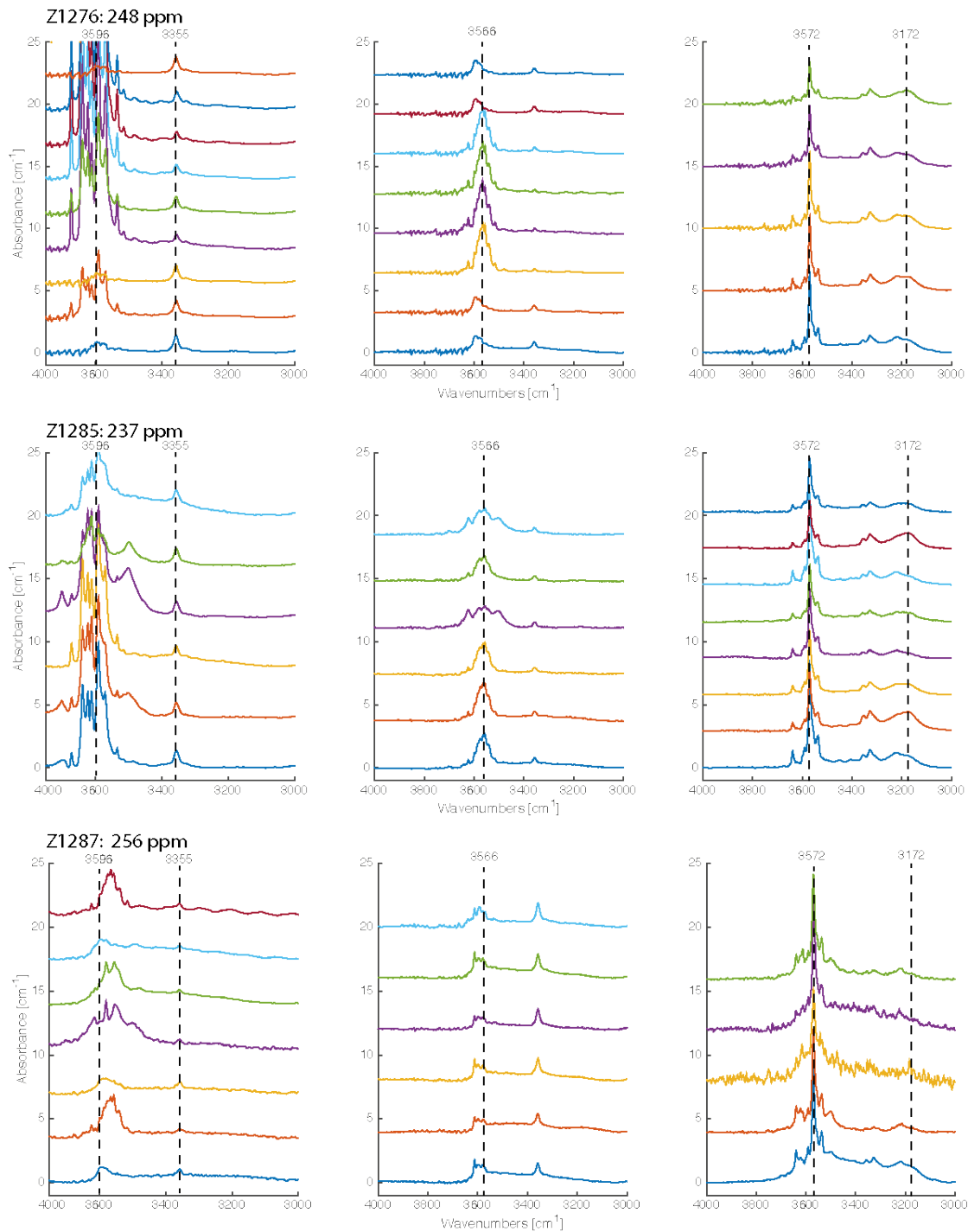


Figure 5.38: Polarised FTIR-spectra of deformed Z1276 and its annealed samples. The left, centre, right diagram of each sample are $E \parallel a$, $E \parallel b$ and $E \parallel c$, respectively.

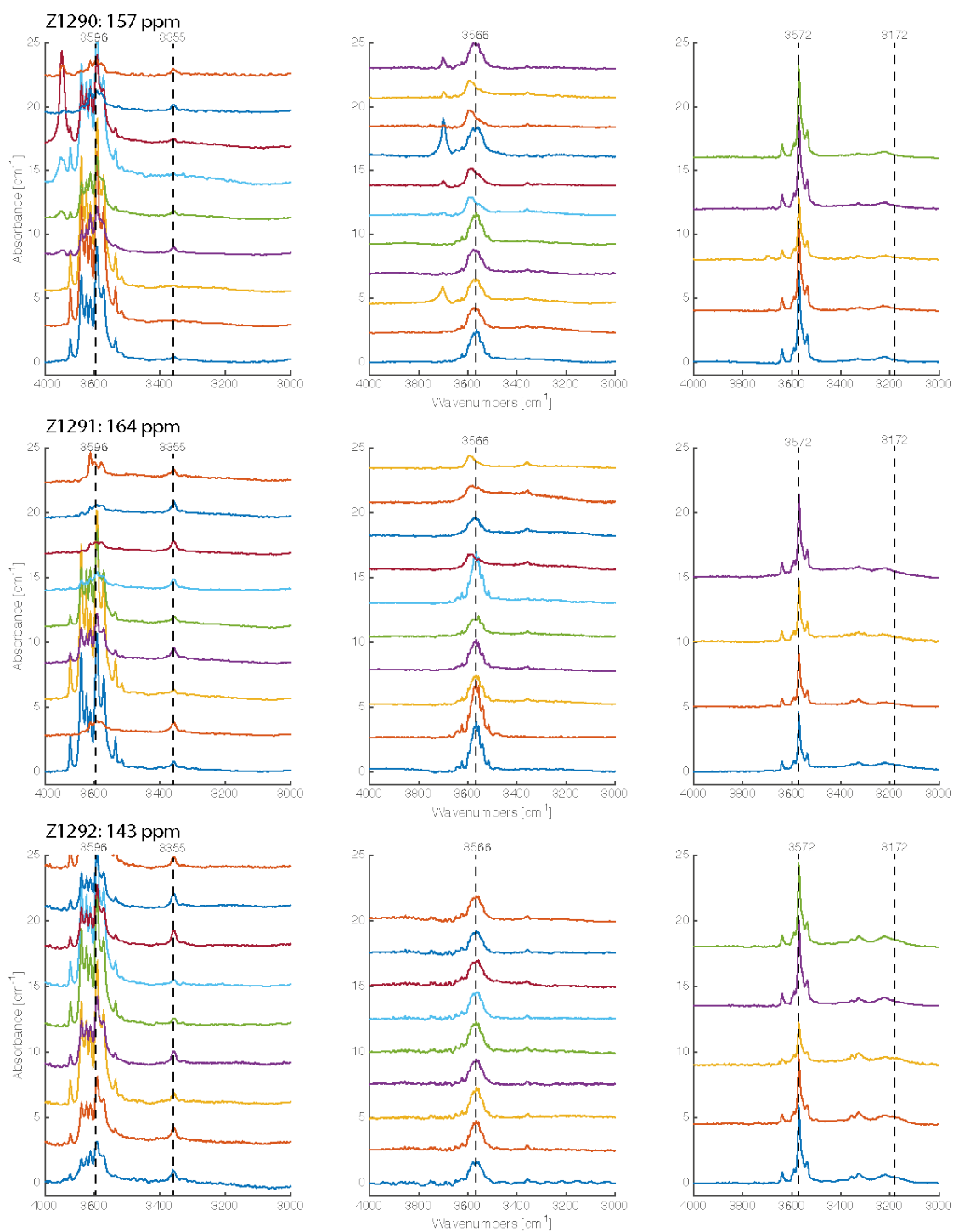


Figure 5.39: Prosecution of 5.38

5.6 Water content vs. Dislocation annihilation rate

The water content was measured as stated above by FTIR-spectroscopy. Table 5.8 summarises the measured water contents of every sample, the annealing duration and dislocation density of the unannealed and annealed samples and the resultant dislocation annihilation rates. The log annihilation rate ranges from -15.6 to -16.6 $\log \text{ m}^2\text{s}^{-1}$, namely its variation is 1.0 order of magnitude. The errors in log annihilation rate are from 0.1 to 1.1 orders of magnitude. These errors of the dislocation annihilation rate are mainly caused by the heterogeneities in dislocation density which were observed in the different images. Unfortunately, these errors are significantly large in comparison with the variation range. On the other hand, the water content ranges from 50 to 380 H_2O ppm by weight, namely its variation is 0.9 orders of magnitude. The errors are from 0.1 to 0.4 orders of magnitude. The errors in water contents are obtained from the standard deviation of measurements in different areas of each sample of FTIR-spectra.

Fig. 5.40 shows the logarithmic dislocation annihilation rate versus the logarithmic water content. The data points show only little or no correlation between water content and dislocation annihilation rate. The data points were fitted to the following equation.

$$k = A \times C_{\text{H}_2\text{O}}^r \quad (5.1)$$

where r is the water content exponent. The fitting results gives the water content exponent of 0.17 ± 0.43 . The water content exponent and its error of 0.17 and 0.43 above are obtained by the Monte Carlo simulation in the following way. First, 10,000 replicas of the present data set of logarithmic annihilation rates and logarithmic water contents were generated by random numbers from the normal distributions. The means and standard deviation of the normal distributions were the measured values and their errors, respectively. Each replica of the data set was fitted to a linear equation to obtain its slope. The average and standard deviation of the 10,000 values of the slope were calculated to obtain above values. These results suggest that the water content dependence of the annihilation rate is nearly zero, and the water-content exponent is at most 0.6. Here, we note that the sample Z1272 shows different features in FT-IR spectra. Its intensity ratio of Group I/Group II is 2:1, and lower than the other samples (3:1 for Z1227 and 4:1 for Z1276). It is possible that the samples of Z1272 may have a different rheological property. If the data points of Z1272 are excluded from the analysis, the resultant water-content exponent is found to be 0.36 ± 0.48 . In this case, the most probable water content exponent is not zero but 0.4. However, its error is even larger than the case in which the data points of the sample Z1272 are not excluded. The water content exponent can be from -0.1 to 0.9.

Deformation experiment	Annealing experiment	t [h]	$\rho_i [\frac{10^{11}}{m^2}]$	$\rho_f [\frac{10^{11}}{m^2}]$	$\log(k) [\frac{m^2}{s}]$	H_2O [ppm by weight]
Z923	Z1248	3	4.2 ± 0.9	3.7 ± 1.9	-16.57 ± 1.1	60 ± 6
	Z1286	5	4.2 ± 0.9	2.8 ± 0.8	-16.22 ± 0.4	51 ± 3
Z931	Z1248	3	6.1 ± 0.9	4.7 ± 0.9	-16.4 ± 0.3	60 ± 6
Z1227	Z1237	1	14 ± 2.6	6.5 ± 1.0	-15.6 ± 0.1	285 ± 44
	Z1244	3	14 ± 2.6	7.0 ± 1.9	-16.2 ± 0.3	378 ± 21
Z1272	Z1285	3	6.4 ± 1.7	4.8 ± 1.0	-16.2 ± 0.2	320 ± 47
	Z1287	1.5	6.8 ± 1.7	5.8 ± 1.0	-16.3 ± 0.4	286 ± 25
	Z1288	3	6.9 ± 1.7	5.3 ± 2.2	-16.4 ± 0.6	380 ± 24
Z1276	Z1285	3	6.1 ± 2.2	4.9 ± 1.2	-16.4 ± 0.4	237 ± 23
	Z1287	1.5	7.5 ± 2.7	3.9 ± 0.9	-15.6 ± 0.2	256 ± 31
	Z1290	3	7.6 ± 2.7	2.7 ± 1.2	-15.7 ± 0.4	157 ± 15
	Z1291	1.5	7.5 ± 2.7	3.6 ± 0.9	-15.6 ± 0.2	165 ± 20
	Z1292	3	7.4 ± 2.7	4.5 ± 1.9	-16.1 ± 0.4	143 ± 11

Table 5.8: Results of recovery experiments. ρ_i is the initial dislocation density after the deformation experiment and ρ_f the final dislocation density after the annealing experiment. Rate constant, k is obtained based on the dislocation density and the annealing duration. The annealing time, h is the time at maximum temperature in hours. Water content is measured by FTIR-spectroscopy.

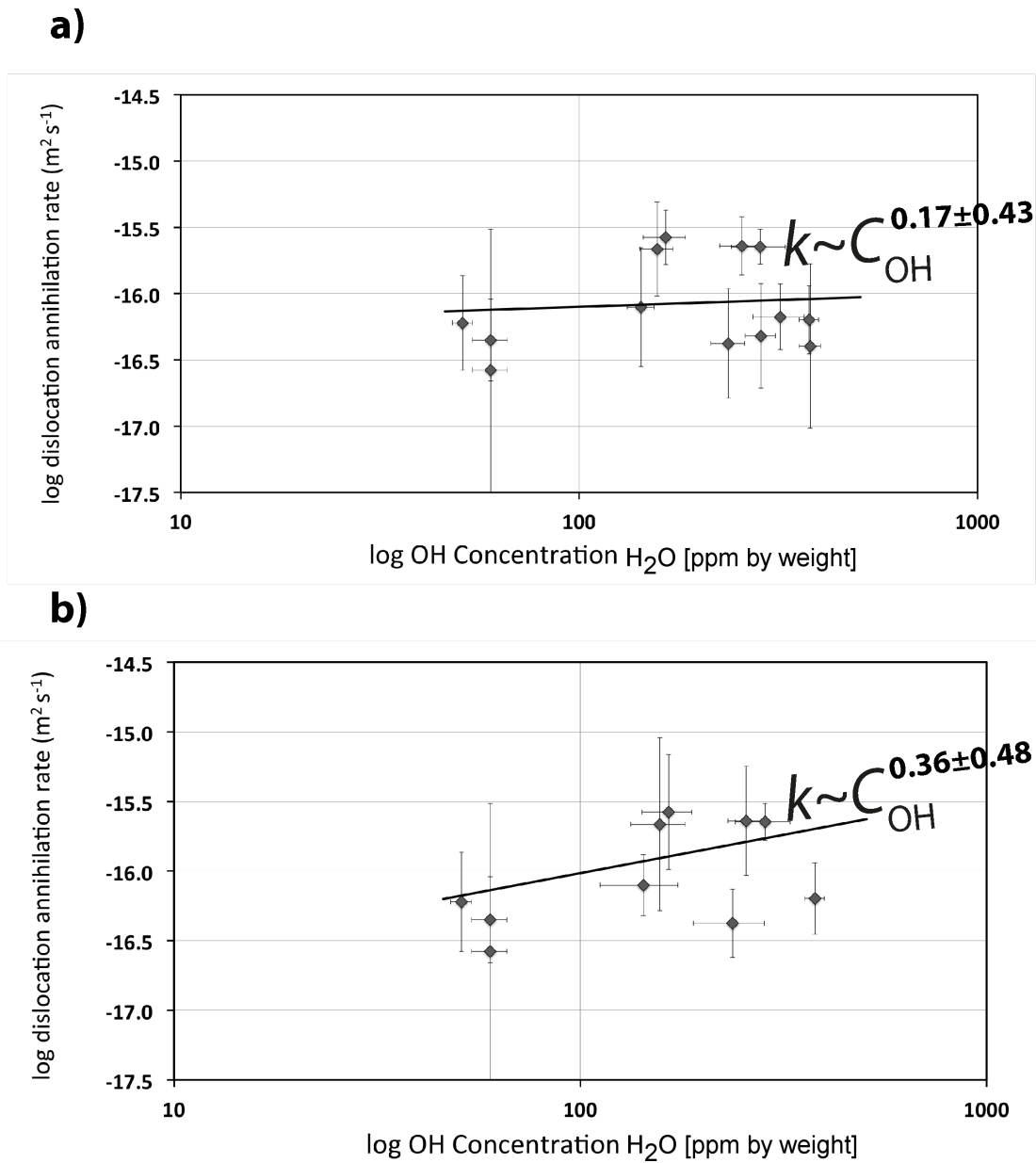


Figure 5.40: Dislocation annihilation rate versus the water content of annealed samples. k values are calculated from a second-order recovery kinetics. Water content is estimated by FTIR-spectroscopy. a) shows the dependence of the dislocation annihilation rate on water for all samples and b) for all samples without Z1272.

6 Discussion

6.1 Comparison with previous studies

6.1.1 Comparison to previous dislocation recovery experiments

In chapter 2 several studies which investigated dislocation annihilation rates of olivine were mentioned [cf. Toriumi and Karato, 1978; Kohlstedt et al. 1980; Karato and Ogawa, 1982; Karato and Sato, 1982; Karato et al., 1993; Farla et al., 2011]. Results of dislocation annihilation rates of several of these studies and results of this study of the 'dry' experiments are shown in Fig. 6.1. Fig. 6.1 a) shows the dislocation annihilation rates plotted against temperature, in which the pressure effects are corrected to ambient pressure according to the activation volume reported in each study. Fig. 6.1 b) shows those plotted against pressure, in which the temperature effects are corrected to 1500 K by using the activation enthalpy reported in each study.

The data by Karato and Ogawa [1982], Kohlstedt et al. [1980] and Toriumi and Karato [1978] were similar or slightly higher than the rate constants in this study. Dislocation annihilation rates are in a good agreement with this study concerning the effect of temperature, as shown in Fig. 6.1 a). In Fig. 6.1 b) the effect of pressure on $\log(k)$ is plotted. The $\log(k)$ -values by Fig. Karato and Ogawa [1982] and Kohlstedt et al. [1980] are decreasing much higher with pressure than shown by the studies of Karato et al. [1993] and Wang et al [2016].

Karato et al. [1993] is a main study to compare with the present one. They activated dislocations in the slip system (100)(010) in San Carlos olivine. They performed high-pressure annealing experiments in the pressure range between ambient pressure and 10 GPa and at temperatures of 1673 and 1773 K, which are by about 200 K higher than that in the present study. Dislocation density was observed on the (001) plane, which is identical to the present study. Furthermore, the silica activity was fixed at $a_{\text{opx}} = 1$ by coexisting with enstatite as well as in the present study. The oxygen fugacity was controlled by the Ni-NiO buffer. The crystals were surrounded by NaCl during annealing to avoid their breakage during compression. The water contents were not controlled and not measured. It is assumed that their experiments were conducted in 'dry' environments. Total dislocation densities are in the orders of 10^{11} - 10^{12} m^{-2} , which is comparable to total dislocation densities of this study. They obtained the activation volume of $6 \pm 1 \text{ cm}^3/\text{mol}$ by assuming the activation energy of 290 kJ/mol. Note that this activation energy was mainly obtained by comparing the data at ambient pressure and at pressures of 7 to 10 GPa.

Farla et al. [2010] conducted dislocation recovery experiments of fine-grained San Carlos olivine at ambient pressure and temperatures between 1372 and 1772 K. Their annihilation

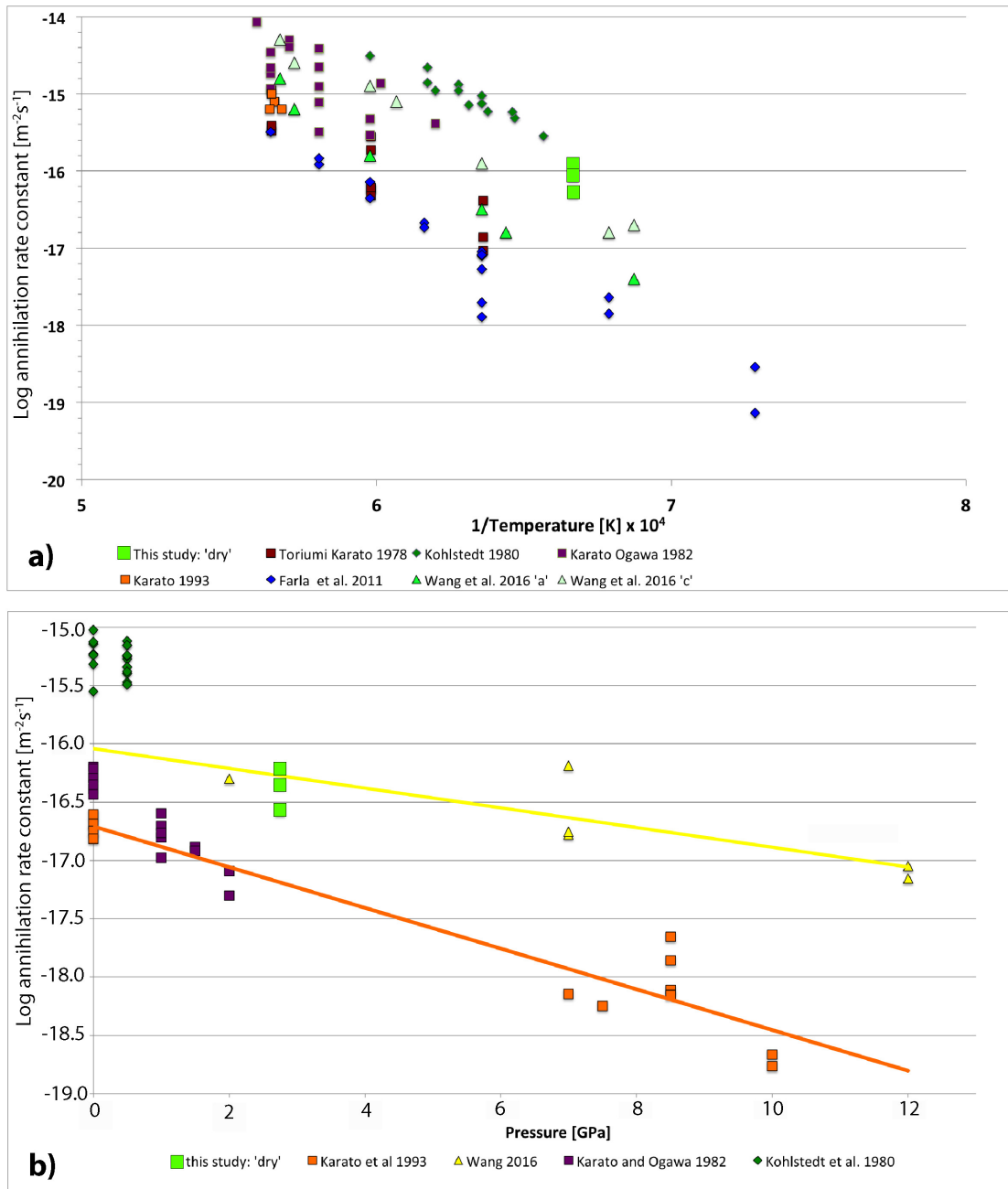


Figure 6.1: a) Comparison of dislocation annihilation rates of the 'dry' data points of this study by correcting to ambient pressure and an activation energy of 390 kJ with Toriumi and Karato [1978], Kohlstedt et al. [1980], Karato and Ogawa [1982], Karato et al. [1993], Farla et al. [2011] and Wang et al. [2016]. b) Comparison of dislocation annihilation rates of the 'dry' data points of this study with Kohlstedt et al. [1980], Karato et al. [1993] and Farla et al. [2011] and Wang et al. [2016]. The data points are corrected to 1500 K.

rates were by two orders lower than those given by the previous studies [Kohlstedt et al., 1980; Toriumi and Karato, 1979; Karato and Ogawa, 1982; Karato et al., 1993] at the same temperature, if their three-dimensional (3D) data are used for comparison. The '3D data' means that dislocation density is estimated by measuring the cumulative lengths of dislocation lines and dividing them by the observation area and penetration depth of electron beams in the SEM observation [Farla et al., 2010]. They discussed that their smaller dislocation annihilation rates than those by the previous studies were due to a grain size effect that should have caused higher internal back stresses which lead to decelerate dislocation motion. On the other hand, their 2D data gave by 1 order of magnitude higher dislocation annihilation rate than the 3D data, whose differences from other studies are smaller, Fig.6.1 a). 2D data represent the number of dislocations per area. Therefore, it is more appropriate to use the 2D data to compare to the others studies in Fig. 6.1, because they were obtained by the same method. They reported the activation energy of 360 ± 80 kJ/mol.

Wang et al. [2016] compared annihilation rates of dislocations activated by [100](010) and [001](010) slip systems, which are called *a*- and *c*-dislocations, respectively, at ambient pressure and temperatures of 1450-1760 K. They reported that the annihilation rates of *c*-dislocations are by 0.3 orders of magnitude higher than those of *a*-dislocations. On the other hand, the activation energy of these two slip systems is identical, namely 400 kJ/mol.

The dislocation annihilation rates given by Karato and Ogawa [1982], Kohlstedt et al. [1980] and Toriumi and Karato [1978] were similar or slightly higher than those obtained in this study, after correcting the temperature effects, as shown in Fig.6.1 a). The reason why their rate constants are higher than those in this study may be due to the use of optical microscope and TEM to study dislocation densities. The present data set from the dry samples is located in the upper end of the literature data sets. Although the reason is unclear, however, the advanced technique to measure dislocation density in this study may have given more accurate values. In other words, many of the old studies may have overlooked dislocation at high density.

The activation energy given by the above literatures are rather consistent, and in the range of 350 to 400 kJ/mol. These values are significantly smaller than the activation energy obtained by deformation experiments, which is discussed later. Fig.6.1 b) shows pressure dependence of annihilation rates. Kohlstedt et al. [1980] and Karato and Ogawa [1982] provided significantly large activation volume, namely, 11 ± 1 and 14 ± 2 cm³/mol, respectively, whereas Karato et al. [1993] provided a relatively small one, namely 6 ± 1 cm³/mol. It is noted that the pressure ranges of Kohlstedt et al [1980] and Karato and Ogawa [1982] are relatively narrow, namely only up to 500 MPa and 2 GPa, whereas that of Karato et al. [1993] is up to 10 GPa. Therefore, it seems that a measurement over a narrow pressure range tends to exaggerate a pressure effect. It is possible that the real activation volume of dislocation annihilation rate constants of olivine would be even smaller than that given by Karato et al. [1993].

6.1.2 Comparison of activation energies between recovery and deformation experiments

Dislocation annihilation rates obtained by dislocation recovery experiments are rather indirect information to understanding rheological properties of matters. On the other hand, it is also not obvious whether creep laws obtained by deformation experiments can be applied to flows in the deep mantle because of the much higher creep rates in deformation apparatus than in nature. Therefore it is useful to compare activation energy of dislocation annihilation rates and dislocation creep laws obtained by deformation experiments to examine applicability of the results of dislocation recovery experiment to understand flows in the deep mantle. For this reason, the activation energy of dislocation creep of olivine is reviewed below. Table 6.1 lists deformation experiment in literatures: [Faul et al., 2011; Ratteron et al., 2007; Ratteron et al., 2004; Mei and Kohlstedt, 2000; Bai et al., 1991; Chopra and Paterson, 1981] and a theoretical study by Korenaga et al., [2008].

Ratteron et al. [2004] conducted deformation experiments on olivine using a DIA-type deformation (D-DIA) apparatus. In this study, they deformed olivine single crystals in a pure shear geometry at relatively low temperatures from 673 to 1163 K. The resulting activation energy was 564 ± 89 kJ/mol. The active slip system in this study is assumed to be [001](010). The following study Ratteron et al. [2007] performed pure-shear deformation experiments in order to determine the dislocation slip-system activities in the geometries of [100](010) (called *a*-slip) and [001](010) (called *c*-slip) at mantle conditions. They obtained activation energy of 104 and 112 kJ/mol for the *a*- and *c*-slip systems, respectively, which is significantly lower than comparable experiments [Mei and Kohlstedt, 2000]. The interpretation is that dislocation cross-slip mechanism may cause athermal-type processes at high pressures. Interestingly, they did not use those values for later papers [Ratteron et al., 2011; Ratteron et al., 2012], but used the values given by Bai et al [1991] instead. Mei and Kohlstedt [2000b] gave the activation energy of 470 ± 40 kJ/mol for olivine under hydrous conditions and 510 ± 10 kJ/mol for that under anhydrous conditions. Those experiments were performed at relatively low pressures (100 - 450 MPa confining pressure). Bai et al. [1991] studied the effects of silica activity and loading orientation on the creep law of olivine in addition to applied stress, temperature and oxygen fugacity. They considered that dislocation creep in olivine is controlled by the following two factors. One is concentrations of kinks and jogs and the other is charges of kinks, jogs and point defects. Their concentrations are controlled not only by temperature and pressure but also by thermodynamic parameters such as the oxygen fugacity and silica activity. The results show an activation energy ranges from 200 to 1000 kJ/mol for orthopyroxene-buffered deformed in [110]^c which should activate the [100](010) slip system. They proposed a creep mechanism called 'number 3', which has activation energy of about 500 kJ/mol. They considered this mechanism is dislocation-climb controlled. Chopra and Paterson [1981] used a gas-medium deformation apparatus at 300 MPa confining pressure to deform polycrystalline dunite under 'dry' and 'wet' conditions at temperatures between 1273 and 1573 K. The resulting activation energies are 444 ± 24 kJ/mol and 498 ± 38 kJ/mol for 'wet' dunite. The following study by Chopra and Paterson [1984] studied the sample samples. They used a gas-medium deformation apparatus at 300 MPa confining pressure to deform polycrystalline dunite under 'dry' and 'wet' conditions at temperatures between 1473 and 1673 K. Water

Author	experimental procedure	Single - or polycrystalline	P [GPa]	T [K]	E_c [kJ/mol]	
Faul et al., [2011]			0.3	1460 - 1630	766 ± 45	
Ratteron et al., [2007]	pure shear exp., in-situ, a- to c-slip	singlecrystalline	3-7	1475 - 1677	112 ± 40 104 ± 40	a-slip c-slip
Ratteron et al., [2004]	pure shear exp., in-situ	polycrystalline	5-9	675 - 1100	564 ± 89	
Mei and Kohlstedt, [2000b]			0.10 - 0.45	1393 - 1553	510 ± 30 470 ± 40	dry wet
Bai, Mackwell and Kohlstedt, [1991]	'deformation apparatus'	singlecrystalline	10 ⁻⁴	1427 - 1800		depending on ox. fug.
Chopra and Paterson, [1984]	'deformation apparatus' by Paterson	polycrystalline dunite	0.3	1473 - 1673	498 ± 38 444 ± 24 535 ± 33	Åheim dunite 'wet' Anita Bay dunite 'wet' Both dunites 'dry'
Chopra and Paterson, [1981]	'deformation apparatus' by Paterson	polycrystalline dunite	0.3	< 1527	498 ± 38 444 ± 24	Åheim dunite Anita Bay dunite
Korenaga et al., [2008]	theoretical calculation				610 ± 10 523 ± 100	dry wet

Table 6.1: Activation energies determined in deformation studies by Faul et al., [2011]; Ratteron et al., [2007]; Ratteron et al., [2004]; Mei and Kohlstedt, [2000]; Bai et al., [1991]; Chopra and Paterson, [1981] and by a theoretical study by Korenaga et al., [2008].

content of the specimens were measured. A 'dry' sample was produced by dehydration at 1473 K. The resulting activation energies are 535 ± 33 kJ/mol for 'dry' dunite, 444 ± 24 kJ/mol and 498 ± 38 kJ/mol for 'wet' dunite.

Chopra and Paterson [1981] and Chopra and Paterson [1984] concluded that water weakening in polycrystalline material is influenced by the presence of water in the grain boundaries, Karato et al. [1986] suggested that water weakening occurs by an effect on intragranular slip.

In summary, I conclude that the activation energy of the olivine creep law obtained by deformation experiments is around 500 kJ/mol. As discussed in the previous section, the activation energy obtained by the recovery experiments are 350-400 kJ/mol (Tab. 6.2). This difference in activation energy between these two experimental methods suggests that mechanisms of movement of dislocation are different between them. In the deformation experiment, very large external deviatoric stresses (several tens MPa to 1 GPa) are applied to the samples to drive dislocation motion. On the other hand, no external stresses are applied to samples in recovery experiments. Instead, the internal stresses caused by dislocations themselves drive dislocation motion. Boioli et al. [2015] showed that the dislocation glide has higher temperature dependence than dislocation climb. Their results and the larger activation energy in the deformation experiments than that in the recovery experiments imply that the dislocation glide dominates in deformation experiments, whereas dislocation climb dominates in recovery experiments. The strain rates in the asthenospheric mantle should be 10^{-14} to 10^{-17} s⁻¹ [Burov et al., 2006; Burov, 2011], whereas those in deformation apparatus are 10^{-4} to 10^{-6} s⁻¹ [Burov, 2011; Cordier et al., 2012; van Hunen et al., 2005]. Therefore, the speeds of dislocation motions in the deformation experiments are too high to investigate flows in the asthenosphere, where dislocation climb is expected to dominate in olivine dislocation creep. Hence, it is considered that the recovery experiments should provide more appropriate information for understanding dynamic motions in the asthenosphere.

6.1.3 Comparison of the water effects with deformation experiments

Workman and Hart [2005] estimated the water contents in the source region of mid-oceanic ridge basalts (MORB), and concluded 70-160 ppm. Workman et al. [2006] suggested that the ocean island basalts (OIB) contain several times more water than MORB. These studies suggested that the oceanic upper mantle is wet to some degree. Furthermore, the wedge mantle should be more hydrated because the subducted slabs are expected to bring significant amounts of water in the subduction zone [Billen and Gurnis, 2001; Dixon et al., 2004; Hirth and Kohlstedt, 2003]. The variation in water contents in the upper mantle could cause viscosity variation, which could cause drastic mantle dynamics. Variations in the viscosity in mantle wedges are one of the main problems to be tackled. For this reason, numerous studies investigated effects of water on rheological properties of olivine by means of the deformation experiment [cf. Chopra and Paterson, 1981, Chopra and Paterson, 1984, Bai et al., 1991a, Raterron et al., 2007, Kohlstedt et al., 1980, Demouchy et al., 2009, Hirth and Kohlstedt, 1996].

Mackwell et al. [1985] reported a strength reduction of hydrothermally treated olivine single crystal by a factor of 1.5-2.5. From microstructural observation of the wet experiments,

Author		Single - or poly-crystalline	P [GPa]	T [K]	E [kJ/mol]	V [$cm^3 mol^{-1}$]
Wang et al., [2016]	natural olivine	single crystal	10^{-4}	1393 - 1553	400 ± 20	
Farla et al., [2011]	synthetic (sol-gel)	polycrystalline	10^{-4}	1393 - 1553	240 ± 43	
	natural San Carlos	polycrystalline	10^{-4}	1393 - 1553	355 ± 81	
Karato et al., [1993]	San Carlos olivine	single crystal	$10^{-4} - 2$	1773		6 ± 1
Karato and Ogawa, [1982]	San Carlos olivine		$10^{-4} - 2$	1663 - 1773	390 ± 59	14 ± 2
Kohlstedt, [1980]	natural olivine	single crystal	$10^{-4} - 0.5$	1523 - 1673	300 ± 15	

Table 6.2: Activation energies E and activation volumes V determined by annealing studies by Wang et al., [2016]; Farla et al., [2011]; Karato et al., [1993] Karato and Ogawa, [1982] and Kohlstedt, [1980].

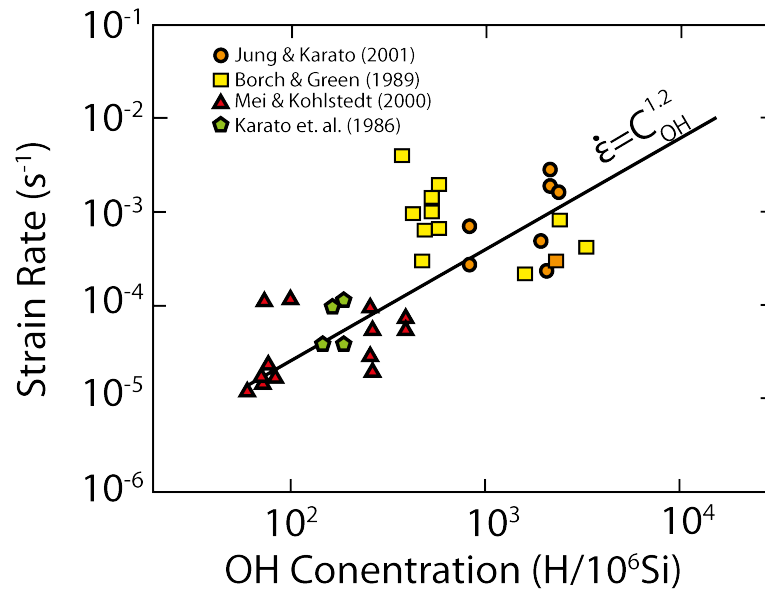


Figure 6.2: Strain rate against the water content for olivine aggregates. The data are normalised to a temperature of 1523 K, a pressure of 300 MPa. Modified from Hirth and Kohlstedt, [2003]

it is suggested that the weakening effect is caused by the enhancement of dislocation climb. Mei and Kohlstedt [2000] demonstrated that dislocation creep of olivine increases by factors of 5-6 at a water fugacity of 520 MPa in comparison with dry conditions. They concluded the water fugacity exponent of dislocation creep rate of 0.69-1.25. Results of these studies indicated that even a small amount of hydrogen (> 50 wt. ppm) has a large effect on viscosity of olivine.

A review article [Hirth and Kohlstedt, 2003] discussed experimental constraints for the viscosity of the upper mantle. Fig. 6.2, which is modified from Hirth and Kohlstedt et al. 2003, revealed the strain rate against the water content for olivine aggregates deformed in the dislocation creep regime. The fit to the global data set results in a value for the water-fugacity exponent of $r = 1.2 \pm 0.4$.

As we discussed in the last chapter, the water-content exponent of the dislocation annihilation rate is 0.2 ± 0.4 if all data in this study are used. If the dislocation mobility is proportional to the dislocation annihilation rate, and the dislocation density is independent from the water content, the present results disagree to the results of the deformation experiments. The upper bound range of the possible water-content exponent of the dislocation annihilation rate is 0.6 in this study, whereas the lower bound of the water-fugacity exponent given by Hirth and Kohlstedt [2003] is 0.8. Note that the larger water-content exponent of 0.4 ± 0.5 is obtained by selecting the data points obtained in this study. However, even though this value is adopted, the probable water-content exponent is still smaller than that obtained by the deformation experiments. The dislocation creep rate should be a product of dislocation velocity, dislocation density and Burgers vector. The dislocation velocity should

be proportional to the dislocation annihilation rate at constant stress. If the dislocation creep rate has higher water-content dependence than the dislocation mobility, the other two factors, namely, the dislocation density and Burgers vector should have significant water-content dependence. However, there is no report of increase in dislocation density with increasing water content. The Burgers vector is essentially independent from the water content because it is of the crystal structure. Therefore, we consider that the water-content dependence of creep rate reported based on deformation experiments may have been biased in some reason. It is unclear why the water-content dependence of creep rate is biased by the deformation experiment. One possibility is lubrication by free fluid phase. Mei and Kohlstedt [2000] controlled the water fugacity by changing the confining pressure under water-saturated conditions. The water saturation inevitably leads to the presence of free fluid. Such free fluids should exist on grain boundaries to lubricate them. The high background of FT-IR spectra presented by Mei and Kohlstedt [2000b] may indicate presence of free fluid during the high P-T deformation experiment. Another possible reason for the discrepancy of the water content exponents between the recovery and deformation experiments is difference in mechanism of dislocation motion. As discussed previously, dislocation glide will dominate in deformation experiment whereas dislocation climb will dominate in recovery experiment. It is possible that the dislocation glide motion has a larger effect of water incorporation, whereas the dislocation climb motion has a smaller one. Actually, it was observed that subgrain-boundary formation and clustering of dislocation developed in wet samples in this study. These phenomena could be driven by dislocation glide, and therefore they could be indication of the larger water effects on dislocation glide motion.

6.2 Dislocation structures

The dislocation distributions of deformed and annealed samples were described in Chapter 5. It was found that the dislocation distribution is changed by annealing. The dislocation distribution is fairly homogeneous after the deformation experiments, but dislocation clustering became more pronounced during the annealing process at high temperatures and pressure. The dislocation density decreases during the annealing process, which is an indication for dislocation annihilation process. The highest rate in dislocation annihilation can be observed under hydrous conditions. Especially samples annealed from Z1276 have a high reduction in dislocation density. Sample Z1290 exhibit a reduction of 60 % in dislocation density after 3 h of annealing and Z1287 and Z1291 of 44 and 47 %, respectively, after 1.5 h of annealing. These are the highest values observed in this study. Sample Z1285 show a reduction by 11 % after 3h and Z1292 27 % after 3 h. The annealed samples of Z1227, Z1237 and Z1244, show a reduction in dislocation density by 46 and 37 % after 3 and 1 h, respectively.

Annealed samples from Z1272 show a significant lower reduction in dislocation density. In samples Z1285 and Z1288 the dislocation density reduced by 20 and 13 %, respectively, after 3 h and sample Z1287 show a reduction by 6 % after 1.5 h.

'Dry' samples are characterized by a lower reduction rate in dislocation density. Annealing for 5 h reduced the density of dislocation in sample Z1286 by 28 %, which was deformed in experiment Z923 and by 8 % in 3h in sample Z1248. Z1248, which was deformed in experiment Z931, exhibits a reduction by 13 % after 3 h.

An important factor of a decrease in density seems to be the number of immobile dislocations. Samples with a low percentage of immobile dislocation show high annihilation rates (Fig. 6.3). A dislocation stays immobile until it is possible to climb to overcome an obstacle or until neighbouring dislocations move or annihilate by climb which leads to a modification of the local internal stress field [Boioli et al., 2015]. Probably, in samples with a low dislocation annihilation rate, the dislocation annihilation by dislocation climb was not effective enough to reduce the total number of dislocations, which led to a high number of dislocation clusters. One possibility for a low climb rate could be the defect type in the samples and is discussed in the next section.

As mentioned in chapter 4, the chosen distance to define dislocation dipoles is 0.25 μ . This distance was chosen empirically by observing dislocation clusters, usually dipoles or tripoles, in the samples. The number of dislocation dipoles is larger in annealed samples rather in the deformed samples. Therefore, calculating dislocation annihilation rates from the total number of dislocations would influence negatively the dislocation annihilation rate. By using 0.45 μ for the distance of dipoles the dislocation annihilation exponent increases to 0.7 which is still lower than the value expected from deformation experiments. However, the distance of 0.45 μ is probably overestimating the number of immobile dislocations.

6.3 Interpretation of hydrogen content

'Wet' samples in this study were hydrated before they were deformed, and then were deformed and annealed under hydrous conditions. During the annealing process the water

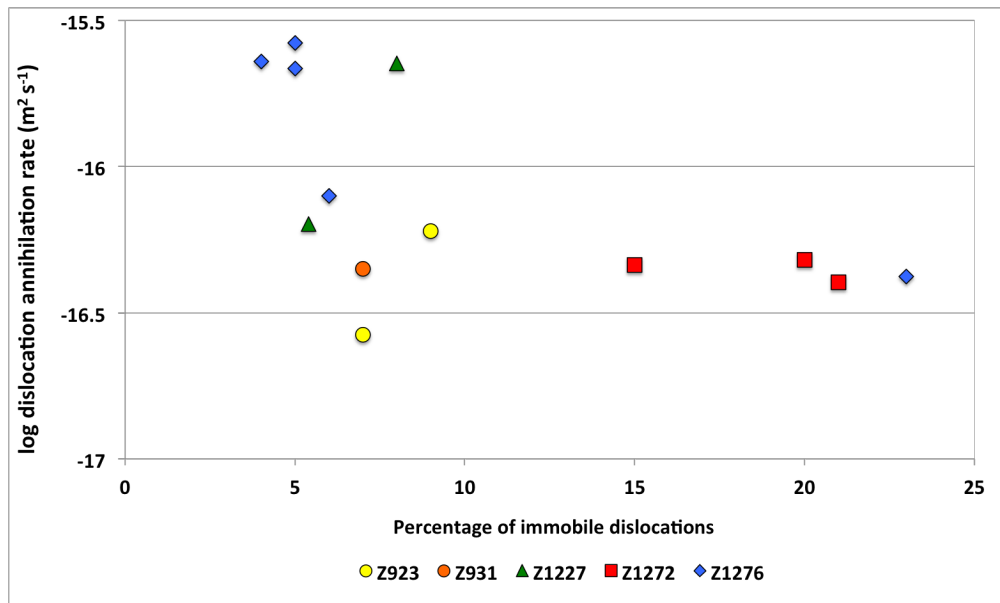


Figure 6.3: Percentage of immobile dislocations plotted against dislocation annihilation rate $\log(k)$.

content is changing at the beginning. The water content is assumed to reach the amount measured after the experiment in a short time period, because of the high diffusion constant of hydrogen. The FTIR-spectra exhibit specific characteristics, which did not change during deformation and annealing experiments. The spectra are characterised by Group I peaks, such as 3565, 3598 and 3612 cm^{-1} . Further, Group II peaks are typical for FT-IR spectra in this study and typical for experiments annealed together with pyroxene.

Lemaire et al. [2004], Kovács et al. [2010] and Demouchy and Mackwell [2006] indicated that the main peaks in FTIR-spectra of natural olivine are around 3600 cm^{-1} . Natural olivine usually shows just this type of peaks. Olivine hydrated in equilibrium with orthopyroxene, which is the more realistic case for the Earth's mantle, showed additional bands at lower wavenumbers, namely the Group II spectra [Demouchy and Mackwell, 2006; Kovács et al., 2010]. Group II spectra are characterised by two bands at 3,220 and 3,160 cm^{-1} and have a maximum absorption when the electric vector is parallel to the *c* direction. Demouchy et al. [2006] showed this kind of peaks in San Carlos olivine. Kovács et al. [2010] showed the same peaks for 'Pakistan' olivine, which is also used in this study.

Lemaire et al. [2004] and Kovács et al. [2010] describe the peaks of 3598 and 3612 cm^{-1} ($E||a$), 3565 cm^{-1} ($E||b$) and 3220, 3170 and 3569 cm^{-1} ($E||c$) as the most dominant one. In these studies, a_{SiO_2} is believed to be fixed by coexisting with pyroxene or periclase by changing bulk Mg/Si ratios. They reported that samples with low a_{SiO_2} show peaks in the range 3620-3450 cm^{-1} , and that those with high a_{SiO_2} shows additional peaks at 3170 and 3220 cm^{-1} . Therefore the former and latter peaks should be related to the protonated Si and Mg vacancies, respectively. As a conclusion, the above mentioned peaks are considered to be related to following vacancies:

- 3612 cm^{-1} : V_{Si}
- 3565 cm^{-1} : V_{Si}
- 3170 cm^{-1} : V_{M_1}
- 3598 cm^{-1} : V_{M_2}
- 3220 cm^{-1} : V_{M_2}

where V_{Si} is a vacancy of the Si site, V_{M_1} and V_{M_2} are vacancies of two crystallographic Mg sites.

Here the spectra of annealed samples of this study are compared to the results of Lemaire et al. [2004] in Figure 6.4 and Figures 6.5 and 6.6. The spectra related to Z1227 and Z1276 have peaks in Group I, which is a distinct feature of the LSA samples. On the other hand, the spectra related to Z1272 have the peak at 3160 cm^{-1} with the electric vector parallel to z , which characterizes MSA, and have the peak at 3,600 cm^{-1} with the electric vector parallel to y , which characterize HSA. Although Lemaire et al. [2004] also described a peak at 3,220 cm^{-1} with the electric vector parallel to z , this peak is not observed in the present samples. Although there is some discrepancy, it is nevertheless concluded that the FT-IR spectra of samples annealed from the deformation experiments Z1227 and Z1276 are similar to those of LSA samples of Lemaire et al. [2004], whereas those from Z1272 are similar to those of MSA and HSA. It is noted that the sample environments are designed so that the olivine crystals were under the orthopyroxene saturated conditions, and therefore, all spectra should have similar features with the HSA samples. Nevertheless, two of three deformed samples show similar features with the LSA samples. Thus, it seems that the peak positions and intensities are not simply related to the Mg/Si ratio of the sample environments. I nevertheless accept the relations of FT-IR peaks with the defect species, because I have no idea to explain the discrepancy between this study and Lemaire et al. [2004].

When the intensities of peaks related to V_{Si} and V_{M} are summed up, the resulting values can be plotted against dislocation annihilation rate. As shown in Fig. 6.8, log dislocation annihilation rate linearly increases with increasing the peak intensity ratio of V_{Si} to V_{M} in FT-IR spectra. Therefore, with increasing V_{Si} the dislocations become more mobile, whereas they become less mobile with increasing V_{M} (Fig. 6.9).

Bai et al. [1991] studied the influence of silica activity on the creep rates of olivine. Silica activity is of great interest for climb controlled deformation, because the strain rate is proportional to the flux of silicon ions in olivine. Strain rate of olivine is expected to be proportional to the self-diffusivity of Si and proportional to the concentration of vacancies on the silicon sub-lattice [Kohlstedt, 2006]. As described by $D_{\text{ion}} = X_{\text{V}} \times D_{\text{V}}$, where D_{ion} is the self-diffusivity of the ion, D_{V} the self-diffusivity of a vacancy on the sub-lattice of that ion and X_{V} is the mole fraction of vacancies on the corresponding sub-lattice. However, the negative correlation between the intensities of V_{Mg} related peaks and the dislocation annihilation rate. The water contents in the sample showing LSA-like spectra (Z1272 related samples) have generally higher water contents (280 - 380 ppm) than the others (143 - 380 ppm). Nevertheless, the dislocation annihilation rates are low. Therefore, the higher intensities of the V_{Mg} -related peaks do not mean low intensities of the V_{Si} -related peaks. We need further investigation to clarify the reason for this negative correlation.

The samples of this study are compared to the work by Lemaire et al. [2004], because this is one of the few studies so far, which was able to produce Group II spectra and gave an explanation for their existence. Other studies doubt the effect of silica activity, because

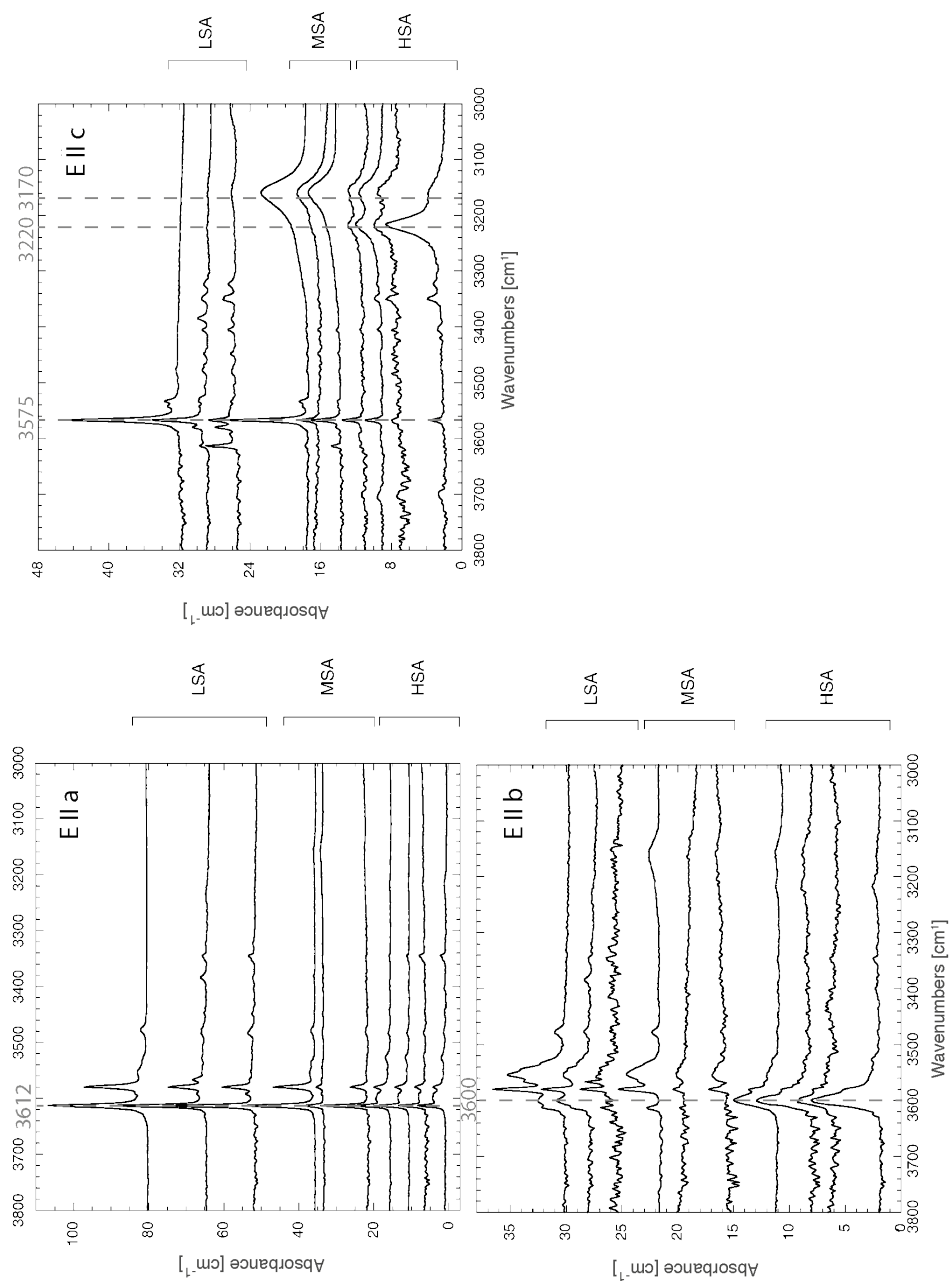


Figure 6.4: Polarised FTIR-spectra with $\mathbf{E}||\mathbf{x}$, $\mathbf{E}||\mathbf{y}$ and $\mathbf{E}||\mathbf{c}$; LSA, MSA and HSA denote samples synthesized with low, medium and high silicon activity, respectively. (modified from [Lemaire et al., 2004])

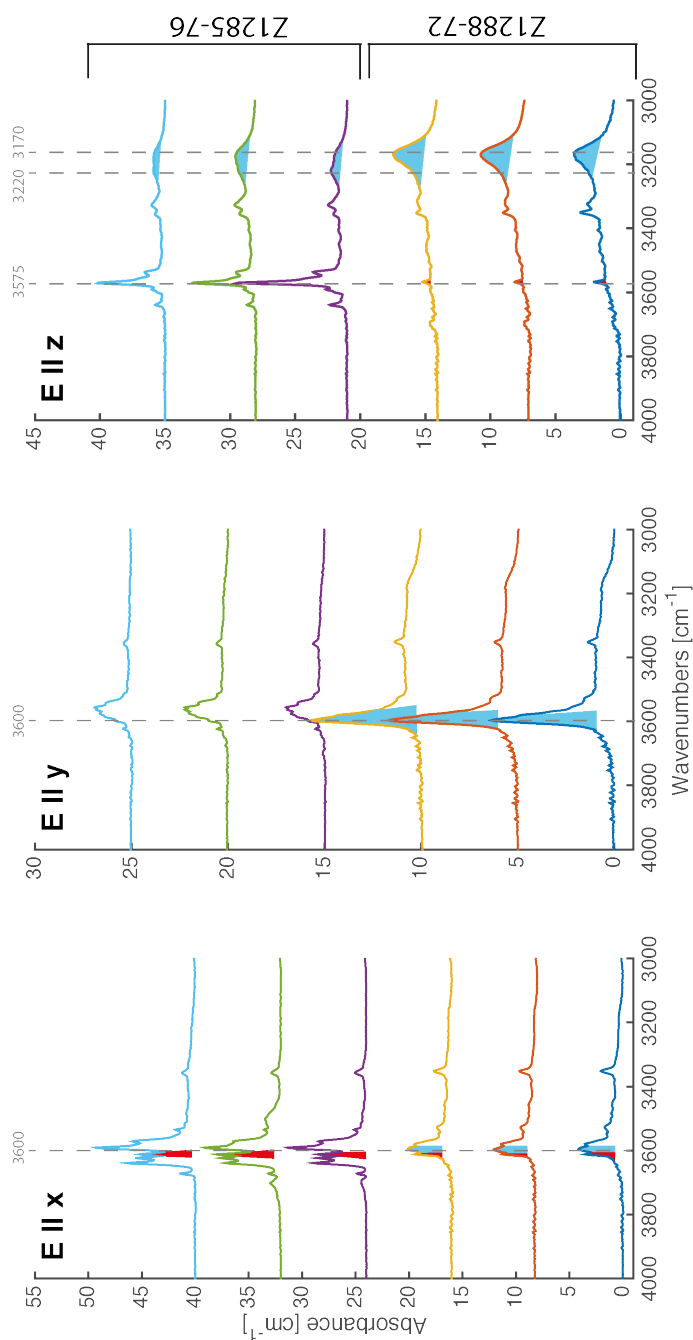


Figure 6.5: Polarised FTIR-spectra with $E||x$, $E||y$ and $E||z$ of the annealed sample Z1290 (top three spectra) and the annealed sample Z1288 (bottom three spectra). Emphasised are peaks at 3600, 3575 and 3170 cm^{-1} . Peaks assumed to be related with M-site vacancies are marked by blue areas and Si-site vacancies by red areas.

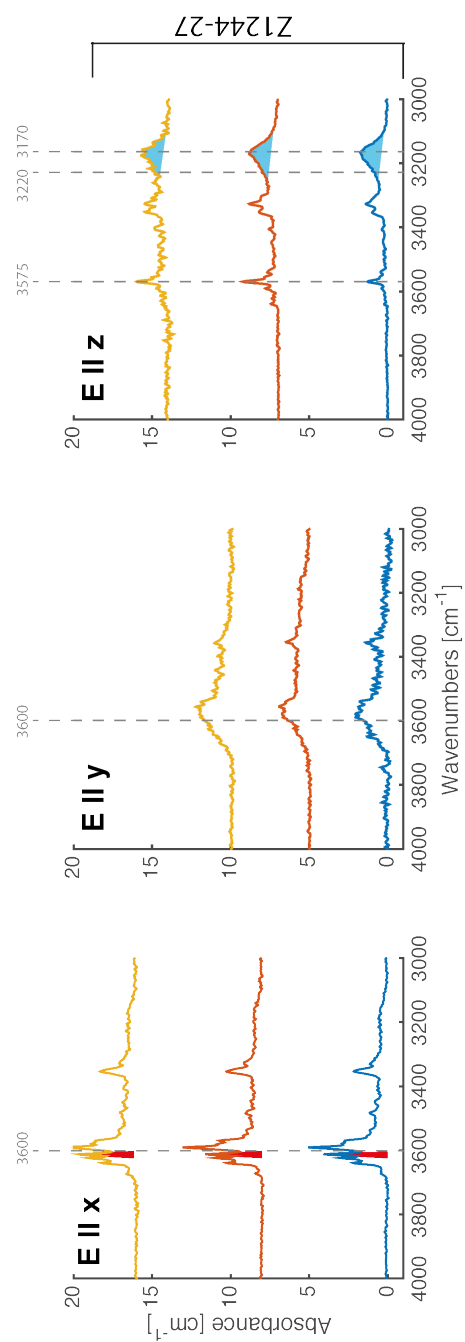


Figure 6.6: Polarised FTIR-spectra with $\mathbf{E} \parallel \mathbf{x}$, $\mathbf{E} \parallel \mathbf{y}$ and $\mathbf{E} \parallel \mathbf{z}$ of the annealed sample Z1244. Emphasised are peaks at 3600 , 3575 and 3170 cm^{-1} . Peaks assumed to be related with M-site vacancies are marked by blue areas and Si-site vacancies by red areas.

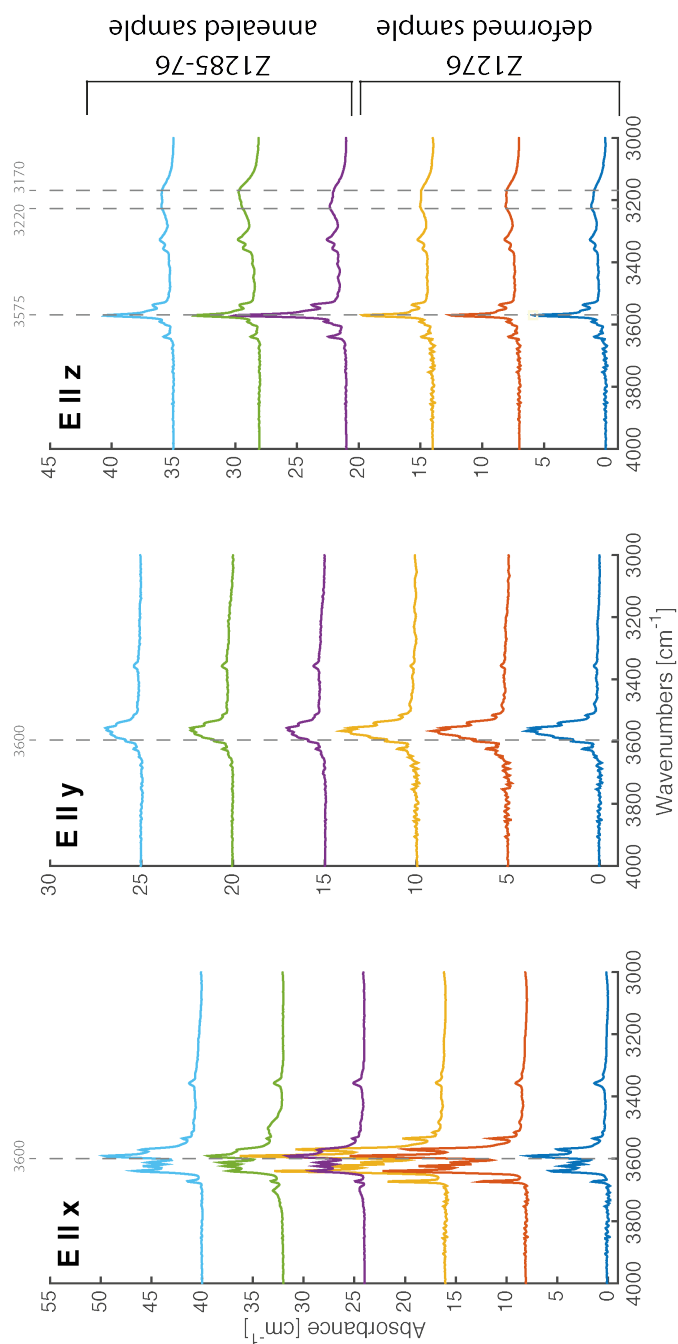


Figure 6.7: Polarised FTIR-spectra with $E \parallel x$, $E \parallel y$ and $E \parallel z$ of the deformed sample Z1276 and the annealed sample Z1285 of the deformed sample Z1276. Emphasised are peaks at 3600, 3575 and 3170 cm^{-1} . This comparison shows that the position of the dominant peaks do not change during the annealing process compared to the deformation experiment.

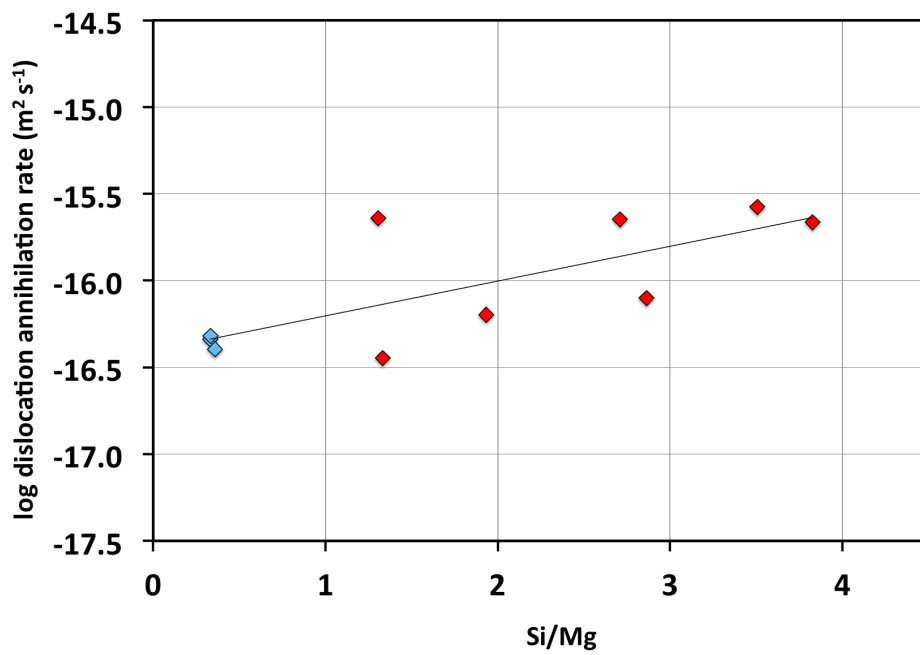


Figure 6.8: Dislocation annihilation rate is plotted against the intensity of peaks in the FTIR-spectra related to V_{Si} (3612 and 3565 cm^{-1}) over V_M (3170 , 3220 and 3598 cm^{-1}). The red and blue symbols denote samples showing LSA and MSA+HAS like spectra, respectively.

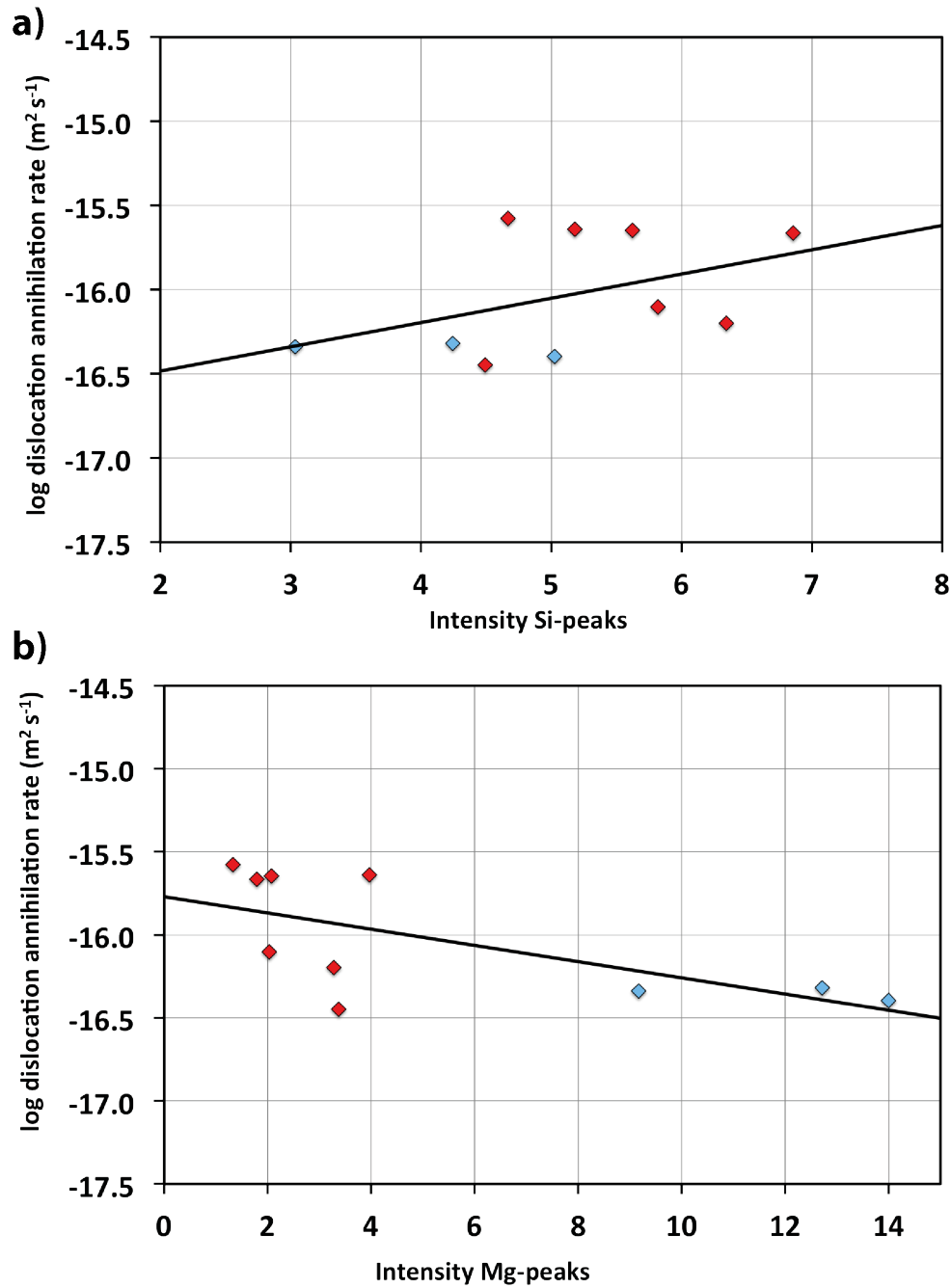


Figure 6.9: Logarithm of the dislocation annihilation rates is plotted against the intensities of peaks in the FTIR-spectra related to V_{Si} (3612 and 3565 cm^{-1}) in picture a) and V_M (3170 , 3220 and 3598 cm^{-1}) in b). The red and blue symbols denote samples showing LSA and MSA+HAS like spectra, respectively.

they were not able to produce those peaks. However, it still remains an open question, which point defects can be linked with a particular wavenumber in FTIR-spectra. If it is assumed that it can be done, as shown by Lemaire et al. [2004], the results shown in Figure 6.8 would indicate that V_{Mg} would prohibit dislocation climb which is essential for dislocation annihilation, whereas V_{Si} would assist dislocation annihilation. In other words, dislocation mobility of orthopyroxene-buffered olivine should be lower than ferropiclasite-buffered olivine under wet conditions. This finding is in contrary to deformation experiments conducted by Bai et al. [1991] under controlled chemical environments, which showed that orthopyroxene-buffered samples deform faster than the magnesiowustite-buffered samples. It is inevitable to understand the chemical environment during deformation and annealing experiments for better understanding of deformation processes in Earth's mantle. The samples in this study represent olivine with mantle composition annealed in equilibrium with orthopyroxene at spinel peridotite conditions. Therefore, results of this study give insights in mantle processes.

6.4 Geophysical applications

The ability to understand viscous flow of solid rocks in Earth's mantle is of great interest to comprehend geological processes on the earth surface. By using values obtained by experimental studies, it is possible to predict the physical state of the upper mantle consisting of olivine and to understand geodynamic processes better. Viscosity in the upper mantle is controlled by olivine, because it is the weakest and most abundant phase. From deformation experiments, it is assumed that viscosity of olivine aggregates is decreasing with increasing water content. This study shows that dislocation mobility is not influenced by water as expected from deformation experiments. Therefore, an open question, what is the effect of water on the strength of Earth's lithosphere, remains.

6.4.1 Strength models of the lithosphere

The lithosphere is the uppermost part of the earth and plays a main role for geological processes on the earth surface. It consists of the crust and uppermost part of the upper mantle. The mechanical behaviour of the lithosphere is described by strength profiles, and varies under different geological setting. Three models are used to describe the strength of the earth continental lithosphere which are indicating the distribution of rheological properties and strength of usually two main layers, crust and upper mantle. These profiles are shown in Fig. 6.10, and are based on experimental observations. Their names are based on food analogies, and are called jelly sandwich model, crème brûlée model and the banana split model [Bürgmann and Dresen, 2008]. The controlling factors for the rheological layering are pressure, temperature and chemical variation.

The jelly sandwich model describes a strong upper crust and mantle confining a soft lower crust. The silicic upper crust is in a state of frictional equilibrium, and the pressure-dependent frictional strength increases with increasing depth. However, the thermally activated creep process reduces viscous strength. Higher melting points of mafic rocks increases viscosity below the Moho. This model is required to explain narrow continental rift and a mountain

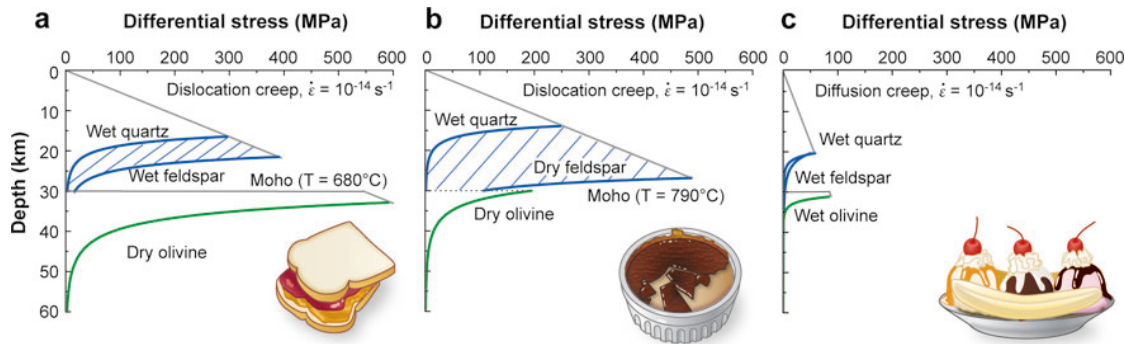


Figure 6.10: Three different strength profiles of the continental crust from Burgmann and Dresen [2008]: (a) A jelly sandwich strength, (b) the crème brûlée model and (c) the banana split model. The jelly sandwich model is characterised by weak mid-to-lower crust and dry mantle, which is strong. brûlée model comprise a strong crust and a weak mantle. The mantle is weakened by a higher geotherm and probably also by water. The Banana split model exhibit also a weak mantle and also a crust whose strength is controlled by major crustal fault zones.

belt and to explain the large elastic thickness below cratons [Précigout and Gueydan, 2009; Burov et al., 2006].

The crème brûlée model by Burov and Watts [2006] is based on the idea of a strong crust and a significantly weaker upper mantle, caused by high temperature and weakening by water. For this model, the strength is restricted to the uppermost brittle layer of the crust and flow occurs mainly in the weak upper mantle [Burov et al., 2006]. In the case of the crème brûlée models, the asthenosphere and the lithospheric mantle can not be distinguished from a mechanical point of view [Burov, 2010]. This is also related to very low effective viscosities of 10^{19} - 10^{20} [Burov, 2010].

The banana split model is characterized by the weakness of major crustal fault zones throughout the thickness of the lithosphere, caused by various strain weakening and feedback processes. It is used to describe processes along plate boundaries, where it is assumed that the strength of the lithosphere is reduced, because of fluids, strain-rates and higher temperature [Burgmann and Dresen, 2008].

In these models areas in the mantle with a low viscosity are usually described by the presence of water. As shown in this study, however, the influence of water on dislocation creeps seems to be very low.

6.4.2 Influence of water on viscosity

Viscosity can be evaluated based on models for sea-level change, glacial rebound and by surface deformation induced by the water load. The global average effective viscosity in the upper mantle under the regions of postglacial rebound is 10^{20} - 10^{21} Pa s [Lambeck et al., 1996; Mitrovica and Forte, 1997; Lambeck et al., 1998]. On the other hand, Nishimura and Tacher [2003] showed much lower viscosity in the asthenosphere under the northwestern part

of the US, which is $4 \times 10^{18 \pm 0.5}$ Pa s, based on postseismic deformation.

The presence of water has been considered to result in a reduction of ductile strength of olivine [Kohlstedt et al., 1995] and therefore be one of the basic parameters for modelling dynamic processes in the upper Earth's mantle. Experimental results by Mei and Kohlstedt [2000b] indicated that the viscosity of olivine aggregates decreases by a factor of 5~6 when water is present at a confining pressure of 300 MPa. The decrease in viscosity depends on the amount of water present in olivine [Hirth and Kohlstedt, 1996]. Results of the deformation experiments showed that viscous creep of olivine aggregates is controlled by diffusion and dislocation processes. With increasing differential stresses, dislocation creep becomes the dominant process both under 'dry' and 'wet' conditions.

Equation 6.1 describes the dependence of strain rate at constant stress on water content for peridotitic rocks. Therefore, it is the basis to model dynamic processes in the Earth's upper mantle.

$$\dot{\epsilon} = AC_{OH}^r \exp\left(-\frac{(E + V \times P)}{RT}\right) \quad (6.1)$$

where $\dot{\epsilon}$ is the strain rate, A is a constant, C_{OH} is the water content and E is the activation energie, R is the gas constant, T is temperature and P pressure [Karato, 2008].

The effect of water on the viscosity can be described in the case of constant stress as $\nu \propto C_{OH}^{-r} (H^*(C_{OH})/RT)$ and for constant strain rate as $\nu \propto C_{OH}^{-r/n} (H^*(C_{OH})/nRT)$, where r is the water content exponent, a constant which is assumed to be $r=1.2$ [Karato, 2008].

By modifying Eq. 6.1 the effect of water on the effective viscosity $\eta_{\dot{\epsilon}}$ can be calculated for constant strain rate:

$$\eta_{\dot{\epsilon}} = A^{1/n} \dot{\epsilon}^{1-n/n} C_{OH}^{-r/n} (\exp^{-(H/RT)})^{-1/n} \quad (6.2)$$

where H is the activation enthalpy ($H = E + PV$) and n is the stress exponent (normally 3.0 - 3.5 for olivine) [Dixon et al., 2004].

6.4.3 Effect of water on strain rates in the upper mantle

Fig. 6.11 shows variations in effective viscosity at 3 GPa depending on the exponential factor r of the equation 6.1. The plot in Fig. 6.11a) is calculated with $r = 0.17$, which is based on the results for dislocation mobility in this study. The increase in water content has a small influence on the strain rate in contrast to the strain rates in the plot in Fig. 6.11b) which are calculated with $r = 1.2$. For $r=0.17$ at a temperature of 1800 K, $\eta_{\dot{\epsilon}}$ decrease from 7×10^{19} to 4×10^{19} Pa s with increasing water content from 20 to 400 ppm. For $r=1.2$ at a temperature of 1800 K, $\eta_{\dot{\epsilon}}$ decrease from 2×10^{19} to 5×10^{17} Pa s with increasing water content from 20 to 400 ppm.

The value $r=1.2$ is stated by Hirth and Kohlstedt, [2003] and is used in numerical models such as Dixon et al., [2004], Fred and Bürgmann, [2004], Alisic et al., [2010]. It is used to explain viscosity contrast in the upper mantle.

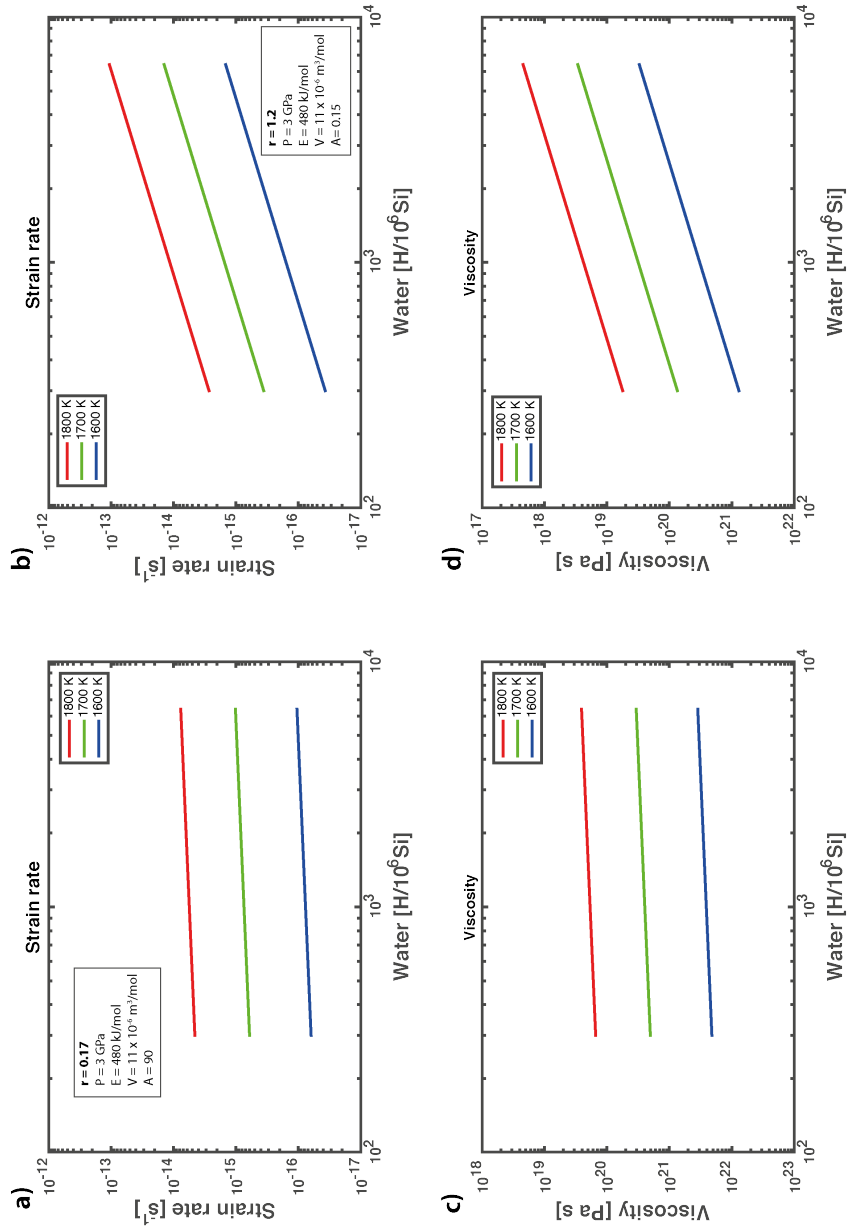


Figure 6.11: Comparison of effective viscosity at 3 GPa depending on the exponential factor r in equation 6.1 for three different temperatures (1600 K: blue, 1700 K: green and 1800 K: blue). a) and b) show the dependence of strain rate on the water content. For a) a exponential factor $r=0.17$ is used and for b) $r=1.2$. The calculated strain rates are used in c) and d) to calculate the effect of water on effective viscosity. The decrease of η_{ϵ} with increasing water content is very small for $r=0.17$ compared to $r=1.2$. At 1800 K η_{ϵ} decrease from 7×10^{19} to 4×10^{19} Pa s.

A viscosity contrast can be observed between different regions of the continental mantle, Fig. 6.12. It is assumed that the contrast in viscosity is directly related to the existent/absence of water.

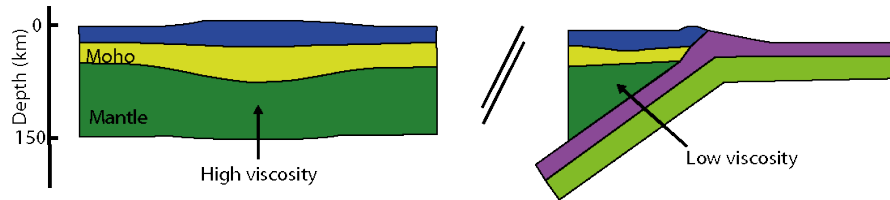


Figure 6.12: Viscosity is assumed to depend on water content. Regions of the upper mantle where water content is high, such as in subduction zones, show low viscosity. In areas where water is extracted, such as continental roots and mid oceanic ridges, are characterised by high viscosity.

'Dry' cratonic lithosphere exhibits long-term stability and are unaffected by orogenic activities. It is known that cratonic lithosphere is thicker, especially at cratonic roots, compared to oceanic lithosphere. Moreover, seismological and geochemical studies show a rheological contrast between oceanic and continental upper mantle to a depth up to 200-300 km [Karato, 2008]. The rheological contrast is assumed to explain the long-term existence of such roots. Since the chemical composition of oceanic and continental upper mantle is more or less similar, the essential controlling factors are temperature and/or water content [Karato, 2008]. The long-term stability of cratonic upper mantle can be explained by assuming more buoyant and more viscous materials than the surrounding mantle [Doin et al., 1997]. The increase in viscosity can be explained by devolatilization [Pollack, 1986]. A difference in viscosity by a factor of around 10^3 would be necessary to stabilise cratonic roots [Lenardic and Moresi, 1999]. Such large difference cannot be achieved by difference in water alone, when a value of 0.17 for r is assumed. Probably, the heat transfer in this region of the upper mantle is damped. Because of the high viscosity, convection in the affected region is suppressed, isolating it from general ongoing convection and leaving heat conduction as the only way of heat transfer [Pollack, 1986].

Mantle wedges are thought to be wet regions of the Earth's mantle where viscosity plays an important role as well. A mantle wedge is part of the mantle above a subducted oceanic lithosphere and below the overriding plate in a converging margin. It is assumed that the viscosity in some parts of mantle wedges is lower than in any other region of the upper mantle [Hirth and Kohlstedt, 2003]. A low viscosity wedge has probably influence on flow, force balance and surface deformation in subduction zones [Billen and Gurnis, 2001]. In case of the flow pattern in the wedge, a low viscosity causing the movement of material upwards into the wedge corner [Billen and Gurnis, 2001]. Further, it is assumed that one of the reasons for a lower viscosity in the deep upper mantle in subduction zones is the weakening effect of water [Billen and Gurnis, 2001]. The source for water can be the influx of fluids from the subducted slab. An oceanic upper mantle contains around $1000 \text{ H}/10^6 \text{ Si}$, which is 20% of the solubility at a depth of 120 km [Hirth and Kohlstedt, 1996]. A mantle wedge can contain up to 5 times more water, when it is water saturated [Hirth and Kohlstedt, 2003].

An example of a mantle with low viscosity can be found below the western part of the US, which indicates low viscosities ($\sim 10^{-18}$ Pa s) [Kaufmann and Amelung, 2000; Bills et al., 1994]. A viscosity of 10^{-18} Pa s is lower compared to values of typical cratonic viscosities of $\sim 10^{-20}$ - 10^{-21} Pa s [Dixon et al., 2004]. Petrological and geochemical studies reveal that most of the upper most mantle below the western US is anomalously wet [Dixon et al., 2004]. As shown in Fig. 6.11, a lowered viscosity of (10^{-18}), however, cannot be explained by the presence of water based on the water-content exponent of $r = 0.17$ obtained in this study. The formation of partial melt could be a reason for a decrease in bulk viscosity of peridotite in low viscosity zones [Hirth and Kohlstedt, 1996]. Further, melt fraction increase with an increasing concentration of water in peridotite [Gaetani and Grove, 1998].

6.4.4 Effect on hotspots

Hotspots represent anomalous areas of surface volcanism and cause intra-plate volcanism, such as the volcanism of the Hawaiian island, and volcanism near oceanic ridges, such as the volcanism of Iceland [Turcotte and Schubert, 2014]. Usually, associated with hotspots are mantle plumes. Mantle plumes are quasi-cylindrical concentrated active upwelling of the mantle [Bercovici et al., 1989; Turcotte and Schubert, 2014]. Typical for hot-spot volcanism is basaltic volcanism, which is assumed to form because of pressure-release melting in the upwelling plume [Turcotte and Schubert, 2014]. The shape of plumes are characterised by a leading diapir or plume head and a following thin cylindrical conduit or plume tail which connects the diapir to the source region [Turcotte and Schubert, 2014]. The shape of mantle plumes is controlled by their physical properties and the surrounding rocks. In general, the mantle rock in the plume head is less dense and less viscous and hotter compared to the surrounding rock. The viscosity of the surrounding material and the mantle plumes itself controls their shape. Ito et al. [1999] studied plume-ridge interaction on the example of the Iceland hot spot. The goal is to explain crustal and mantle structures, which are assumed to be controlled by the effect of dehydration on the viscosity structure. The extraction of water from the upwelling mantle caused by partial melting increases the viscosity, which leads to reduction in upwelling rates. Dehydration is assumed to take place at a depth of 180 km, corresponding to a pressure of 5.8 GPa and a temperature of 1803 K. Dehydration leads to an water loss of 75 % at the dry solidus and simultaneously to and plume viscosity is fifty times greater [Ito et al., 1999]. The reduction in viscosity leads to a reduced upwelling rate, which leads to lower melting rates and thinner crust. The calculated change in viscosity from less than 5×10^{19} to 3×10^{20} Pa s. The water content is assumed to be 125 ppm before dehydration.

Fig. 6.13 compares the effect of water on viscosity depending on the exponential factor r of the equation 6.1. Conditions are chosen according to Ito et al. [1999] for a depth where the onset of dehydration is assumed. The green line indicates the supposed water content of the peridotite. As Fig. 6.13 indicates, a reduction of viscosity cannot be explained by the extraction of water on dislocation creep alone ($r=0.17$). Probably, water on the grain-boundaries is the more realistic reason to explain the phenomenon.

Ballmer et al. [2007] describe an alternative concept to explain intra-plate volcanism which violates the prediction of the hotspot hypothesis. The mechanism which is described

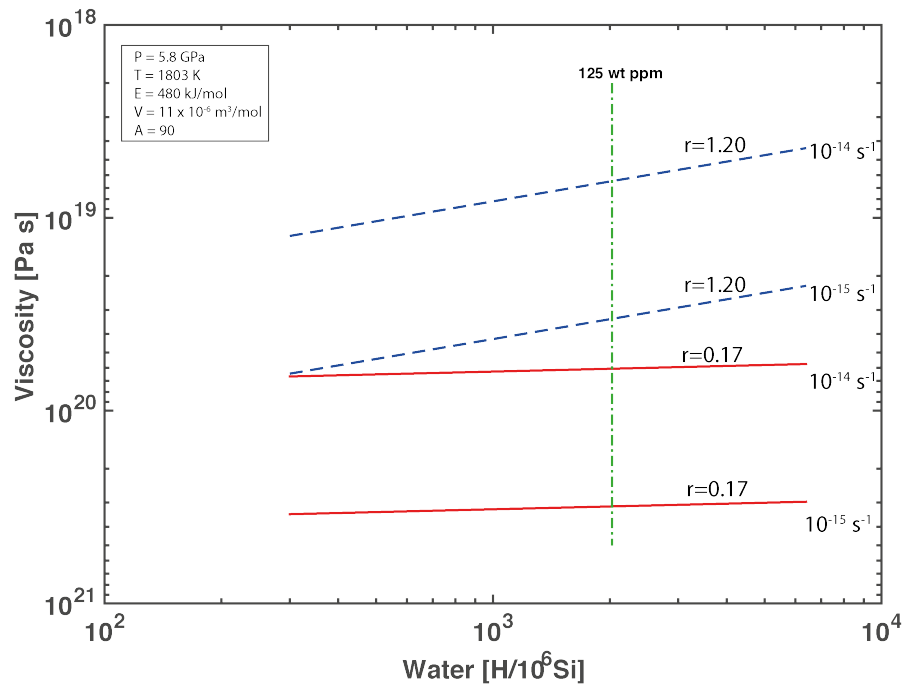


Figure 6.13: Comparison of effective viscosity at 5.8 GPa depending on the exponential factor r in equation 6.1 at a temperature of 1803 K. The green line indicates a water content of 125 wt ppm. The strain-rates, 10^{-14} and 10^{-15} s^{-1} , are indicated on the right.

by Ballmer is sublithospheric convection. In this theory, small changes in effective viscosity ($\pm 1 \times 10^{19}$) controls the rate of melt production. The viscosity must be low, in a range between 10^{19} to 2×10^{19} Pa s. Such small variations in effective viscosity can be explained by the finding in this study, as shown in Fig. 6.13. Therefore, in this case of sublithospheric convection, the effect of water on dislocation creep can play an important role.

6.4.5 Extrapolation of single crystal data to aggregates

In section 6.4 strain rates and the influence of water on effective viscosity were calculated with the experimental results of this work using the [100](010) slip system of olivine. Data from single crystals and the [100](010) slip system were used to explain strain rates of mantle rocks, which were assumed to be pure polycrystalline olivine for simplicity. This extrapolation is not straight forward, because peridotites, the rocks in the upper earth mantle, are aggregates of olivine, pyroxene and garnet. The physical properties of pyroxene and garnet also influence the plastic behaviour of a peridotite. Nevertheless, the simplification mentioned above can be made because olivine is the most abundant mineral and also considered to be the rheologically weakest phase in the upper mantle. Because of this, the rheology of the upper mantle is significantly influenced by the rheology of olivine. Moreover, focusing on olivine makes it possible to compare results from this work to other results presented in literature where polycrystalline olivine aggregates were also used for deformation experiments [cf. Toriumi and Karato, 1978; Kohlstedt et al. 1980; Karato and Ogawa, 1982; Karato and Sato, 1982; Karato et al., 1993; Farla et al., 2011].

As mentioned in chapter 2, olivine has at least five different slip systems, such as [100](010), [001](010), [001](100), [100](*okl*) and [100](001). Therefore, the rheological properties of a single crystal in an aggregate depend on the orientation of the crystal relative to the stress during deformation [Karato, 2008]. In case of a polycrystalline aggregate of randomly oriented grains, it is assumed in theory that the deformation of individual grains and of the aggregate be maintained only if the grains have five independent slip systems and strain is homogeneous. This behaviour is called the von Mises criterion. In practice the incompatibility between grains can be compensated by a variety of processes, such as bending of the lattice, kinking, twinning, polygonization, recrystallization and diffusional flows [Ranalli, 1995].

With regard to the von Mises criterion it might be necessary to collect data for all slip systems of olivine. Nevertheless, it was described by Karato 2008 that deformation processes can also be controlled by a single slip system, such as [100](010). It was proposed by this author that a single slip system can dominate the deformation process in an end-member case when lattice deformation orientation develops close to the dislocation?diffusional creep boundary and dislocation and diffusional creep contribute to total strain extensively [Karato, 2008]. This end-member lattice-preferred orientation is commonly observed in earth material, because deformation processes in most parts of Earth occur close to the boundary between dislocation and diffusional creep [Karato, 2008].

Furthermore, the simplification to use single crystal samples is beneficial because the effect of water on intracrystalline processes can be studied. Further, it can be assumed that the reduction in strain rates in the presence of water in olivine aggregates is controlled by

other processes, such as water on the grain boundaries or diffusion processes, because effects on dislocation mobilities can be ruled out.

7 Conclusion

Water weakening of olivine aggregates in the Earth's upper mantle is known from numerous studies of deformation. It was explained by the influence of water on the mobility of dislocations [Karato et al., 1986]. This study reveals that dislocation mobility in the slip system [100](010), the main slip system in the upper earth mantle, is less influenced by water than expected from deformation experiments. The water content exponent r of the equation 6.1 is of significant importance. It is used in numerical models which describe deformation processes in the earth mantle. From deformation experiments at conditions where dislocation creep is the controlling process, it is assumed $r=1.2$. This study shows $r=0.17\pm 0.43$. This finding is significantly lower. According to this study, the idea of water having an intracrystalline effect on olivine rheology must be reconsidered. The weakening by water must be explained by other processes, such as effects of partial melt and of grain-boundary water in olivine aggregates, which was already pointed out by Chopra and Paterson [1981] and Chopra and Paterson [1984]. The real situation is that the upper mantle is made of polycrystalline olivine and not a giant single crystal. According to this study, water has a small effect on intragranular deformation processes, water at the grain boundaries or formation of partial melt are the controlling factors for deformation processes under 'wet' condition.

The most important results of this study:

- By using the experimental techniques described in this study, the mobility of the main slip systems of olivine can be observed under 'dry' and 'wet' conditions.
- The calculated log dislocation annihilation rate values k are in the same range as previous experiments
- Water has an effect on dislocation mobility, but the effect is not as large as assumed from deformation experiment.
- The water content exponent of the dislocation annihilation rate is 0.17 ± 0.43
- Samples annealed in this study show FTIR-spectra which can be found in natural samples, coming directly from the Earth's mantle. Therefore, annealed samples in this study are assumed to be representative of mantle olivine and can be used to study creep processes at mantle conditions.

Bibliography

- Aki, K. and Kaminuma, K. (1963). Phase velocity of low waves in japan (part 1): Love waves from the aleutian shock of march 9, 1957.
- Alicic, L., Gurnis, M., Stadler, G., Burstedde, C., Wilcox, L. C., and Ghattas, O. (2010). Slab stress and strain rate as constraints on global mantle flow. *Geophysical Research Letters*, 37(22).
- Bai, Q. and Kohlstedt, D. (1993). Effects of chemical environment on the solubility and incorporation mechanism for hydrogen in olivine. *Physics and Chemistry of Minerals*, 19(7):460–471.
- Bai, Q., Mackwell, S., and Kohlstedt, D. (1991). High-temperature creep of olivine single crystals 1. mechanical results for buffered samples. *Journal of Geophysical Research: Solid Earth (1978–2012)*, 96(B2):2441–2463.
- Ballmer, M., Van Hunen, J., Ito, G., Tackley, P., and Bianco, T. (2007). Non-hotspot volcano chains originating from small-scale sublithospheric convection. *Geophysical Research Letters*, 34(23).
- Bell, D. R. and Rossman, G. R. (1992). Water in earth's mantle: The role of nominally anhydrous minerals. *Science*, 255(5050):1391–1397.
- Bell, D. R., Rossman, G. R., Maldener, J., Endisch, D., and Rauch, F. (2003). Hydroxide in olivine: A quantitative determination of the absolute amount and calibration of the ir spectrum. *Journal of Geophysical Research: Solid Earth*, 108(B2):2156–2202.
- Beran, A. and Libowitzky, E. (2006). Water in natural mantle minerals ii: Olivine, garnet and accessory minerals. *Reviews in Mineralogy and Geochemistry*, 62(1):169–191.
- Bercovici, D., Schubert, G., and Glatzmaier, G. (1989). Three-dimensional spherical models of convection in the earth's mantle. *Science*, 244(4907):950–955.
- Berry, A. J., Hermann, J., O'Neill, H. S., and Foran, G. J. (2005). Fingerprinting the water site in mantle olivine. *Geology*, 33(11):869–872.
- Billen, M. I. and Gurnis, M. (2001). A low viscosity wedge in subduction zones. *Earth and Planetary Science Letters*, 193(1):227–236.
- Bills, B. G., Currey, D. R., and Marshall, G. A. (1994). Viscosity estimates for the crust and upper mantle from patterns of lacustrine shoreline deformation in the eastern great basin. *Journal of Geophysical Research: Solid Earth*, 99(B11):22059–22086.

- Boioli, F., Carrez, P., Cordier, P., Devincere, B., and Marquille, M. (2015). Modeling the creep properties of olivine by 2.5-dimensional dislocation dynamics simulations. *Phys. Rev. B*, 92:014115.
- Bürgmann, R. and Dresen, G. (2008). Rheology of the lower crust and upper mantle: Evidence from rock mechanics, geodesy, and field observations. *Annual Review of Earth and Planetary Sciences*, 36.
- Burov, E. (2010). The equivalent elastic thickness (t_e), seismicity and the long-term rheology of continental lithosphere: Time to burn-out "crème brûlée"? Insights from large-scale geodynamic modeling. *Tectonophysics*, 484(1–4):4 – 26. Quantitative modelling of geological processes.
- Burov, E., Watts, A., et al. (2006). The long-term strength of continental lithosphere: "jelly sandwich" or "crème brûlée"? *GSA today*, 16(1):4.
- Burov, E. B. (2011). Rheology and strength of the lithosphere. *Marine and Petroleum Geology*, 28(8):1402–1443.
- Chopra, P. and Paterson, M. (1981). The experimental deformation of dunite. *Tectonophysics*, 78(1–4):453 – 473. The Effect of Deformation on Rocks.
- Chopra, P. and Paterson, M. (1984). The role of water in the deformation of dunite. *Journal of Geophysical Research: Solid Earth*, 89(B9):7861–7876.
- Cordier, P. (2002). Dislocations and slip systems of mantle minerals. *Reviews in Mineralogy and Geochemistry*, 51(1):137–179.
- Cordier, P., Amodeo, J., and Carrez, P. (2012). Modelling the rheology of MgO under earth's mantle pressure, temperature and strain rates. *Nature*, 481(7380):177–180.
- Costa, F. and Chakraborty, S. (2008). The effect of water on si and o diffusion rates in olivine and implications for transport properties and processes in the upper mantle. *Physics of the Earth and Planetary Interiors*, 166:11–29.
- Couvy, H., Frost, D. J., Heidelbach, F., Nyilas, K., Ungár, T., Mackwell, S., and Cordier, P. (2004). Shear deformation experiments of forsterite at 11 GPa - 1400 °C in the multianvil apparatus. *European Journal of Mineralogy*, 16(6):877–889.
- Davies, G. (2000). *Dynamic Earth Plates, Plumes and Mantle Convection*. Cambridge University Press.
- Demouchy, S. and Mackwell, S. (2006). Mechanisms of hydrogen incorporation and diffusion in iron-bearing olivine. *Physics and Chemistry of Minerals*, 33.
- Demouchy, S., Schneider, S. E., Mackwell, S. J., Zimmerman, M. E., and Kohlstedt, D. L. (2009). Experimental deformation of olivine single crystals at lithospheric temperatures. *Geophysical Research Letters*, 36(4).

- Dixon, J. E., Dixon, T., Bell, D., and Malservisi, R. (2004). Lateral variation in upper mantle viscosity: role of water. *Earth and Planetary Science Letters*, 222(2):451 – 467.
- Dohmen, R., Chakraborty, S., and Becker, H.-W. (2002). Si and o diffusion in olivine and implications for characterizing plastic flow in the mantle. *Geophysical Research Letters*, 29(21).
- Doin, M.-P., Fleitout, L., and Christensen, U. (1997). Mantle convection and stability of depleted and undepleted continental lithosphere. *Journal of Geophysical Research: Solid Earth*, 102(B2):2771–2787.
- Farla, R. J. M., Kokkonen, H., Fitz Gerald, J. D., Barnhoorn, A., Faul, U. H., and Jackson, I. (2010). Dislocation recovery in fine-grained polycrystalline olivine. *Physics and Chemistry of Minerals*, 38(5):363–377.
- Faul, U. H., Fitz Gerald, J. D., Farla, R. J. M., Ahlefeldt, R., and Jackson, I. (2011). Dislocation creep of fine-grained olivine. *Journal of Geophysical Research: Solid Earth*, 116(B1):n/a–n/a.
- Fei, H., Wiedenbeck, M., Yamazaki, D., and Katsura, T. (2013). Small effect of water on upper-mantle rheology based on silicon self-diffusion coefficients. *Nature*, 498(7453):213–215.
- Fei, H., Wiedenbeck, M., Yamazaki, D., and Katsura, T. (2014). No effect of water on oxygen self-diffusion rate in forsterite. *Journal of Geophysical Research: Solid Earth*, 119(10):7598–7606.
- Fowler, C. M. R. (2004). *The Solid Earth: An Introduction to Global Geophysics*. Cambridge University Press.
- Freed, A. M. and Bürgmann, R. (2004). Evidence of power-law flow in the mojave desert mantle. *Nature*, 430(6999):548–551.
- Gaetani, G. A. and Grove, T. L. (1998). The influence of water on melting of mantle peridotite. *Contributions to Mineralogy and Petrology*, 131(4):323–346.
- Gerya, T. (2010). *Introduction to Numerical Geodynamic Modelling*. Cambridge University Press.
- Gillis, P. P. and Gilman, J. J. (1965). Dynamical dislocation theory of crystal plasticity. i. the yield stress. *Journal of Applied Physics*, 36(11):3370–3380.
- Goldstein, J., Newbury, D. E., Joy, D. C., Lyman, C. E., Echlin, P., Lifshin, E., Sawyer, L. C., and Michael, J. R. (2002). *Scanning Electron Microscopy and X-ray Microanalysis*. Springer, 3rd edition.
- Griggs, D. (1967). Hydrolytic weakening of quartz and other silicates. *Geophysical Journal International*, 14(1-4):19–31.

- Hansen, L. N., Zhao, Y.-H., Zimmerman, M. E., and Kohlstedt, D. L. (2014). Protracted fabric evolution in olivine: Implications for the relationship among strain, crystallographic fabric, and seismic anisotropy. *Earth and Planetary Science Letters*, 387(0):157 – 168.
- Hirth, G. and Kohlstedt, D. (2003). *Rheology of the Upper Mantle and the Mantle Wedge: A View from the Experimentalists*, pages 83–105. American Geophysical Union.
- Hirth, G. and Kohlstedt, D. L. (1996). Water in the oceanic upper mantle: implications for rheology, melt extraction and the evolution of the lithosphere. *Earth and Planetary Science Letters*, 144(1):93–108.
- Ismail, W. B. and Mainprice, D. (1998). An olivine fabric database: an overview of upper mantle fabrics and seismic anisotropy. *Tectonophysics*, 296(1):145–157.
- Ito, G., Shen, Y., Hirth, G., and Wolfe, C. J. (1999). Mantle flow, melting, and dehydration of the iceland mantle plume. *Earth and Planetary Science Letters*, 165(1):81–96.
- Jackson, I., editor (2000). *The Earth's Mantle*. Cambridge University Press.
- Jacobsen, S. D. (2006). Effect of water on the equation of state of nominally anhydrous minerals. *Reviews in Mineralogy and Geochemistry*, 62(1):321–342.
- Jung, H. and Karato, S. I. (2001). Water-induced fabric transitions in olivine. *Science*, 293(5534):1460–1463.
- Jung, H., Katayama, I., Jiang, Z., Hiraga, T., and Karato, S. (2006). Effect of water and stress on the lattice-preferred orientation of olivine. *Tectonophysics*, 421(1-2):1–22.
- Karato, S. (1987a). Scanning electron microscope observation of dislocations in olivine. *Physics and Chemistry of Minerals*, 14(3):245–248.
- Karato, S. (2008). *Deformation of earth materials an introduction to the rheology of solid earth*. Cambridge University Press, Cambridge (GB); New York (N.Y.); Melbourne [etc.].
- Karato, S. and Ogawa, M. (1982). High-pressure recovery of olivine: implications for creep mechanisms and creep activation volume. *Physics of the Earth and Planetary Interiors*, 28(2):102–117.
- Karato, S.-I. (1987b). Seismic anisotropy due to lattice preferred orientation of minerals: kinematic or dynamic? *High-Pressure Research in Mineral Physics: A Volume in Honor of Syun-iti Akimoto*, pages 455–471.
- Karato, S.-i., Jung, H., Katayama, I., and Skemer, P. (2008). Geodynamic significance of seismic anisotropy of the upper mantle: New insights from laboratory studies. *Annual Review of Earth and Planetary Sciences*, 36(1):59–95.
- Karato, S.-I., Paterson, M. S., and FitzGerald, J. D. (1986). Rheology of synthetic olivine aggregates: influence of grain size and water. *Journal of Geophysical Research: Solid Earth (1978–2012)*, 91(B8):8151–8176.

- Karato, S. I., Rubie, D. C., and Yan, H. (1993). Dislocation recovery in olivine under deep upper mantle conditions: Implications for creep and diffusion. *Journal of Geophysical Research*, 98(B6):9761–9768.
- Karato, S.-i. and Sato, H. (1982). Effect of oxygen partial pressure on the dislocation recovery in olivine: a new constraint on creep mechanisms. *Physics of the Earth and Planetary Interiors*, 28(4):312 – 319.
- Karato, S.-i. and Wu, P. (1993). Rheology of the upper mantle: A synthesis. *Science*, 260(5109):771–778.
- Katayama, I., Jung, H., and Karato, S.-i. (2004). New type of olivine fabric from deformation experiments at modest water content and low stress. *Geology*, 32(12):1045–1048.
- Kaufmann, G. and Amelung, F. (2000). Reservoir-induced deformation and continental rheology in vicinity of lake mead, nevada. *Journal of Geophysical Research: Solid Earth*, 105(B7):16341–16358.
- Keppler, H. and Bolfan-Casanova, N. (2006). Thermodynamics of water solubility and partitioning. *Reviews in Mineralogy and Geochemistry*, 62(1):193–230.
- Kohlstedt, D., Evans, B., and Mackwell, S. (1995). Strength of the lithosphere: Constraints imposed by laboratory experiments. *Journal of Geophysical Research: Solid Earth*, 100(B9):17587–17602.
- Kohlstedt, D. L. (2006). The role of water in high-temperature rock deformation. *Reviews in Mineralogy and Geochemistry*, 62(1):377–396.
- Kohlstedt, D. L., Goetze, C., Durham, W. B., and Sande, J. V. (1976). New technique for decorating dislocations in olivine. *Science*, 191(4231):1045–1046.
- Kohlstedt, D. L., Keppler, H., and Rubie, D. C. (1996). Solubility of water in the α , β and γ phases of $(\text{mg,fe})_2\text{SiO}_4$. *Contributions to Mineralogy and Petrology*, 123(4):345–357.
- Kohlstedt, D. L., Nichols, H. P. K., and Hornack, P. (1980). The effect of pressure on the rate of dislocation recovery in olivine. *Journal of Geophysical Research: Solid Earth*, 85(B6):3122–3130.
- Kovács, I., O'Neill, H., Hermann, J., and Hauri, E. (2010). Site-specific infrared o-h absorption coefficients for water substitution into olivine. *American Mineralogist*, 95(2-3):292–299.
- Kumazawa, M. and Anderson, O. L. (1969). Elastic moduli, pressure derivatives, and temperature derivatives of single-crystal olivine and single-crystal forsterite. *Journal of Geophysical Research*, 74(25):5961–5972.
- Lambeck, K., Johnston, P., Smither, C., and Nakada, M. (1996). Glacial rebound of the british isles-iii. constraints on mantle viscosity. *Geophysical Journal International*, 125(2):340–354.

- Lambeck, K., Smither, C., and Johnston, P. (1998). Sea-level change, glacial rebound and mantle viscosity for northern Europe. *Geophysical Journal International*, 134(1):102–144.
- Lemaire, C., Kohn, S. C., and Brooker, R. A. (2004). The effect of silica activity on the incorporation mechanisms of water in synthetic forsterite: a polarised infrared spectroscopic study. *Contributions to Mineralogy and Petrology*, 147(1):48–57.
- Lenardic, A. and Moresi, L.-N. (1999). Some thoughts on the stability of cratonic lithosphere: effects of buoyancy and viscosity. *Journal of Geophysical Research: Solid Earth*, 104(B6):12747–12758.
- Libowitzky, E. and Beran, A. (1995). Oh defects in forsterite. *Physics and Chemistry of Minerals*, 22(6):387–392.
- Libowitzky, E. and Beran, A. (2006). The structure of hydrous species in nominally anhydrous minerals: Information from polarized ir spectroscopy. *Reviews in Mineralogy and Geochemistry*, 62(1):29–52.
- Libowitzky, E. and Rossman, G. R. (1996). Principles of quantitative absorbance measurements in anisotropic crystals. *Physics and Chemistry of Minerals*, 23:319 – 327.
- Mackwell, S. J., Kohlstedt, D. L., and Paterson, M. S. (1985). The role of water in the deformation of olivine single crystals. *Journal of Geophysical Research: Solid Earth*, 90(B13):11319–11333.
- Mainprice, D., Barruol, G., and Ismail, W. B. (2000). *The Seismic Anisotropy of the Earth's Mantle: from Single Crystal to Polycrystal*, pages 237–264. American Geophysical Union.
- Matveev, S., O'Neill, H. S. C., Ballhaus, C., Taylor, W. R., and Green, D. H. (2001). Effect of silica activity on oh^- ir spectra of olivine: Implications for low- asio_2 mantle metasomatism. *Journal of Petrology*, 42(4):721–729.
- Mei, S. and Kohlstedt, D. L. (2000). Influence of water on plastic deformation of olivine aggregates: 2. dislocation creep regime. *Journal of Geophysical Research: Solid Earth*, 105(B9):21471–21481.
- Messerschmidt, U. (2010). *Dislocation Dynamics During Plastic Deformation*, volume 129 of *Springer Series in Materials Science*. Springer.
- Mitrovica, J. X. and Forte, A. M. (1997). Radial profile of mantle viscosity: results from the joint inversion of convection and postglacial rebound observables. *Journal of Geophysical Research: Solid Earth*, 102(B2):2751–2769.
- Mitsuhiro Toriumi, S.-I. K. (1985). Preferred orientation development of dynamically recrystallized olivine during high temperature creep. *The Journal of Geology*, 93(4):407–417.
- Mittemeijer, E. J. (2010). *Fundamentals of Materials Science*. Springer.

- Mosenfelder, J. L., Deligne, N. I., Asimow, P. D., and Rossman, G. R. (2006). Hydrogen incorporation in olivine from 2–12 gpa. *American Mineralogist*, 91(2-3):285–294.
- Nataf, H.-C., Nakanishi, I., and Anderson, D. L. (1984). Anisotropy and shear-velocity heterogeneities in the upper mantle. *Geophysical Research Letters*, 11(2):109–112.
- Nishimura, T. and Thatcher, W. (2003). Rheology of the lithosphere inferred from postseismic uplift following the 1959 Hebgen Lake earthquake. *Journal of Geophysical Research: Solid Earth*, 108(B8).
- Poirier, J.-P. (1985). *Creep of crystals*. Cambridge University Press.
- Pollack, H. N. (1986). Cratonization and thermal evolution of the mantle. *Earth and Planetary Science Letters*, 80(1-2):175–182.
- Précigout, J. and Gueydan, F. (2009). Mantle weakening and strain localization: Implications for the long-term strength of the continental lithosphere. *Geology*, 37(2):147–150.
- Ranalli, G. (1995). *Rheology of the Earth*. Chapman and Hall.
- Raterron, P., Chen, J., Geenen, T., and Girard, J. (2011). Pressure effect on forsterite dislocation slip systems: Implications for upper-mantle {LPO} and low viscosity zone. *Physics of the Earth and Planetary Interiors*, 188(1–2):26 – 36.
- Raterron, P., Chen, J., Li, L., Weidner, D., and Cordier, P. (2007). Pressure-induced slip-system transition in forsterite: Single-crystal rheological properties at mantle pressure and temperature. *American Mineralogist*, 92(8-9):1436–1445.
- Raterron, P., Girard, J., and Chen, J. (2012). Activities of olivine slip systems in the upper mantle. *Physics of the Earth and Planetary Interiors*, 200–201(0):105 – 112.
- Rubie, D., Karato, S., Yan, H., and O'Neill, H. (1993). Low differential stress and controlled chemical environment in multianvil high-pressure experiments. *Physics and Chemistry of Minerals*, 20(5).
- Schubert, G., Turcotte, D. L., and Olson, P. (2011). *Mantle Convection in the Earth and Planets*. Cambridge University Press.
- Shearer, P. M. (2009). *Introduction to seismology*. Cambridge University Press.
- Skemer, P., Warren, J. M., Hansen, L. N., Hirth, G., and Kelemen, P. B. (2013). The influence of water and lpo on the initiation and evolution of mantle shear zones. *Earth and Planetary Science Letters*, 375:222–233.
- Smyth, J. R., Frost, D. J., Nestola, F., Holl, C. M., and Bromiley, G. (2006). Olivine hydration in the deep upper mantle: Effects of temperature and silica activity. *Geophysical Research Letters*, 33(15):n/a–n/a.
- Stokes, D. J. (2008). *Principles of SEM*, pages 17–62. John Wiley and Sons, Ltd.

- Stuart, B. H. (2004). *Infrared Spectroscopy: Fundamentals and Applications*. Wiley.
- Tackley, P. J. (2000). Mantle convection and plate tectonics: Toward an integrated physical and chemical theory. *Science*, 288(5473):2002–2007.
- Toriumi, M. and Karato, S.-I. (1978). Experimental studies on the recovery process of deformed olivines and the mechanical state of the upper mantle. *Tectonophysics*, 49(1–2):79 – 95.
- Tullis, J. (2002). Deformation of granitic rocks: Experimental studies and natural examples. *Reviews in Mineralogy and Geochemistry*, 51(1):51–95.
- Turcotte, D. L. and Schubert, G. (2014). *Geodynamics*. Cambridge University Press.
- van Hunen, J., Zhong, S., Shapiro, N. M., and Ritzwoller, M. H. (2005). New evidence for dislocation creep from 3-d geodynamic modeling of the Pacific upper mantle structure. *Earth and Planetary Science Letters*, 238(1):146–155.
- Wang, D., Mookherjee, M., Xu, Y., and Karato, S.-i. (2006). The effect of water on the electrical conductivity of olivine. *Nature*, 443(7114):977–980.
- Wang, L., Blaha, S., Pintér, Z., Farla, R., Kawazoe, T., Miyajima, N., Michibayashi, K., and Katsura, T. (2016). Temperature dependence of [100](010) and [001](010) dislocation mobility in natural olivine. *Earth and Planetary Science Letters*, 441:81 – 90.
- Weertman, J. (1955). Theory of steady-state creep based on dislocation climb. *Journal of Applied Physics*, 26(10):1213–1217.
- Weertman, J. (1957). Steady-state creep of crystals. *Journal of Applied Physics*, 28(10):1185–1189.
- Weertman, J. and Weertman, J. R. (1975). High temperature creep of rock and mantle viscosity. *Annual Review of Earth and Planetary Sciences*, 3(1):293–315.
- Wenk, H.-R. (2002). Texture and anisotropy. *Reviews in mineralogy and geochemistry*, 51(1):291–329.
- Wenk, H.-R. and Christie, J. (1991). Comments on the interpretation of deformation textures in rocks. *Journal of Structural Geology*, 13(10):1091–1110.
- Withers, A., Bureau, H., Raepsaet, C., and Hirschmann, M. (2012). Calibration of infrared spectroscopy by elastic recoil detection analysis of H in synthetic olivine. *Chemical Geology*, 334:92 – 98.
- Workman, R. K. and Hart, S. R. (2005). Major and trace element composition of the depleted morib mantle (dmm). *Earth and Planetary Science Letters*, 231(1):53–72.
- Zhao, Y.-H., Ginsberg, S., and Kohlstedt, D. (2004). Solubility of hydrogen in olivine: dependence on temperature and iron content. *Contributions to Mineralogy and Petrology*, 147(2):155–161.

8 Appendix

8.1 Matlab code

This matlab code was used for identifying objects in the SEM-images.

Contents

- load image
- choose smaller area of the image if necessary
- Filter to improve image quality
- Manually change the image contrast
- Global image threshold using Otsu's method
- close open circle
- contour plot of grey-scale image
- Remove large objects
- Trace region boundaries in binary image
- Find connected components in binary image
- Create label matrix from bwconncomp structure
- plot the probability to access a random disl. from the disl.dataset which is smaller than a certain area
- plot the area fraction, i.e. the probability to pick spatially a disl. less than a certain area.
- select dislocations of certain size
- histogram area
- Calculate pairwise distance between pairs of objects

load image

```
clear all
close all
clf('reset')
imtool close all

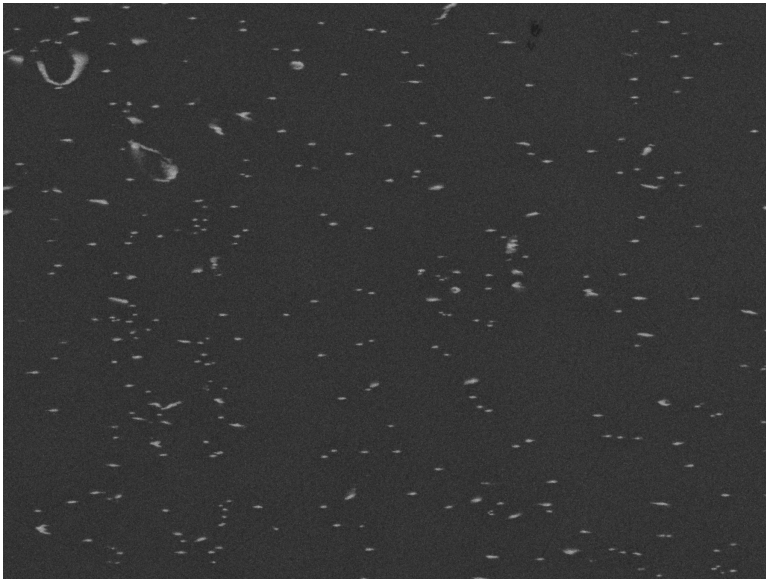
RGB = imread('image.tif');
t = 780 % number of pixels of 'large' object
%imshow(RGB)
```

Choose smaller area of the image if necessary

```
%R1= RGB(1:1450, 1:1300);  
%imshow(R1)
```

Filter to improve image quality, usually the wiener2-filter is used

```
R2 = wiener2(RGB,[3,3]);  
%R3 = medfilt2(RGB,[3 3]);  
imshow(R2)
```



Manually change the image contrast, if necessary; *usually not used*

```
%I3 = imadjust(R2,[0.3 .85],[0 1]);  
%figure, imshow(I3);
```

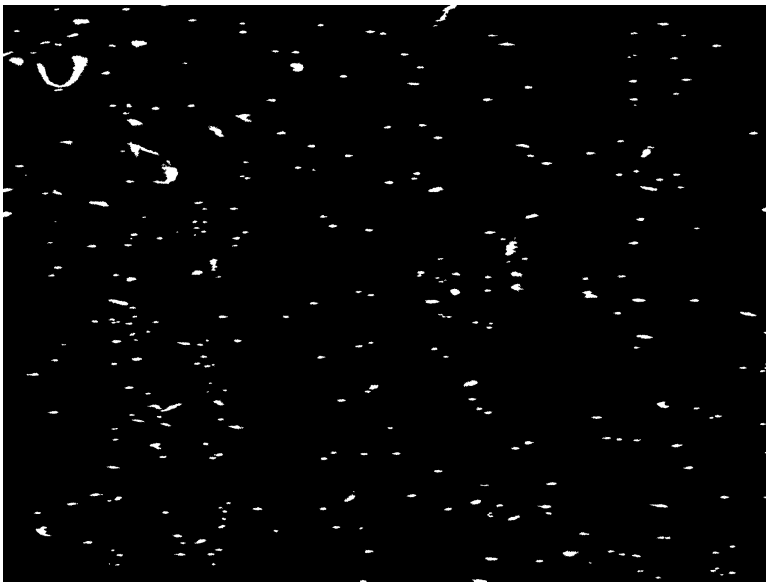
```
%subplot(2,3,1), imshow(R2)  
%subplot(2,3,2), imshow(R3)  
%subplot(2,3,3), imshow(RGB)
```

Global image threshold using Otsu's method

```
threshold = graythresh(R2);  
bw = im2bw(R2,threshold);  
subplot(1,2,1), imshow(bw)  
subplot(1,2,2), imshow(R2)
```

Fill image regions and holes

```
clear bww  
% remove all object containing fewer than 8 pixels  
    bww = bwareaopen(bw,8);  
% fill any holes, so that regionprops can be used to estimate  
% the area enclosed by each of the boundaries  
  
bww = imfill(bww,'holes');  
imshow(bww)
```



```
se = strel('disk',5) % a straight line of 5 pixels  
%  
BW = imclose(bww, se);
```

```
clear BW2  
se2= strel('arbitrary',200)  
BW2 = imerode(bww,se2);  
figure(4), imshow(BW2, 'InitialMagnification',200)  
title('closeBW');
```



contour plot of grey-scale image

```
%t = imcontour(BW)
%plot(t)
```

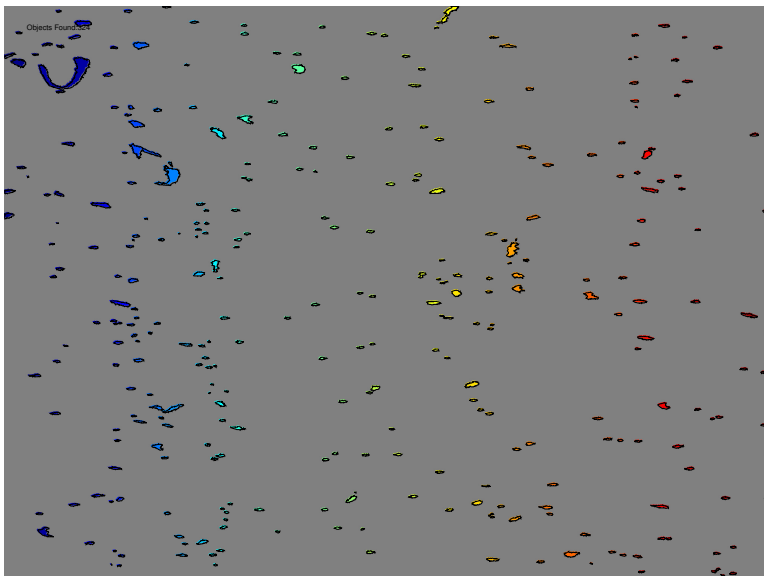
Remove large objects

```
%[bigObjects] = bwareaopen(BW, 450);
%
%z= BW - bigObjects;
%imshow(z)
```

Trace region boundaries in binary image

```
clear L
[B,L] = bwboundaries(BW2, 'noholes');

% Display the label matrix and draw each boundary
%subplot(2,2,4),
imshow(label2rgb(L, @jet, [.5 .5 .5]))
text(60,60, strcat('Objects Found:', num2str(length(B))))
hold on
for k = 1:length(B)
    boundary = B{k};
    plot(boundary(:,2), boundary(:,1), 'w', 'LineWidth', .5)
end
```



Find connected components in binary image

```

cc = bwconncomp(BW2);
cc.NumObjects;
number = cc.NumObjects
idx = cc.PixelIdxList
dis_prop = regionprops(cc, 'all')
centroids = cat(1, dis_prop.Centroid);

%imtool(R2)
%hold(imgca,'on')
%plot(imgca,centroids(:,1), centroids(:,2), 'r*')
%hold(imgca,'off')

```

Create label matrix from bwconncomp structure

```

labeled = labelmatrix(cc);
whos labeled
graindata = regionprops(cc, 'all')
grain_areas = [graindata.Area];

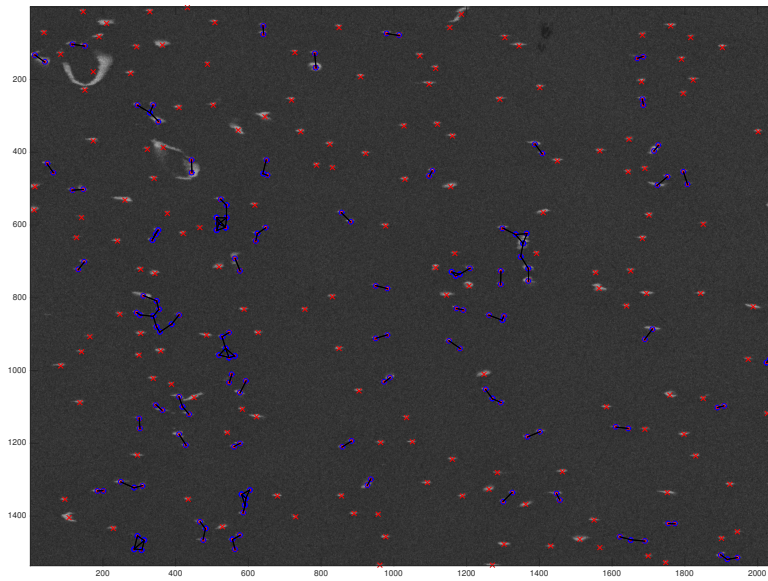
\subsection*{select dislocations of certain size}

\begin{verbatim}
dd = graindata(grain_areas > t)

dd.PixelIdxList
sidx = dd.PixelIdxList
%sel_dis_prop = regionprops(dd, 'all')
selcentroids = cat(1, dd.Centroid);

imtool(RGB)
hold(imgca,'on')
plot(imgca,centroids(:,1), centroids(:,2),'+g','MarkerSize',10)
    plot(imgca,selcentroids(:,1), selcentroids(:,2), 'r*')
hold(imgca,'off')

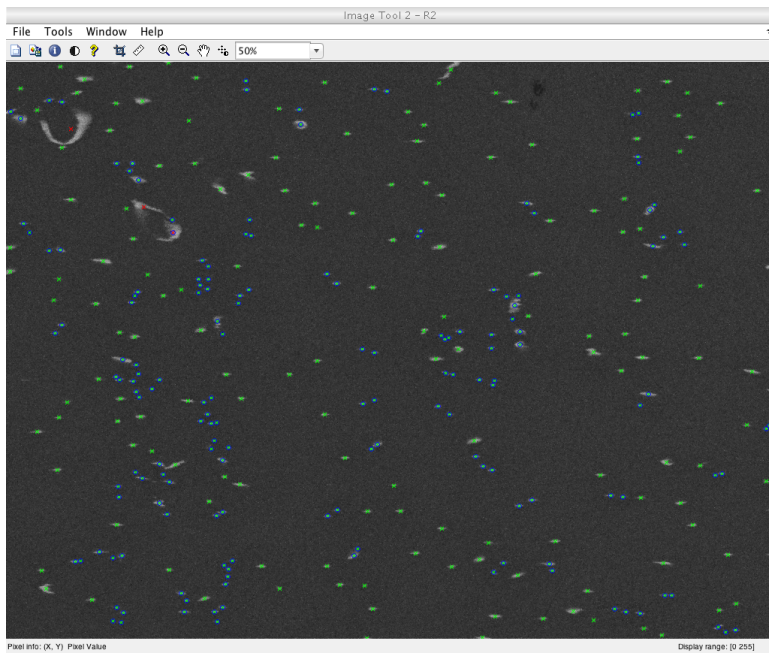
```



```
imtool(R2)
hold(imgca,'on')
plot(imgca, centroids(:,1), centroids(:,2),'gx')
plot(imgca, selcentroids(:,1), selcentroids(:,2),'rx')
plot(imgca, B(:,1), B(:,2),'b0' )
for k = 1 : size(A)
    xb = B(k,1);
    xc = C(k,1);
    yb = B(k,2);
    yc = C(k,2);

    line([xb,xc], [yb,yc], 'Color', 'k');
end

hold 'off'
```



Acknowledgment

First of all, I would like to appreciate my supervisor, Prof. T. Katsura, who patiently and largely guides my work during the Ph.D period. I also thank Nobuyoshi Miyajima, Prof. H. Kepler, and F. Heidelbach at University of Bayreuth for their help in sample analyses and discussions in this project. Further, I want to thank all the colleagues and technicians and staff members at Bayerisches Geoinstitut for their help.

(Eidesstattliche) Versicherungen und Erklärungen

(§ 8 S. 2 Nr. 6 PromO)

Hiermit erkläre ich mich damit einverstanden, dass die elektronische Fassung meiner Dissertation unter Wahrung meiner Urheberrechte und des Datenschutzes einer gesonderten Überprüfung hinsichtlich der eigenständigen Anfertigung der Dissertation unterzogen werden kann.

(§ 8 S. 2 Nr. 8 PromO)

Hiermit erkläre ich eidesstattlich, dass ich die Dissertation selbständig verfasst und keine anderen als die von mir angegebenen Quellen und Hilfsmittel benutzt habe.

(§ 8 S. 2 Nr. 9 PromO)

Ich habe die Dissertation nicht bereits zur Erlangung eines akademischen Grades anderweitig eingereicht und habe auch nicht bereits diese oder eine gleichartige Doktorprüfung endgültig nicht bestanden.

(§ 8 S. 2 Nr. 10 PromO)

Hiermit erkläre ich, dass ich keine Hilfe von gewerblichen Promotionsberatern bzw. -vermittlern in Anspruch genommen habe und auch künftig nicht nehmen werde.

.....
Ort, Datum, Unterschrift